



Rapid Prototyping Journal

The effects of moisture and temperature on the mechanical properties of additive manufacturing components: fused deposition modeling

Kim Eun-Seob Yong-Jun Shin Sung-Hoon Ahn

Article information:

To cite this document:

Kim Eun-Seob Yong-Jun Shin Sung-Hoon Ahn , (2016), "The effects of moisture and temperature on the mechanical properties of additive manufacturing components: fused deposition modeling", Rapid Prototyping Journal, Vol. 22 Iss 6 pp. - Permanent link to this document:

<http://dx.doi.org/10.1108/RPJ-08-2015-0095>

Downloaded on: 13 September 2016, At: 07:48 (PT)

References: this document contains references to 0 other documents.

To copy this document: permissions@emeraldinsight.com

The fulltext of this document has been downloaded 6 times since 2016*

Access to this document was granted through an Emerald subscription provided by emerald-srm:333301 []

For Authors

If you would like to write for this, or any other Emerald publication, then please use our Emerald for Authors service information about how to choose which publication to write for and submission guidelines are available for all. Please visit www.emeraldinsight.com/authors for more information.

About Emerald www.emeraldinsight.com

Emerald is a global publisher linking research and practice to the benefit of society. The company manages a portfolio of more than 290 journals and over 2,350 books and book series volumes, as well as providing an extensive range of online products and additional customer resources and services.

Emerald is both COUNTER 4 and TRANSFER compliant. The organization is a partner of the Committee on Publication Ethics (COPE) and also works with Portico and the LOCKSS initiative for digital archive preservation.

*Related content and download information correct at time of download.

The Effects of Moisture and Temperature on the Mechanical Properties of Additive Manufacturing Components: Fused Deposition Modeling

1. Introduction

Additive manufacturing (AM) has been widely used in the automotive, aerospace, biomedical, mechanical and jewelry industries (Gibson et al., 2010, Petrovic et al., 2011). AM can be used in the fabrication of complex three-dimensional (3-D) parts, aiding design optimization and the rapid production of customized parts (Huang et al., 2012). During the early development, AM was used only for initial prototypes and visual models owing to the low surface quality and weak strength of fabricated components. Given recent advances, AM is now also used for end-products (Wong and Hernandez, 2012). According to one study, the most common use for AM is in the fabrication of the final products of functional models (Wohlers and Caffrey, 2013). High quality AM components require high load carrying strength.

A typical AM process uses a 3-D printer (Stratasys) for fused deposition modeling (FDM) of acrylonitrile-Butadiene-styrene (ABS) plastic. Parts fabricated by FDM are formed in layers composed of fibers. A heater in the FDM head liquefies the material, which is extruded through a fine nozzle and deposited onto a platform (Upcraft and Fletcher, 2003). The FDM process is shown in **Figure 1**. FDM parts are used under various environmental conditions. For example, FDM components have been used as a mold for fabricating smart soft composites (SSCs) to cure polydimethylsiloxane (PDMS) (Kim et al., 2013, Rodrigue et al., 2014). Therefore, FDM parts are exposed to diverse environmental conditions, and there have been many studies on their mechanical properties and process conditions.

Agarwala et al. developed and implemented processing strategies to reduce internal defects in FDM-processed parts for structural ceramics and metals (Agarwala et al., 1996). Ahn et al. studied the characteristics of ABS parts fabricated by FDM 1650 (Ahn et al., 2002). Parameters such as bead width, air gap, build temperature, raster orientation, and color were investigated to identify their influence on the mechanical properties of FDM components. Air gap and raster orientation were found to be the most influential variables. Anisotropic tensile failure models of FDM parts were produced using composite classical lamination theory, and Tsai-Wu failure criterion (Ahn et al., 2003). The results showed that orientation strategy and raster angle were the most significant parameters in the fabrication of FDM components. Constitutive models of FDM parts have been investigated, demonstrating that finite element analysis can be used to predict their mechanical behavior (Bellini and Güceri, 2003, Mamadapur, 2007).

One quantitative benchmark study, of several RP processes and machines that use polymer materials (Oh and Kim, 2008), compared the mechanical properties of processes including stereolithography (SLA), laminated object manufacturing (LOM) and FDM. Several environmental conditions and build orientations were applied during the SL process, and the effects on the mechanical properties of a final product were studied (Puebla et al., 2012). The effect of moisture on the FDM of ABS material was tested by fabrication under ambient conditions, and in a desiccant chamber (Halidi and Abdullah, 2012).

However, there are insufficient studies on the effect of the environment on properties such as the water absorption, and thermal degradation of FDM parts.

In this study, FDM samples were produced in three different orientations, and the effects of moisture and temperature on their mechanical properties were tested. The results were compared with those collected from injection molded equivalents.

2. Experimental procedure

2.1. Fabrication of specimens

Reference injection molded samples were fabricated from ABS P400 material, which was also used for FDM samples. The fabrication procedure is shown in *Figure 2*. Aluminum molds for ASTM D3039 were fabricated by a three-axis CNC machine. Injection molding pellets were made by cutting 5-mm-long pieces from the FDM spool of ABS P400. A Morgan Press G-100T injection molding machine was used, and the control parameters are given in *Table 1*. Injection molded specimens are denoted by (a) in this paper. The tap for the tensile specimen was fabricated by PLA using an FDM machine (3DISON, Rokit Inc., Seoul, Korea).

A Dimension SST 768 machine (Stratasys®, Edina, MN, US) was used for the fabrication of FDM samples from ABS P400. The Catalysis software package (ver. 2.2) was used to convert 3-D CAD files as required. Catalysis uses an appropriate cross-deposition strategy, irrespective of shape and position. The cross-deposition and definition of the FDM build parameters is shown in *Figure 3*. The machine had no air gap, and cross-deposition meant that the raster angle of the upper and lower layers was at 90°.

As discussed previously, the raster angle is the most important factor in the manufacture of FDM parts (Ahn et al., 2002), but is not a controllable parameter in Catalysis (ver. 2.2). Though raster angle cannot be controlled, the orientation and deposition angle of FDM components can be selected. The plate and orientation controls are shown in *Figure 4*. The x, y and z axes are global coordinates shared between the software and the machine. Axes 1, 2, and 3 in *Figure 4* represent the principal direction of the FDM parts. The raster angle is always parallel to axis 1 or 2. The raster angle of the upper layer should be perpendicular to the lower layer when the lower layer is parallel with axis 1. Test specimens are shown in *Figure 4*. The air gap and layer thickness of the machine were 0 mm and 0.254 mm, respectively.

Three orientation configurations were considered in this experiment. FDM specimens with longitudinal axes that were parallel to the y-axis ((b) [-45°/45°]₅) were considered. As the mechanical properties of specimens whose longitudinal axes were parallel to the y-axis and x-axis were equivalent, specimens parallel to the x-axis were not considered (Mamadapur, 2007). FDM samples were fabricated in the xy plane at an angle of 45° to the machine's x-axis (parallel to the 1-axis) ((c) [0°/90°]₅). Finally, FDM specimens were fabricated with the longitudinal axis parallel to the z-axis ((d) vertical build). All specimens were fabricated based on ASTM 3039 (ASTM, 2000). The FDM sample dimensions were 127 ×

12.7× 2.54 mm.

2.2. Environmental testing

An environmental test was conducted to determine the tensile strength and Young's modulus, as a function of temperature and water absorption. ABS P400 begins to deform at 90°C, and the building temperature of the Dimensions SST 768 was 75 °C (Stratasys, 2006, Stratasys, 2011); tests were carried out at 20°C, 40°C, and 60°C.

Five samples without taps, and three samples with taps, were prepared for the water absorption and tensile tests. Water absorption tests were conducted by immersing specimens in distilled water at room temperature for increasing durations. When samples were removed from the bath, surface water was removed by a dry paper towel. Three specimens were weighed on a precision balance (AUX220, Shimadzu Co., Kyoto, Japan) with 0.001 g resolution, and their relative weight changes were measured. All samples were weighed in 2 hour intervals over 12 hours as the initial absorption rate was expected to be high. All specimens were then weighed at 12 hour intervals over a 100 hour period, followed by 24 hour intervals over 300 hours. Similarly, specimens were placed in a distilled water bath at 60°C to determine the water absorption rate at an increased temperature. For this test, the samples were placed in an environmental chamber (DWTH-155, Daihan, Gangwon-do, Korea). The measuring process and time intervals were kept the same. Tensile strength was tested after 200 hours, and compared with dry samples at room temperature, and at high temperature. A test matrix for these experiments is shown in

Table 2.

2.3. Mechanical testing

Tensile tests were conducted for each temperature and moisture condition with an Instron 5548 testing unit (Instron®, Norwood, MA, USA). The crosshead speed was set to 2 mm min⁻¹ in accordance with ASTM D3930 (ASTM, 2000). The tensile test unit calculates the tensile strength, elongation, and Young's modulus based on the material behavior. Temperature was controlled by performing the measurements in a forced convection chamber comprising a space heater (KSH-G2-10, KACON Co., Incheon, Korea), forced convection axial flow fan (9225S2HT, Shenzhen Motor Ltd., Quandong, China), temperature controller (FC-142, Taejin Electronics Co., Daejon, Korea), and temperature sensor (NTSE10K; Thinking Electronic Co., Kaohsiung, Taiwan). The forced convection temperature chamber could regulate the temperature within ± 1°C.

3. Results and Discussion

3.1 Water absorption behavior

A composite absorption model was used to calculate the water absorption rate (Shen and Springer, 1976). As FDM is a process based on laminating materials, the final product was considered to be a composite for the analysis of water absorption behavior. Weight gain as a result of water absorption was calculated with the following equation:

$$M(t) = \frac{m_t - m_0}{m_0} \times 100, \quad (1)$$

where $M(t)$ is the moisture content of the specimen at time t as a percentage of its mass, m_0 is the initial mass of the specimen, and m_t is the mass of the specimen after t seconds. The moisture content of the specimen can be expressed by the following equation (Shen and Springer, 1976):

$$M(t) = G(M_m - M_i) - M_i, \quad (2)$$

where M_i is the initial moisture content of the sample, M_m is the maximum moisture content that can be attained under the given environmental conditions, and G is a time-dependent total moisture content parameter that can be expressed by the following equation:

$$G = 1 - \frac{8}{\pi} \sum_{j=0}^{\infty} \frac{\exp\left[-(2j+1)^2 \pi^2 \left(\frac{Dt}{h^2}\right)\right]}{(2j+1)^2}. \quad (3)$$

where j is the summation index, D is the mass diffusivity in the material, and h is the sample thickness (2 mm). The diffusion coefficient, D , is a key parameter in the one-dimensional form of Fick's law (Bullions *et al.*, 2003, Dhakal *et al.*, 2007), according to the following formula:

$$D = \pi \left(\frac{h}{4M_m} \right)^2 \left(\frac{M_2 - M_1}{\sqrt{t_2} - \sqrt{t_1}} \right)^2, \quad (4)$$

where M_1 and M_2 are the moisture content at times t_1 and t_2 respectively. M_1 and M_2 are determined before 100 hours in each condition. **Figure 5** shows the weight change profiles for all specimens. Under each temperature condition, the water absorption behavior exhibited Fickian diffusion. Higher temperatures appeared to increase the water absorption rate. Although little difference was observed between the maximum moisture absorption rates as a function of temperature, the moisture content saturated in approximately half the time at 60°C. The maximum moisture absorption rate and diffusion coefficient of each sample is shown in **Table 3**. For injection molding, cross, crisscross, and vertically built components, the maximum moisture absorption rates at room temperature were 0.339%, 5.972%, 5.131%,

and 7.879%, respectively. The difference between the water absorption rates of the injection molded and FDM components shows that FDM parts have the void (Ahn *et al.*, 2002, Wang *et al.*, 2006).

3.2 Effect of environmental conditions on mechanical properties

Tensile test results showed that the tensile strength of FDM parts had approximately 26–56% of the strength of injection molded parts under dry, room temperature conditions. Stress and strain curves for each sample are given in **Figure 6**. The stress–strain curves differ by sample. Injection molded and cross specimens showed stiff, tough properties. Crisscross specimens showed soft and tough properties while vertically built samples were brittle (**Figure 6**). The temperature-dependent tensile strength profiles of each sample under dry conditions are given in **Figure 7**. The tensile strength of all specimens decreased linearly as temperature was increased. Tensile strength under dry, room temperature conditions was 32.6, 18.0, 15.8, and 8.6 MPa, for injection molded, cross, crisscross and vertical build specimens, respectively. Tensile strength was reduced by 19.9%, 30.6%, 24.5%, and 31.2%, respectively, at high temperatures. The Young's modulus was 1,530, 1073, 995.9, and 848.4 MPa, respectively, under dry, room temperature conditions. The modulus of FDM parts was approximately 55–70% that of the injection molded components.

The decrease in tensile strength, of FDM components as a result of high temperature under dry conditions, was greater than the decrease observed for injection molded components. The failure modes are shown in **Figure 8**. The failure modes of all samples were perpendicular to the loading direction, except for the crisscross specimen. The crisscross specimen was broken at 45° to the loading direction, as failure was caused by both shearing and tension (Ahn *et al.*, 2003). The failure modes did not differ with respect to temperature or moisture. **Figure 9** shows the tensile strength, Young's modulus and strain of each specimen under wet and dry conditions as a function of temperature. The effects of water absorption and temperature on mechanical properties can be quantified by the data given in **Figure 9**. Increasing the temperature of ABS increases strain, but strength and Young's modulus decreases (McKeen, 2007). Absorbing water decreased the strain, and increased temperature increased the strain. Under wet and hot conditions, the tensile strengths of the injection molded, cross, crisscross, and vertical build specimens were 22.0, 12.3, 11.3, and 5.81 MPa, respectively. The Young's modulus of each sample under wet and hot conditions was 1,208, 1,023, 946.5, and 769.1 MPa, respectively.

4. Conclusion

The effects of temperature and water absorption on the mechanical properties of FDM parts in three different orientations was studied and compared to injection molded components. The water absorption behaviors of each sample were also studied following immersion at room and high temperature. The water absorption at all temperatures was found to follow Fickian diffusion. FDM components were found to absorb water at a greater rate than injection molded parts because FDM components have cavities. The water absorption rate was accelerated by an increase in temperature, although the maximum water

absorption volume was not changed. As temperature and water absorption rates increased, the tensile strength and Young's modulus of both the injection molded and FDM components decreased linearly. Moisture had a more significant effect on ABS components. Under wet and hot conditions, the tensile strengths of injection molded, cross, crisscross, and vertical build samples were 67.5%, 68.4%, 71.6%, and 67.6% less, respectively, than under dry, room temperature conditions.

Acknowledgments:

This work was supported by Cooperative R&D between Industry, Academy, and Research Institute funded Korea Small and Medium Business Administration in 2013 (Grants No. C0097484), the Brain Korea 21 Plus Project in 2015, Bio-Mimetic Robot Research Center funded by Defense Acquisition Program Administration, the Industrial Strategic technology development program(10049258) funded by the Ministry of Knowledge Economy(MKE, Korea), and National Research Foundation of Korea (NRF-2010-0029227).

5. Reference

- AGARWALA, M. K., JAMALABAD, V. R., LANGRANA, N. A., SAFARI, A., WHALEN, P. J. and DANFORTH, S. C. (1996). "Structural quality of parts processed by fused deposition". *Rapid Prototyping Journal*, Vol. 2 No. 4, pp. 4 - 19.
- AHN, S.-H., BAEK, C., LEE, S. and AHN, I. S. (2003). "Anisotropic Tensile Failure Model of Rapid Prototyping Parts - Fused Deposition Modeling (FDM)". *International Journal of Modern Physics B*, Vol. 17 No. 8, pp. 1510 - 1516.
- AHN, S. H., MONTERO, M., ODELL, D., ROUNDY, S. and WRIGHT, P. K. (2002). "Anisotropic material properties of fused deposition modeling ABS". *Rapid Prototyping Journal*, Vol. 8 No. 4, pp. 248-257.
- ASTM (2000). Standard Test Method for Tensile Properties of Polymer Matrix Composite Materials. *Annual Book of ASTM Standards, Vol. 15.03*. West Conshohocken, PA: American Society for Testing and Materials.
- BELLINI, A. and G ERI, S. (2003). "Mechanical characterization of parts fabricated using fused deposition modeling". *Rapid Prototyping Journal*, Vol. 9 No. 4, pp. 252-264.
- BULLIONS, T. A., LOOS, A. C. and MCGRATH, J. E. (2003). "Moisture Sorption Effects on and Properties of a Carbon Fiber-reinforced Phenylethynyl-terminated Poly(etherimide)". *Journal of Composite Materials*, Vol. 37 No. 9, pp. 791-809.
- DHAKAL, H., ZHANG, Z. and RICHARDSON, M. (2007). "Effect of water absorption on the mechanical properties of hemp fibre reinforced unsaturated polyester composites". *Composites Science and Technology*, Vol. 67 No. 7-8, pp. 1674-1683.
- GIBSON, I., ROSEN, D. W. and STUCKER, B. (2010). *Additive Manufacturing Technologies*, Springer, New York.
- HALIDI, S. N. A. M. and ABDULLAH, J. "Moisture effects on the ABS used for Fused Deposition Modeling Rapid Prototyping Machine". 2012 IEEE Symposium on Humanities, Science and Engineering Research, 2012 Kuala Lumpur. IEEE, 839 - 843.
- HUANG, S. H., LIU, P., MOKASDAR, A. and HOU, L. (2012). "Additive manufacturing and its societal impact: a literature review". *The International Journal of Advanced Manufacturing Technology*, Vol. 67 No. 5-8, pp. 1191-1203.
- KIM, H.-J., SONG, S.-H. and AHN, S.-H. (2013). "A turtle-like swimming robot using a smart soft composite (SSC) structure". *Smart Materials and Structures*, Vol. 22 No. 1, pp. 014007.
- MAMADAPUR, M. S. A. (2007). *Constitutive Modeling Of Fused Deposition Modeling Acrylonitrile Butadiene Styrene (ABS)*. Master, Texax A&M University.
- MCKEEN, L. W. (2007). *Effect of Temperature and other Factors on Plastics and Elastomers*, Elsevier, Waltham, MA.
- OH, Y. T. and KIM, G. D. (2008). "A benchmark study on rapid prototyping processes and machines: quantitative comparisons of mechanical properties, accuracy, roughness, speed, and material cost". *Proceedings of the Institution of Mechanical Engineers, Part B: Journal of Engineering Manufacture*, Vol. 222 No. 2, pp. 201-215.
- PETROVIC, V., VICENTE HARO GONZALEZ, J., JORD FERRANDO, O., DELGADO GORDILLO, J., RAM N BLASCO PUCHADES, J. and PORTOL S GRI AN, L. (2011). "Additive layered manufacturing: sectors

- of industrial application shown through case studies". *International Journal of Production Research*, Vol. 49 No. 4, pp. 1061-1079.
- PUEBLA, K., ARCAUTE, K., QUINTANA, R. and WICKER, R. B. (2012). "Effects of environmental conditions, aging, and build orientations on the mechanical properties of ASTM type I specimens manufactured via stereolithography". *Rapid Prototyping Journal*, Vol. 18 No. 5, pp. 374 - 388.
- RODRIGUE, H., WANG, W., BHANDARI, B., HAN, M.-W. and AHN, S.-H. (2014). "Cross-shaped twisting structure using SMA-based smart soft composite". *International Journal of Precision Engineering and Manufacturing-Green Technology*, Vol. 1 No. 2, pp. 153-156.
- SHEN, C.-H. and SPRINGER, G. S. (1976). "Moisture Absorption and Desorption of Composite Materials". *Journal of Composite Materials*, Vol. 10 No. 1, pp. 2 - 20.
- STRATASYS (2006). Dimension BST 768/SST 768 User Guide. Eden Prairie, MN: Staratasys®.
- STRATASYS (2011). ABS P400. Eden Prairie: Staratasys®.
- UPCRAFT, S. and FLETCHER, R. (2003). "The rapid prototyping technologies". *Assembly Automation*, Vol. 23 No. 4, pp. 318-330.
- WANG, T.-M., XI, J.-T. and JIN, Y. (2006). "A model research for prototype warp deformation in the FDM process". *The International Journal of Advanced Manufacturing Technology*, Vol. 33 No. 11-12, pp. 1087-1096.
- WOHLERS, T. and CAFFREY, T. (2013). Wohlers Report 2013. *Additive Manufacturing and 3D Printing State of the Industry*.
- WONG, K. V. and HERNANDEZ, A. (2012). "A Review of Additive Manufacturing". *ISRN Mechanical Engineering*, Vol. 2012, pp. 1-10.

Author Biographies:

Eun-Seob Kim is a graduate student at the Innovative Design and Integrated Manufacturing Lab. in Department of Mechanical and Aerospace Engineering at Seoul National University. He received his B.S. degree majoring in mechanical engineering from Gyeongsang National University in 2013. His research interests include additive manufacturing technology, micro contact mechanics and adhesion properties deposited material.

Yong-Jun Shin graduated with master degree from the Innovative Design and Integrated Manufacturing Lab. in Department of Mechanical and Aerospace Engineering at Seoul National University. He received his B.S. degree majoring in mechanical engineering from Korea Advanced Institute of Science and Technology in 2013. He currently works at Hyundai Motor Company as a researcher. His research interests include energy efficient manufacturing and design optimization for a machine tool.

Professor Sung-Hoon Ahn is a director of the Innovative Design and Integrated Manufacturing Lab. in Department of Mechanical and Aerospace Engineering at Seoul National University. He received his B.S. degree in aerospace engineering from the University of Michigan, Ann Arbor, in 1992 and his M.S. and Ph.D. degrees in aeronautics and astronautics from Stanford University in 1994 and 1997, respectively. Before joining Seoul National University, he worked as a research associate at the University of California, Berkeley (1997-2000) and an assistant professor of Department of Mechanical and Aerospace

Engineering at Gyeongsang National University (2001-2003). His research interests include additive manufacturing, smart soft composite materials, green manufacturing, Internet-based design and manufacturing, micro/nano fabrication, nanocomposites, and appropriate technology.

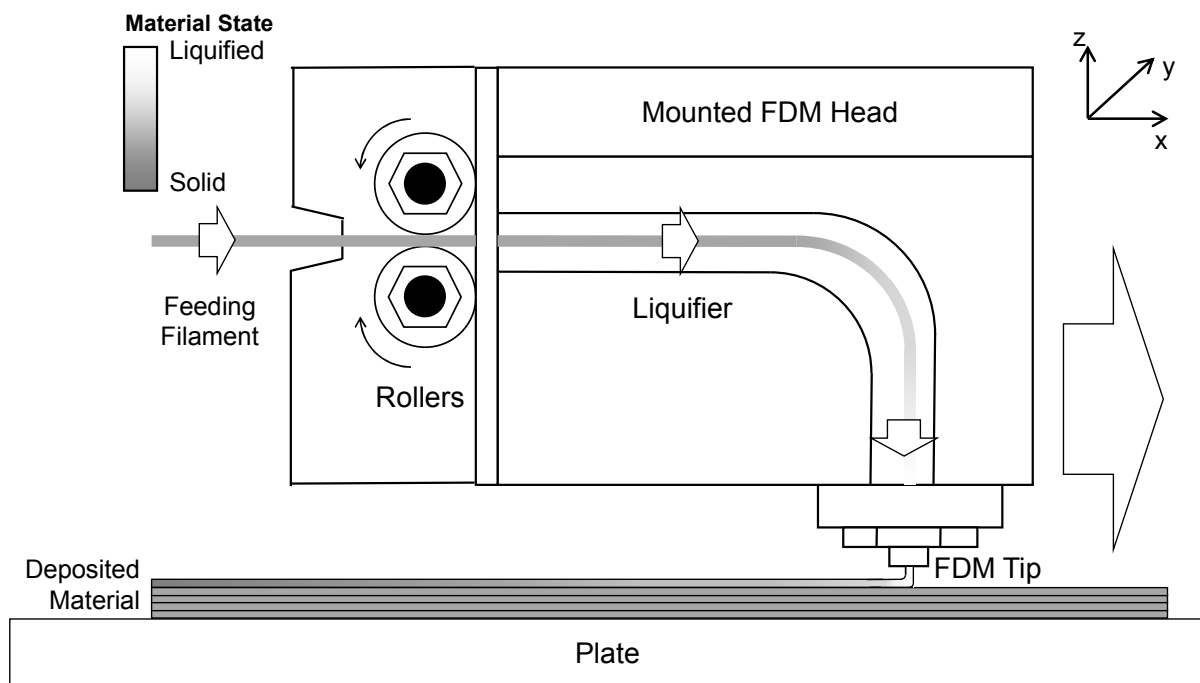


Figure 1 The fused deposition modeling (FDM) process (Ahn et al., 2002).

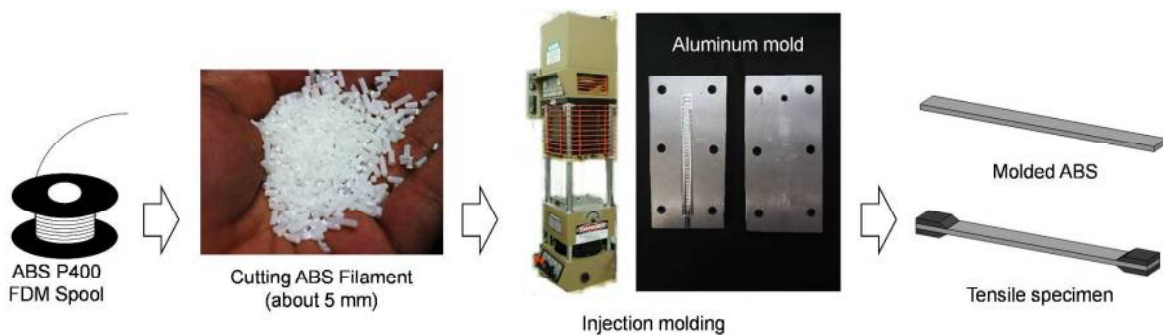


Figure 2 Fabrication procedure of injection molded specimens.

Table 1 Conditions of the injection molding process.

Description	Value
Nozzle temperature	270°C

Barrel temperature	260°C
Mold temperature	120°C
Clamping force	70 kN
Injection pressure	40 MPa

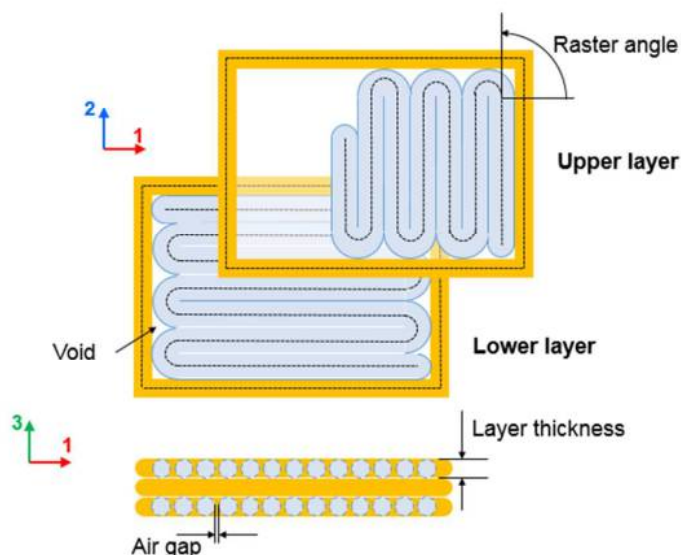


Figure 3 FDM building parameters, and cross deposition.

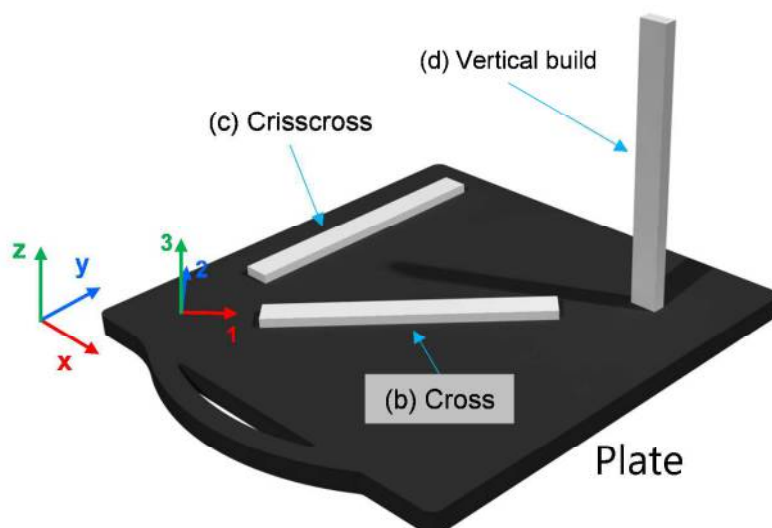


Figure 4 FDM specimens on the plate with coordinates.

Table 2 Test matrix of the environmental test.

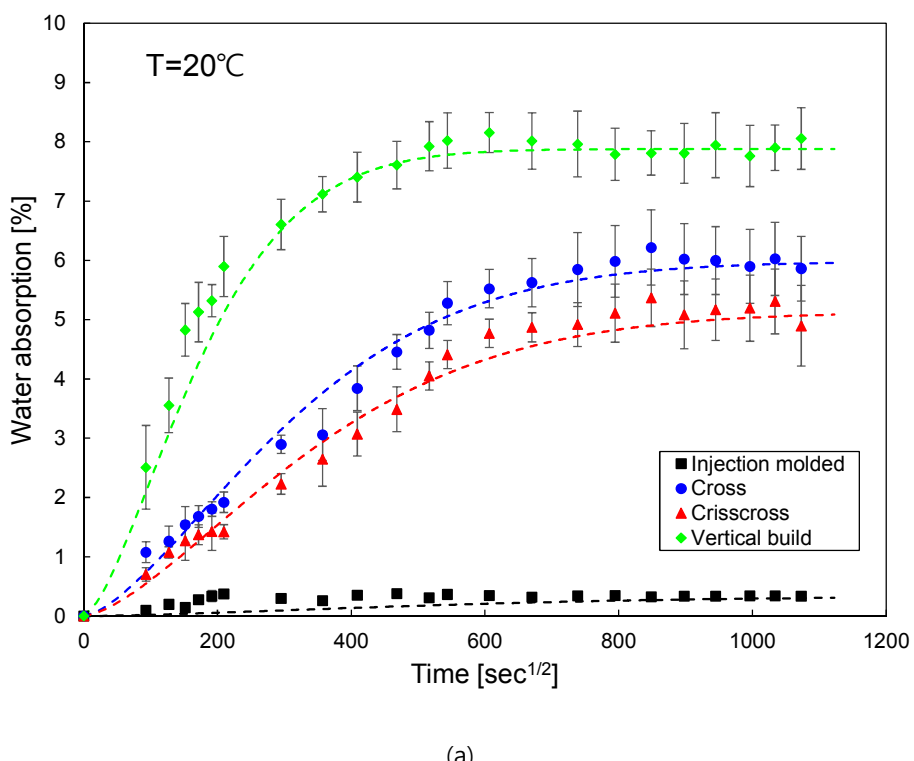
Environmental conditions	Test conditions	Type of specimens
Dry/RT, 40°C, 60°C ^a	RT, 40°C, 60°C	(a) Injection molded
Water/RT (200 hours) ^b	Dry/RT	(b) Cross (c) Crisscross
Water/60°C (200 hours) ^c	Dry/60°C	(d) Vertical build

a Temperature effect test

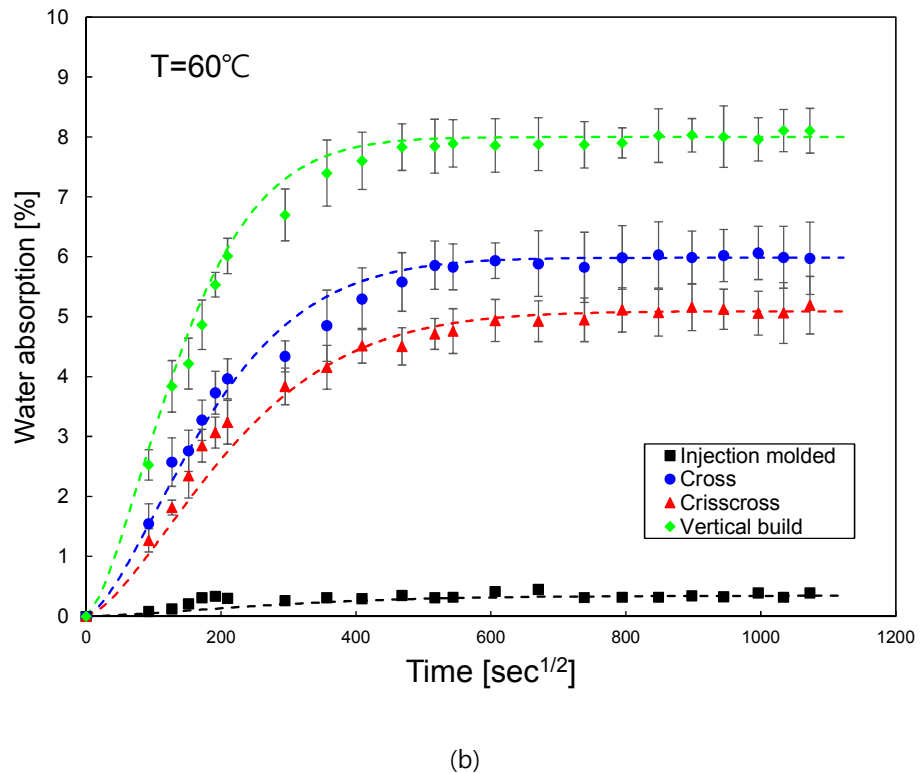
b Humidity effect test

c Temperature and humidity effect test

* Three specimens were used for each test condition.



(a)



(b)

Figure 5 Water absorption rate against square root time according to the environmental conditions: (a) room temperature (RT) and (b) high temperature (dashed lines indicate the theoretical Fickian diffusion).

Table 3 Water absorption results in water at RT and 60 °C

Type of specimen	Maximum water absorption, M_m (%)		Diffusion coefficient, D [mm^2/s] $\times 10^{-5}$	
	RT	60°C	RT	60°C
(a) Injection molded	0.339	0.341	0.176	0.182
(b) Cross	5.972	5.984	0.564	1.545
(c) Crisscross	5.131	5.090	0.428	1.099
(d) Vertical build	7.879	7.998	1.642	2.554

* Data are means of three samples for each specimen group
RT, room temperature

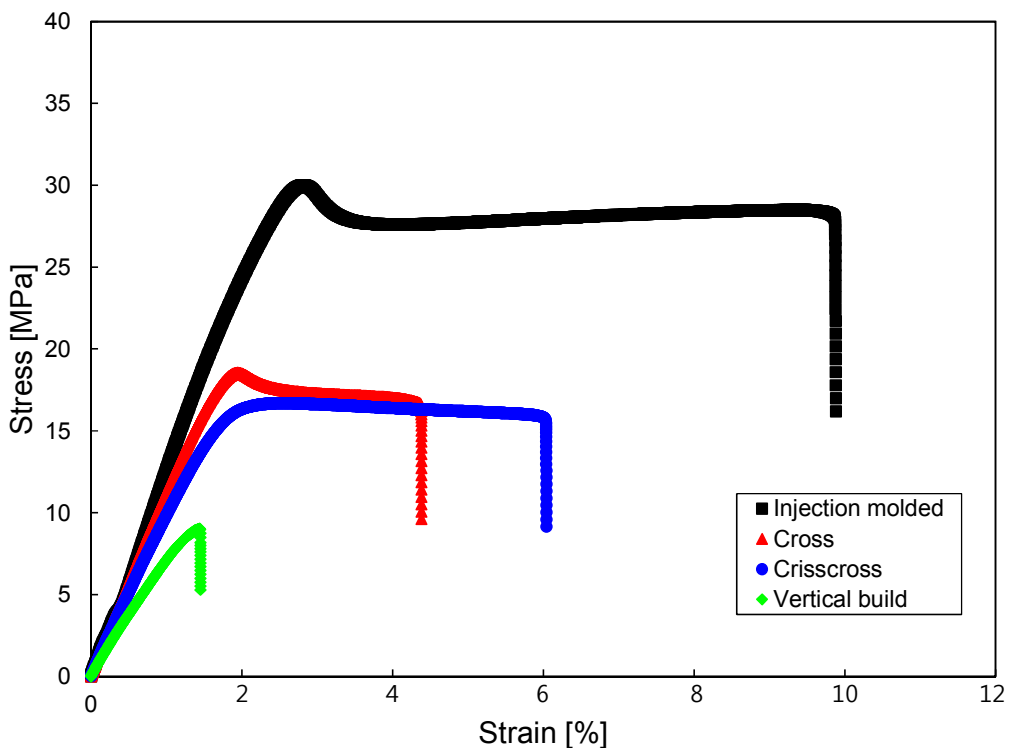


Figure 6 Representative stress-strain curves for specimens under dry, RT conditions.

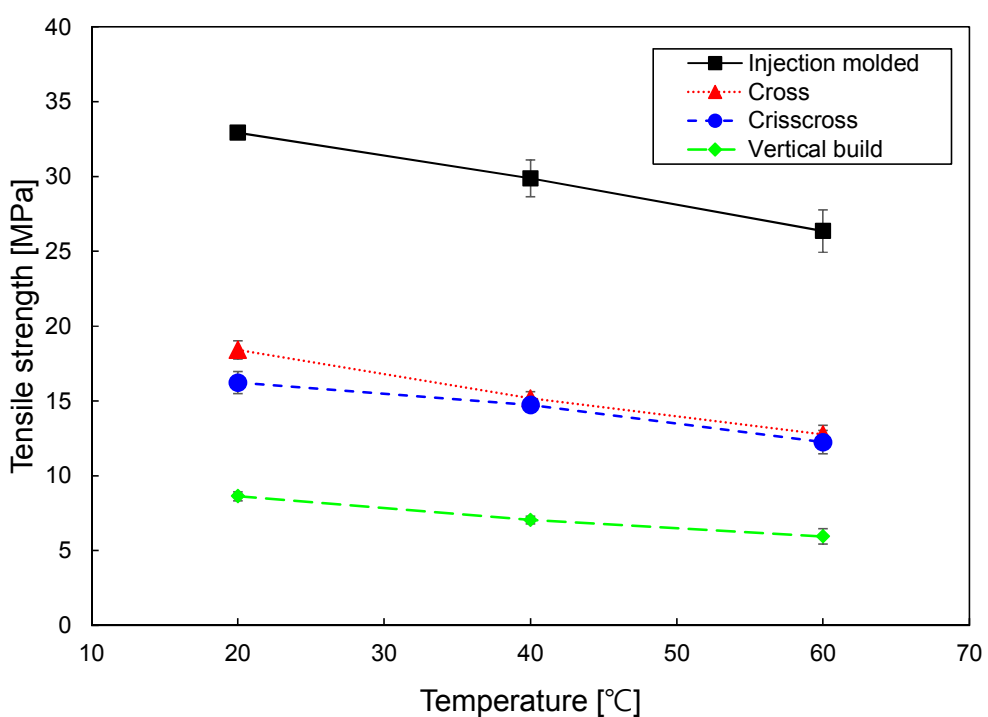


Figure 7 Tensile strength of several specimens under dry conditions at different temperatures.

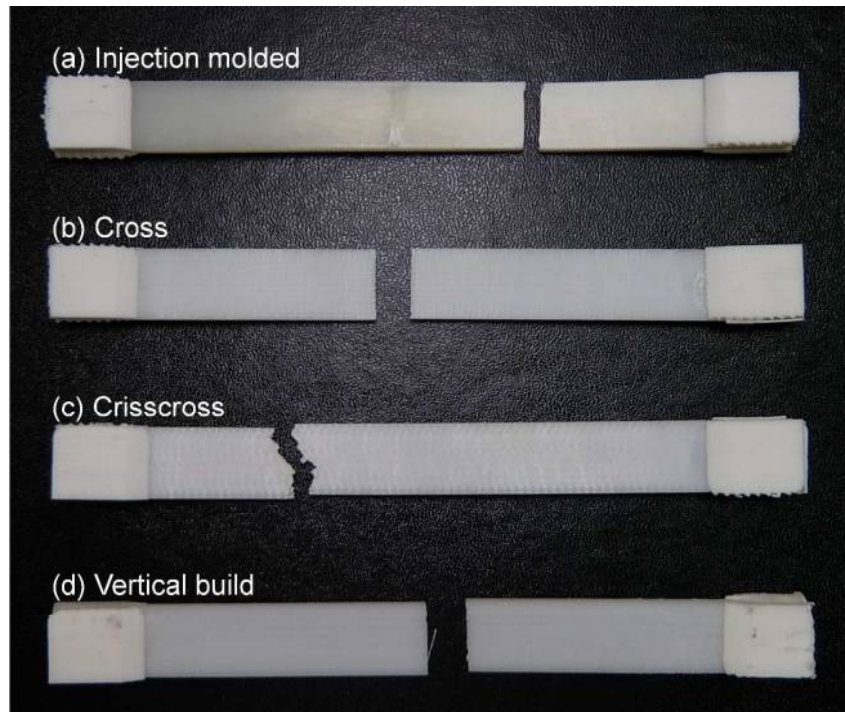
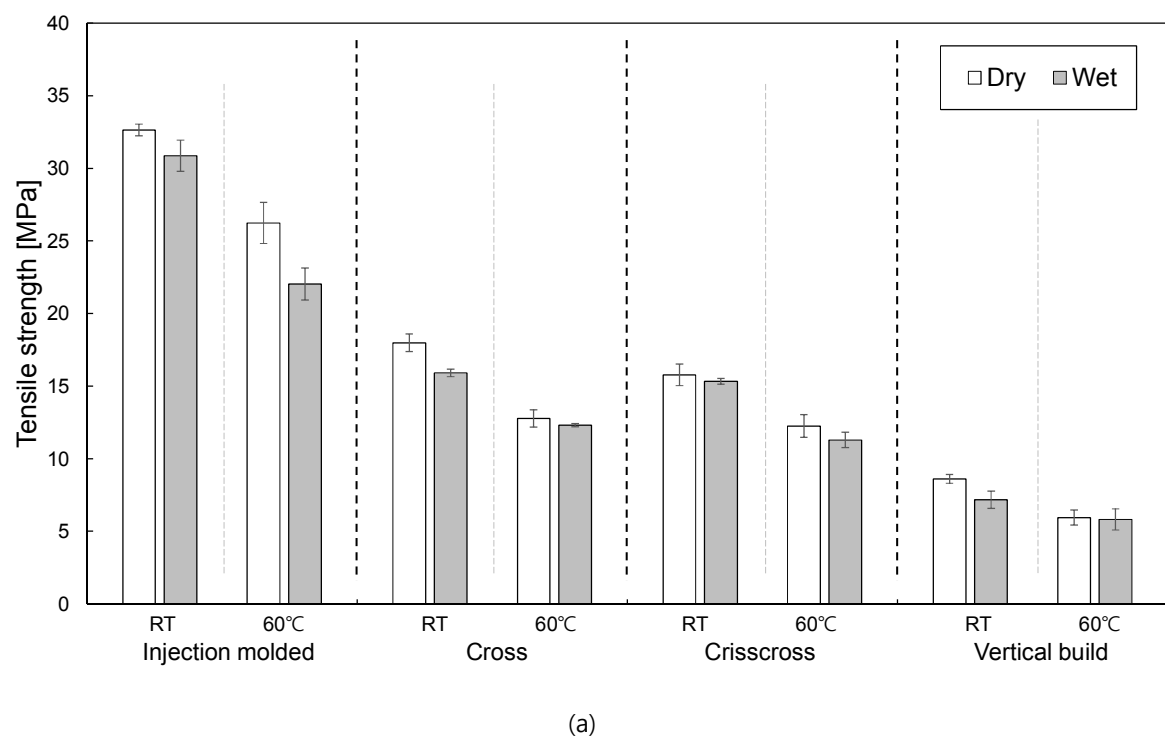


Figure 8 Failure modes of the specimens.



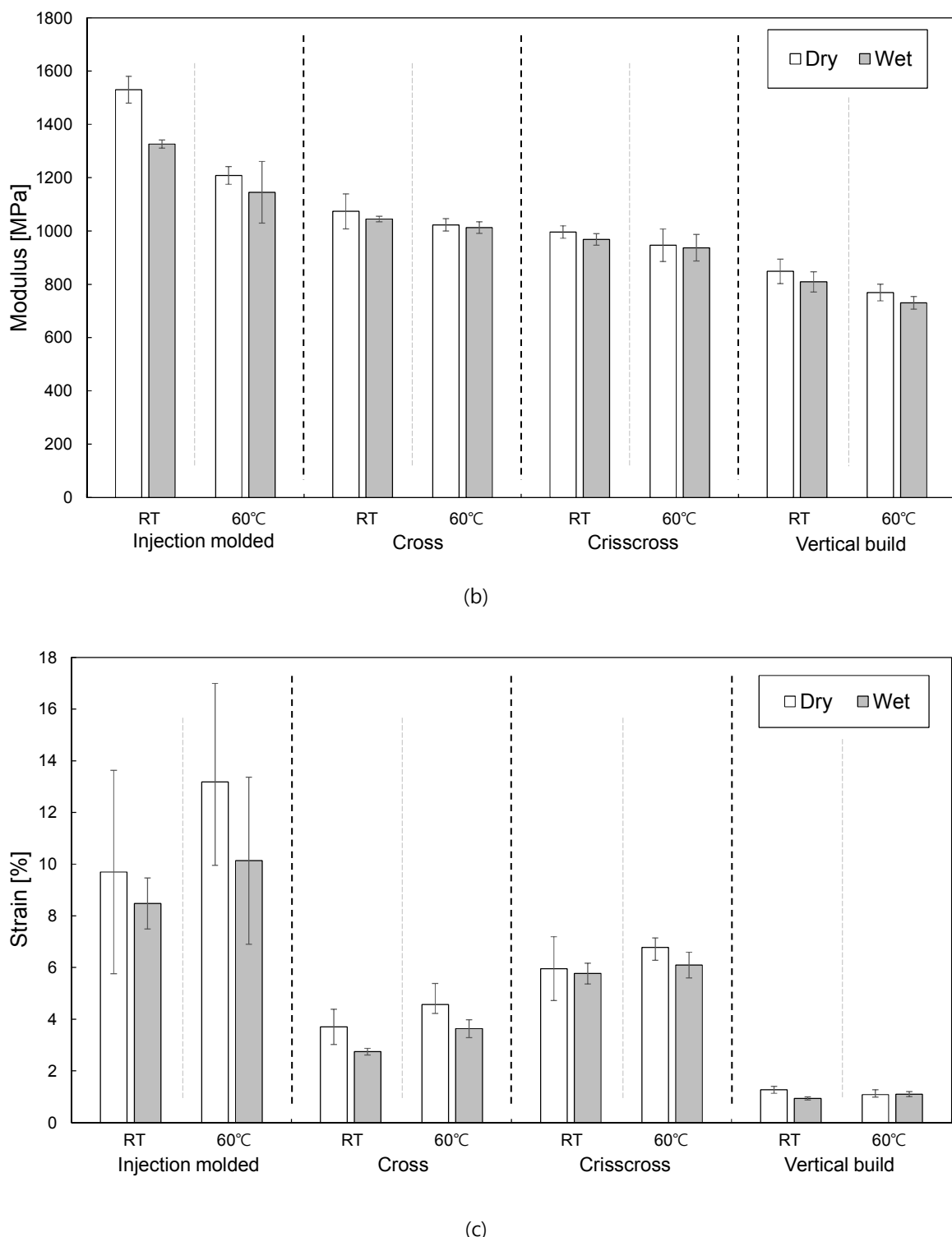
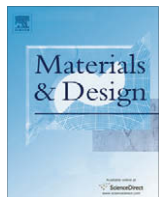


Figure 9 Tensile test results according to temperature and water absorption conditions for each specimen:
 (a) tensile strength, (b) modulus, and (c) strain.



Additive manufacturing of Ti-6Al-4V components by shaped metal deposition: Microstructure and mechanical properties

Bernd Baufeld^{a,*}, Omer Van der Biest^a, Rosemary Gault^b

^aKatholieke Universiteit Leuven, MTM, Kasteelpark Arenberg 44, 3001 Leuven, Belgium

^bUniversity of Sheffield, AMRC, Advanced Manufacturing Park, Wallis Way, Catcliffe Rotherham, S60 5TZ Sheffield, United Kingdom

ARTICLE INFO

Article history:

Received 17 July 2009

Accepted 16 November 2009

Available online 20 November 2009

Keywords:

- A. Non-ferrous metals and alloys
- D. Welding
- E. Mechanical

ABSTRACT

Shaped metal deposition (SMD) is a relatively new technology of additive manufacturing, which creates near-net shaped components by additive manufacture utilizing tungsten inert gas welding.

Especially for Ti alloys, which are difficult to shape by traditional methods and for which the loss of material during machining is also very costly, SMD has great advantages.

In the case of Ti-6Al-4V the dense SMD components exhibit large, columnar prior β grains, with a Widmanstätten α/β microstructure. These prior β grains are slightly tilted in a direction following the temperature field resulting from the moving welding torch. The ultimate tensile strength is between 929 and 1014 MPa, depending on orientation and location of the tensile specimens. Tensile testing vertically to the deposition layers exhibits a strain at failure of $16 \pm 3\%$, while testing parallel to the layers gives a lower value of about 9%.

© 2009 Elsevier Ltd. All rights reserved.

1. Introduction

Additive manufacturing is a relatively novel idea to fabricate complex, net-shaped metal components in successive layers. As a rapid prototyping technique, short lead-times are obtained and design changes can easily be incorporated. By omitting extensive machining, material costs and scrap can be reduced, leading to a lower environmental impact with a good economic balance.

Basically, three different additive manufacturing techniques for metals are currently under investigation: direct laser deposition [1–10], electron beam deposition [8,9,11,12] and shaped metal deposition (SMD) [13–20], which latter utilizes tungsten inert gas (TIG) welding. The different welding techniques may be complementary and selected depending on the required deposition velocity, size and surface quality, and on their applicability considering the complexity of the technique and the necessary atmosphere.

Direct laser deposition is a well established technique creating metal parts usually by direct sintering in a powder bed [1–7]. The laser set-up generally is large, requires high investments, and stringent safety measures have to be incorporated. A good surface finish is obtained, but the build volumes are limited to the size of the bed and the production rates are of the order of 50s of grams per hour. Recently, also wire instead of powder was used in order

to overcome contamination problems and high prices of high quality powders [8–10].

Electron beam deposition depends also on powders. Surface finish is not as good as for laser deposition, but mechanical properties are improved. However, high vacuum is required, which is more costly and technically complex than Ar atmosphere applied for direct laser deposition or SMD.

SMD uses TIG welding technologies and wire producing fully dense parts. The components are built layer by layer in a protected atmosphere and the welding robot is controlled directly according to a computer aided design model. Usually, the accuracy and surface finish are not as good as for either laser or electron beam processes. Yet, parts of up to 1 m^3 may be produced and up to 1 kg per hour can be deposited. Therefore, the speed of the process and ability to fabricate large near-net fully dense parts gives SMD an advantage to the other techniques.

SMD can be applied for any material which can be welded and is currently under investigation for different metals, such as Ni alloys [20], steels [18,19] and Ti alloys [13–17]. Especially for Ti alloys, which are difficult to shape by traditional methods and for which the loss of material during machining is also very costly, SMD has great advantages.

The alloy studied in the present paper is Ti-6Al-4V, one of the most important Ti alloys which is used in more than 50% of all commercial Ti applications [21]. The microstructure of this α/β alloy is very sensitive to the thermal history and different microstructures such as lamellar, equiaxed or bimodal microstructures can be obtained [22,23]. Additive manufacturing induces repeated

* Corresponding author. Tel.: +32 16321534; fax: +32 16321992.

E-mail addresses: bernd.baufeld@mtm.kuleuven.be (B. Baufeld), omer.vanderbiest@mtm.kuleuven.be (O. Van der Biest), r.gault@sheffield.ac.uk (R. Gault).

heat treatments with high cooling rates, leading to microstructures possibly different to the one of conventional material.

2. Experimental method and materials

2.1. Shaped metal deposition

The SMD set-up operates in an airtight chamber with controlled protecting Ar atmosphere with a purity of 99.999%. The TIG welding head is attached to a 6-axis Kuka robot, which is linked to a 2-axis table.

The welding wire is fed into the chamber through an annular feed pipe and is controlled via a motorized roller guide to ensure consistent delivery. Ti-6Al-4V wire with a diameter of 1.2 mm is used. The welding usually is performed in the forward feed mode, i.e. wire in front of the welding head, and anti-clockwise. Only component 31 was done rear feed and clockwise.

The applied welding parameters, such as electrical current, wire feed speed (WFS), and travel speed, are given in [Table 1](#). Here, travel speed is the resultant of the rotation and tilting of the table and the movement of the robot. Components were created rotating the table to keep a constant torch direction. Tubular shapes either with squared or circular cross sections were built. The size of the cross sections, the heights, and the wall thicknesses are also given in [Table 1](#). Examples of differently shaped components are shown in [Fig. 1](#).

While most components have wall thicknesses between 5 and 12 mm, the adjustment of the right welding parameters with minimized travel speed and maximized WFS resulted in single run the outstanding wall thickness of 20 mm ([Fig. 1c](#)).

Flat, dog-bone shape tensile specimens with a gauge length of 10 mm and a 3×2 mm² cross section within the gauge length have been prepared from different locations and orientations within component 09. The very top region of a component is denoted with location 1. Location 2 comprises a tested region between 1 and 5 cm, and location 3 a region more than 8 cm below the top. The different orientations are designated with H and V, standing for specimens with tensile direction horizontal and vertical to the deposition plane. Further tensile tests with components fabricated with different deposition parameters are scheduled.

The tensile tests were performed in an Instron testing machine (TTDL model with a maximum load of 100 kN) with a displacement rate of 0.5 mm/min. The strain at failure was determined by measuring the length of the parts of the fractured specimens.

Vickers micro-hardness was measured with a Leitz micro-hardness tester with a load of 100 g on polished cross sections. Lines of about 40 indents from top towards the bottom were performed on

cross sections in order to get reasonable statistics and information on possible changes over the component height.

3. Results

3.1. Surface morphology

Viewed from the side, all components exhibit periodic bulges, reflecting the layers of separate SMD steps, and large columnar grains ([Fig. 2](#)). These are prior β grains which have grown epitaxially, pervading the weld layers ([Fig. 2b](#)). They are inclined along the steepest temperature gradient during welding. By reversing the travel direction of the weld head the inclination can be changed ([Fig. 2a](#)). Similar large columnar grains were also observed for components fabricated by laser [[2–4,6,10](#)] and electron beam deposition [[11](#)].

Despite the high purity Ar atmosphere, some, but not all, of the components have a colorized surface after manufacturing ([Fig. 1b](#) and c), indicating a very thin oxide layer. It is not yet understood, how to prevent this colorization. Yet, it is believed that this colorization is just a cosmetic fault not degrading the properties. This belief is supported by bulk oxygen concentrations of 0.16 wt.% and nitrogen concentrations of 0.0041 wt.%, which are similar to the original concentration of the wire [[16](#)].

3.2. Microstructure

Etched cross sections of all components reveal aslant cut prior β grains ([Fig. 3a](#)). Furthermore, two distinct regions can be discerned: a bottom region with parallel bands and a top region without these bands. The parallel bands are not directly related with the deposition layers, since they do not coincide with them ([Fig. 3b](#)). Similar parallel bands in the bottom region were not only reported for SMD components [[14,16](#)], but also for components fabricated by laser [[2,3](#)] and electro beam deposition [[11](#)].

The microstructure in both regions consists for all components mostly of Widmanstätten structures [[23,24](#)]. These are α phase lamellae in a β phase matrix exhibiting either a basket weave or a colony structure, which are different in size in both regions. The top region displays very fine lamellae ([Fig. 4a](#)), whereas the bottom region consists of much thicker lamellae ([Fig. 4b](#)). Colonies habitually grow from prior β grain boundaries, which are decorated by an α phase ligament, and from the component surfaces. Colony structures also characterize the boundary of the parallel bands [[3,14,16](#)]. Basket weave structures commonly are in the center of the parallel bands, and also in the lower part of the top region. This agrees with results from components built by laser deposition [[3](#)].

Table 1
Exemplary deposition parameters and the resulting geometry of different SMD components.

Component name	Geometry				Deposition parameters			Height of top region (mm)	Hardness (GPa)
	Shape	Wall width (mm)	Size (mm)	Height (mm)	Current (A)	WFS (m/min)	Travel speed (m/min)		
9	Square	8.8	150	120	150	2.1	0.30	8.8	3.2
21	Square	9.5	150	70	183	2.2	0.25	8.7	3.3
22	Square	9.5	150	70	165	1.4	0.25	8.8	3.5
24	Square	9.9	150	70	183	2.4	0.30	8.9	3.7
36	Square	9.1	275	70	177	2.0	0.30	7.5	3.5
50	Square	19.8	100	25	221	7.7	0.10	12.2	3.4
31	Cylinder	8.6	100	100	164	2.1	0.30	13.0	3.4
32	Cylinder	10.2	100	100	171	2.4	0.30	13.6	3.4
42	Cylinder	7.7	200	75	163	1.3	0.40	8.0	3.6
44	Cylinder	5.0	200	75	110	0.7	0.40	4.8	3.5
45	Cylinder	6.7	100	75	110	0.6	0.25	7.6	3.5

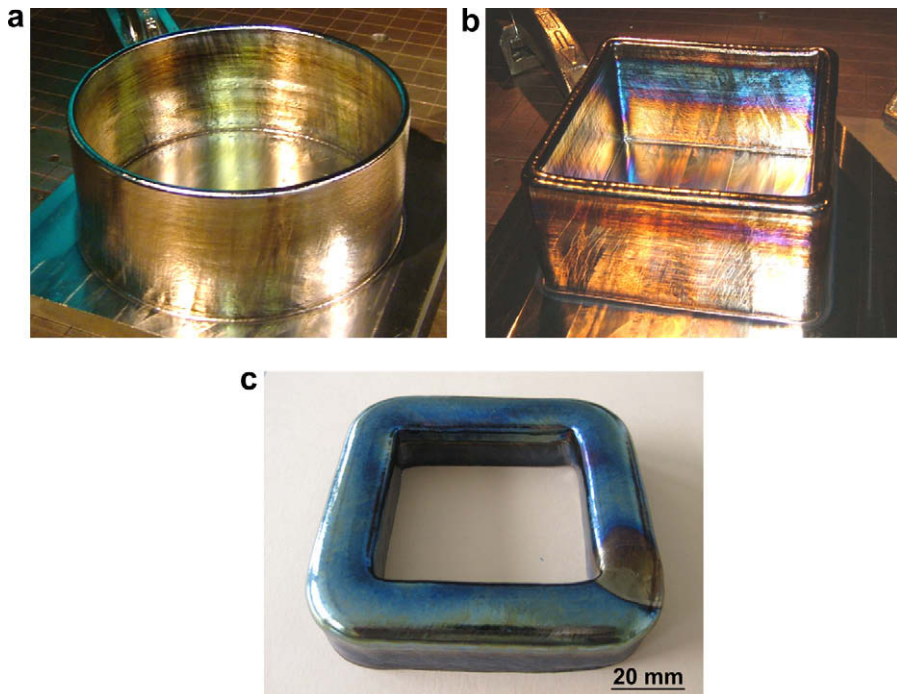


Fig. 1. Examples for tubular components with round (a: component 43) and squared cross section (b: component 24, c: component 50). Component 50 exhibits maximized wall thickness of 20 mm.

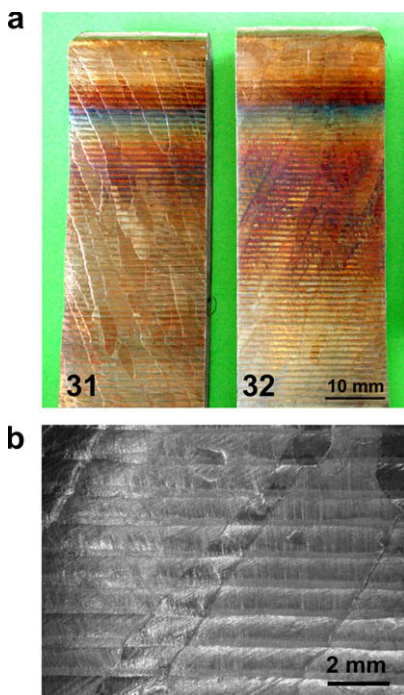


Fig. 2. View on the outer surfaces of component 31 (clockwise deposition) and 32 (anti-clockwise deposition) in overview (a) and of component 32 in detail (b), exhibiting the layers and the inclined, elongated, prior β grains.

In addition, convex bands however much weaker in contrast than for the parallel bands are observed (Fig. 3a). They occur in the top and in the bottom region (Fig. 3a), but in the bottom region they are frequently difficult to discern. If possible to trail these bands towards the surfaces, they end in the dent between two layer bulges. The very top convex band always ends at the dent be-

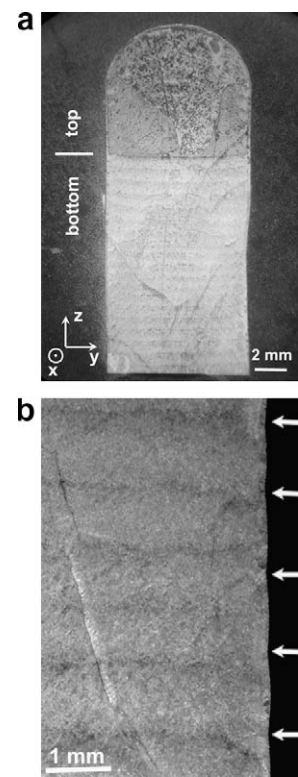


Fig. 3. Light optical micrographs of etched cross sections of component 22 (a) and in detail the parallel bands of component 9 (b).

tween the top and the second top layer. It must be stressed, that melted material may not only consist of the deposition material but also may include remelted material of previous depositions. To the authors knowledge these convex bands are not yet reported for other additive manufactured components.

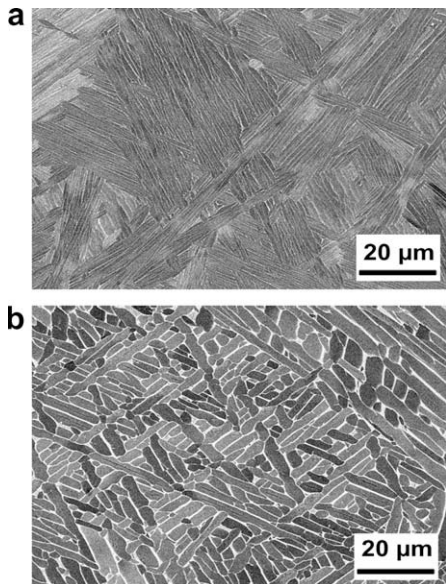


Fig. 4. Scanning electron micrograph from the top (a) and the bottom region (b) of component 31.

While within one component a large variety of different microstructures was found, no significant difference between the different components was observed.

3.3. Mechanical testing

The tensile deformation curves exhibit extensive plastic deformation with limited work hardening. Fig. 5a shows the ultimate tensile strength (UTS) and the strain at failure of tensile specimens derived from component 9. The UTS is between 929 and 1014 MPa, depending on orientation and location of the tensile specimens. H1 specimens from the top region exhibit a higher UTS than H2 specimens from the bottom region. The UTS for H orientations is slightly higher than for V orientation. No significant difference was observed between V2 and V3. Relating the UTS with the lamellae width gives an inverse correlation (Fig. 5b).

The strain at failure is very sensitive to orientation and to some extent to location. Generally, it is significantly smaller for H (9 and 10%) than for V orientation (9–21%). Furthermore, the strain at failure is somewhat higher for V2 than for V3.

The micro-hardness shows a certain scatter for all components, yet no dependence on the wall height: the hardness in the top and in the bottom region does not differ. No clear dependence on the deposition parameters can be reported (Table 1).

4. Discussion

4.1. Band structures

The two differently shaped bands must result from the thermal history of repeated SMD steps. The parallel bands in the bottom part must form late in the fabrication history, since such straight horizontal lines agree with isotherms only at a certain distance from the curved weld front [14]. Since they do not coincide with the bulges at the component surfaces (Fig. 3b), which represent the molten material during one deposition step, and since the top parallel band is too far from the region of the molten material of the last deposition step, they cannot result from the liquidus line. Several authors have ascribed the β transus to the formation

of the parallel bands [3,4,14–16]. The top of the uppermost parallel band indicates the β transus line during the last SMD step and the bands below result from β transus lines from previous SMD steps. Kelly and Kampe have modeled this in detail [3,4].

The convex bands, however, are related with the layered bulges at the wall surface. Especially the very top convex band coincides with the melted material during the last SMD step. Furthermore, modeled isotherms near the top exhibit similar convex shapes [15]. Hence, these convex bands represent the liquidus of subsequent SMD steps.

4.2. Microstructure

The fine Widmanstätten structure in the top and a coarse Widmanstätten structure in the bottom region result from the repeated heat treatment by SMD. During the last SMD step, the top region has been in the β phase field, and has only short time to transform during the relatively fast cooling into a fine Widmanstätten structure [4,16]. The bottom region however was subjected to subsequent heat treatments in the α/β phase field allowing diffusive element partition which results into a coarsening of the α lamellae [4,16].

4.3. Mechanical properties

The additive manufacturing of Ti–6Al–4V components by SMD leads to large columnar prior β grains. Similar columnar grains were also reported for components fabricated by laser [2,3,6,10] and electron beam deposition [11]. Such large grains naturally are very striking and, considering the Hall Petch relation of grain boundary strengthening, could be interpreted as an adverse property for the strength. However, one has to keep in mind that not the size of the prior β grains but rather the much finer Widmanstätten structure may determine the strength. It is claimed for Ti alloys with fully lamellar microstructure that the yield stress decreases with increasing slip length [25]. Since in the present case little work hardening is observed, also the UTS should decrease with the slip length. In the case of α lamellae separated by the β phase, it is assumed that the width of the α lamellae determines the effective slip length. Therefore, the UTS should decrease with increasing lamellae width, which agrees with experimental results as shown in Fig. 5b. Specimens from the top region of the component (H1), comprising finer α lamellae, exhibit a higher UTS than specimens from the bottom region (H2), which show much coarser lamellae.

The higher strain at failure for V orientation compared to H orientation, also observed for components fabricated by laser or electron beam deposition [9,10], must be attributed to the orientation of the prior β grains growing roughly in the vertical direction (Fig. 2a) [17]. Due to the orientation of these grains, tensile H specimens contain grains which are in average smaller and have a higher amount of grain boundaries than V specimens. Because grain boundaries are potential sources of failure, the H orientation exhibits a lower strain at failure compared to the V orientation.

In the present work the tensile properties were investigated for just one set of SMD parameters. In future, more work will be dedicated to investigate the influence of the deposition parameters on the tensile properties. However, since the hardness, which is related with the strength, does not vary much for different components, not much variation in the tensile properties is expected. Since only within a relatively small parameter window good components are obtained, no large variation can be investigated.

ASTM asks as minimum requirements for cast material a strain at failure of 8% and an UTS of 860 MPa (ASTM F1108) and for wrought material 10% and 930 MPa (ASTM F1472).

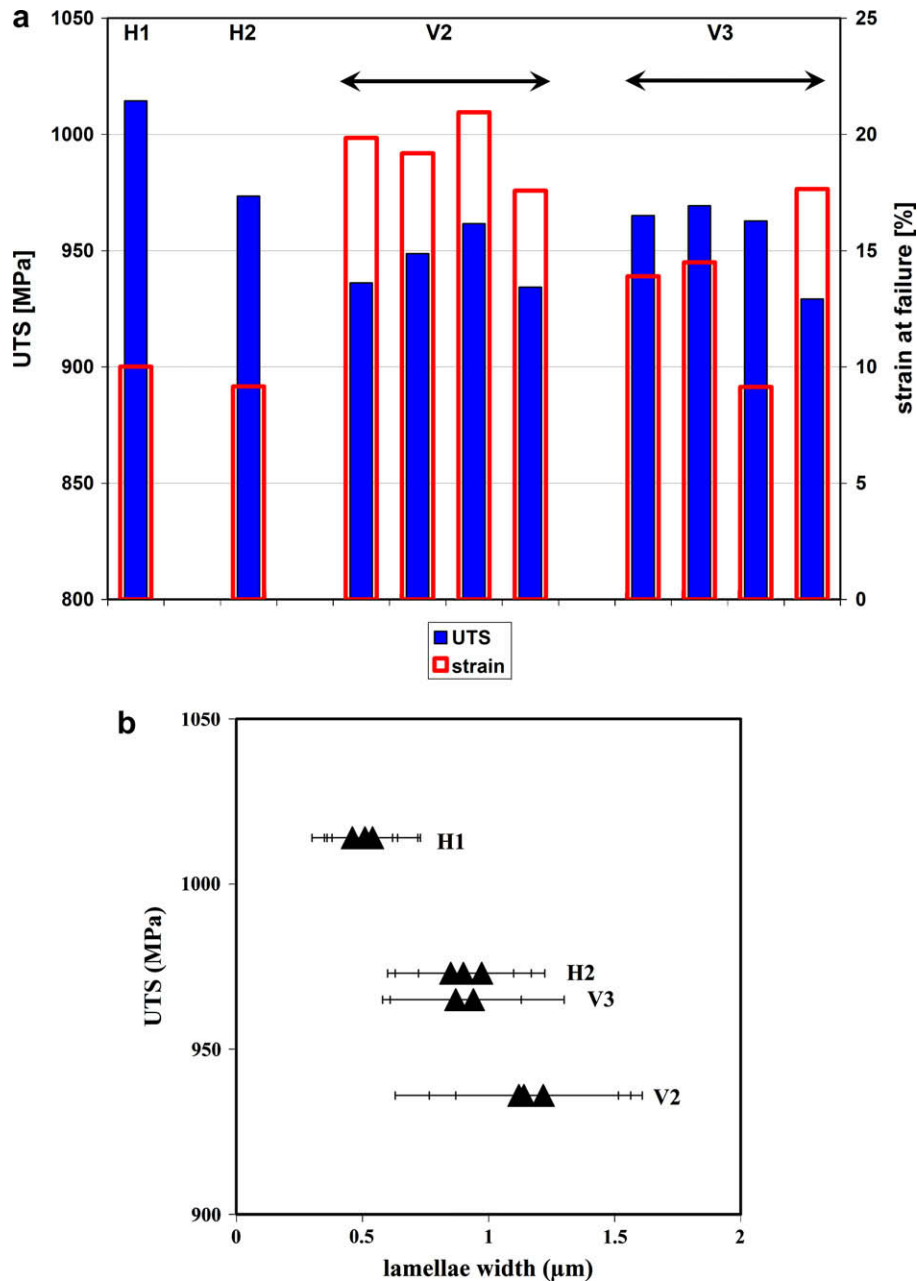


Fig. 5. UTS and strain at failure (a) and UTS in dependence on the lamellae width (b) of tensile specimens from component 9 with different orientations and from different locations.

Hence, in the current investigation the quality of SMD components fulfill at least the requirements for cast material. In comparison with other techniques are the results for SMD within the range of results reported for laser [1,7–10] and electron beam deposition [8,9,11]. Early work with laser deposition [1] probably suffers of high porosity between deposited layers. Very low ductility is reported for the *V* direction (0.8%) and a higher ductility (4.9%) for the *H* direction. This behavior, opposite to the present investigation, was related to lack of fusion porosity. In agreement with the present findings, Brandl et al. [9] show a much higher ductility for the *V* than for the *H* orientation for laser deposited components. Yet, their ductility values are a bit lower than the present SMD experiments. The ductility of electron beam deposited components is almost independent on the direction (*H*: ~12%, *V*: ~13.8%) [9].

5. Conclusions

Shaped metal deposition allows the production of large and dense Ti-6Al-4V components with different shapes. In a single run, wall widths between 5 and 20 mm can be achieved. A top and a bottom region can be discerned for all components, where the Widmanstätten microstructure consists of fine α lamellae in the top and coarse lamellae in the bottom region.

The mechanical properties are competitive to cast material and components built by other additive manufacturing techniques. The UTS varies between 929 and 1014 MPa, depending on orientation and location of the specimens. Generally, the strain at failure is two to three times larger in *V* than in *H* direction. The differences in the UTS and strain at failure can be related to the α lath size and to the orientation of the elongated, prior β grains.

Acknowledgments

The research is performed with financial assistance from the RAPOLAC STREP project under contract number 030953 of the 6th Framework Programme of the European Commission (www.RAPOLAC.eu), which is gratefully acknowledged.

References

- [1] Kobryn PA, Semiatin SL. Mechanical properties of laser-deposited Ti-6Al-4V. In: Bourrell DL, Beaman JJ, Crawford RH, Marcus HL, Wood L, Barlow JW, editors. Solid freeform fabrication. The University of Texas at Austin: Austin (TX, USA); 2001.
- [2] Kobryn PA, Semiatin SL. Microstructure and texture evolution during solidification processing of Ti-6Al-4V. *J Mater Process Tech* 2003;135:330–9.
- [3] Kelly SM, Kampe SL. Microstructural evolution in laser-deposited multilayer Ti-M-4V builds: Part I. Microstructural characterization. *Metall Mater Trans A* 2004;35A:1861–7.
- [4] Kelly SM, Kampe SL. Microstructural evolution in laser-deposited multilayer Ti-6Al-4V builds: Part II. Thermal modeling. *Metall Mater Trans A* 2004;35A:1869–79.
- [5] Qian L, Mei J, Liang J, Wu X. Influence of position and laser power on thermal history and microstructure of direct laser fabricated Ti-6Al-4V samples. *Mater Sci Tech* 2005;21:597–605.
- [6] Nowotny S, Scharek S, Beyer E, Richter K-H. Laser beam build-up welding: precision in repair, surface cladding, and direct 3D metal deposition. *J Therm Spray Tech* 2007;16:344–8.
- [7] Dinda GP, Song L, Mazumder J. Fabrication of Ti-6Al-4V scaffolds by direct metal deposition. *Metall Mater Trans A–Phys Metall Mater Sci* 2008;39A:2914–22.
- [8] Brandl E, Leyens C, Palm F, Schoberth A, Onteniente P. Wire instead of powder? Properties of additive manufactured Ti-6Al-4V for aerospace applications. Berlin, Germany, Fraunhofer-Allianz: Euro-uRapid; 2008.
- [9] Brandl E, Leyens C, Palm F. Mechanical properties of additive manufactured Ti-6Al-4V using wire and powder based processes. Sheffield (UK): Trends in Aerospace Manufacturing (TRAM); 2009.
- [10] Brandl E, Leyens C, Dalle-Donne C, Holzinger V. Deposition of Ti-6Al-4V using Nd:YAG laser and wire: microstructure and mechanical properties. In: NATO AVTZ-163 Specialists meeting on additive technology for repair of military hardware. Bonn, NATO/PFP; 2009
- [11] Taminger KM, Hafley RA. Electron beam freeform fabrication for cost effective near-net shape manufacturing. In: NATO/RTOAVT-139 specialists' meeting on cost effective manufacture via net shape processing. Amsterdam (The Netherlands): NATO; 2006
- [12] Arcam; 2008. <www.arcam.com>.
- [13] Katou M, Oh J, Miyamoto Y, Matsuura K, Kudoh M. Freeform fabrication of titanium metal and intermetallic alloys by three-dimensional micro welding. *Mater Des* 2007;28:2093–8.
- [14] Charles C, Järstrat N. Development of a microstructure model for metal deposition of titanium alloy Ti-6Al-4V. In: 11th World conference on titanium (Ti-2007). Kyoto, Japan; 2007
- [15] Charles C, Järstrat N. Modelling Ti-6Al-4V microstructure by evolution laws implemented as finite element subroutines: application to TIG metal deposition. In: 8th International conference on trends in welding research. Pine Mountain, GA, USA; 2008.
- [16] Baufeld B, Van der Biest O, Gault R. Microstructure of Ti-6Al-4V specimens produced by shaped metal deposition. *Int J Mater Res* 2009;100.
- [17] Baufeld B, Van der Biest O. Mechanical properties of Ti-6Al-4V specimens produced by shaped metal deposition. *Sci Tech Adv Mater* 2009;10:10.
- [18] Skiba T, Baufeld B, van der Biest O. Microstructure and properties of 300M steel components prepared by shaped metal deposition. *J Iron Steel Res Int*, in press.
- [19] Skiba T, Baufeld B, Van der Biest O. Microstructure and mechanical properties of stainless steel component manufactured by shaped metal deposition. *ISIJ Int* 2009;49:1588–91.
- [20] Clark D, Bache M, Whittaker M. Shaped metal deposition of a nickel alloy for aero engine applications. *J Mater Process Tech* 2008;203:439–48.
- [21] Peters M, Leyens C. Titanium and titanium alloys. Wiley-VCH: Weinheim; 2003. 513 p.
- [22] Boyer R, Welsch G, Collings EW. Materials properties handbook: titanium alloys. The Materials Information Society; 1994.
- [23] Lampman SR. Wrought titanium and titanium alloys. In: Davis JR, Allen P, editors. ASM Handbook. Properties and selection: nonferrous alloys and special-purpose materials, vol. 2. ASM International; 1990.
- [24] Ahmed T, Rack HJ. Phase transformations during cooling in $\alpha + \beta$ titanium alloys. *Mater Sci Eng A* 1998;243:206–11.
- [25] Lütjering G. Influence of processing on microstructure and mechanical properties of $(\alpha + \beta)$ titanium alloys. *Mater Sci Eng A* 1998;243:32–45.



Microstructure and mechanical properties of additive manufactured copper alloy



A. Popovich, V. Sufiarov, I. Polozov*, E. Borisov, D. Masaylo, A. Orlov

Peter the Great St. Petersburg Polytechnic University, 195251, Polytechnicheskaya, 29, Saint Petersburg, Russia

ARTICLE INFO

Article history:

Received 27 February 2016

Received in revised form

16 April 2016

Accepted 7 May 2016

Available online 9 May 2016

Keywords:

Additive manufacturing

Selective laser melting

Copper alloy

Microstructure

Mechanical properties

ABSTRACT

Cu-Cr-Zr-Ti alloy specimens have been fabricated by selective laser melting (SLM) technology with a high relative density. Their microstructure and mechanical properties at room conditions as related to elevated temperatures have been investigated after solution annealing and aging of the material and compared to hot-rolled samples. The microstructure of the SLM material consists of grains elongated along build direction with the size in the range from 30 to 250 μm . The mechanical test showed that the SLM material has 195–211 MPa ultimate tensile strength (UTS) and 11–16% elongation at break at 20 °C. Samples produced parallel to the build direction show slightly higher UTS and elongation at break in comparison with samples fabricated perpendicular to the build direction. The UTS of the SLM samples is approximately 20–25% lower compared to the hot-rolled samples. The study revealed that SLM technology can be successfully utilized to produce complex-shaped copper alloy parts with high density and good mechanical properties.

© 2016 Elsevier B.V. All rights reserved.

1. Introduction

Additive manufacturing (AM) allows producing complex parts from different materials by adding layers of materials and fusing them together accordingly to CAD-data of a part. SLM technology involves forming a layer of powder material, melting of this layer by laser accordingly to a CAD-file cross-section shape and joining each following layer with the previous one [1]. SLM technology provides several advantages in comparison with conventional techniques, such as a possibility of creating complex-shaped parts without tooling, increased manufacturing speed and a capability to use a wide range of materials [2–4].

Copper and its alloys have high electrical and thermal conductivity and are one of the most important conducting material in electrical engineering. Besides, high corrosion resistance, machinability and relatively low cost determine copper wide use in industry in pure state as well as in alloys [5]. Copper is widely used for manufacturing of tooling inserts, cooling components of semiconductor devices. Precipitation strengthening copper alloys are considered promising materials for such application as promising materials for blanket electrical attachment, heat sink for the various type of equipment in the heating systems owing to their combination of high strength and thermal conductivity [6,7]. Cu-Cr and Cu-Cr-Zr alloys are widely used in aerospace and

nuclear industry, however binary Cu-Cr alloys are known to suffer from dynamic embrittlement due to segregation of elemental sulphur at the grain boundaries [8]. Minor additions of Zr and Ti improve material's hot ductility by forming zirconium and titanium sulphides [9]. Using SLM for producing complex-shaped parts from copper alloys, in particular with internal cooling channels, can significantly shorten the manufacturing cycle and improve the overall performance of such parts.

There are some difficulties in manufacturing dense parts by SLM using copper or its alloys. Copper's low laser absorption and high thermal conductivity require high energy input to fully melt the powder material [10,11]. At the moment, SLM of copper alloys and Cu-Cr-Zr-Ti alloy in particular has not achieved enough attention.

In order to explore the production of Cu-Cr-Zr-Ti alloy parts by additive manufacturing, in this work, copper alloy specimens have been fabricated by SLM for microstructure, phase formation and mechanical behavior characterization. The heat treatment consisting of solution annealing and aging has been applied to achieve better mechanical properties.

2. Material and methods

Cu-Cr-Zr-Ti precipitation strengthening alloy plasma atomized powder with the particles size distribution being from 16 to 79 μm was used as the initial material. The chemical composition of the alloy is following (wt%): 0.50–0.70 Cr, 0.02–0.05 Zr, 0.02–0.05 Ti,

* Corresponding author.

E-mail address: igor.polozov@gmail.com (I. Polozov).

balance – Cu. Small additions of Zr and Ti to Cu-Cr alloy suppress embrittlement at intermediate temperatures, while the Cu-Cr-Zr-Ti alloy possess good thermal conductivity comparable with binary Cu-Cr alloys [6,8].

The SLM process was carried out using SLM Solution SLM 280HL system in argon atmosphere with the following optimized parameters: laser power 400 W, scanning speed 400 mm/s, hatch distance 100 μm , layer thickness 50 μm . These parameters have been chosen based on the previous study and allow manufacturing Cu-Cr-Zr-Ti alloy parts with relative density of about 97.9% (evaluated by the Archimedes principle).

The microsections for microstructure studies were prepared using standard metallography methodology and FeCl_3 water solution as an etchant. The microstructure was characterized by optical microscopy using Leica DMI5000 M microscope.

Phase analysis was performed by Bruker D8 Advance diffractometer at Cu-K α radiation.

The heat treatment consisted of solution annealing at 980 °C for 30 min and subsequent aging at 480 °C for 3 h both with air cooling.

Cylindrical bulk specimens with 15 mm diameter and 90 mm length were produced by SLM and then machined to the form of standard specimens for mechanical tests. Mechanical tests were carried out using Zwick/Roell – Z100 testing machine for room temperature tests and Zwick/Roell – Z050 testing machine for tests at elevated temperatures. Cu-Cr-Zr-Ti alloys parts are generally intended to be exposed at high temperatures during their application [6,9], therefore the specimens were tested at temperatures 20 °C, 600 °C and 800 °C.

3. Results and discussion

Fig. 1(a) shows the microsection of Cu-Cr-Zr-Ti alloy specimens, produced by SLM, without etching. There are a few micropores present with their size ranging from 5 to 20 μm . The density of the bulk material is approximately 97.9%. **Fig. 1(b)** shows the bulk specimens fabricated for porosity and microstructure studies.

The microstructure of the Cu-Cr-Zr-Ti alloy after SLM consists of grains elongated along the build direction (**Fig. 2**), which is favored by the direction of heat dissipation during SLM process [12]. The grain size is approximately in range from 30 to 250 μm . A few micropores are seen on the microstructure. There are also characteristic lines which correspond to the layers' boundaries in areas of their remelting during SLM. The microstructure after heat treatment still features elongated along build direction grains, which became much coarser and have the approximate size of 40–450 μm .

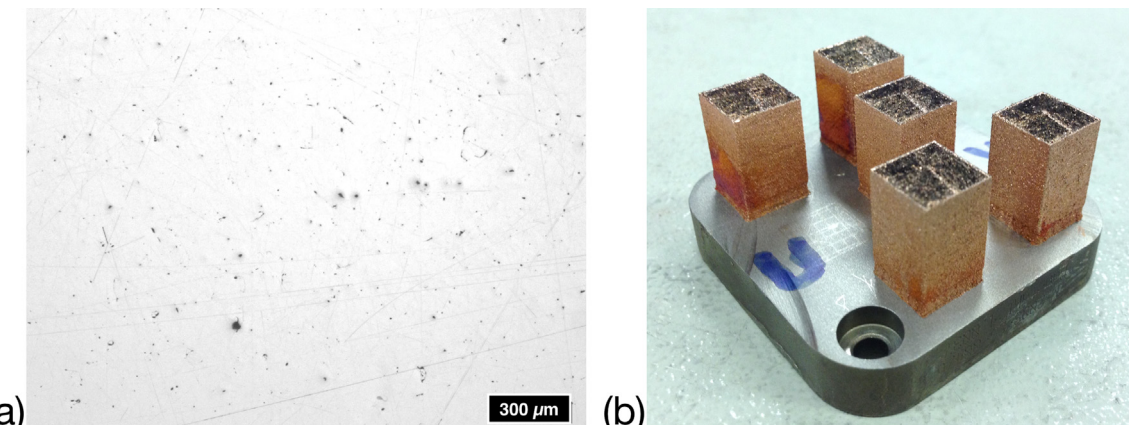


Fig. 1. Microsection of Cu-Cr-Zr-Ti SLM specimen (a) and bulk specimens for microstructure and porosity studies (b).

The heat treatment of the Cu-Cr-Zr-Ti alloy is usually used to achieve higher strength by obtaining solid solution of the alloying elements in the copper matrix by solution annealing and further formation of the precipitates during aging [13]. **Fig. 3** shows the XRD patterns of the Cu-Cr-Zr-Ti bulk specimen, obtained by SLM, after solution annealing at 980 °C for 30 min and subsequent aging at 480 °C for 3 h. Solution annealing leads to formation of supersaturated solid solution of alloying elements and its fixation during cooling. During aging, formation of strengthening precipitates in the form of Guinier-Preston zones occurs [13]. The XRD pattern of the aged material shifts in the area of smaller diffraction angles, which says about the decrease in the copper lattice parameter due to precipitation of alloying elements from the solid solution.

Table 1 presents the results of mechanical tests of Cu-Cr-Zr-Ti alloy specimens, obtained by SLM, at room and elevated temperatures after heat treatment. Specimens were built both perpendicular and parallel to the build direction. Produced room-temperature samples have ultimate tensile strength comparable with hot-rolled material, however their elongation is much lower. Samples produced parallel to the build direction show slightly higher UTS and elongation at break in comparison with the samples fabricated perpendicular to the build direction. The overall UTS of the SLM samples is approximately 20–25% lower compared to the hot-rolled samples. This might be caused by residual porosity in the SLM material, which might act as stress concentrator during loading and needs to be reduced by further optimization of process parameters or hot isostatic pressure post-treatment.

4. Conclusions

Bulk Cu-Cr-Zr-Ti alloy specimens with high density (97.9%) have been manufactured by selective laser melting. Their microstructure, mechanical properties at room and elevated temperatures have been analyzed. The microstructure of the SLM material consists of grains elongated along build direction with the size in the range from 30 to 250 μm . The solution annealing and aging have been applied which resulted in the grain enlargement without changing predominant elongated grain form. The mechanical tests showed that the SLM material have 195–211 MPa ultimate tensile strength and 11–16% elongation at break at 20 °C. Mechanical tests at 600 °C and 800 °C demonstrate decrease in both UTS and elongation. Samples produced parallel to the build direction show slightly higher UTS and elongation at break in comparison with samples fabricated perpendicular to the build direction. The UTS of the SLM samples is approximately 20–25% lower compared to the hot-rolled samples, which might be caused by residual porosity in the SLM material and needs to be reduced

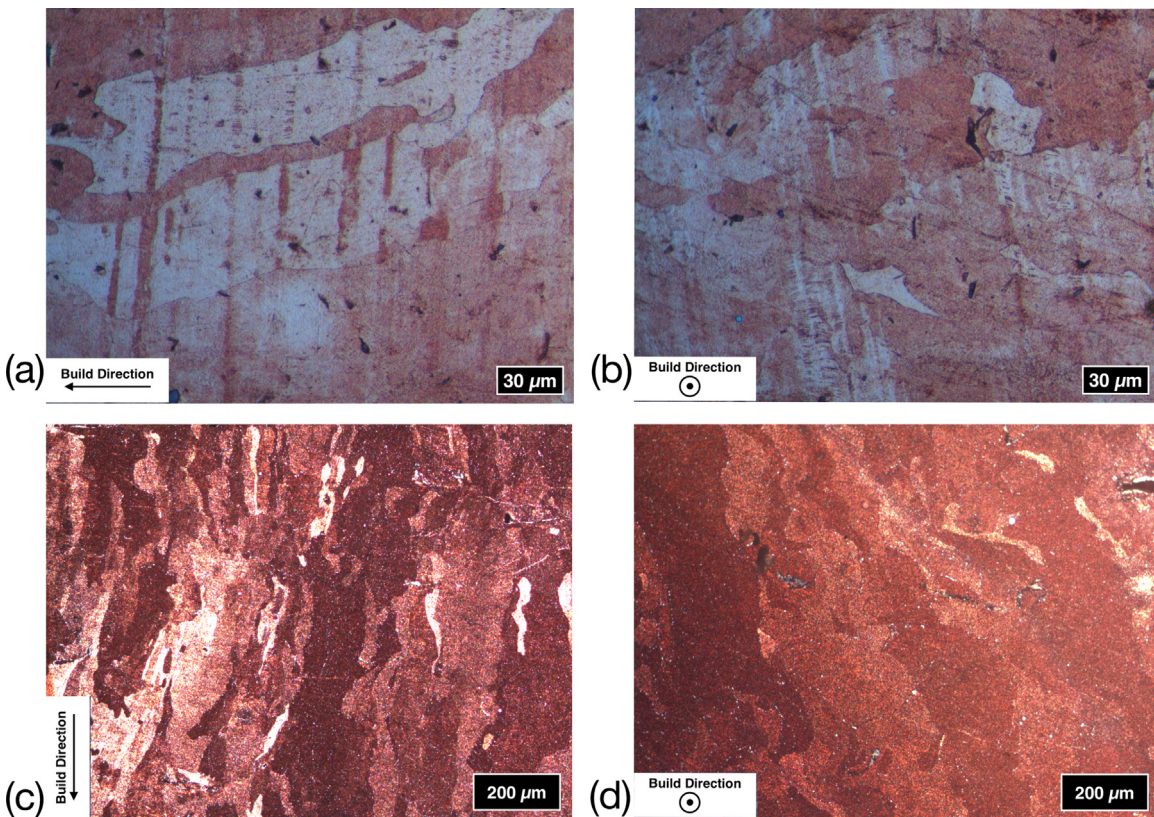


Fig. 2. Microstructure of the Cu-Cr-Zr-Ti samples produced by SLM before (a, b) and after solution annealing at 980 °C for 30 min and aging at 480 °C for 3 h (c, d).

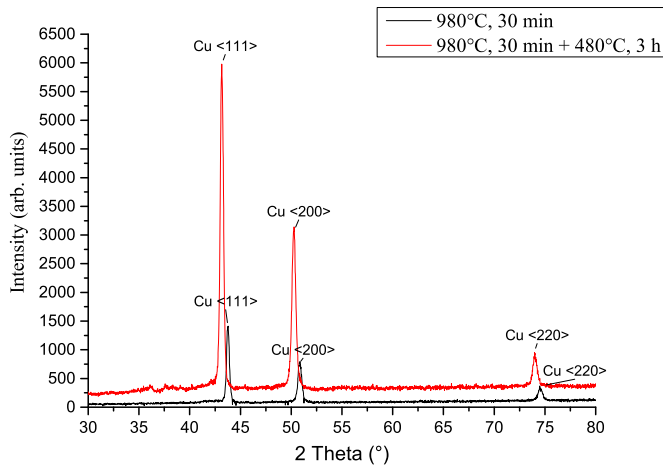


Fig. 3. XRD pattern for the Cu-Cr-Zr-Ti sample produced by SLM after solution annealing and subsequent aging.

Table 1
Mechanical properties of the SLM Cu-Cr-Zr-Ti samples after heat treatment.

Specimen type	UTS, MPa			Elongation at break, %		
	20 °C	600 °C	800 °C	20 °C	600 °C	800 °C
Perpendicular to build direction	195.1–198.0	69.5–86.2	31.3–33.3	10.8–11.7	4.4–5.7	6.3–12.0
Parallel to build direction	210.0–211.0	82.2–82.3	41.2–46.6	13.1–15.8	4.2–7.7	7.8–12.1
Hot-rolled + heat treated [9]	249	107	–	40	6	–

by further optimization of process parameters or hot isostatic pressure post-treatment.

References

- [1] L.E. Murr, S.M. Gaytan, D. a Ramirez, E. Martinez, J. Hernandez, K.N. Amato, et al., Metal fabrication by additive manufacturing using laser and electron beam melting technologies, *J. Mater. Sci. Technol.* 28 (2012) 1–14, [http://dx.doi.org/10.1016/S1005-0302\(12\)60016-4](http://dx.doi.org/10.1016/S1005-0302(12)60016-4).
- [2] W.E. Frazier, Metal additive manufacturing: a review, *J. Mater. Eng. Perform.* 23 (2014) 1917–1928, <http://dx.doi.org/10.1007/s11665-014-0958-z>.
- [3] A. Popovich, V. Sufiarov, E. Borisov, I. Polozov, Microstructure and mechanical properties of Ti-6Al-4V manufactured by SLM, *Key Eng. Mater.* 651–653 (2015) 677–682, <http://dx.doi.org/10.4028/www.scientific.net/KEM.651-653.677>.
- [4] A.A. Popovich, V.S. Sufiarov, I.A. Polozov, E.V. Borisov, Microstructure and mechanical properties of Inconel 718 produced by SLM and subsequent heat treatment, *Key Eng. Mater.* 651–653 (2015) 665–670, <http://dx.doi.org/10.4028/www.scientific.net/KEM.651-653.665>.
- [5] L. Lu, Y. Shen, X. Chen, L. Qian, K. Lu, Ultrahigh strength and high electrical conductivity in copper, *Science* 304 (2004) 422–426.
- [6] H.C. DeGroh, D.L. Ellis, W.S. Loewenthal, Comparison of GRCop-84 to other Cu alloys with high thermal conductivities, *J. Mater. Eng. Perform.* 17 (2008) 594–606, <http://dx.doi.org/10.1007/s11665-007-9175-3>.
- [7] A. Nagesha, P. Parameswaran, A. Biswas, R. Sandhya, A.K. Asraff, M.D. Mathew, Microstructural investigations into the low cycle fatigue deformation of a Cu-Cr-Zr-Ti alloy, *Mater. Sci. Eng. A* 582 (2013) 91–95, <http://dx.doi.org/10.1016/j.msea.2013.06.034>.
- [8] S. Chenna Krishna, K.V. Radhika, K.T. Tharian, M. Swathi Kiranmayee, G. Sudarshan Rao, A.K. Jha, et al., Dynamic embrittlement in Cu-Cr-Zr-Ti alloy: evidence of intergranular segregation of sulphur, *J. Mater. Eng. Perform.* 22 (2013) 2331–2336, <http://dx.doi.org/10.1007/s11665-013-0510-6>.
- [9] S.C. Krishna, K.V. Radhika, K. Thomas Tharian, G. Sudarshan Rao, M. Swathi Kiranmayee, B. Pant, Effect of simulated brazing cycle on the microstructure and mechanical properties of Cu-Cr-Zr-Ti alloy, *Mater. Sci. Forum* 710 (2012) 626–631, <http://dx.doi.org/10.4028/www.scientific.net/MSF.710.626>.
- [10] D.Q. Zhang, Z.H. Liu, C.K. Chua, Investigation on forming process of copper alloys via Selective Laser Melting, *High. Value Manuf. Adv. Res. Virtual Rapid Prototyp.* (2014) 285–289.
- [11] Z.H. Liu, D.Q. Zhang, S.L. Sing, C.K. Chua, L.E. Loh, Interfacial characterization of SLM parts in multi-material processing: metallurgical diffusion between 316L stainless steel and C18400 copper alloy, *Mater. Charact.* 94 (2014) 116–125,

- <http://dx.doi.org/10.1016/j.matchar.2014.05.001>.
- [12] K. Kunze, T. Etter, J. Grässlin, V. Shklover, Texture, anisotropy in microstructure and mechanical properties of IN738LC alloy processed by selective laser melting (SLM), Mater. Sci. Eng. A 620 (2014) 213–222, <http://dx.doi.org/>
- [10.1016/j.msea.2014.10.003](http://dx.doi.org/10.1016/j.msea.2014.10.003).
- [13] D.J. Edwards, B.N. Singh, S. Tähtinen, Effect of heat treatments on precipitate microstructure and mechanical properties of a CuCrZr alloy, J. Nucl. Mater. 367–370 B (2007) 904–909, <http://dx.doi.org/10.1016/j.jnucmat.2007.03.064>.



Additive manufacturing of PLA structures using fused deposition modelling: Effect of process parameters on mechanical properties and their optimal selection

J.M. Chacón^a, M.A. Caminero^{b,*}, E. García-Plaza^b, P.J. Núñez^b

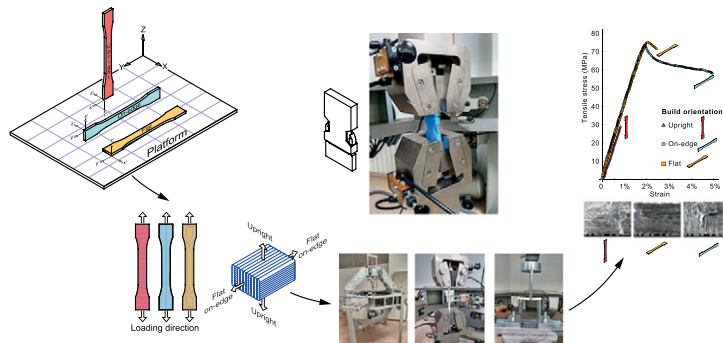
^aEscuela Técnica Superior de Ingenieros Industriales, IMACI, Universidad de Castilla-La Mancha, Campus Universitario s/n, Ciudad Real 13071, Spain

^bEscuela Técnica Superior de Ingenieros Industriales, INEI, Universidad de Castilla-La Mancha, Campus Universitario s/n, Ciudad Real 13071, Spain

HIGHLIGHTS

- The effect of 3D printing process parameters on the mechanical performance of PLA samples is assessed.
- On-edge oriented samples show the optimal mechanical performance.
- Ductility decreases as layer thickness and feed rate increase.
- Low layer thickness and high feed rate values are recommended for the optimal mechanical performance.

GRAPHICAL ABSTRACT



ARTICLE INFO

Article history:

Received 23 December 2016

Received in revised form 20 March 2017

Accepted 22 March 2017

Available online 28 March 2017

Keywords:

Fused deposition modelling

Polylactic acid (PLA)

Mechanical characterization

Process parameters

Failure analysis

ABSTRACT

Fused deposition modelling is a rapidly growing additive manufacturing technology due to its ability to build functional parts having complex geometries. The mechanical properties of a built part depend on several process parameters. The aim of this study is to characterize the effect of build orientation, layer thickness and feed rate on the mechanical performance of PLA samples manufactured with a low cost 3D printer. Tensile and three-point bending tests are carried out to determine the mechanical response of the printed specimens. Due to the layer-by-layer process, 3D printed samples exhibit anisotropic behaviour. Upright orientation shows the lowest mechanical properties. On the other hand, on-edge and flat orientation show the highest strength and stiffness. From a layer thickness and feed rate point of view, it is observed that ductility decreases as layer thickness and feed rate increase. In addition, the mechanical properties increase as layer thickness increases and decrease as the feed rate increases for the upright orientation. However, the variations in mechanical properties with layer thickness and feed rate are of slight significance for on-edge and flat orientations, except in the particular case of low layer thickness. Finally, the practicality of the results is assessed by testing an evaluation structure.

© 2017 Elsevier Ltd. All rights reserved.

1. Background

Additive manufacturing (AM) technologies are one of the most promising areas in the manufacturing of components [1–6].

Furthermore, they enable the manufacture of a large range of prototypes or functional components with complex geometries, such as those obtained from a topology optimization process [7,8] or generated from a fitting process in Computer-Aided Design [9]. AM technology is a very broad term encompassing numerous methods such as Stereolithography (STL) of a photopolymer liquid, Fused Deposition Modelling (FDM) from plastic filaments, Laminated Object

* Corresponding author.

E-mail address: miguelangel.caminero@uclm.es (M. Caminero).



Manufacturing from plastic laminations, and Selective Laser Sintering from plastic or metal powders [3,10]. However, the FDM technique is of particular interest due to its association to desktop 3D printers [11,12]. FDM forms a 3D geometry by assembling individual layers of extruded thermoplastic filament, such as acrylonitrile butadiene styrene (ABS) or polylactic acid (PLA), which have melting temperatures low enough for use in melt extrusion in outdoor non-dedicated facilities [1].

FDM is a complex process with a large number of parameters that influence product quality and material properties, and the combination of these parameters is often difficult to understand [5,13]. Printing parameters such as build orientation, layer thickness, raster angle, raster width, air gap, infill density and pattern, and feed rate, among others, have a substantial effect on the quality and performance of FDM printed parts [1,4,5,14–20]. Since mechanical properties are crucial for functional parts, it is absolutely essential to examine the influence of process parameters on mechanical performance [17,21–24]. Thus, further research is required to determine printer parameters such as build orientation, layer thickness and feed rate, particularly since the literature on the mechanical properties of parts processed by low cost 3D printers is somewhat scarce. This applies to the PLA material used in this study that, unlike ABS material, has not been extensively analysed [1,18,25]. Furthermore, the analysis of the effects of FDM process parameters on mechanical performance are of special interest for the fabrication of continuous reinforced fibre 3D printed structures [2,3,11,16,26,27].

To date, a number of studies have highlighted the impact of build orientation on aspects such as surface quality, geometric accuracy, build time and overall manufacturing cost [20]. In addition, build orientation has a major role on the structural properties of FDM parts. Build orientation refers to how and which direction a sample is placed on the 3D printing platform. This is often observed in the form of anisotropically printed objects, making structural performance highly dependent on build orientation in a similar way to composites laminates [28–30]. The effects of build orientation on mechanical performance of FDM parts have been previously studied [1,4–6,15,24,31–33]. These authors agree that the strongest printing orientation is obtained when the fused filament deposition coincided with the pull direction. However, a range of orientations may be found along this pull direction, which have not been analysed in other studies.

A more controversial parameter is layer thickness (L_t). Rankouhi et al. [6] stated that although layer thickness has been studied extensively, it should be further analysed due to the disparity of results. For example, Sood et al. [15] concluded that tensile strength first decreased and then increased as layer thickness increased for $L_t = \{0.127, 0.178, 0.254\}$ mm. Tymrak et al. [1] stated that the lowest thickness had the highest tensile strength for $L_t = \{0.2, 0.4\}$ mm. However, the authors concluded that PLA specimens showed greater variability between parameters. Lanzotti et al. [18] inferred that as the number of shell perimeters increased, the variation of tensile strength with the layer thickness was slightly significant in PLA samples. Ahn et al. [32] deduced a low level of significance of the effect of layer thickness on the final material properties of ABS samples. Finally, Vaezi and Chua [17] reported that for flat oriented samples, a decrease from $L_t = 0.1$ mm to $L_t = 0.087$ mm increased the tensile strength and decreased flexural strength.

Furthermore, the effect of feed rate on the mechanical performance of PLA samples has not been extensively studied [13]. For example, the results of Ning et al. [16] and Christiyana et al. [34] have shown that tensile and flexural strengths decreased as the feed rate increased. This process variable is also directly related to build time, and consequently, to manufacturing cost.

In this study, the characterization and assessment of the effect of build orientation, layer thickness and feed rate on the mechanical properties of PLA samples manufactured with a low cost desktop

3D printer using FDM technique are examined. For this purpose, ANOVA analysis, regression models and response surfaces were used to perform a parametric characterization of the mechanical properties and to establish an optimal selection of the process parameters. Additionally, manufacturing costs as a function of printing time are evaluated. Tensile and three-point bending tests are carried out to determine the mechanical response in terms of strength and stiffness of the printed samples. In addition, SEM images of fractured surfaces of tensile samples are evaluated to determine the effects of process parameters on failure modes. Finally, the practicality of the previous results is assessed further by testing a functionally static load-bearing assembly as a case example.

The rest of the paper is organized as follows. First the experimental methodology carried out in this study is briefly summarized with particular emphasis on specimen preparation, 3D printing process parameters and the experimental set-up. Thereafter, the key results of the investigation are summarized, and the effects of the different process parameters are highlighted. Finally, conclusions and extensions of this work are outlined.

2. Experimental methodology

2.1. Materials, 3D printers and specimen preparation

The goal of this study is to analyse the mechanical performance of PLA samples. In this study, the commercial SMARTFIL PLA filament manufactured by Smart Materials 3D [35] with a diameter of 1.75 mm was used. Typical values of the main mechanical properties of PLA materials manufactured by FDM technology [10,18] are presented in Table 1.

PLA samples were manufactured using a WitBox desktop 3D printer developed by BQ [36]. WitBox is a low cost desktop printer that uses PLA material with a 0.4 mm nozzle size. WitBox can be controlled with any open source software. In this study, Cura software [37] was used to generate G-code files and to command and control all the process parameters. There are no standard test methods for tensile and flexural properties of parts manufactured using FDM. In this study, the ASTM D638 [38] and D790 [39] methods were applied for testing tensile and flexural specimens, respectively. The geometry of the 3D printed specimens were modelled using SolidWorks software exported as an STL file and imported to the 3D printing software. The main dimensions of the specimens are shown in Fig. 1.

2.2. Process parameters

The mechanical properties of parts fabricated using FDM technology depend on the selection of process parameters. Table 2 outlines the FDM process parameters used in this study. Three build orientations were assessed (Fig. 2a): Flat (F) and On-edge(O), where the fused filament deposition is positioned in the same direction as the pull direction and Upright (U) in which layers were deposited perpendicular to the pull direction.

Table 1
Typical ranges of mechanical properties for PLA materials fabricated with FDM technology [10,18].

Properties	PLA
Tensile strength (MPa)	15.5–72.2
Tensile modulus (GPa)	2.020–3.550
Elongation at break (%)	0.5–9.2
Flexural strength (MPa)	52–115.1
Flexural modulus (GPa)	2.392–4.930

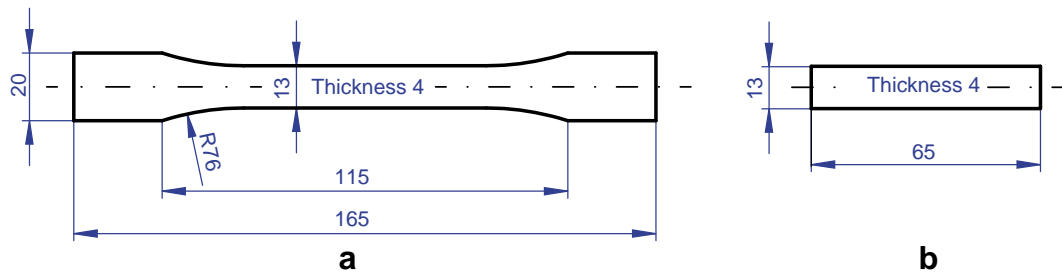


Fig. 1. Standard specimens for mechanical testing. (a) Tensile specimen. (b) 3-point bending specimen. Dimensions are in mm [38,39].

Table 2
Process parameters and their levels used in this work.

Parameter	Value
Build orientation	Flat (F), On-edge (O), Upright (U)
Layer thickness (mm)	$L_t = \{0.06, 0.12, 0.18, 0.24\}$
Feed rate (mm/s) (Flow rate mm ³ /s)	$F_r = \{20(1.9), 50(4.8), 80(7.7)\}$

In addition, four different layer thickness were considered in order to analyse the influence of this parameter $L_t = \{0.06, 0.12, 0.18, 0.24\}$ mm. Layer thickness was measured in the Z direction (Fig. 2). These values were selected according to the Witbox 3D printer range. The minimum layer thickness that could be selected in the 3D printer was $L_t = 0.06$ mm. This layer thickness value is lower than the minimum value of the range of layer thickness studied in most of the related studies found in the literature, where the usual minimum layer thickness was $L_t = 0.1$ mm, as shown in References [1,6,14,15,18,40].

Furthermore, the effect of feed rate (F_r) on mechanical properties was evaluated. Three different feed rates were considered: $F_r = \{20, 50, 80\}$ mm/s. The flow rate of the extruded material was changed in order to keep a constant width of the perimeter lines.

The influence of the raster pattern, air gap, raster angle or raster width in the mechanical performance of FDM printed parts has been

extensively studied [13,14]. There is a broad spectrum of infill patterns, making it difficult to analyse the influence of raster patterns. In this study, solid samples filled with a perimeter raster were analysed, which is where the tool paths are the offsets from the perimeter with a distance equivalent to the nozzle size (Fig. 2b). Hence, shell thickness was selected long enough to fill the sample with a raster angle of 0°. Certain parameters such as air gap, raster angle or temperature were fixed for all the samples in order to focus on the influence of the previous three parameters (Table 3).

2.3. Experimental set-up

Each sample set consisted of five specimens for a given group of process parameters, with a total of 360 specimens (tensile and flexural specimens). It is well known that moisture absorption adversely affects the mechanical performance of PLA printed materials [41]. Once the vacuum packaged PLA filament was opened, it was stored in a dry box in order to minimize moisture absorption in the same way as the manufactured specimens prior to testing. Average strength and stiffness values of the mechanical test were taken as the results. Since the physical properties of many materials (especially thermoplastics) can vary depending on ambient temperature, tests were carried out according to the standards for room temperature.

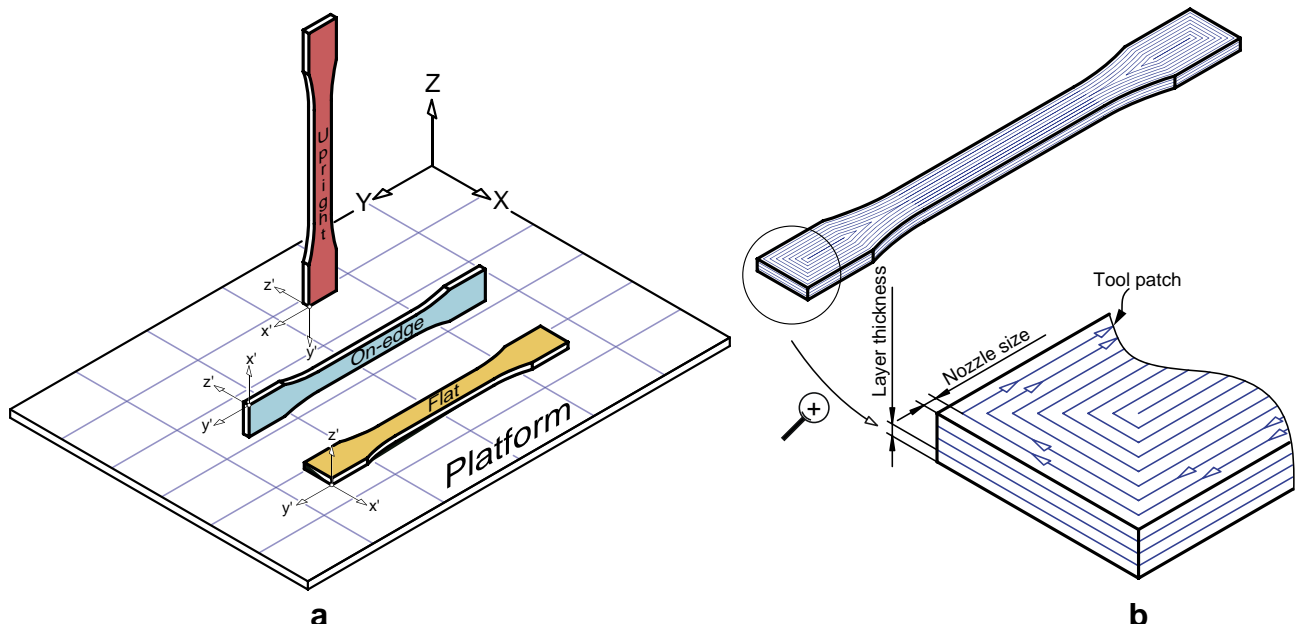


Fig. 2. Process parameters: a) Build orientation. b) Layer thickness and perimeter raster.

Table 3
Fixed parameters.

Parameter	Value
Air gap (mm), Raster angle	0, 0°. Solid sample. Perimeter raster
Temperature (°C)	210

The uniaxial tensile tests were performed following the standard ASTM D638-10 standard [38]. A 50 kN universal electro-mechanical testing machine with a 5 kN load cell at a fixed loading rate of 2 mm/min was used for both the tensile and 3-point bending tests. This displacement rate was within the proposed ASTM test speed range: D638-10 and D790 propose a test speed range of 1–5 mm/min. The selection of this displacement rate was in agreement with the displacement rate used in other studies [1,5,6,14,18]. Strain was measured using a MTS 634.14 high-performance axial extensometer. The experimental data were processed following the recommendations of the previous standard, for the determination of the maximum tensile strength (σ_t) and the tensile Young's modulus (E). Young's modulus was determined considering the linear part of the stress-strain curve and the slope was estimated by a linear fit. σ_t was calculated as a ratio between the maximum load reached during the test and the cross-sectional area.

The 3-point bending tests were performed following the ASTM D790-10 procedure [39] using a three point bending test fixture. The radius of the loading nose and the radii of the support noses of the 3-point bending specimen test fixture were 3 mm. The flexural modulus of elasticity (E_f) was determined following the previous standard, based on the Classical Beam Theory, supposing that shear effects are negligible. We can define the maximum normal stress σ_f in the three-point bending test as

$$\sigma_f = \frac{3PL}{2wt^2},$$

where P is the fracture force, L is the support span, w is the width of the specimen, t is the thickness of the specimen, and the maximum strain ε of the outer surface at mid-span, which was calculated as follows

$$\varepsilon = \frac{6\delta t}{L^2},$$

where δ is the mid-span deflection. The flexural modulus of elasticity E_f is the ratio of stress to the corresponding strain at a given point on the stress-strain curve. Hence, it can be calculated as

$$E_f = \frac{L^3 m}{4wt^3},$$

where m is the slope of the secant of the load-displacement curve. The slope m was measured between the 25% and 75% of the maximum load (Fig. 3). It is also recommended to prescribe a strain range instead of a load range. If the ultimate strain of the material is higher than 1%, a 0.3–0.5% strain range or even higher can be used [42]. A regression analysis using least squares was employed in the interval $([0.25F_{max}, \delta_{0.25F_{max}}], [0.75F_{max}, \delta_{0.75F_{max}}])$.

3. Results and discussion

Average and standard deviation of the test results of the maximum strengths (σ_t, σ_f) and stiffnesses (E, E_f) for the printed PLA samples are tabulated for the tensile tests in Table 4 and for 3-point bending tests in Table 5.

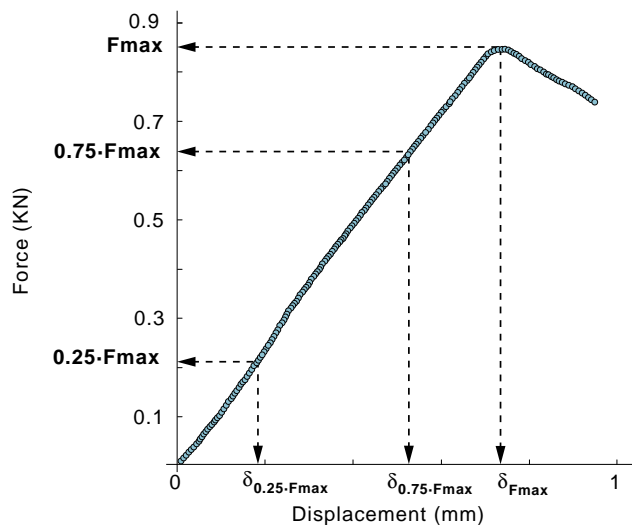


Fig. 3. Procedure for calculating the slope m of the force–displacement curve.

The comparison of the minimum and maximum average values of tensile and flexural strengths (σ_t, σ_f) and stiffnesses (E, E_f) showed variations between specimens manufactured under different printing conditions in the range of $\sigma_t = [20.2, 89.1]$ MPa, $E = [2765.5, 4409.7]$ MPa, $\sigma_f = [14.3, 65]$ MPa, and $E_f = [1282, 1886]$ MPa, respectively. In other words, process parameters had significant influence on strength and stiffness properties. These results were in line with those reported in literature for the PLA material manufactured under different printing conditions [1,5,18]. Larger standard deviations for the strength and stiffness values under certain printing conditions are shown in Tables 4 and 5. This phenomenon has been observed in previous studies [1,15,18,22]. In addition, Table 6 depicts the number of layers and printing time for the tensile samples as a function of the process parameters. Printing time is a key material process parameter because it is related to manufacturing cost.

In order to clarify the results for a better understand of the correlation between the different ranges of process parameters on mechanical performance, the graphical representation of these results is shown in Figs. 4 and 5. These figures show the average maximum tensile and flexural strengths as a function of layer thickness. In addition, Figs. 6 and 7 report some representative stress–strain curves for the tensile and flexural samples with different process parameters in order to characterize and assess different types of damage observed.

The main effects of the process parameters (build orientation, layer thickness and feed rate) on the mechanical characteristics of PLA samples are summarized in the following sections.

3.1. Parametric analysis of experimental tensile and flexural strengths

A response surface methodology for tensile and flexural strengths was developed to relate the mechanical response and process parameters in accordance with previous studies [15,18]. Experimental data were analysed using the Statgraphics Centurion XVII software. An analysis of variance (ANOVA) was performed to determine the level of statistical significance of several factors (Table 7). In this case, a categorical factor Bo (Build orientation), and two quantitative factors, F_r (Feed rate) and L_t (Layer thickness) were used in the analysis. Therefore, a quadratic model was performed because the maximum order of the quantitative factors was $L_t \times L_t, F_r \times F_r$ and their interactions. If p -value is <0.05 , the significance of the corresponding factor is established. The results of ANOVA in Table 7 show that

Table 4

Average tensile test results of the samples and process parameter ranges. Standard deviation is depicted in brackets.

Build O.	$F_r = 20 \text{ mm/s}$		$F_r = 50 \text{ mm/s}$		$F_r = 80 \text{ mm/s}$	
	$\sigma_t(\text{MPa})$	$E(\text{GPa})$	$\sigma_t(\text{MPa})$	$E(\text{GPa})$	$\sigma_t(\text{MPa})$	$E(\text{GPa})$
$L_t = 0.06\text{mm}$						
Upright	28.8(0.2)	4.011(0.040)	20.2(1.3)	3.765(0.127)	22.4(1.7)	3.266(0.122)
On-edge	73.2(0.9)	4.042(0.075)	84.7(0.5)	4.018(0.002)	83.4(0.2)	4.040(0.082)
Flat	75.2(0.3)	3.867(0.034)	89.1(0.2)	4.192(0.070)	88.2(0.4)	4.409(0.109)
$L_t = 0.12\text{mm}$						
Upright	34.9(1.5)	3.599(0.251)	46.2(0.7)	3.887(0.145)	27.5(2.2)	3.796(0.128)
On-edge	72.4(0.6)	4.018(0.063)	77.3(0.1)	3.992(0.034)	65.4(1.3)	3.976(0.039)
Flat	72.8(1.4)	3.925(0.006)	74.5(3.0)	3.860(0.048)	68.6(1.0)	3.892(0.035)
$L_t = 0.18\text{mm}$						
Upright	40.9(4.8)	3.521(0.089)	41.1(1.7)	3.726(0.169)	32.6(0.4)	3.668(0.061)
On-edge	78.5(1.2)	3.913(0.057)	64.9(1.8)	4.004(0.073)	66.1(2.7)	3.955(0.033)
Flat	76.5(0.9)	3.882(0.056)	77.3(0.8)	4.017(0.037)	69.8(1.5)	4.030(0.023)
$L_t = 0.24\text{mm}$						
Upright	46.6(2.8)	3.356(0.097)	40.5(3.3)	3.451(0.175)	39.5(4.4)	3.468(0.046)
On-edge	78.4(1.7)	3.924(0.031)	78.1(0.3)	4.025(0.058)	71.9(1.2)	3.934(0.063)
Flat	73.6(0.7)	3.915(0.112)	72.3(0.2)	3.769(0.034)	64.6(0.5)	3.622(0.028)

all terms are statistically significant at the 95.0% confidence level, except the interaction $B_o \times F_r$ and $B_o \times L_t$ with a p -value > 0.05 for tensile and flexural strengths. The goodness-of-fit of the model to the experimental data was analysed using the adjusted determination coefficient (R^2_{adj}), which indicates the percentage of total variation in the response explained by the terms in the model. R^2_{adj} was 97.75% and 98.35% for tensile and flexural strengths, respectively.

Following the analysis of the significance level of factors and verified that they were significance, a regression model based on a multivariable polynomial regression was developed for each level of qualitative factor (build orientation). In all cases, models were diagnosed by analysing the following aspects: atypical values, multicollinearity, independence and normality of the residuals, homoscedasticity, and contrasts and hypothesis tests. The best models obtained were quadratic models by forward selection variables. Model equations, goodness-of-fit to the experimental data, and the p -value of significant factors for each model are shown in Table 8.

Fig. 8 shows the normality test of the residuals of the respective models, where the p -value of the normality plots was found to be above 0.05, indicating the residue followed normal distribution. Fig. 9 depicts the response surfaces for tensile and flexural strengths as a function of their respective build orientation.

3.2. Effects of build orientation on mechanical properties

A first glance at the results of Tables 4 and 5, Figs. 4 and 5 and the response surface analysis (Fig. 9) reveal that the PLA samples exhibited a remarkable anisotropy. Build orientation significantly affected the mechanical properties and, in particular, ductility and failure behaviour. On-edge and flat orientations showed the highest values for maximum tensile and flexural strengths and stiffness, while upright orientation resulted in the lowest ones. For example, the maximum tensile strength for the upright orientation σ_t was about 78% ($L_t = 0.06 \text{ mm}$, $F_r = 80 \text{ mm/s}$) to 37% ($L_t = 0.24 \text{ mm}$,

Table 5

Average 3-point bending test results of the samples and process parameters ranges. Standard deviation is depicted in brackets.

Build O.	$F_r = 20 \text{ mm/s}$		$F_r = 50 \text{ mm/s}$		$F_r = 80 \text{ mm/s}$	
	$\sigma_f(\text{MPa})$	$E_f(\text{GPa})$	$\sigma_f(\text{MPa})$	$E_f(\text{GPa})$	$\sigma_f(\text{MPa})$	$E_f(\text{GPa})$
$L_t = 0.06\text{mm}$						
Upright	25.1(1.2)	1.590(0.105)	15.4(0.5)	1.482(0.049)	14.3(0.9)	1.318(0.111)
On-edge	53.0(2.5)	1.555(0.089)	52.8(1.3)	1.540(0.034)	65.0(2.9)	1.852(0.072)
Flat	53.0(2.1)	1.471(0.053)	55.3(2.4)	1.519(0.043)	56.0(2.8)	1.596(0.086)
$L_t = 0.12\text{mm}$						
Upright	34.5(1.6)	1.389(0.002)	32.2(0.8)	1.384(0.036)	23.8(2.8)	1.392(0.022)
On-edge	64.8(2.2)	1.772(0.096)	64.2(1.5)	1.757(0.071)	61.3(3.7)	1.729(0.112)
Flat	51.4(3.8)	1.480(0.089)	47.0(0.4)	1.369(0.006)	49.0(5.4)	1.434(0.142)
$L_t = 0.18\text{mm}$						
Upright	29.8(3.1)	1.464(0.024)	29.9(0.8)	1.402(0.002)	19.4(2.1)	1.302(0.022)
On-edge	62.9(10)	1.805(0.330)	62.0(1.5)	1.447(0.208)	61.0(1.2)	1.519(0.085)
Flat	51.4(2.5)	1.470(0.054)	53.4(3.6)	1.550(0.100)	51.4(1.9)	1.518(0.042)
$L_t = 0.24\text{mm}$						
Upright	32.4(1.4)	1.473(0.027)	31.0(0.4)	1.339(0.018)	28.4(0.4)	1.414(0.045)
On-edge	61.1(6.0)	1.754(0.159)	61.7(3.9)	1.717(0.130)	64.2(2.3)	1.886(0.065)
Flat	46.3(2.2)	1.326(0.046)	46.0(0.5)	1.526(0.084)	46.2(2.1)	1.246(0.053)

Table 6

Number of layers and printing time for the PLA tensile samples as a function of the process parameters.

Build O.	Layers no.	$F_r = 20 \text{ mm/s}$	$F_r = 50 \text{ mm/s}$	$F_r = 80 \text{ mm/s}$
		Time (min)	Time (min)	Time (min)
$L_t = 0.06 \text{ mm}$				
Upright	2746	360	252	253
On-edge	316	344	143	93
Flat	63	333	149	105
$L_t = 0.12 \text{ mm}$				
Upright	1374	303	129	129
On-edge	159	173	72	47
Flat	32	169	79	56
$L_t = 0.18 \text{ mm}$				
Upright	916	222	86	86
On-edge	106	175	48	31
Flat	22	176	56	41
$L_t = 0.24 \text{ mm}$				
Upright	687	91	64	65
On-edge	80	86	36	24
Flat	16	85	42	32

$F_r = 20 \text{ mm/s}$) lower than on-edge and flat orientations, whose values were similar. These results have confirmed the observations of previous studies [1,4,5,18]. In the case of the flexural samples, on-edge orientation depicted the highest value for the maximum flexural strength, with an average σ_f about 38% ($L_t = 0.24 \text{ mm}$, $F_r = 80 \text{ mm/s}$) to 350% ($L_t = 0.06 \text{ mm}$, $F_r = 80 \text{ mm/s}$) higher than flat and upright orientations, respectively.

These differences can be explained by considering two main failure modes: inter-layer fusion bond failure (inter-layer failure) and trans-layer failure. For the upright orientation, the samples were pulled parallel to the layer deposition direction and the load was perpendicular to their fibres (Fig. 2), resulting in inter-layer fusion bond failure. In this case, layer or fibre-to-fibre adhesion significantly affected tensile strength given that inter-layer fusion bonds between adjacent layers or fibres withstood most of the applied load and not the fibres themselves. A lower tensile strength than the individual fibres was expected [4,6,18,32,43]. In the case of the on-edge and flat orientations, the specimens were pulled perpendicular to the layer deposition direction and hence fibres were pulled parallel to the loading direction, resulting in trans-layer failure. In this case, individual fibres withstood most of the applied load and fibre breakage was observed [6,18,32,43]. If flat and on-edge orientations were pulled parallel to the layer deposition direction, inter-layer failure is expected in a similar way to the upright orientation with lower tensile strength than in the case of trans-layer failure.

Figs. 6 and 7 show the average stress-strain behaviour for the PLA samples under tensile and flexural loading, respectively. In general, the results highlighted a brittle behaviour for the upright orientation. However, on-edge and flat orientations showed a ductile behaviour, with significant plastic deformation. More specifically, on-edge samples depicted the value of maximum tensile deformation at fracture (Fig. 6), with similar values for both elastic modulus and tensile strength as in flat samples, since more layers were pulled longitudinally. From a flexural point of view, Fig. 7 shows that the trends of the flexural stress-strain behaviour results were similar to the tensile ones, where upright orientation depicted a brittle performance and on-edge and flat orientations showed a ductile behaviour and plastic deformation with a similar amount of flexural deformation.

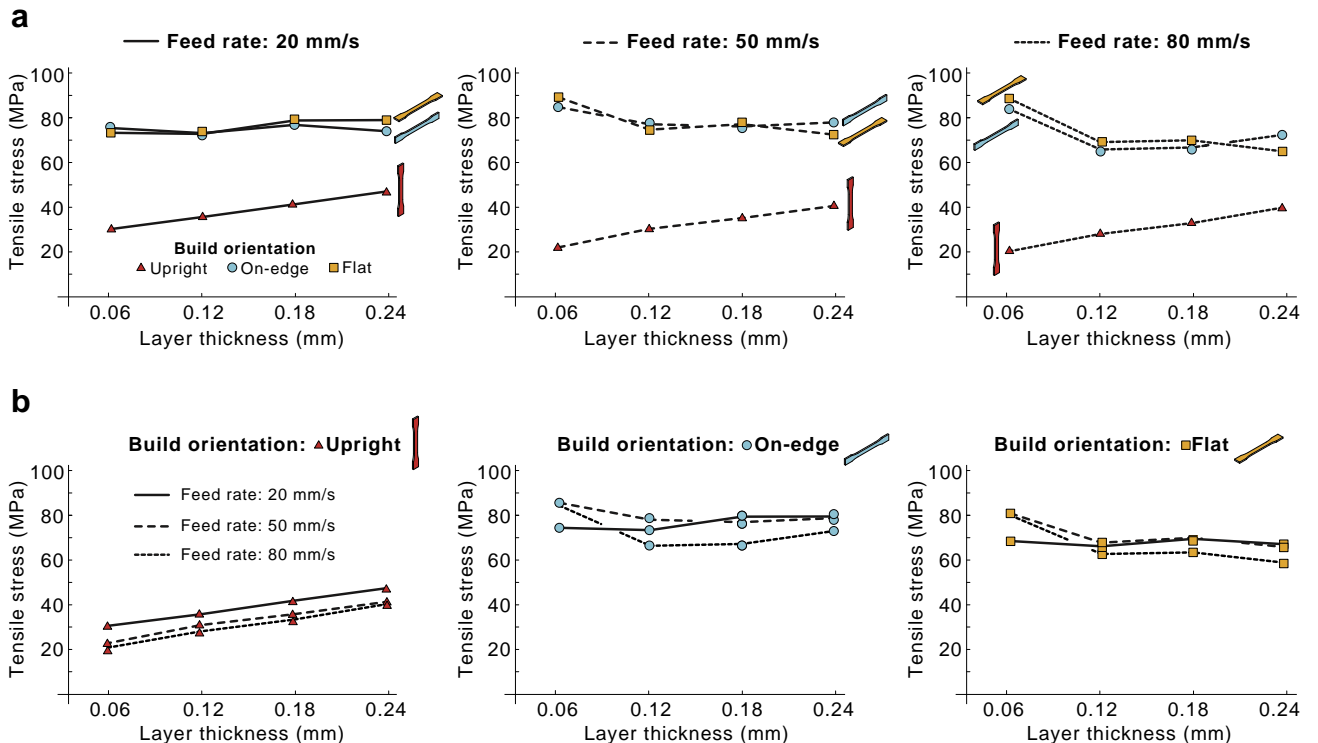


Fig. 4. Graphical comparison of average maximum tensile strength (σ_t) for the tensile specimens as a function of layer thickness. (a) The effect of build orientation for a fixed feed rate. (b) The effect of feed rate for a given build orientation.

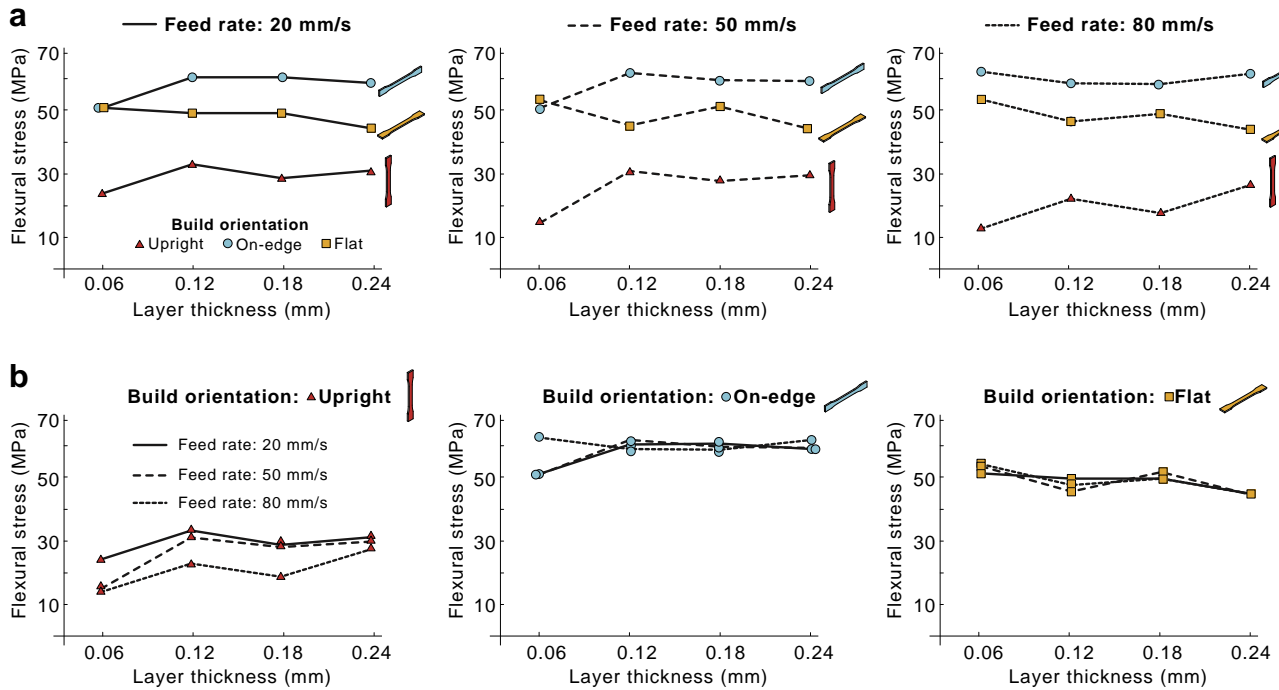


Fig. 5. Graphical comparison of average maximum flexural strength (σ_f) for the flexural specimens as a function of layer thickness. (a) The effect of the build orientation for a fixed feed rate. (b) The effect of the feed rate for a given build orientation.

As for stiffness, the results of Tables 4 and 5 revealed that upright orientated samples exhibited the lowest values for the tensile and flexural elastic moduli. It is worth noting that upright oriented samples presented a wider variability in the tensile elastic modulus due to their brittle behaviour. In contrast, on-edge and flat oriented samples showed the highest tensile and flexural stiffness values. These results were in accordance with previous studies where the specimens were pulled along their longitudinal axis, resulting in reduced specimen deformability and increased stiffness [1,4–6,18,31].

These findings underscored that the selection of build orientation of the PLA samples had a crucial impact on the strength, stiffness and deformation at fracture. Hence, it is reasonable to conclude that the on-edge orientation showed the optimal mechanical performance in terms of strength and stiffness. It exhibited the best flexural performance, and the tensile strength and stiffness were similar to the flat orientation (the maximum on-edge strength was only 5% lower than the highest strength exhibited by the flat orientation). Moreover, it depicted a ductile behaviour with the highest tensile deformation at fracture.

3.3. Effects of layer thickness on mechanical properties

Layer thickness is directly related to the number of layers needed to print a part and hence to printing time. Thus, manufacturing costs decrease as layer thickness increases (Table 6).

Figs. 4 and 5 show the average maximum tensile and flexural strengths as a function of layer thickness, among other process parameters. The effect of layer thickness on the mechanical properties due to the build orientation was different for upright samples and on-edge and flat samples. In the case of upright samples, higher layer thickness tended to promote higher strength. These results were in accordance with previous works [15,18]. This effect can be explained by considering that with increased layer thickness, fewer layers were needed for a given total thickness and, therefore the

number of layer bonds was reduced and strength increased. In addition, this trend was heightened when the feed rate increased. Table 9 depicts the percentage variation of maximum tensile and flexural strengths for the upright printed samples with an increase of layer thickness from $L_t = 0.06$ to 0.24 mm for different feed rates.

In the case of on-edge and flat printed samples, the variations of maximum tensile and flexural strengths in the range of layer thickness $L_t = \{0.12, 0.18, 0.24\}$ mm were marginally significant. Nevertheless, for the particular case of $L_t = 0.06$ mm, the results showed higher tensile strength and lower flexural strength than the specimens with layer thickness $L_t = \{0.12, 0.18, 0.24\}$ mm, which it was in good agreement with the results found in Reference [17] for on-edge and flat orientations with low values of layer thickness. The previous authors remarked that a decrease of layer thickness from $L_t = 0.1$ to 0.087 mm increased the tensile strength and decreased flexural strength. Table 10 depicts this trend of maximum tensile strength with increased layer thickness from $L_t = 0.06$ to 0.12 mm. In the case of on-edge and flat orientations, the variation of the stress-strain behaviour was more meaningful in terms of ductility with layer thickness for the tensile and flexural specimens than the variations of tensile and flexural strengths (Figs. 6 and 7).

Furthermore, in relation to stiffness, tensile and flexural elastic moduli exhibited high variability with layer thickness. In general, low layer thickness values resulted in increased in stiffness, as shown in Refs. [1,3,6]. Finally, according to Figs. 6 and 7, the maximum tensile and flexural plastic strain at fracture decreased as layer thickness increased. Nevertheless, a significant reduction in printing time was achieved.

In short, the result underscored that in the case of upright orientation, tensile and flexural strengths increased as the layer thickness increased. In addition, in the case of on-edge and flat orientations, the variation of tensile and flexural strengths were of slight significance, except in the case of low layer thickness $L_t = 0.06$ mm. These results were in agreement with the response surface analysis (Fig. 9).

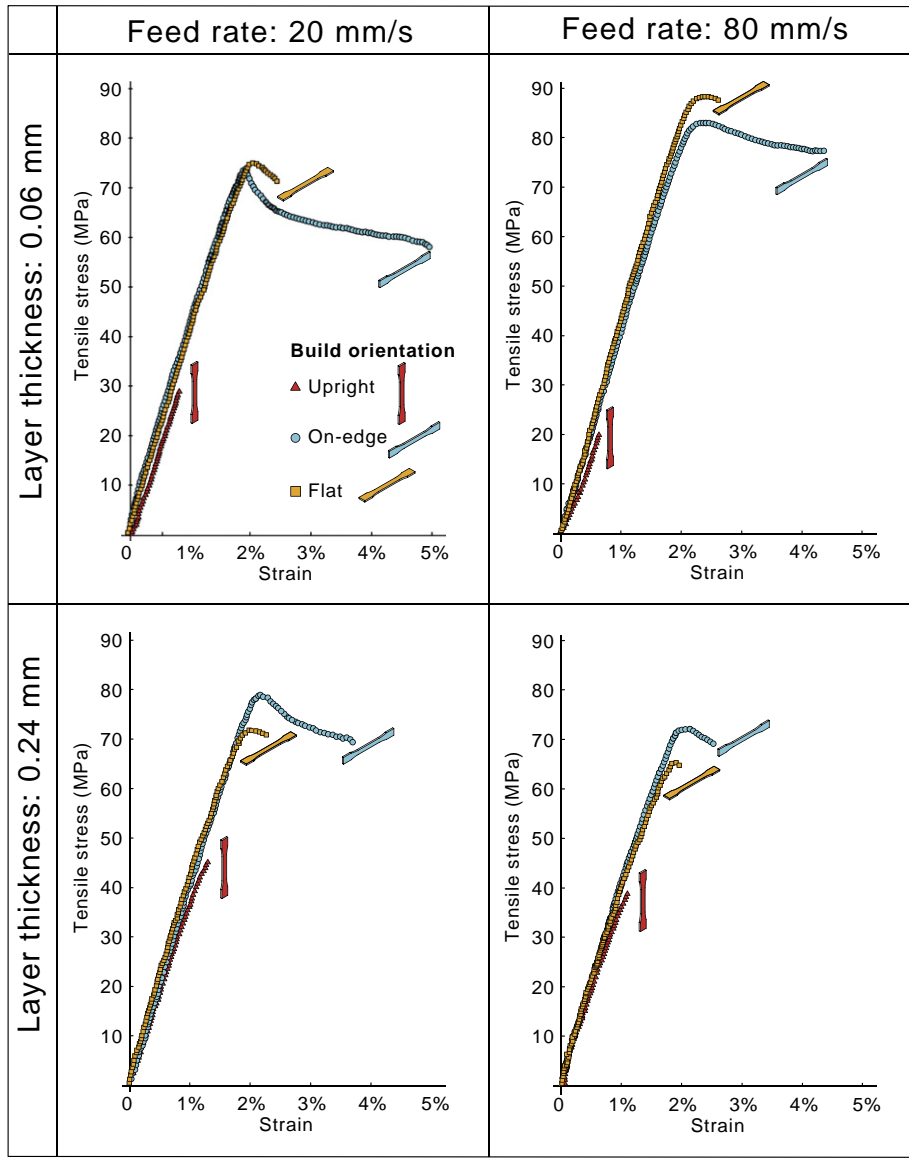


Fig. 6. Average stress–strain curves for the tensile specimens under different printing conditions.

3.4. The effects of feed rate on mechanical properties

The effects of feed rate on mechanical properties are illustrated in Figs. 4b and 5b. Table 6 depicts a significant drop in printing time with increased feed rate, i.e., manufacturing costs decreased as feed rate increased. For the upright orientation, the maximum tensile and flexural strengths decreased as the feed rate increased. These results were in agreement with previous findings [16,34]. In the case of on-edge and flat orientations, the effect of feed rate on the tensile and flexural strengths was of slight significance, except in the case of high feed rate ($F_r = 80$ mm/s) under tensile loading, and two atypical situations for the on-edge oriented samples with $L_t = 0.06$ mm: the tensile performance with $F_r = 20$ mm/s and the flexural performance with $F_r = 80$ mm/s.

In relation to the ductile or brittle behaviour of the samples, the variation of ductility with the feed rate was more meaningful than the variations of tensile and flexural strengths (Figs. 6 and 7). The maximum tensile plastic strain at fracture decreased as the feed rate

increased but to a lesser extent than with increased layer thickness. According to Fig. 7, the reduction of flexural plastic strain at fracture was negligible with increased feed rate. Finally, in terms of stiffness, it should be noted that tensile and flexural elastic moduli exhibited considerable high variability regardless the feed rate.

In short, in the upright orientation, tensile and flexural strengths decreased as the feed rate increased. In this case, high feed rate values should be avoided since there was no significant reduction in printing time. However, taking into account on-edge and flat orientations, the variation of tensile and flexural strengths were slight significance except for low layer thickness ($L_t = 0.06$ mm) as shown in the response surface analysis of Fig. 9. In this case, it is suitable to select high feed rate values with significant savings in printing time.

3.5. Effects of process parameters on printing time

Table 6 depicts printing time and the number of layers for the tensile samples as a function of build orientation, layer thickness, and

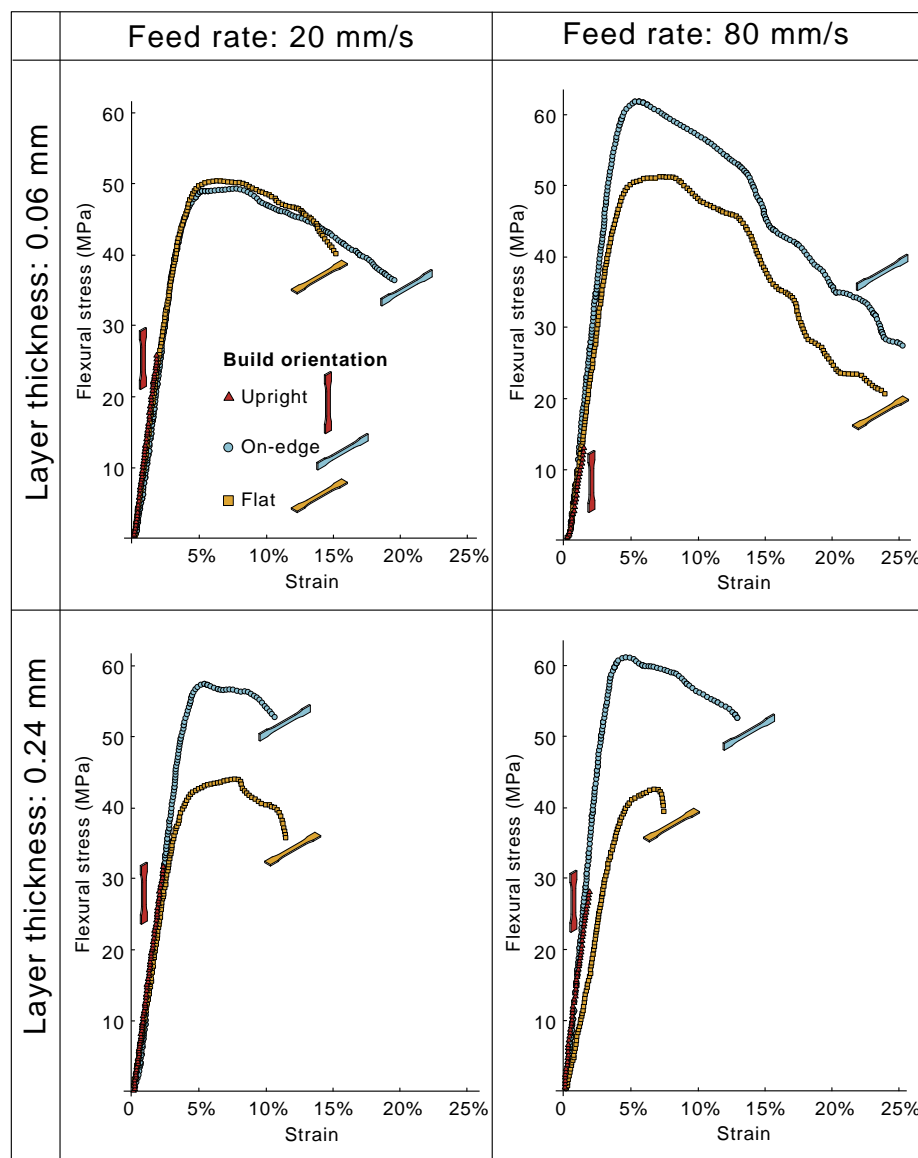


Fig. 7. Average stress–strain curves for the flexural specimens under different printing conditions.

feed rate. As discussed above, printing time was directly related to manufacturing costs and hence it is crucial to bear this in mind. It is also clear from the previous results that printing time was directly

related to the build orientation. Upright samples had the longest printing time and on-edge samples the shortest one. Furthermore, layer thickness and feed rate were the main process parameters

Table 7

Analysis of variance (ANOVA) of full quadratic model for tensile and flexural strengths. Degree of freedom (DF); sum of squares (SS); mean square (MS); F-ratio (F); p-value (p).

Source	Df	Tensile strength (Ts)				Flexural strength (Fs)			
		SS	MS	F	p	SS	MS	F	p
Model	11	149,602.03	13,600.20	139.32	0.0000	82,965.79	7542.34	190.82	0.0000
B_o	2	12,119.10	6059.57	62.07	0.0000	7968.82	3984.41	100.81	0.0000
F_r	1	107,750.00	107,750.00	1103.80	0.0000	59,365.40	59,365.40	1501.95	0.0000
L_t	1	14,777.50	14,777.50	151.38	0.0000	8267.93	8267.93	209.18	0.0000
$F_r \times F_r$	1	11,456.60	11,456.60	117.36	0.0000	4977.97	4977.97	125.94	0.0000
$L_t \times L_t$	1	1549.73	1549.73	15.88	0.0005	1638.05	1638.05	41.44	0.0000
$B_o \times F_r$	2	62.0575	31.0288	0.32	0.7306	191.718	95.8592	2.43	0.1090
$B_o \times L_t$	2	628.371	314.185	3.22	0.0570	186.003	93.0014	2.35	0.1158
$F_r \times L_t$	1	1258.67	1258.67	12.89	0.0014	369.899	369.899	9.36	0.0052
Residual	25	2440.43	97.6174			988.137	39.5255		
Total	36	152,042.46				83,953.93			

Table 8

Regression models for each build orientation in the tensile strength and flexural strength tests.

Position	Optimum model	$R^2_{adj}(\%)$	p-Value	
<i>Tensile strength</i>				
Upright	$T_s = 403.431L_t - 0.726019L_t \times F_r - 827.733L_t \times L_t$	98.5914	L_t	0.0000
			$L_t \times F_r$	0.0404
			$L_t \times L_t$	0.0004
On-edge	$T_s = 256.537L_t + 2.54604F_r - 4.73451L_t \times F_r - 0.0180551F_r \times F_r$	98.0014	L_t	0.0102
			F_r	0.0004
			$L_t \times F_r$	0.0139
			$F_r \times F_r$	0.0159
Flat	$T_s = 239.932L_t + 2.6754F_r - 5.29614L_t \times F_r - 0.0180834F_r \times F_r$	97.8438	L_t	0.0167
			F_r	0.0003
			$L_t \times F_r$	0.0096
			$F_r \times F_r$	0.0186
<i>Flexural strength</i>				
Upright	$F_s = 394.365L_t - 1084.36L_t \times L_t - 0.00129941F_r \times F_r$	97.1857	L_t	0.0000
			$L_t \times L_t$	0.0002
			$F_r \times F_r$	0.0387
On-edge	$F_s = 622.043L_t + 0.538345F_r - 2.85053L_t \times F_r - 1429.2L_t \times L_t$	98.5755	L_t	0.0002
			F_r	0.0110
			$L_t \times F_r$	0.0276
			$L_t \times L_t$	0.0137
Flat	$F_s = 548.51L_t + 0.516918F_r - 1365.74L_t \times L_t - 2.88973L_t \times F_r$	96.8969	L_t	0.0016
			F_r	0.0325
			$L_t \times L_t$	0.0396
			$L_t \times F_r$	0.0496

to have the biggest impact on printing time. Finally, printing time decreased as feed rate increased for on-edge and flat orientations. However, as explained above in the case of the upright orientation, printing time remained almost constant for high feed rate values.

4. Fractographic analysis of the tensile failure of PLA samples

SEM images of the fractured tensile interfaces of samples ($L_t = 0.06$ mm, $F_r = 20$ mm/s) for upright, on-edge and flat orientations are shown in Fig. 10. The comparison of fractured morphologies showed that failure modes changed with respect to build orientation, passing from an essential brittle fracture (Fig. 10a) to a ductile behaviour (Fig. 10c). This transition in fracture behaviour agreed with results obtained from tensile tests (Fig. 6). Failure in tensile specimens with on-edge orientation was mainly associated to trans-layer tensile failure and hence they exhibited a ductile fracture with different planes on the fractured surface with considerable fibre deformation (Fig. 10c). In comparison, specimens with upright orientation experienced a more brittle fracture, with the fractured surface contained in a plane almost perpendicular to the direction of the applied load due to inter-layer fusion bonds failure (Fig. 10a). Finally, specimens with flat orientation displayed an intermediate brittle–ductile fracture behaviour (Fig. 10b).

5. Functional structure test results

A two-part arbitrary functional structural assembly was designed and manufactured to demonstrate the practicality of the previous results. This assembly was selected as a functional static load-bearing structural component. Fig. 11 depicts the 3D geometry of the proposed structural assembly and its main dimensions. Tensile tests were performed to evaluate the functional structural assembly printed with the settings mentioned in Table 11.

Fig. 11(b) depicts the test set-up for determining the maximum strength of the assembly. Owing to the complex geometry of the selected functional structure, the maximum load at failure was considered for strength comparison. Each structural assembly set tested

consisted of five samples for a given group of process parameters. Table 12 shows the average and standard deviation of the maximum load at failure for the selected combinations of build orientation, layer thickness, and feed rate.

As a general remark, the assembly tensile performance was in agreement with the coupons results, and followed the general trends observed for upright samples (i.e., strength increased as layer thickness increased and strength decreased as feed rate increased). In the case of on-edge and flat samples, minor differences in the assembly tensile performance as a function of layer thickness and feed rate were observed. These results were in accordance with the coupon ones, except for the specific case of low layer thickness ($L_t = 0.06$ mm). It is worth noting that a higher standard deviation was observed in the results with $L_t = 0.06$ mm. Moreover, the assembly tensile performance could be affected by the complex geometry of the functional assembly and the combination of different stress states induced during the test.

Fig. 12 shows different failure modes as a function of the build orientation for $L_t = 0.06$ mm and $F_r = 20$ mm/s. As expected, on-edge and flat samples (Fig. 12a and b) depict a ductile fracture behaviour, while upright oriented samples showed a brittle fracture behaviour (Fig. 12c). Hence, the combination of build orientation, layer thickness, and feed rate had a significant effect on the final strength (F_{max}) of the functional assembly, showing variations in terms of average values between different process parameter sets in the range of 149–341 N.

6. Conclusions

We have studied the effect of build orientation, layer thickness and feed rate on the mechanical properties of PLA samples manufactured with a low cost desktop 3D printer. Different ranges of the three process parameters were analysed: build orientation (Flat, On-edge, Upright), layer thickness ($L_t = \{0.06, 0.12, 0.18, 0.24\}$ mm), and feed rate ($F_r = \{20, 50, 80\}$ mm/s). Manufacturing cost is directly related to layer thickness and feed rate, i.e., printing time decreases as layer thickness and feed rate increase. Tensile and three-point

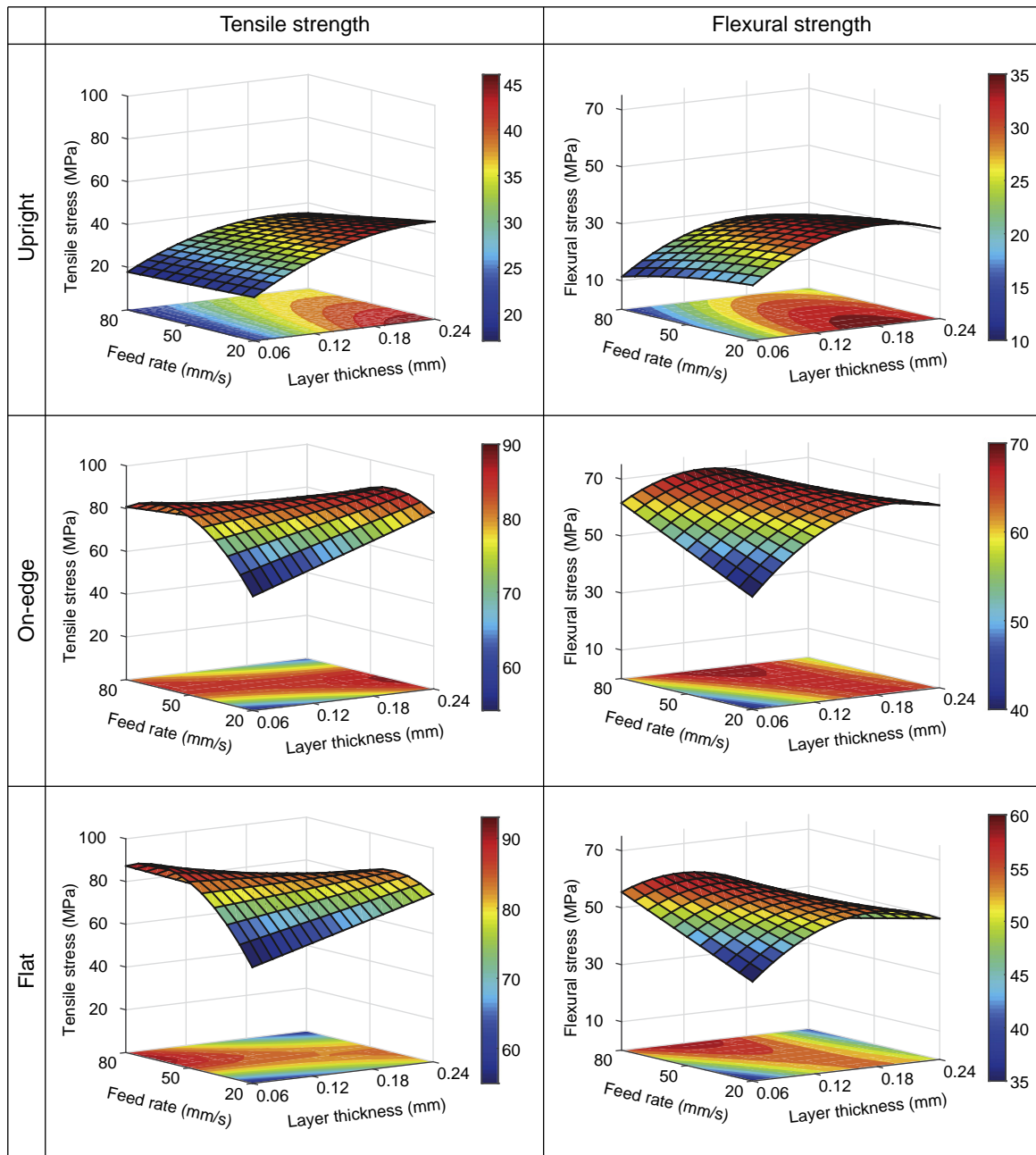


Fig. 8. Normal probability plot of residual at 95% of confidence interval for tensile and flexural strengths as a function of the build orientation.

bending test series were carried out to determine the mechanical response of the printed specimens following the ASTM standard recommendations. Moreover, a parametric analysis of the process parameters was performed. The following conclusions can be drawn from this study:

Build orientation: Upright samples exhibited inter-layer failure with lower strength and stiffness performance. On the other hand, on-edge and flat samples showed trans-layer failure with the highest mechanical properties. In addition, the results have highlighted brittle fracture behaviour for the upright orientation and ductile fracture behaviour for the on-edge and flat orientations. On-edge oriented samples exhibited the best flexural

performance and the tensile strength and stiffness were of the same order as flat samples. In addition, on-edge samples exhibited the best stress-strain behaviour in terms of ductility. It is reasonable to conclude that on-edge samples showed the optimal mechanical performance in terms of strength, stiffness and ductility.

Layer thickness: This parameter had a different effect on the tensile and flexural strengths of PLA samples as a function of the build orientation. In upright samples, tensile and flexural strengths increased as layer thickness increased. In the case of on-edge and flat orientations, the variations of maximum tensile and flexural strengths from $L_t = 0.12$ to 0.24 mm were of slight significance. Nevertheless, for the particular case of $L_t = 0.06$ mm, the results showed higher tensile strength and lower

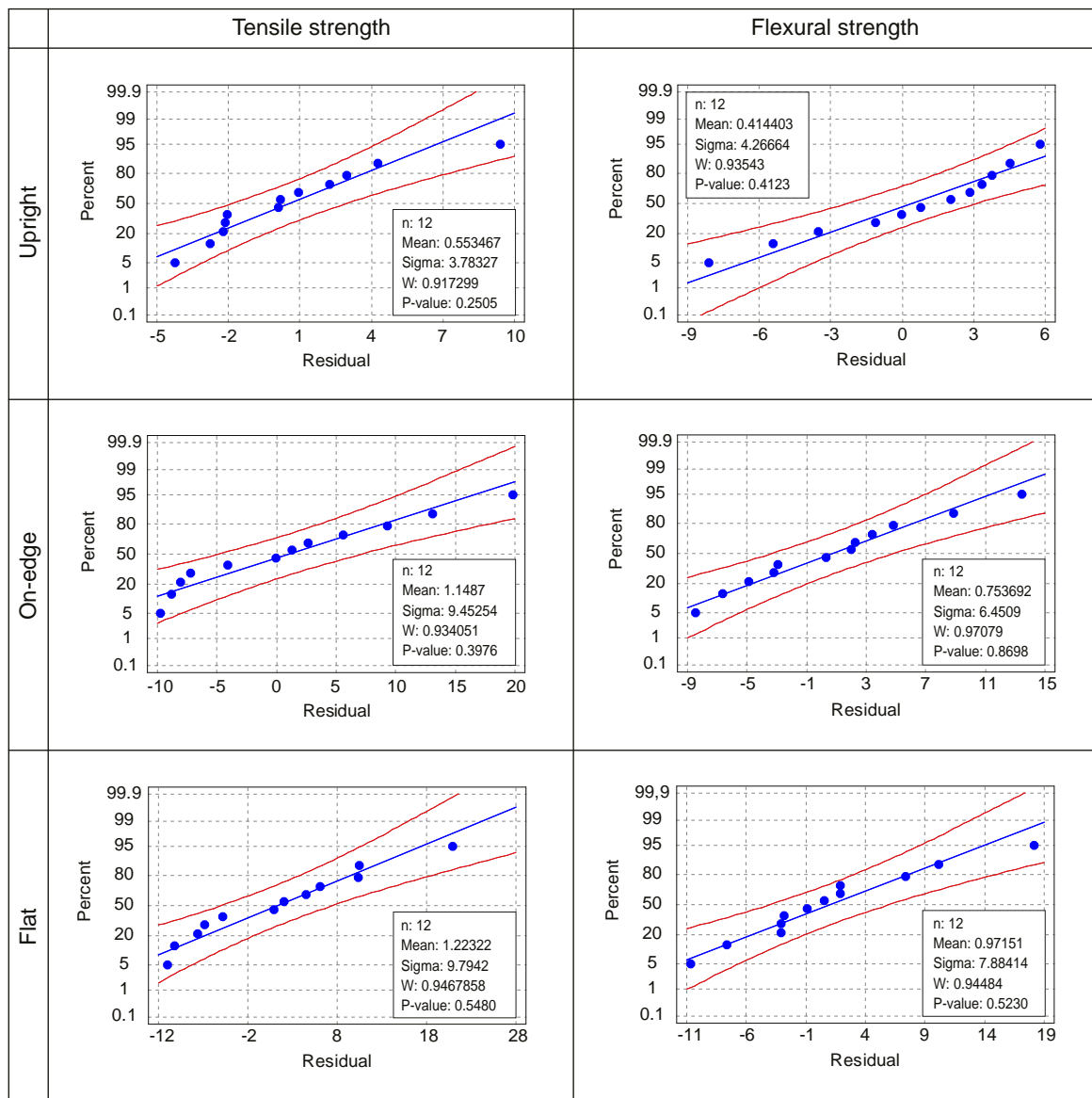


Fig. 9. Response surface analysis for tensile and flexural strengths.

flexural strength. Moreover, it is worth noting that ductility decreased as layer thickness increased.

Feed rate: In upright samples, tensile and flexural strengths decreased as the feed rate increased. In the case of on-edge and flat orientations, the effect of feed rate on the tensile and flexural strengths was of slight significance, except in the case of $F_r = 80 \text{ mm/s}$ under tensile loading. The effect of feed rate on the mechanical performance showed a different trend for $L_t =$

0.06 mm, as shown above. In addition, as in the case of the effect of layer thickness, ductility decreased as layer thickness increased.

In the light of the previous conclusions and the response surfaces, the following print guidelines can be established:

1. As a general remark, on-edge orientation may be selected for the optimal mechanical performance in terms of strength, stiffness and ductility.

Table 9

Percentage variation of maximum tensile and flexural strengths of upright printed samples with layer thickness for different feed rates.

Upright orientation		
From $L_t = 0.06$ to 0.24 mm		
Feed rate (F_r)	σ_t (% of variation)	σ_f (% of variation)
20 mm/s	56%	29%
50 mm/s	84%	101%
80 mm/s	97%	98%

σ_t (% of variation): From $L_t = 0.06$ to 0.12 mm		
Feed rate (F_r)	On-edge orientation	Flat orientation
20 mm/s	-1%	-3%
50 mm/s	-8%	-16%
80 mm/s	-21%	-22%

Table 10

Percentage variation of maximum tensile strength for on-edge and flat printed PLA samples with low values of layer thickness for different feed rates.

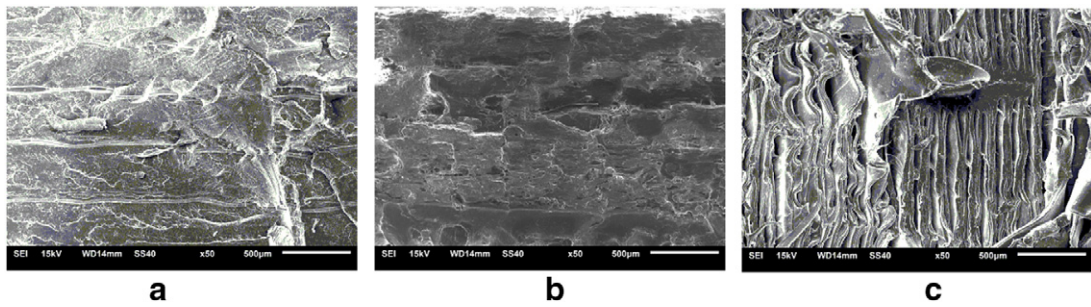


Fig. 10. SEM images showing details of the fractured surfaces of $L_t = 0.06$ mm tensile specimens with $F_r = 20$ mm/s at different orientations of 50×: (a) Upright orientation, (b) Flat orientation, (c) On-edge orientation.

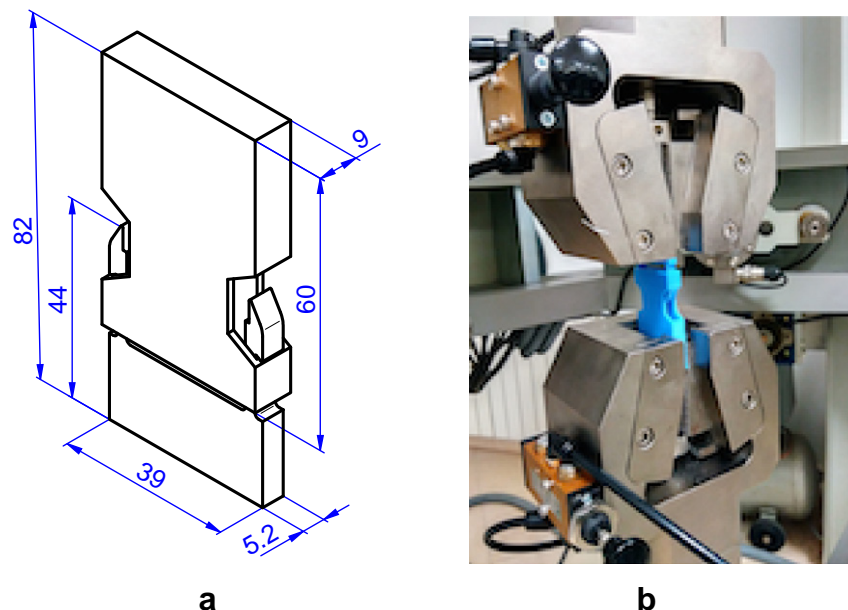


Fig. 11. Functional load-bearing structural assembly, (a) Details of the main dimensions, (b) Test set-up. Dimensions are in mm.

2. If ductile behaviour is desired with the optimal printing time, strength and stiffness:
 - a) High layer thickness and low feed rate values are recommended for upright and on-edge orientations.
 - b) Low layer thickness and high feed rate values are recommended for on-edge and flat orientations.
3. If minimum printing time is desired: high layer thickness and high feed rate are recommended. Though this is not a new finding, the analysis has highlighted that in this situation a slight reduction in strength and stiffness was observed, but a more brittle behaviour was achieved.

The lack of experimental data in the literature as well as the study of potential variables such as extruder temperature, shell thickness

and build material, underscore the need for further research to improve our understanding of the optimal settings and the mechanical behaviour of 3D printed components. Moreover, studies are required to assess the impact of low layer thickness ($L_t = 0.06$ mm) on mechanical performance given the different trend observed in this study.

Table 12

Average maximum load of tensile test results of the functional assembly with different process parameters ranges. Standard deviation is shown in brackets.

Build O.	$F_r = 20$ mm/s			$F_r = 50$ mm/s			$F_r = 80$ mm/s		
	$F_{max}(N)$		$F_{max}(N)$		$F_{max}(N)$		$F_{max}(N)$		$F_{max}(N)$
$L_t = 0.06$ mm									
Upright	194(26.3)		163(22.1)		149(19.6)				
On-edge	341(32.7)		339(20.7)		328(14.5)				
Flat	335(26.9)		329(21.2)		320(53.4)				
$L_t = 0.24$ mm									
Upright	223(29.7)		192(18.9)		174(17.6)				
On-edge	334(31.9)		328(5.3)		323(23.6)				
Flat	327(10.5)		321(19.1)		317(31.9)				

Table 11

Printing settings used in the functional load-bearing structural assembly.

Parameter	Value
Build orientation	Flat (F), On-edge (O), Upright (U)
Layer thickness (mm)	$L_t = 0.06, 0.24$
Feed rate (mm/s)	$F_r = 20, 50, 80$

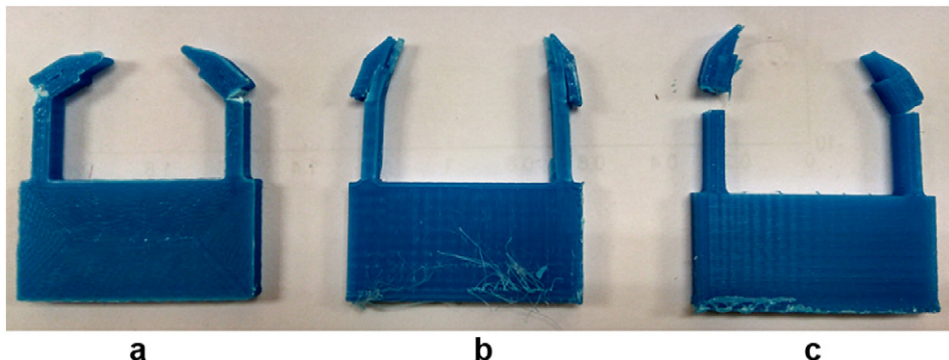


Fig. 12. Different failure modes of the functional load bearing assembly under tensile loading. (a) Flat orientation (brittle–ductile fracture), (b) On-edge orientation (ductile fracture), (c) Upright orientation (brittle fracture).

Acknowledgments

This research was supported by the Spanish Ministerio de Economía y Competitividad (Plan Nacional de I + D + i), under research grant DPI2015-65472-R, co-financed by the ERDF (European Regional Development Fund) and Grant no. GI20163590financed by University of Castilla-la Mancha. We are grateful to Dr. G.P. Rodríguez and Dr. A. Romero for their assistance in taking SEM images of Fig. 10, and to the referees for their suggestions, which improved the quality of this article.

References

- [1] B.M. Tymrak, M. Kreiger, J.M. Pearce, Mechanical properties of components fabricated with open-source 3D printers under realistic environmental conditions, *Mater. Des.* 58 (2014) 242–246.
- [2] M. Sugavaneswaran, G. Arumaikkannu, Analytical and experimental investigation on elastic modulus of reinforced additive manufactured structure, *Mater. Des.* 66 (2015) 29–36.
- [3] G.W. Melenka, B.K.O. Cheung, J.S. Schofield, M.R. Dawson, J.P. Carey, Evaluation and prediction of the tensile properties of continuous fiber-reinforced 3D printed structures, *Compos. Struct.* 153 (2016) 866–875.
- [4] M. Domingo, J.M. Puigriol, A.A. García, J. Lluma, S. Borros, G. Reyes, Mechanical property characterization and simulation of fused deposition modeling polycarbonate parts, *Mater. Des.* 83 (2015) 670–677.
- [5] C. Casavola, A. Cazzato, V. Moramarco, C. Pappalettere, Orthotropic mechanical properties of fused deposition modelling parts described by classical laminate theory, *Mater. Des.* 90 (2016) 453–458.
- [6] B. Rankouhi, S. Javadpour, F. Delfanian, T. Letcher, Failure analysis and mechanical characterization of 3D printed ABS respect to later thickness and orientation, *J. Fail. Anal. Prev.* 16 (2016) 467–481.
- [7] J.M. Chacon, J.C. Bellido, A. Donoso, Integration of topology optimized designs into CAD/CAM via an IGES translator, *Struct. Multidiscip. Optim.* 50 (2014) 1115–1125.
- [8] A. Donoso, J.C. Bellido, J.M. Chacon, Numerical and analytical method for the design of piezoelectric modal sensors/actuators for shell-type structures, *Int. J. Numer. Methods Eng.* 81 (2010) 1700–1712.
- [9] J.M. Chacon, F.P. Garcia, M. Papaelias, Railroad inspection based on ACFM employing a non-uniform B-spline approach, *Mech. Syst. Signal Process.* 42 (2013) 605–617.
- [10] J. Kotlinski, Mechanical properties of commercial rapid prototyping materials, *Rapid Prototyping Journal* 20 (2014) 499–510.
- [11] R. Matsuzaki, M. Ueda, M. Namiki, K. Joeong, H. Asahara, K. Horiguchi, T. Nakamura, A. Todoroki, Y. Hirano, Three dimensional printing of continuous fibre composites by in-nozzle impregnation, *Sci. Rep.* 6 (2016) 23058.
- [12] F. van der Klift, Y. Koga, A. Todoroki, M. Ueda, Y. Hirano, R. Matsuzaki, 3D printing of continuous carbon fibre reinforced thermo-plastic CFRTCP tensile test specimens, *Open Journal of Composite Materials* 6 (2016) 18–27.
- [13] O.A. Mohamed, S.H. Masood, J.L. Bhowmik, Optimization of fused deposition modeling process parameters: a review of current research and future prospects, *Advances in Manufacturing* 3 (2015) 42–53.
- [14] W. Wu, P. Geng, G. Li, D. Zhao, H. Zhang, J. Zhao, Influence of layer thickness and raster angle on the mechanical properties of 3D-printed PEEK and a comparative mechanical study between PEEK and ABS, *Materials* 8 (2015) 5834–5846.
- [15] A.K. Sood, R.K. Ohdar, S.S. Mahapatra, Parametric appraisal of mechanical property of fused deposition modelling processed parts, *Mater. Des.* 31 (2010) 287–295.
- [16] F. Ning, W. Cong, Y. Hu, H. Wang, Additive manufacturing of carbon fiber-reinforced plastic composites using fused deposition modeling: effects of process parameters on tensile properties, *Journal of Composites Materials* 28 (2016) 1–12.
- [17] M. Vaezi, C.K. Chua, Effects of layer thickness and binder saturation level parameters on 3D printing process, *Int. J. Adv. Manuf. Technol.* 53 (2011) 275–284.
- [18] A. Lanzotti, M. Grasso, G. Staiano, M. Martorelli, The impact of process parameters on mechanical properties of parts fabricated in PLA with an open-source 3D printer, *Rapid Prototyping Journal* 21 (2015) 604–617.
- [19] A. Farzadi, M. Solati-Hasjin, M. Asadi-Eydvand, N.A.A. Osman, Effect of layer thickness and printing orientation on mechanical properties and dimensional accuracy of 3D printed porous samples for bone tissue engineering, *PLoS ONE* 9 (2014)
- [20] E. Ullu, E. Korkmaz, K. Yay, O.B. Ozdoganlar, L.B. Kara, Enhancing the structural performance of additively manufactured objects through build orientation optimization, *J. Mech. Des.* 137 (2015) 111410–111419.
- [21] R. Anhita, S. Arunachalam, P. Radhakrishnan, Critical parameters influencing the quality of prototypes in fused deposition modelling, *J. Mater. Process. Technol.* 118 (2001) 385–388.
- [22] J.F. Rodriguez, J.P. Thomas, J.E. Renaud, Design of fused-deposition ABS components for stiffness and strength, *J. Mech. Des.* 125 (2003) 545–551.
- [23] B.H. Lee, J. Abdullah, Z.A. Khan, Optimization of rapid prototyping parameters for production of flexible ABS object, *J. Mater. Process. Technol.* 169 (2005) 54–61.
- [24] J.F. Rodriguez, J.P. Thomas, J.E. Renaud, Mechanical behavior of acrylonitrile butadiene styrene ABS fused deposition materials. Experimental investigation, *Rapid Prototyping Journal* 7 (2001) 148–158.
- [25] G.W. Melenka, J.S. Schofield, M.R. Dawson, J.P. Carey, Evaluation of dimensional accuracy and material properties of the makerbot 3D desktop printer, *Rapid Prototyping Journal* 21 (2015) 618–627.
- [26] Z. Li, A. Haigh, C. Sotis, A. Gibson, R. Sloan, N. Kariman, Detection and evaluation of damage in aircraft composites using electromagnetically coupled inductors, *Compos. Struct.* 140 (2016) 252–261.
- [27] F. Ning, W. Cong, J. Qiu, J. Wei, S. Wang, Additive manufacturing of carbon fiber reinforced thermoplastic composites using fused deposition modeling, *Composites Part B* 80 (2015) 369–378.
- [28] M.A. Caminero, S. Pavlopoulou, M. Lopez-Pedrosa, B.G. Nicolaïsson, C. Pinna, C. Soutis, Analysis of adhesively bonded repairs in composites: damage detection and prognosis, *Composites Structures* 95 (2013) 500–517.
- [29] M.A. Caminero, M. Lopez-Pedrosa, C. Pinna, C. Soutis, Damage monitoring and analysis of composite laminates with an open hole and adhesively bonded repairs using digital image correlation, *Composites Part B* 53 (2013) 76–91.
- [30] M.A. Caminero, G.P. Rodriguez, V. Munoz, Effect of stacking sequence on charpy impact and flexural damage behavior of composite laminates, *Compos. Struct.* 136 (2016) 345–357.
- [31] R. Zou, Y. Xia, S. Liu, P. Hu, W. Hou, Q. Hu, C. Shan, Isotropic and anisotropic elasticity and yielding of 3D printed material, *Composites Part B* 99 (2016) 506–513.
- [32] S.H. Ahn, M. Montero, D. Odell, S. Roundy, P.K. Wright, Anisotropic material properties of fused deposition modelling ABS, *Rapid Prototyping Journal* 8 (2002) 248–257.
- [33] C.S. Lee, S.G. Kim, S.H. Ahn, Measurement of anisotropic compressive strength of rapid prototyping parts, *J. Mater. Process. Technol.* 8 (2002) 248–257.
- [34] K.G.J. Christiyana, U. Chandrasekhar, K. Venkateswarlu, A study on the influence of process parameters on the mechanical properties of 3d printed ABS composite, *IOP Conf. Series: Materials Science and Engineering* 114 (2016) 012109.
- [35] P.L.A. SMARFIL, 2016, www.smartmaterials3d.com.
- [36] BQ, BQ Witbox, 2016, https://www.bq.com/es/witbox-_2.
- [37] Ultimaker, CURA Software, 2016, <https://ultimaker.com/en/products/cura-software>.

- [38] D638, ASTM Standard test method for tensile properties of plastics, Annual Book of ASTM Standards 10 (2010) 1–16.
- [39] D790, ASTM Standard test method for flexural properties of unreinforced and reinforced plastics and electrical insulating materials, Annual Book of ASTM Standards 10 (2010) 1–11.
- [40] A.K. Sood, V. Chaturvedi, S. Datta, S.S. Mahapatra, Optimization of process parameters in fused deposition modeling using weighted principal component analysis, *J. Adv. Manuf. Syst.* 2 (2011) 241–259.
- [41] E. Kiam, Y.J. Shin, S.H. Ahn, The effects of moisture and temperature on the mechanical properties of additive manufacturing components: fused deposition modeling, *Rapid Prototyping Journal* 22 (2016) 887–894.
- [42] F. Mujika, On the effect of shear and local deformation in three-point bending test, *Polym. Test.* 26 (2007) 869–877.
- [43] C. Ziemian, M. Sharma, Anisotropic mechanical properties of ABS parts fabricated by fused deposition modelling, *Mechanical Engineering* 7 (2012) ISBN 978-953-51-0505-3.



Anisotropy and heterogeneity of microstructure and mechanical properties in metal additive manufacturing: A critical review

Y. Kok ^a, X.P. Tan ^{a,*}, P. Wang ^{c,*}, M.L.S. Nai ^c, N.H. Loh ^b, E. Liu ^{a,b}, S.B. Tor ^{a,b}

^a Singapore Centre for 3D Printing, School of Mechanical and Aerospace Engineering, Nanyang Technological University, 50 Nanyang Avenue, 639798, Singapore

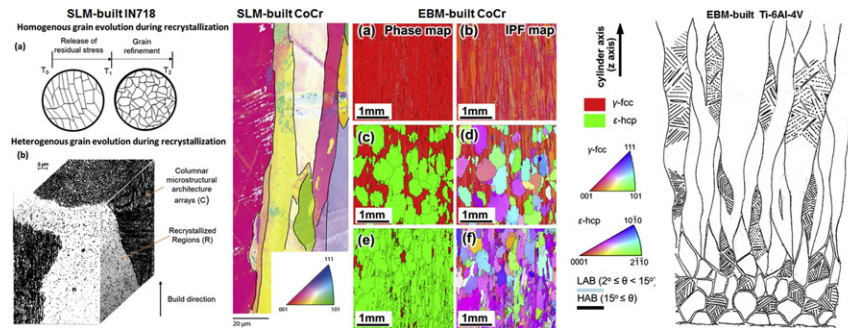
^b School of Mechanical and Aerospace Engineering, Nanyang Technological University, 50 Nanyang Avenue, 639798, Singapore

^c Singapore Institute of Manufacturing Technology, 73 Nanyang Drive, 637662, Singapore

HIGHLIGHTS

- The major metal AM systems and their processing conditions
- The contributing factors on anisotropy and heterogeneity of microstructure and mechanical properties in metal AM parts
- A critical review on anisotropic and heterogeneous mechanical properties of various metal AM parts
- State-of-the-art development in numerical modelling to predict anisotropy and heterogeneity in metal AM parts

GRAPHICAL ABSTRACT



ARTICLE INFO

Article history:

Received 8 July 2017

Received in revised form 9 October 2017

Accepted 9 November 2017

Available online 11 November 2017

Keywords:

Additive manufacturing
Metals
Anisotropy
Heterogeneity
Microstructure
Properties

ABSTRACT

Metal additive manufacturing (AM) has developed rapidly over the last decade to become a disruptive technology capable of revolutionizing the way that products from various industrial sectors such as biomedical, aerospace, automotive, marine and offshore are designed. Early adopters of the technology like the biomedical and aerospace industries have shown that the better-designed components offer substantial performance improvements over current designs. However, in-depth and comprehensive views on the microstructure and mechanical properties of additively manufactured metals and alloys are less reported. To realize the full design potential that metal AM can offer, especially for load-bearing structural components, it is imperative to provide a thorough understanding on the anisotropic and heterogeneous microstructure and mechanical properties that often occur within metal AM parts. This paper outlines a broad range of metal AM technologies and reviews literatures on the anisotropy and heterogeneity of microstructure and mechanical properties for metal AM parts. It can be highlighted that the contributing factors to the anisotropy and heterogeneity within metal AM parts were either their unique microstructural features or manufacturing deficiencies. Concluding remarks on the state-of-the-art research regarding this topic and the possible solutions to overcome the anisotropy and heterogeneity of metal AM parts are provided.

© 2017 Elsevier Ltd. All rights reserved.

1. Introduction

Metal additive manufacturing (AM), popularly known as metal three-dimensional (3D) printing, is a process of joining metallic materials (in powder, wire, sheet forms, etc.) to make objects from 3D

* Corresponding authors.

E-mail addresses: xptan1985@gmail.com, xptan@ntu.edu.sg (X.P. Tan), wangp@simtech.a-star.edu.sg (P. Wang).



models usually layer upon layer [1,2]. Metal AM has the potential of revolutionizing how metallic items are designed and constructed in the digital industrial era [3–5]. Sales of metal AM systems have been increased dramatically over the past few years [6]. Moreover, technologies have become increasingly mature for industrial adoption [7]. Correspondingly, there is an obvious boom in research interest in the area of metal AM, particularly in the last five years [8].

Most of studies have clearly stated benefits of metal AM technology, while there are still some limitations such as anisotropy and heterogeneity in microstructure and mechanical properties [9]. Anisotropy depicts a variety of orientation-dependent features of a material, while heterogeneity is defined as uniformity in its features. Recent studies have found that metal AM parts exhibited anisotropy and heterogeneity in microstructure and mechanical properties [10–15]. In conventional practice, superior and consistent mechanical properties of metal AM parts are prerequisites for engineering applications [16–18]. The use of functionally graded materials (FGM) is less common in conventional applications, though recent research has suggested that FGM are a possible way to meet future demands of the modern industry [19]. There have been extensive studies on the microstructure, mechanical properties, and processability of various metals and alloys in a variety of metal AM systems [8,9,20–22]. In particular, the formation of anisotropic and heterogeneous microstructure and its influence on mechanical properties are becoming hot research topics in metal AM field [9,23–25].

Metal AM parts usually undergo complex cyclic thermal history consisting of directional heat extraction, repeated melting and rapid solidification [21,26], which would create anisotropic and heterogeneous microstructures that intrinsically differed from the metallic parts manufactured via conventional methods [11,12]. As a result, anisotropic and heterogeneous properties may occur in metal AM parts. In addition, AM defects such as pores, rough surfaces and lack of fusion layers, etc., would also induce the anisotropic and heterogeneous properties of metal AM parts [27,28]. This paper will review the published literatures regarding the anisotropy and heterogeneity in microstructure and mechanical properties of metallic parts manufactured by the various metal AM techniques. The main objective is to better understand the microstructure and property of as-built AM materials so that direct manufacturing of metallic parts could be achieved in the short run.

2. Metal AM systems

2.1. Classification

The American Society for Testing and Materials (ASTM) international committee F42 on AM technologies classified AM technologies into 7 process categories in total [29]. The categories pertaining to metal AM are the following directed energy deposition (DED), powder-bed fusion (PBF), and sheet lamination (SL). The abbreviations of metal AM

systems mentioned in this paper are listed in Table 1. Fig. 1 shows a summary of the metal AM methods for each category.

2.1.1. Powder-bed fusion (PBF)

PBF processes typically involve selective sintering or melting of powder materials using either a laser or an electron beam based on a powder-bed [30]. The laser beam imparts energy to the metallic powder via the absorption of radiation, while the electron beam works via the kinetic collisions between electrons and powder [31]. At the beginning of the process, a fresh layer of metallic powder was spread evenly using a rake or roller mechanism. The high-energy laser/electron beam then selectively melted the deposited layer of powder. After a layer was built, build table was lowered and the cycle repeated till the part was fully fabricated.

A generic schematic of a PBF system is shown in Fig. 2. There are a number of laser-based AM techniques such as Laser Cusing, Direct Metal Laser Sintering, Selective Laser Sintering and Selective Laser Melting, though they are all essentially share a similar working principle [8]. The term “SLM” will be used to refer to all laser-based AM techniques under the PBF process for clarity in the following section. Unlike the SLM technologies, Arcam AB (Mölnadal, Sweden) is currently the only commercial manufacturer of electron beam-based PBF systems, i.e. EBM.

2.1.2. Directed energy deposition (DED)

DED processes cover the following systems such as Laser Engineer Net Shaping (LENS), Direct Metal Deposition (DMD), Laser Metal Deposition (LMD) and Shaped Metal Deposition (SMD). The DED process can be further sub categorized according to their material feedstock mode (i.e. powder-fed systems and wire-fed systems) as shown in Fig. 1.

Generic illustrations of the DED powder-fed system and wire-fed system are shown in Fig. 3. DED process is a category of AM techniques that use a focused beam or an electric arc to fuse metallic powder or wire materials feedstock by layer-wise melting [20,33]. Metal parts fabricated by DED processes exhibited high cooling rate solidified microstructures [2]. The layer of material being deposited can vary between 0.1 to a few millimetres in thickness [20]. Powder-fed AM systems have shown unique advantages in repair of worn or damaged metal components as they are not restricted to a powder bed [34].

Of particular interest is that DED processes are capable of producing functionally graded (heterogeneous) parts due to its flexibility to change materials' compositions at each layer, by simply adjusting feeding materials and process parameters [2,35]. Additionally, wire-fed systems have the highest deposition rates due to the feedstock of wire materials.

2.1.3. Sheet lamination (SL)

Sheet lamination (SL) processes include ultrasonic additive manufacturing (UAM) and laminated object manufacturing (LOM). SL processes typically bond thin sheets of metallic foils by brazing, diffusion bonding, laser welding, resistance welding, or ultrasonic seam welding. A promising SL process is UAM, which uses ultrasonic vibrations to bond metal tapes into near net shape components [36]. Generic schematics of two SLAM systems are shown in Fig. 4. An advantage of SL process is in its capability of processing different metal materials. The process does require additional post machining to remove unbound metals and to produce features such as channels and holes in order to achieve the desired geometry. Due to the joining of metal sheets, anisotropy in mechanical properties was prevalent in SL parts [20]. This is mainly due to the weaker bonding formed across the foil interfaces as compared with the intergranular bonding within each foil tape [2].

We found that each metal AM system may have their specific applications based on their own advantages. PBF systems are typically employed to produce complex geometries requiring high resolution and rigorous build accuracy. While DED systems are commonly applied to repair and refurbishment of metal parts and large-scale

Table 1
Abbreviations of metal AM terms mentioned in this paper (in alphabetic order).

Nomenclature	
DED	Direct energy deposition
DMLS	Direct metal laser sintering
EBF ³	Electron beam freeform fabrication
EBM	Electron beam melting
LF3	Laser free-form fabrication
LENS	Laser engineered net shaping
LMD	Laser metal deposition
LOM	Laminated object manufacturing
PBF	Powder bed fusion
SL	Sheet lamination
SLM	Selective laser melting
SLS	Selective laser sintering
SMD	Shaped metal deposition
UAM	Ultrasonic additive manufacturing

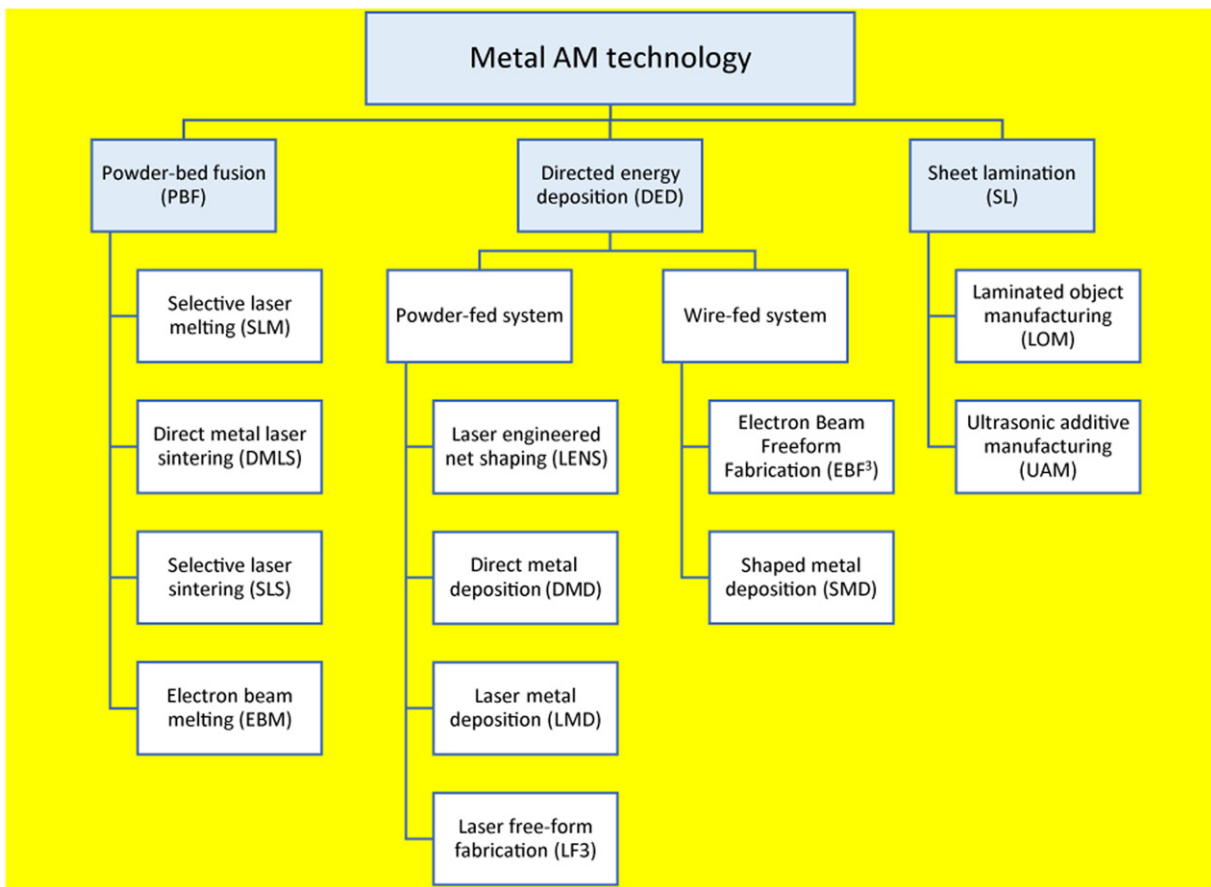


Fig. 1. Summary of metal AM systems.

manufacturing. Lastly, sheet lamination systems have the capability of joining dissimilar metals to produce components with some specific properties.

2.2. Influence of processing variables on anisotropy and heterogeneity

A brief summary of the operating conditions and specifications of typical PBF, DED and SL systems is shown in Table 2. AM processing variables such as deposition rate, beam size, process temperature, deposition rates, deposition mode or scanning strategy, materials would result in differences in the microstructure of the as-fabricated part. The following sub sections will discuss such processing variables

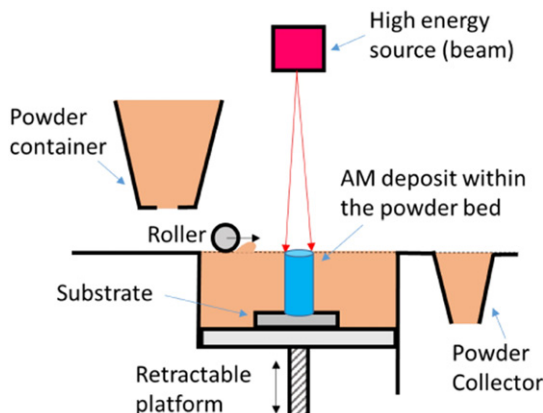


Fig. 2. Generic illustration of a PBF AM system [32].

with regards to their influence towards anisotropy and heterogeneity of microstructures and properties for metal AM parts.

2.2.1. Deposition rate

Some AM processes such as powder-fed DED are capable of producing material heterogeneity through in-situ variation in the deposition rate [53]. Fig. 5a and b shows the result of a study that investigated the effect of deposition rates on the area fraction of equiaxed or columnar grains in the microstructure of DED titanium parts [53]. Though the reduction in deposition rate and beam size are often required to achieve better geometrical accuracy in such processes [2]. Fig. 5c and d shows simulation results that supports the previous findings that the higher deposition rate results in the greater percentage of equiaxed grains. As a high deposition rate would correspond to a larger melt pool geometry and higher scanning velocity.

2.2.2. Beam size and power

Beam size and power may influence particle ejection during the layer-wise melting process. There are three basic particle ejection modes in beam melting processes: (1) the convective transport of liquid or plasma metal out of the molten pool commonly called spatter ejection or sometimes referred to "fireworks" during the melting process, (2) kinetic recoil of powder in DED and (3) electrostatic repulsion of powder particles in EBM [20]. The former has been known to result in welding defects and is an underlying mechanism for the formation of process-induced porosity [20,55]. Such defects can in turn affect the anisotropy and heterogeneity of the metal AM part.

2.2.3. Build environment

The AM build environment is an important processing variable. It was found that the absorption of atmospheric gasses during the

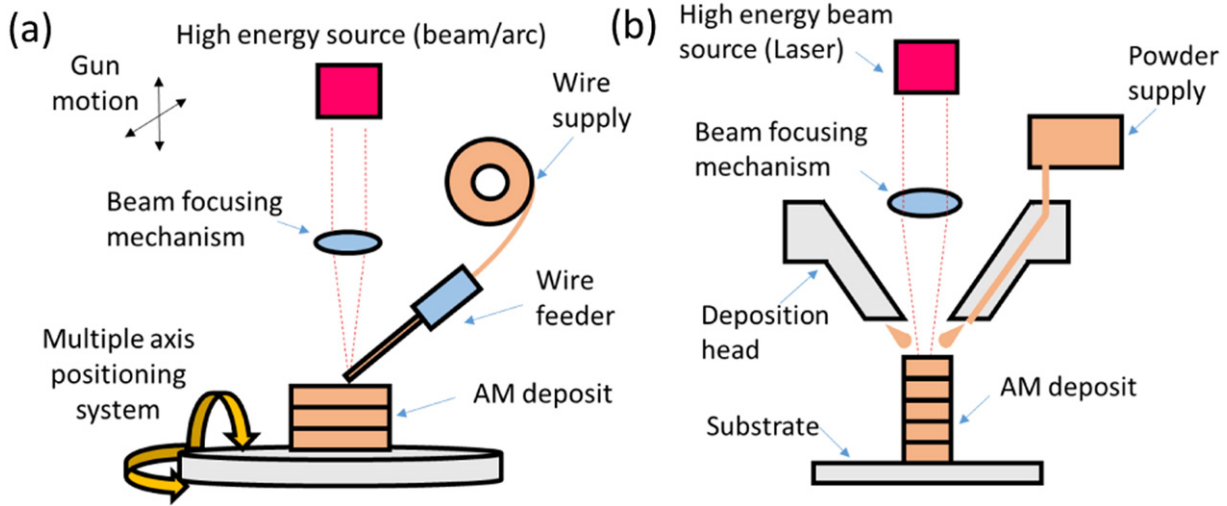


Fig. 3. Generic illustrations of a DED AM systems: (a) powder-blown system, (b) wire-fed system [21].

building process might negatively impact the mechanical properties of the materials [56]. Thus, inert gas or vacuum atmosphere were often used during the metal AM processes [8]. However, operating in high vacuum environment will lead to an increased melt vaporization and outgassing of impurities [20,57], which could cause heterogeneity in chemical composition. In addition, it was reported that the flow rate and the pathway of inert gas had an effect on the porosity in SLM-built Ti-6Al-4V [58] due to the fact that impurities generated from the melting process were re-deposited onto the scanned area.

2.2.4. Processing temperature

Processing temperature varies among the different metal AM systems. Some metal AM systems like LENS and UAM typically work at low process temperatures, while others such as EBM could require a processing temperature as high as ~1000 °C for some high-temperature materials [59]. Low substrate temperature in metal AM systems can reduce the heterogeneity in microstructure due to differences in part size [60]. However, the low substrate temperature could induce a higher magnitude of residual stress distributed unevenly in metal AM parts [61], which has been reported to negatively affect the bulk mechanical behaviour [20].

2.2.5. Deposition mode and scan strategy

Deposition mode is the way in which material is delivered onto the melt surface in the metal AM system. The angle at which the material

is fed in DED processes has been shown to be significant to minimize the defects during melting [62]. In the case of PBF processes, the beam scanning strategy is the important factor for controlling build defects [63]. The scan strategies that are commonly used in PBF systems include bi-directional, snaking and checker box [64–66]. Scan strategies have been reported to influence the crystal texture of the grains due to differences in the overall direction of the thermal gradient [67,68]. Crystallographic texture mainly contributes to anisotropy in the material [69,70]. Other than crystallographic texture, scan strategy has also been attributed to be able to control the formation of either equiaxed or columnar grains, by altering the scan strategy across layers [71,72]. As such it can be seen that deposition mode and scan strategy could play an important role in controlling the anisotropy and heterogeneity in metal AM parts.

2.2.6. Materials

Most of metal AM technologies such as PBF, DED and SL, adopt raw material in the forms of powder, wire and sheet. The quality of powder (e.g. morphology and size distribution) used in PBF systems can determine the uniformity of powder spreading across the build plate [73, 74]. Such physical properties can also affect the density of metal AM parts [75]. The difference in the powder's quality is due to the different powder production methods [20]. Some powder production methods such as gas atomization can induce gas porosity into the final AM part. Post heat treatment processes (e.g. hot isostatic pressing) was needed to eliminate such pores [57]. The technology for the production of

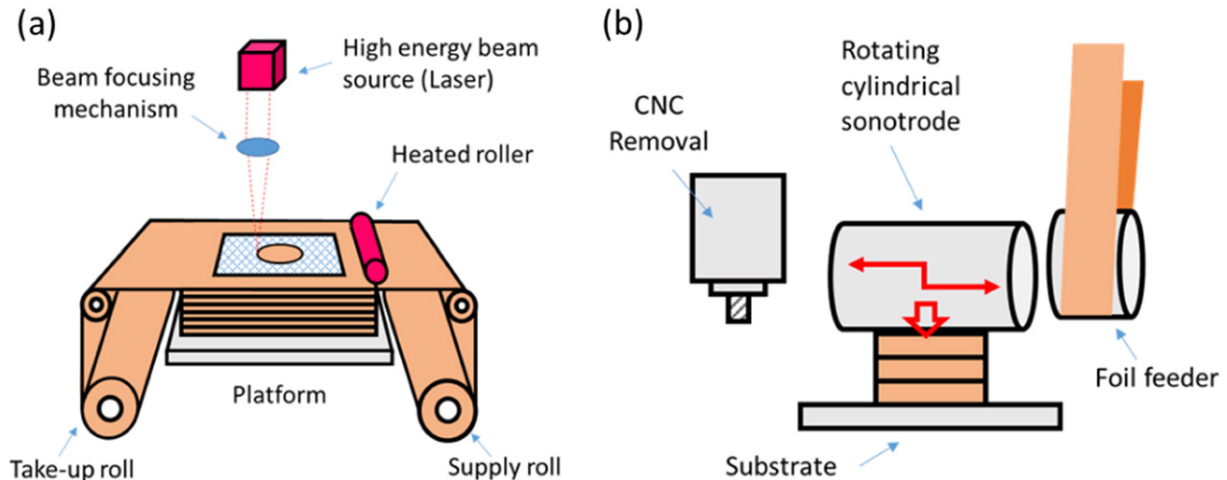


Fig. 4. Generic illustrations of SL AM systems: (a) laminated object manufacturing (LOM) [2] and (b) ultrasonic additive manufacturing (UAM) [37].

Table 2

Various operating conditions and specifications of PBF, DED and SL systems.

System	Build volume (mm)	Energy source	Preheat temperature (°C)	Beam dia. (μm)	Deposition rate/cc h ⁻¹	Layer thickness (μm)	Ref.
Powder-bed system							
Electron beam based							
Arcam (A2XX)	Ø420 × 380	3 kW electron beam	Up to 850 (Ti-6Al-4V, CoCr etc.)	~250	Up to 60	50	[20,38,39]
Arcam (A2X)	200 × 200 × 380	3 kW electron beam	Up to 1100 (Ti-6Al-4V, Inconel, Ti-Al etc.)	~200	Up to 80	25–90	[40–45]
Arcam (Q10)	200 × 200 × 180	3 kW electron beam	Up to 850 (Ti-6Al-4V)	~100	Up to 80	50	[46]
Laser beam based							
SLM (SLM250)	250 × 250 × 350	400 W Nd: YAG laser	Up to 200	~80	~20	20–50	[20,47]
EOS (EOS 400)	400 × 400 × 400	1000 W: fiber laser	Up to 80	~80	~40	40	[28]
Concept Laser (M2)	250 × 250 × 300	200 W: fiber laser	Up to 80	70–200	~20	30	[48–50]
Powder-fed systems							
Optomec	900 × 1500 × 900	1–4 kW IPG fiber laser	–	~250	~230	250	[1,20]
Wire-fed systems							
Sciaky (EBAM 300)	7620 × 2743 × 3353	>40 kW @ 60 kV welder	–	~380	~2000	3000	[1,20]
Sheet lamination systems							
VHP UAM	1500 × 1500 × 600	9 kW @ 20 kHz	–	–	–	150	[51,52]

wire feedstock for the DED process is more mature as compared to the production of powder feedstock [20]. However, there still exist some defects relating to wire-type feedstock. Defects such as cracks or scratches on the wire surfaces can directly lead to porosity in the final AM part [20].

3. Anisotropy in metal AM

Metal AM systems allow the fabrication of near-net-shaped parts with excellent tensile properties [9]. Some researchers reported anisotropic mechanical properties in metal AM parts, while other researchers reported on the contrary [11,76–81]. The discrepancy in the studies may be due to the complex microstructure that exists in metal AM parts [82],

83]. This section thus aims to discuss the relationship between microstructure and mechanical properties on anisotropy.

3.1. Anisotropy in microstructure

3.1.1. Grain morphology

A common microstructure feature observed in metal AM parts was the epitaxial columnar grain morphology [11,15,38,43,84–86]. Fig. 6 shows an example of the epitaxial columnar grain morphology in SLM Co-Cr-Mo-alloy via an SEM micrograph and its corresponding crystal orientation map [87]. Such columnar grains that are aligned parallel to the build direction have been mainly attributed to causing anisotropy of mechanical properties in metal AM parts [10]. In the build direction, the accumulation of slip dislocations along the prior β grain boundaries

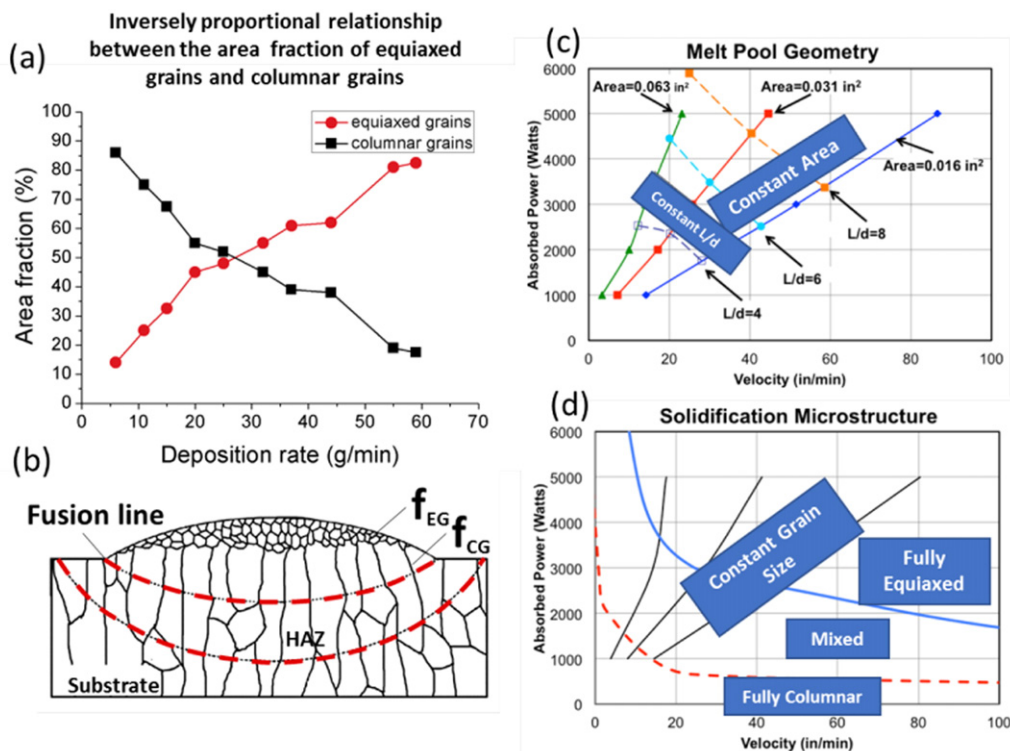


Fig. 5. (a) A plot of the deposition rate against the area fraction of the equiaxed and columnar grains within a melt pool for the powder-fed DED process. (b) A schematic illustrating the measurements of area fractions of equiaxed and columnar grains f_{EG} and f_{CG} based on DED Ti-6.5Al-3.5Mo-1.5Zr-0.3Si alloy [53]. (c) Simulated Beam Power-Velocity process map for melt pool dimension control and (d) microstructure of a single bead deposit of electron beam wire-fed AM Ti-6Al-4V [54]. These show that the formation of a particular grain morphology can be controlled via the deposition rate.

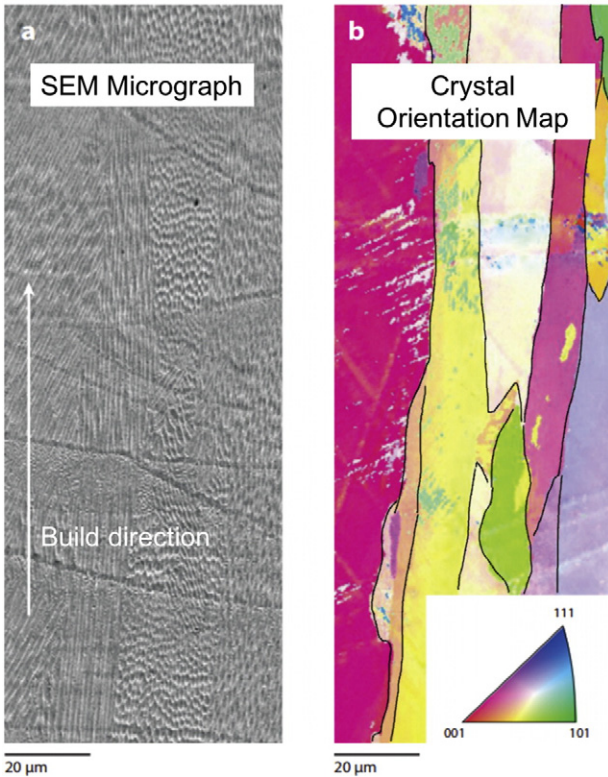


Fig. 6. (a) SEM micrograph of the cross section of a Co-29Cr-6Mo alloy produced using the SLM process. (b) The corresponding crystal orientation map of the micrograph [87] showing the epitaxial columnar grain morphology in metal AM parts.

is greater as compared to the orientation perpendicular to the build direction due to the longer length of the prior β grain boundaries [88]. As such more plastic deformation before failure is generally reported in the vertically orientated samples [9]. Epitaxial columnar grain growth is because of the re-melting of previous layers during the material deposition process. It induced sufficient thermal gradient within the melt pool, which would prevent nucleation ahead of the solidification front [72]. It is worthwhile to note that the novel use of rolling deformation step to refine the columnar grains in AM-processed Ti-6Al-4V alloy has been demonstrated to be effective in refining the grain size [89]. This could lead to new development to metal AM processes.

3.1.2. Crystallographic texture

Given the steep thermal gradient along the build direction, the EBM-built Ti-6Al-4V exhibited a preferential $\langle 001 \rangle$ crystallographic texture for the reconstructed prior β grains [90]. Fig. 7 shows that the $\langle 001 \rangle_{\beta}$ texture of the reconstructed prior β grains of EBM-built Ti-6Al-4V improved with build height due to the grains with a $\langle 001 \rangle$ orientation having the greatest growth advantage [90]. Strong crystallographic texture has been known to result in anisotropy in mechanical properties [91]. However, due to the phase transformation from β to α phase following the Burgers orientation relationship and a near random distribution of α phase across the 12 variants during the phase transformation, the resultant crystallographic orientation of the predominantly α phase showed an almost isotropic distribution [82,85]. It is thus likely that the resultant crystallographic texture in the case of EBM-built Ti-6Al-4V may not be a significant contributor to anisotropy. Another study on laser based PBF tantalum likewise suggested that the elongated grain morphology along the build direction had a larger influence on the anisotropy as compared to the crystallographic texture [69].

3.1.3. Lack-of-fusion defects

Lack-of-fusion defects can be formed possibly due to unoptimized process parameters [92]. Such processing defects can range from ~50–500 μm in size [93]. More importantly, such defects often act as stress concentration sites as they are orientated perpendicularly to the build direction. The directionality of such defects plays an important role on the anisotropy in mechanical properties [27]. This is attributed to the tensile stress being normal to the plane of the defect, thus inducing crack propagation along the tip of the defect leading to material failure. As such, it is important to identify such processing induced defects during the AM process. Many are actively conducting research in the area of in-situ process monitoring, to identify such material discontinuities during the manufacturing process [93]. Post heat treatment process like HIP can eliminate a majority such lack-of-fusion defects from metal AM parts [9].

In summary, columnar grain morphology, crystallographic texture and lack-of-fusion defects are the three factors contributing to the anisotropy in the microstructure of metal AM part. With on-going research to improve the quality of metal AM parts, it can be foreseen that such lack-of-fusion defects will be significantly reduced [9]. Therefore, the columnar grain and the strong crystallographic texture mainly contribute to anisotropy in metal AM parts.

3.2. Anisotropy in mechanical properties

The published literatures regarding the anisotropic mechanical properties (e.g. tensile, compressive, fracture and fatigue) from metal AM parts will be discussed in the following sections. The majority of the available results was based on AM-processed titanium alloys. Other metals or alloys (e.g. cobalt chrome (CoCr), Inconel superalloys, stainless steels and aluminium alloys, etc.) will also be discussed in this article. In addition, the article will examine whether the anisotropic mechanical properties of metal AM-processed parts could meet the minimum requirements for practical applications. As anisotropy is an orientation-dependent property, the orientation designation standard will be presented to provide clarity.

3.2.1. Orientation designation standard

In order to develop standards for AM, the ASTM international formed a committee in 2009 and the International Organization for Standardisation (ISO) formed a committee in 2013. Then the two organizations signed a partnership to jointly develop standards for AM [94]. This article will adopt the ISO and ASTM standard regarding the orientation designations for mechanical testing to provide consistency in comparison [94]. Fig. 8a shows the orientation designation for mechanical testing based on the ISO and ASTM standard. In this terminology, rectangular test coupon requires three alphabets (X, Y, and Z) to provide a complete orientation designation. The X-axis is designated to be parallel to the front of the machine while the Z-axis is in the vertical direction. The Y-axis is perpendicular to both the X and Z-axis, with a positive direction following a right-hand rule coordinate system. The first alphabet in the designation corresponds to the axis parallel to the longest overall dimension and the second and third alphabets correspond to the axis parallel to the second and third longest overall dimensions.

Additionally, Fig. 8b shows the possible ISO designations for determining the orientation dependence of mechanical properties for AM-processed samples based on a study [24]. The first letter in this nomenclature represents the directions normal to the crack plane, and the second letter represents the predicted direction of the crack propagation. The last letter represents the plane in which the crack begins (e.g. start (s), end (e), middle (m) and both (b)). These orientation designation standards thus provide a starting point for comparison of the published literature in the current work. Further standards to designate the orientation and location dependent properties need to be developed given the reported heterogeneity in metal AM parts [9].

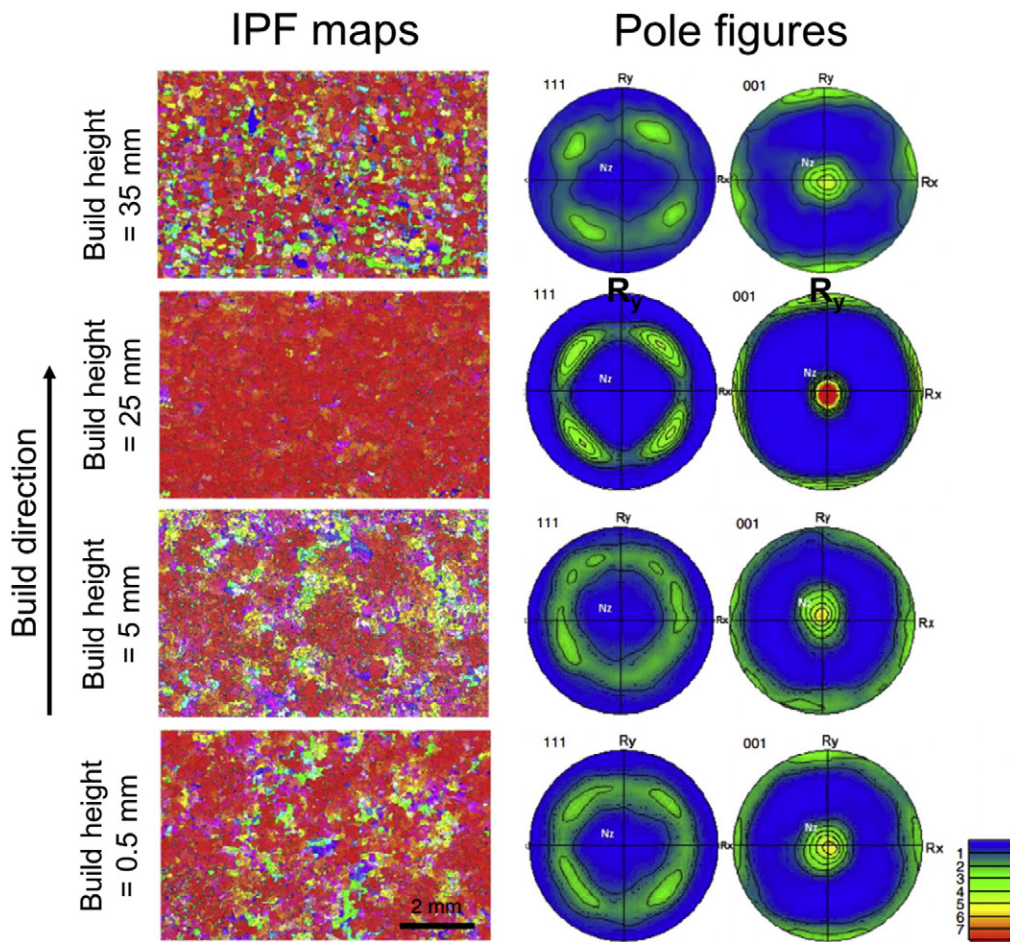


Fig. 7. Reconstructed β -phase IPF maps and their corresponding texture pole figures for EBM-built Ti-6Al-4V alloy at different build heights of (a) 0.5 mm, (b) 5 mm, (c) 25 mm, (d) 35 mm near the build top surface [90] showing the heterogeneity in crystal orientation with build height.

3.2.2. Tensile properties

Many studies have shown that the tensile properties of AM-processed Ti-6Al-4V are comparable to their cast and wrought material equivalents [9,11,21,95]. However, less emphasis has been placed on investigating the anisotropic mechanical properties of metal AM parts using various technologies. More importantly, it is still not well understood if the lower limit of anisotropic mechanical properties in metal AM parts could meet the minimum requirements of their cast and wrought equivalents. Table 3 summarises the anisotropic tensile properties of various metal AM parts. Anisotropy will be defined as $\frac{\sigma_x - \sigma_z}{\sigma_x} \times 100\%$ [96], where σ_x and σ_z denotes the mechanical properties (e.g. yield strength, elongation, fracture toughness and fatigue threshold) in the x and z directions, respectively. It is worth noting that the trend of anisotropy is opposing for tensile strength and ductility [97]. In the majority of the studies on EBM-built and DED-built Ti-6Al-4V, no significant anisotropy in yield strength was observed [11]. However, in the case of SLM-built Ti-6Al-4V, there existed higher anisotropy in the yield strength between the different build orientations. Anisotropy in tensile properties was also observed in SL aluminium alloy [14]. Despite anisotropy being exhibited by the SLM-built Ti-6Al-4V, a majority of the reported yield strength either matched or surpassed the minimum values for their cast and wrought equivalents.

However, the majority of ductility results observed in SLM-built and DED-built Ti-6Al-4V was below the minimum value of 8–10% elongation for wrought material. The low ductility of SLM-built and DED-built Ti-6Al-4V is mainly attributed to the brittle martensitic phase formed during the SLM and DED processes [10,98]. By contrast, EBM-built Ti-6Al-4V parts usually have better ductility properties [11,43,84,

99]. It is noted that SLM, DED and EBM-fabricated parts all showed better ductility in the vertical orientation as compared to the horizontal orientation as can be observed by the high anisotropy percentages [11, 60]. Ductility of metal AM parts can be improved through post heat treatment processes [96,100,101]. In some studies, anisotropy in ductility remains between the different orientations, suggesting that the anisotropic property is most likely due to the columnar grains [11,80,97].

3.2.3. Fracture toughness

Fracture toughness is a property describing the ability of a material containing a crack to resist fracture [120,121]. Table 4 compiles the reported fracture toughness values of some metal AM parts from a variety of studies. In both SLM-built and EBM-built Ti-6Al-4V, anisotropy in fracture toughness was reported [23]. Anisotropy in fracture toughness had a strong influence on the propagation path of cracks [122]. In horizontally orientated samples, cracks propagated through the columnar grains while in vertically orientated samples, cracks propagated along the columnar grain boundary instead [23]. It is worth to note that the fracture toughness of EBM-built Ti-6Al-4V, was comparable to the ASM standard of 44–66 MPa $m^{1/2}$ and 88–110 MPa $m^{1/2}$ for wrought and cast Ti-6Al-4V, respectively [123,124]. The lower toughness values observed in SLM-built Ti-6Al-4V is due to the fine acicular α' martensitic microstructure that is brittle as compared to the α/β duplex microstructure observed in the EBM-built Ti-6Al-4V [125].

Additionally, residual stresses within the metal AM parts can lead to anisotropy in fracture toughness [80]. Such residual stresses can be reduced by post heat treatment processes such as HIP or stress relief treatment. A study based on SLM Ti-6Al-4V observed an increase in fracture

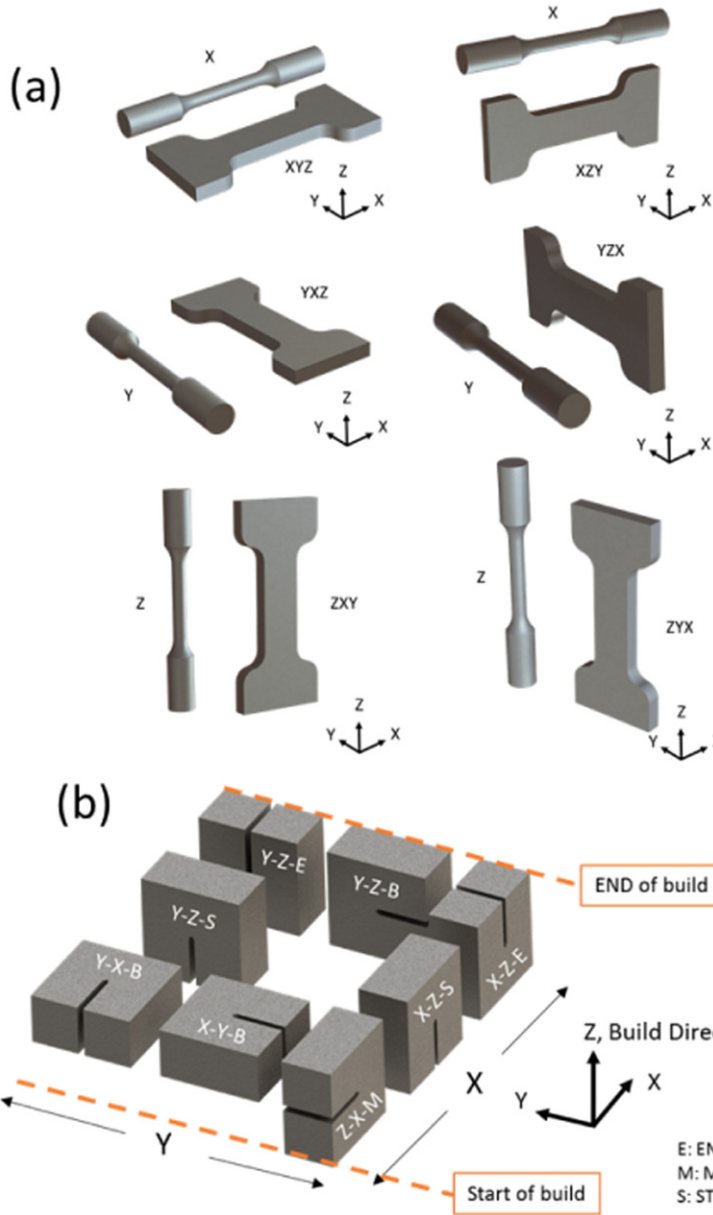


Fig. 8. Orientation designations for mechanical testing of AM-processed materials, (a) tensile test [9] (b) determining the orientation dependence of mechanical properties [24].

toughness and the loss in anisotropy after HIP and stress relief heat treatments for SLM-built Ti-6Al-4V [80]. A study on EBM-built Ti-6Al-4V however reported a decrease in fracture toughness after heat treatment processes, which was due to the coarsening of the microstructure [23]. Thus, understanding of the as-built microstructures for the different metal AM systems is important in determining the post heat treatment schemes in order to achieve superior fracture toughness.

3.2.4. Compressive properties

Compressive testing was also commonly used to evaluate the mechanical properties of metal AM parts [44,126,127]. A study on SLM-built tantalum alloy reported that compressive yield strength was higher in the vertical direction as compared to that in the horizontal direction. This is attributed to the varying crystallographic textures [69]. The mechanical properties of SLM tantalum alloy were found to be better than those fabricated by either electron beam furnace or powder metallurgy despite the anisotropic tensile strength [69]. Anisotropy in mechanical properties can be designed into a part through structural design [128]. A study on EBM builds (Ti-6Al-4V) showed that different

lattice designs exhibited varying degrees of anisotropy [56]. Anisotropy in compressive strength was shown to be dependent on the unit size of the lattice structure [129].

3.2.5. Fatigue properties

The evaluation of fatigue properties is critical to understand how metal AM parts fail under cyclic loading. Table 5 provides a summary of the published data regarding fatigue properties of metal AM parts. It can be observed that higher fatigue strengths were exhibited in the horizontal orientation as compared to the vertical orientation in PBF systems. In general, SLM fabricated parts exhibited a higher Paris slope as compared to the counterparts fabricated by EBM, indicating a higher fatigue crack growth rate [9]. The cycles to failure of the as-fabricated metal AM parts are significantly lower as compared to their wrought equivalent, due to the rough build surface and the presence of internal defects acting as crack initiation sites [9]. However, the fatigue strength of metal AM parts can be improved through post heat treatment and surface machining as shown in Fig. 9 [9,130]. In addition to surface roughness and internal defects, fatigue crack propagation was also

Table 3

Summary of tensile properties of various metal AM parts.

Material	Condition	Process	Tensile axis orientation	Anisotropy in yield strength (%)	Anisotropy in elongation (%)	Yield strength (MPa)	Ultimate tensile strength (MPa)	Elongation (%)	Ref.
Powder-bed fusion									
Electron beam based									
Ti-6Al-4V	As-built	Arcam	Horizontal (XY) Vertical (Z)	−1.0 12.0	−14.0	870.0 ± 8.1 879.0 ± 15.0	971.0 ± 3.1 953.0 ± 8.8	12.1 ± 0.8 13.8 ± 0.9	[102]
Ti-6Al-4V	As-built	Arcam A1	Horizontal (XY & YX) Vertical (ZXY)	−3.7 12.0	−33.3	783.0 ± 15.0 812.0 ± 12.0	833.0 ± 22.0 851.0 ± 19.0	2.7 ± 0.4 3.6 ± 0.9	[81]
Ti-6Al-4V	Machined	Arcam S400	Horizontal (X/Y) Vertical (Z)	27.3 19.0	−98.0	1195.0 ± 19.0 869.0 ± 7.2	1269.0 ± 9	5.0 ± 0.5 9.9 ± 1.7	[103]
Ti-6Al-4V	As-built	Arcam S2	Horizontal (XY) Vertical (Z)	−0.1 12.9	26.2	982.9 ± 5.7 984.1 ± 8.5	982.9 ± 5.7 1032.9 ± 12.9	12.2 ± 0.8 9.0 ± 2.9	[79]
Ti-6Al-4V	As-built	Arcam A2	Horizontal (XYZ) Vertical (ZXY)	23.6	−	825	907	−	[88]
Ti-6Al-4V	HIP	Arcam	Horizontal (XYZ) Vertical (Z)	−0.2 1.8	5.1	630 866 ± 6.4	792 959 ± 8.2	−	[102]
Ti-6Al-4V	As-built	Arcam A2X	Horizontal (XY) Vertical (Z)	−2.8	−28.6	868 ± 2.9 ~875	942 ± 2.6 ~950	12.9 ± 0.8 ~14	[11]
Ti-6Al-4V ELI	As-built	Arcam	Horizontal (XYZ) Vertical (Z)	0.0	−4.1	~900 803	~950 896	~18 17	[104]
Ti-6Al-4V ELI	As-built	Arcam	Horizontal (XYZ) Vertical (Z)	1.8	−9.5	803 817 ± 4.3	896 918 ± 1.0	17.7 12.6 ± 0.8	[102]
Ti-6Al-4V ELI	HIP	Arcam	Horizontal (XYZ) Vertical (Z)	0.9	−8.8	802 ± 7.9 814 ± 2.4	904 ± 6.9 916 ± 2.5	13.8 ± 0.9 13.6 ± 1.2	[102]
CoCrMo	As-built	Arcam	Horizontal (XYZ) Vertical (Z)	−9.6	84.0	807 ± 8.4 717	902 ± 8.7 1110	14.8 ± 0.5 5	[105]
CoCrMo	HIP & HT	Arcam	Horizontal (XYZ) Vertical (Z)	0.2	0.0	786 586	869 1145	0.8 30	[105]
Laser beam based									
Ti-6Al-4V	As-built	SLM	Horizontal (XYZ)	−2.9	0.0	1093 ± 64	1279 ± 13	6 ± 0.7	[80]
Ti-6Al-4V	As-built	Renishaw AM250	Vertical (ZXY) Horizontal (XYZ)	10.0	−17.1	1125 ± 22 1075 ± 25	1216 ± 8 1199 ± 49	6 ± 0.4 7.6 ± 0.5	[97]
Ti-6Al-4V	Machined	EOS M270 SLM	Horizontal (XYZ) Vertical (ZXY)	1.1	24.6	978 ± 5	1143 ± 6	11.8 ± 0.5	
Ti-6Al-4V	Machined	SLM	Horizontal (XYZ) Vertical (Z)	4.4	2.2	967 ± 10 1195 ± 19 1143 ± 30	1117 ± 3 1269 ± 9 1219 ± 20	8.9 ± 0.4 5 ± 0.5 4.89 ± 0.6	[103]
Ti-6Al-4V	Machined	Concept Laser M2	Horizontal (XY) Vertical (Z)	15.4	77.6	1137 ± 20	1206 ± 8	7.6 ± 2	[101]
Ti-6Al-4V	As-built	Concept Laser M2	Horizontal (XY) Vertical (Z)	1.9	−54.5	1070 ± 50	1250 ± 50	5.5 ± 1	[98]
Ti-6Al-4V	SR	SLM	Horizontal (XYZ) Vertical (ZXY)	1.1	−14.3	1050 ± 40 1145 ± 17	1180 ± 30 1187 ± 10	8.5 ± 1.5 7 ± 2.7	[80]
Ti-6Al-4V	SR	Renishaw AM250	Horizontal (XYZ) Vertical (ZXY)	3.8	−37.1	1132 ± 13 974 ± 7	1156 ± 13 1065 ± 21	8 ± 0.4 7.0 ± 0.5	[97]
Ti-6Al-4V	HT	SLM	Horizontal (XYZ) Vertical (ZXY)	2.2	22.6	958 ± 6	1057 ± 8	12.4 ± 0.7	
Ti-6Al-4V	HT	SLM	Horizontal (XYZ) Vertical (ZXY)	0.9	−100.0	937 ± 9 973 ± 8	1052 ± 11 996 ± 10	9.6 ± 0.9 3 ± 0.4	[80]
Ti-6Al-4V	HT	SLM	Horizontal (XYZ) Vertical (Z)	2.0	11.8	964 ± 7 944 ± 8 925 ± 14	998 ± 14 1036 ± 30 1040 ± 4	6 ± 2 8.5 ± 1 7.5 ± 2	[101]
IN718	—	SLM	Horizontal (X/Y) Vertical (Z)	9.7	−7.9	816 ± 24	1085 ± 11	19.1 ± 0.7	[106]
IN718	HT	SLM	Horizontal (XYZ)	2.9	−9.4	737 ± 4 1222 ± 26	1010 ± 10 1417 ± 4	20.6 ± 2.1 15.9 ± 1.0	[106]

(continued on next page)

Table 3 (continued)

Material	Condition	Process	Tensile axis orientation	Anisotropy in yield strength (%)	Anisotropy in elongation (%)	Yield strength (MPa)	Ultimate tensile strength (MPa)	Elongation (%)	Ref.
Al-Si-10Mg	As built	SLM	(X/Y) Vertical (Z) Horizontal (XY)	0.1	−11.0	1186 ± 23 169 ± 1 168.8 ± 1.3	1387 ± 12 272.8 ± 2.9 267	17.4 ± 0.4 8.2 ± 0.3 9.1 ± 0.5	[107]
Al-12Si	As built	SLM	Horizontal (XY)	−1.7	50	270.1 ± 10	325 ± 20	4.4 ± 0.7	
Al-12Si	HT	SLM	Vertical (Z)			274.8 ± 8	296.1 ± 20	2.2 ± 0.3	[108]
Al-Si-10Mg	As-built	Concept laser M2	Horizontal (XY)	2.0	20.8	153.4 ± 5 150.3 ± 17	228 ± 13 210.1 ± 20	5.3 ± 0.7 4.2 ± 0.3	[108]
Al-Si-10Mg	—	Concept laser M1	Horizontal (X/Y)	4.0	16.7	250 240	330 320	1.2 1	[109]
CoCrMo	As-built	Dimetal-100	Vertical (Z)			391 ± 6 398 ± 8	5.55 ± 0.4 3.47 ± 0.6	3.9 ± 0.2	[110]
Horizontal (XY)			Horizontal (XY)	7.1	25.0	738 ± 9.9 685.3 ± 10.5	1050 ± 12.2 970 ± 9.8	5.2 ± 0.3	[111]
DED systems			Vertical (Z)						
Powder-fed deposition									
Ti-6Al-4V	Machined	Trumpf system	Horizontal (X/Y)	0.0	58.3	950 ± 2	1025 ± 10	12 ± 1	[112]
Ti-6Al-4V	As-built	Tritons Laser Free-Form Fabrication (LF3)	Vertical (Z)			950 ± 2	1025 ± 2	5 ± 1	
Ti-6Al-4V	Machined	Tritons Laser Free-Form Fabrication (LF3)	Horizontal (XYZ)	41.5	73.4	892 ± 10	911 ± 10	6.4 ± 0.6	[96]
Ti-6Al-4V			Vertical (ZXY)			522	797 ± 27	1.7 ± 0.3	
TC21 (Ti6Al2Sn2Zr3Mo1.5Cr2Nb)	HT	LAM	Horizontal (XYZ)	2.6	29.6	984 ± 25	1069 ± 19	5.4 ± 1	[96]
Ti-6Al-4V	Machined	DED	Vertical (ZXY)			958 ± 14	1026 ± 17	3.8 ± 0.9	
Ti-6Al-4V	ASTM F1472	As-cast	Horizontal (X/Y)	2.6	−471.4	868	997	2.8	[113]
Ti-6Al-4V	ASTM F1108	Wrought	Vertical (Z)			845	933	16	
CoCrMo	ASTM F75	As-cast	Horizontal (YZX)			960 ± 26	1063 ± 20	10.9 ± 1.4	[10]
CoCrMo	ASTM F1537	Wrought	Vertical	0.2	−28.4	958 ± 19 >758	1064 ± 26 >860	14 ± 1 >8	[114]
Al-Si-10Mg									
IN718	AMS 5382	As-cast				160	325	3	[118]
IN718	AMS 5662	As-cast				758	802	5	[119]
IN718		Wrought				1034	1241	10	[119]

*SR = stress-relieved, HT = heat-treated, HIP = hot isostatic pressing.

found to be dependent on the crystallographic orientation of the grain containing the crack tip, the number of grain boundaries surrounding it and the direction of internal residual stress [97,125].

To sum up, it can be concluded that anisotropy in mechanical properties was indeed exhibited in metal AM parts. Nevertheless, some parts fabricated from certain metal AM systems could exhibit less anisotropy. This is due to the differences in processing variables that lead to a more homogenous microstructure and residual stress distribution. Moreover, it is important to note that post-processing such as surface machining and heat treatment can effectively improve the comprehensive mechanical properties of metal AM parts to be comparable and even superior to their cast and wrought equivalents.

4. Heterogeneity in metal AM

Given that one of the main advantages of AM is its ability to directly manufacture complex geometries, understanding the heterogeneity that exists in metal AM parts is equally important as the anisotropy [20]. A comprehensive set of materials data base would allow designers

better utilize metal AM technologies for more demanding end-use applications [133]. Microstructural heterogeneity of metal AM parts can arise from differences in morphology, size, orientation, and chemical composition of phases and grains. Such differences were resulted from the varying thermal conditions (e.g. thermal gradient and cooling rate) that were included in different metal AM processes [26,134,135].

4.1. Heterogeneity in microstructure

4.1.1. Phase constitution

Difference in phase constitution is an important source of microstructural heterogeneity in metal AM parts. For example, in the case of $\alpha + \beta$ titanium alloys (Ti-6Al-4V), three phases were often reported, i.e. α phase, β phase and α' martensitic phase [85]. Due to the complex phase transformation processes [136], it is difficult to predict the phase constitution in AM titanium alloys accurately. A thorough study has recently described a complete phase transformation sequence that Ti-6Al-4V underwent during EBM process [136,137]. It was reported that the cooling rate and build temperature were the two key process

Table 4

Summary of fracture toughness of various metal AM parts.

Material	Condition	Process	Orientation	Anisotropy in fracture toughness (%)	Fracture toughness (MPa $\sqrt{\text{m}}$)	Ref.
Powder-bed fusion						
Electron beam based						
Ti-6Al-4V	As-built	Arcam A1	Horizontal (Y-X-B, X-Y-B) Vertical (Z-X-M, Z-Y-M)	7.3	110 ± 7.4 102 ± 8.9	[81]
Ti-6Al-4V	As-built	Arcam A2	Horizontal (X-Z-E, X-Y-B, Y-X-B) Vertical (Z-X-M)	18.8	67–80 65	[24]
Laser beam based						
Ti-6Al-4V	As-built	SLM	Horizontal (X-Y-B) Vertical (X-Z-E, Z-X-M)	17.9	28 ± 2 16–23	[80]
Ti-6Al-4V	As-built	MTT 250	Horizontal (Y-X-B) Vertical (Z-X-M, Z-Y-M)	3.1	66.9 ± 2.6 41.8–64.8 ± 16.9	[125]
Ti-6Al-4V	SR	SLM	Horizontal (X-Y-B) Vertical (X-Z-E, Z-X-M)	–10.7	28 ± 2 30–31 ± 2	[80]
Ti-6Al-4V	HT	SLM	Horizontal (X-Y-B) Vertical (X-Z-E, Z-X-M)	–19.5	41 ± 2 49 ± 2	[80]
Al-12Si	As-built	SLM	Horizontal (X-Y-B) Vertical (X-Z-E, Z-X-M)	18.8	46.7 37.9	[108]
Al-12Si	HT	SLM	Horizontal (X-Y-B) Vertical (X-Z-E, Z-X-M)	11.1	21.7 19.3	[108]

conditions to influence the final phase constitutions in the metal AM parts [136]. The proposed phase transformation sequence provides a glimpse of the relationship between the complex thermal history of the EBM process and the final microstructure obtained. A study on SLM-built Ti-6Al-4V has also shown microstructural variation along the build direction [138]. It was suggested that the microstructural variations were caused by a cyclic thermal history from successive depositions. Moreover, the top region only exhibited α' martensitic phase that indicated the as-deposited condition without phase decomposition [138]. Likewise, for the CoCr alloys processed with EBM, the elevated build temperature caused the metastable γ -face centered cubic (fcc) phase transform to the stable ϵ -hexagonal closed packed (hcp) phase during the build process [139,140], resulting in microstructural heterogeneity along the build direction as shown in Fig. 10 [139].

A study regarding the build thickness dependent microstructure and mechanical properties of EBM-built Ti-6Al-4V have reported that the phase constitution highly relied on the cross-sectional area of the metal AM part [134]. Microstructure of thin cross-sectional area would

have a phase constitution that predominantly consists of brittle martensitic phase while it would be ductile $\alpha + \beta$ dual phase for thick cross-sectional area [134]. This is due to the fact that the thick cross sectional area could retain a higher temperature with to lower cooling rates [134,141]. Another study based on DED-built IN718 superalloy has also attributed the formation of precipitates to cause heterogeneity in hardness [13]. Microstructural heterogeneity was thought to be due to solidification segregation, with the presence of niobium along the grain boundary promoting the heterogeneous nucleation and growth of γ' phase [13]. Thus, it can be seen that the varying phase constitution at different locations for varying geometry may induce heterogeneity in metal AM parts.

4.1.2. Layer banding and microstructure coarsening

Layer bandings is a popular observed phenomenon in metal AM materials [26,44,142,143]. Prior research has shown that in titanium alloys, layer banding was a result of segregation of vanadium and aluminium. However, a study by Kelly & Kampe revealed no systematic elemental

Table 5

Summary of fatigue properties of PBF metal AM Ti-6Al-4V parts and ASTM wrought Ti-6Al-4V.

Material	Condition	Process	Test orientation	Load ratio (R)	Anisotropy in fatigue overload (%)	Fatigue overload (MPa $\sqrt{\text{m}}$)	Cycles (m/cycle)	Paris slope	Anisotropy in fatigue threshold (%)	Threshold (MPa $\sqrt{\text{m}}$)	Ref.
Electron beam based											
Ti-6Al-4V	As-built	Arcam A2	Horizontal (X-Z,X-Y) Vertical (Z-X)	0.1,0.3,0.7	28.1	63–96		1.4–3.1	33.3	3.5–5.7	[24]
Ti-6Al-4V	As-built	MTT 250	Horizontal (X-Y) Vertical (X-Z,Y-Z)	0.3	32.7	69 33.3 22.4–36.0	1.2 × 10 ⁷ 2.61 1.7 × 10 ⁷ –2.1 × 10 ⁷	2.6 7.9 2.37–2.45		3.8 6.3 5.8–5.9	[125]
Laser beam based											
Ti-6Al-4V	As-built	SLM	Horizontal (X-Y-B) Vertical (X-Z-E,Z-X-M)				5.79 × 10 ¹²	3.37			[80]
Ti-6Al-4V	SR	SLM	Horizontal (X-Y-B) Vertical (X-Z-E,Z-X-M)				2.08 × 10 ¹² –7.51 × 10 ¹²	4.17–4.41			[80]
Ti-6Al-4V	HT	SLM	Horizontal (X-Y-B) Vertical (X-Z-E,Z-X-M)				9.93 × 10 ¹⁵	5.84			[80]
Ti-6Al-4V	HT	SLM	Horizontal (X-Y-B) Vertical (X-Z-E,Z-X-M)				1.16 × 10 ¹¹ –8.85 × 10 ¹²	3.24–3.35			[80]
Ti-6Al-4V	Wrought						2.04 × 10 ¹²	3.83			[80]
Ti-6Al-4V							1.71 × 10 ¹¹ –2.58 × 10 ¹¹	3.11–3.35			[131,132]
								2.3–4.2			

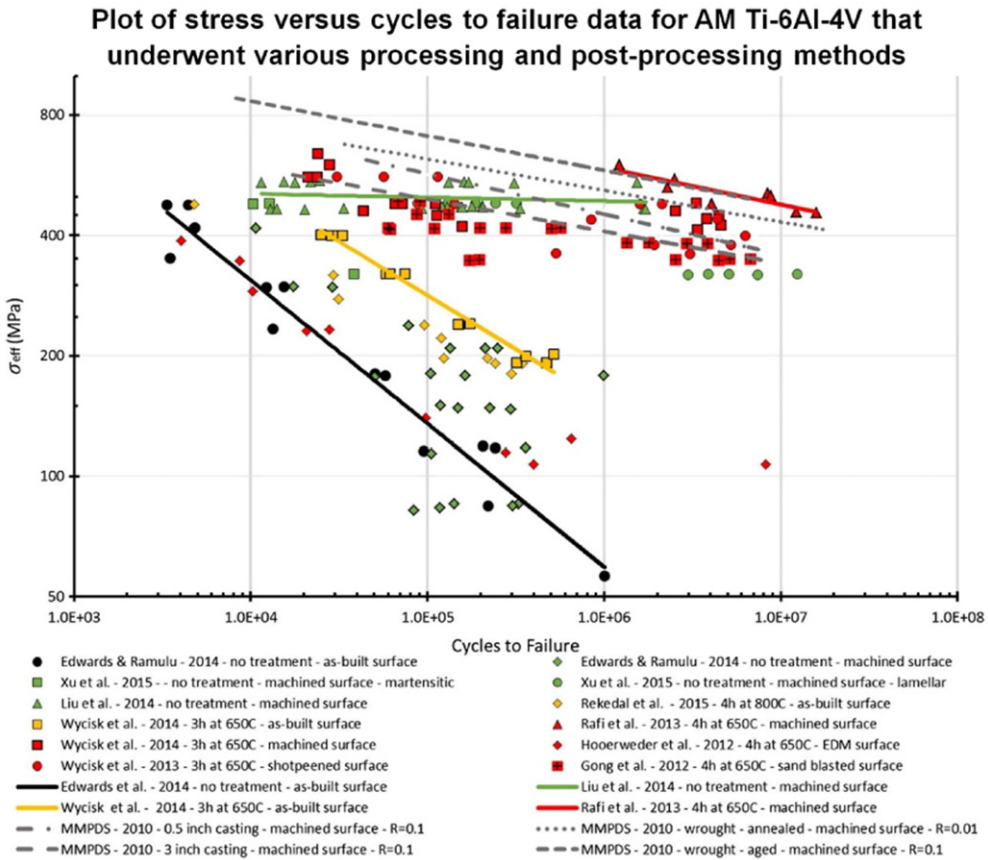


Fig. 9. Fatigue test results compiled by [130] shows the effect of various post-processing treatments on improving the fatigue properties of AM-processed Ti-6Al-4V.

variation in DED-built Ti-6Al-4V [142], and concluded that such layer bands were resulted from the cyclic thermal history that the part experienced after multiple layers' deposition [26,143]. A study on wire-fed DED-built Ti-6Al-4V developed a schematic diagram showing the formation of the layer bands as shown in Fig. 11 [142]. Differences in the microstructure feature (e.g. mean width of α laths) could be clearly observed between the top and the bottom of a layer band [142]. Despite the unique microstructural morphology, it is still unclear how such heterogeneity affects Ti-6Al-4V AM parts' mechanical properties. Another study conducted by Nakano et al. also reported the layer band in EBM-built Ti-48Al-2Nb-Cr alloy and also concluded that this layer bands was resulted from cyclic thermal history. Moreover, this layer band improves the ductility of Ti-48Al-2Nb-Cr alloy in a certain loading direction [42].

4.1.3. Grain morphology

The grain morphology within metal AM parts has been shown to depend on the process parameters and materials [67,72,84,144,145]. Studies on EBM-built IN718 has shown that site specific control of the grain morphology by varying the processing parameters (e.g. line offset, speed function) was possible with metal AM [72,144]. Heterogeneity in grain morphology was also observed in EBM-built CoCr parts, due to recrystallization caused by the high build temperature [140]. While in EBM-built Ti-6Al-4V parts, the increase in columnar grain width was observed with the increased build height [84]. Additionally, an equiaxed-to-columnar transition of prior β grains in Ti-6Al-4V was reported at the start of the EBM build as shown in Fig. 12 [84]. It was suggested in the study that the higher heat conductivity of the start plate material resulted in a higher degree of super cooling which led to the transition of grain morphology [84].

4.1.4. Microstructural feature size

Several studies have shown that the microstructure of AM-processed Ti-6Al-4V tended to become finer at the top region as compared to the bottom [146–148]. While other studies showed opposite trends instead [11,84]. Microstructural scale is known to decrease with increasing cooling rate [149]. There are three main paths that heat was lost in the metal AM process (1) radially through the surrounding powder bed or environment, (2) vertically downwards through the build start plate via conduction and (3) vertically upwards from the top layer via convection and/or radiation towards the ambient [15,141]. At the very top region of the metal AM parts, the fine microstructure is likely due to the high cooling rate induced by heat loss of convection and radiation and the lack of remelting and thermal cycling that prior layers experienced [142]. Additionally, microstructural scale was found to be dependent on cross-sectional thickness due to differences in the hatch lengths and thermal mass as can be observed in Fig. 13 [141,150,151]. Coarse microstructure size could be observed in the thick cross-sectional parts due to the slow cooling rates within high thermal mass [134]. A study has also shown that it is possible to induce refinement of microstructure through the use of in-situ printed heat sinks in EBM-built Ti-6Al-4V [152].

4.1.5. Processing deficiency

AM processing defects have been reported to contribute to anisotropy in mechanical properties of metal AM parts such as fracture toughness and tensile strength [9,101]. Additionally, there have also been studies reported that such defects were not homogenously distributed within the build as shown in Fig. 14a and b [23]. Unfortunately, the mechanism for the formation of location specific defects is not well understood yet [153]. The spherical pore defects with a diameter of 10–50 μm were reported to be due to the trapped gas pore in gas atomized

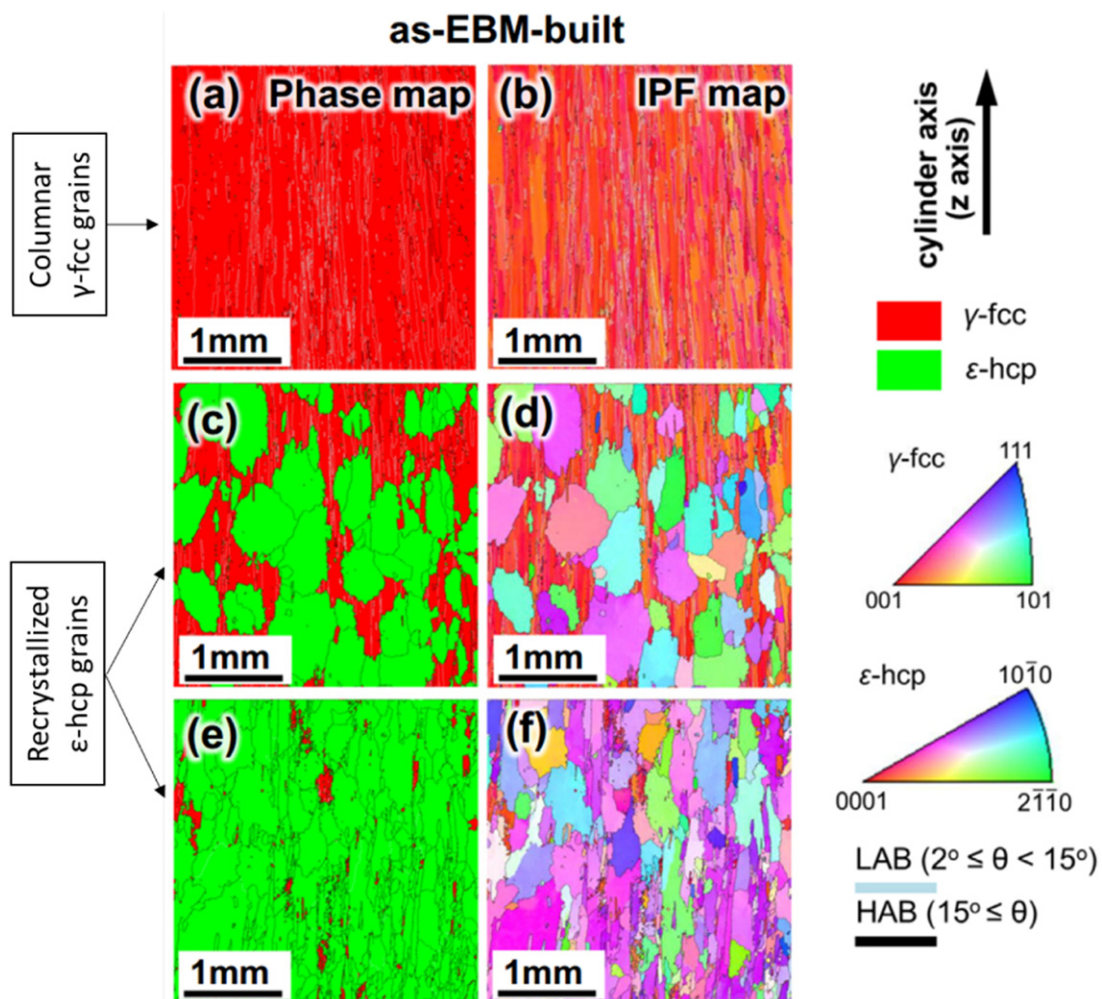


Fig. 10. EBSD phase map (a, c, e) and IPF crystallographic orientation map (b, d, f) on the longitudinal cross-section of EBM-built CoCrMo showing variation in phase composition and grain morphology [140].

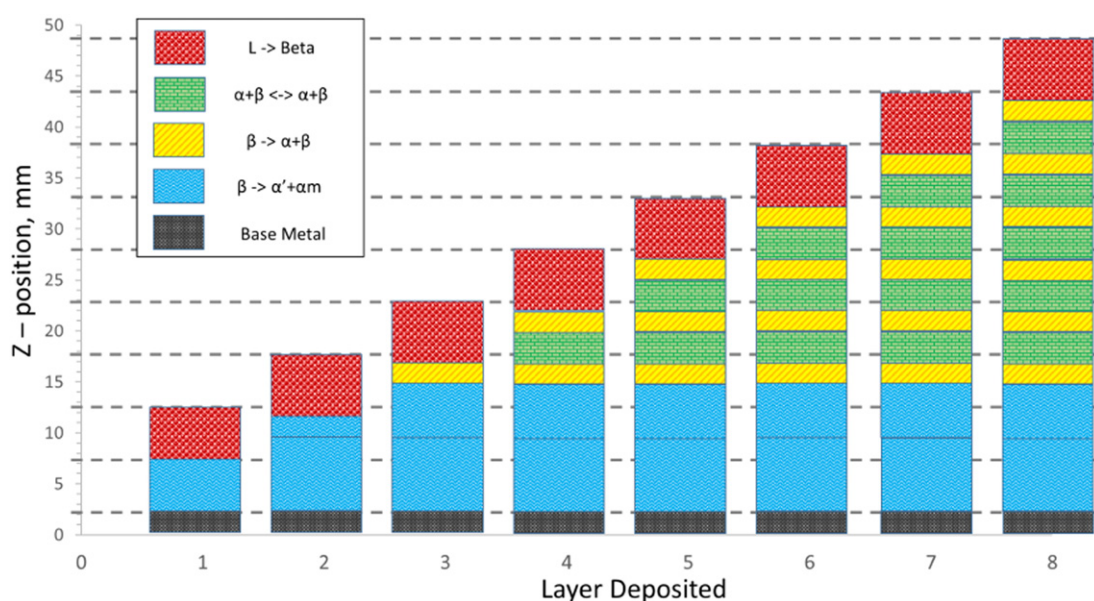


Fig. 11. Microstructural evolution map of the build as each layer is deposited (reproduced from [26,142]) showing the formation of the layer banding microstructure in DED Ti-6Al-4V.

Equiaxed-to-columnar grain transition

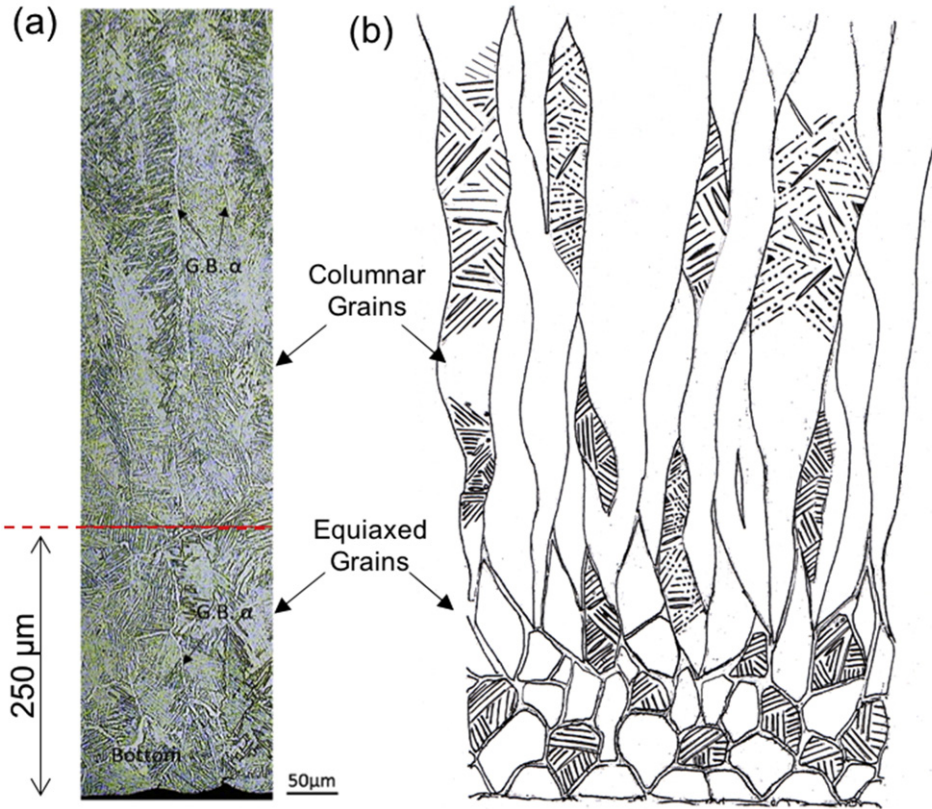


Fig. 12. (a) OM micrograph and (b) schematic showing the equiaxed-to-columnar transition of prior β grains in EBM-built Ti-6Al-4V [84].

powders [135,137,154]. A study has also shown that such trapped gas porosity decreased with decreasing speed function parameter of EBM, possibly by allowing more time for the trapped gas to escape from the slowly moved melt pool [154]. Other processing defects such as unmelted powder and layer gaps can also occur during the AM process. HIP treatment has shown to be able to reduce the amount of such processing defects effectively [9]. Fig. 14c shows that the defect density has a significant effect on the fracture toughness of the metal AM part [23].

A study on a SL process reported that defect distribution within the aluminium alloy sample was not homogenous [14]. A point to note from the study was that region where cracks originate did not correspond to the location of voids. Instead, it attributed the mechanism of the formation of the cracks to the strain localization caused by the high strain rate deformation induced from the rotating sonotrode that was used to fuse the metal sheets together [14].

4.1.6. Heterogeneous recrystallization

Post heat treatment is a common method to homogenize the microstructure of the as-deposited metal AM part [100,101]. Fig. 15a shows a schematic of how vacuum annealing treatment can induce homogenous grain recrystallization within SLM-built iron part [155]. However, a study has reported that partial recrystallization in heat treated SLM-built IN718 resulted in a heterogeneous grain structure as shown in Fig. 15 [156] instead. It was suggested that heterogeneous residual stresses within the metal AM parts may account for such partial recrystallization [20]. Moreover, homogeneous grains sizes ($\sim 500\text{--}3000 \mu\text{m}$) were found in DED-built Ti-6Al-4V after post heat treatment [157]. Of note is that such post-processing procedures for metal AM parts may have to take into account of both the materials and manufacturing techniques.

4.2. Heterogeneity in mechanical properties

4.2.1. Tensile properties

Table 6 lists the differences in tensile strength along the build direction of the AM Ti-6Al-4V by various studies [10,11,84,99,158–161]. Higher tensile properties were reported in the lower half of the block samples as compared to the upper half, which was attributed to oxygen strengthening and finer microstructure [10,11]. The tensile strength of Ti-6Al-4V parts typically increases with increasing oxygen content and finer microstructure [112,162]. Furthermore, a study on EBM-built Ti-6Al-4V also reported an increase in strain hardening effect with increasing build height due to lesser annealing [84].

4.2.2. Hardness

Hardness testing is an effective method to characterize the localized mechanical strength of metal AM parts. Table 7 summarised of hardness properties of various AM metal alloys. A recent study has shown that Vickers microhardness correlated well with the microstructural features of AM titanium alloy and it obeyed the Hall-Petch's relationship [134]. Studies have been carried out to investigate the effect of cross-sectional area on hardness values [15,83,134]. An earlier study reported that the effect of metal AM part size on the microhardness was little, possibly due to the insufficient thermal isolation between them [83]. While a recent study reported that hardness property was dependent on cross-sectional area [15,134,141]. It was shown that with increasing cross-sectional area, the microhardness was decreased due to microstructural coarsening [15,40,90,134,141]. The rationale for the microstructural coarsening is due to greater thermal input and slower cooling rates experienced by the part with the thicker cross-sectional area [15,141]. The study also showed that differences in the 2D-planar geometry had

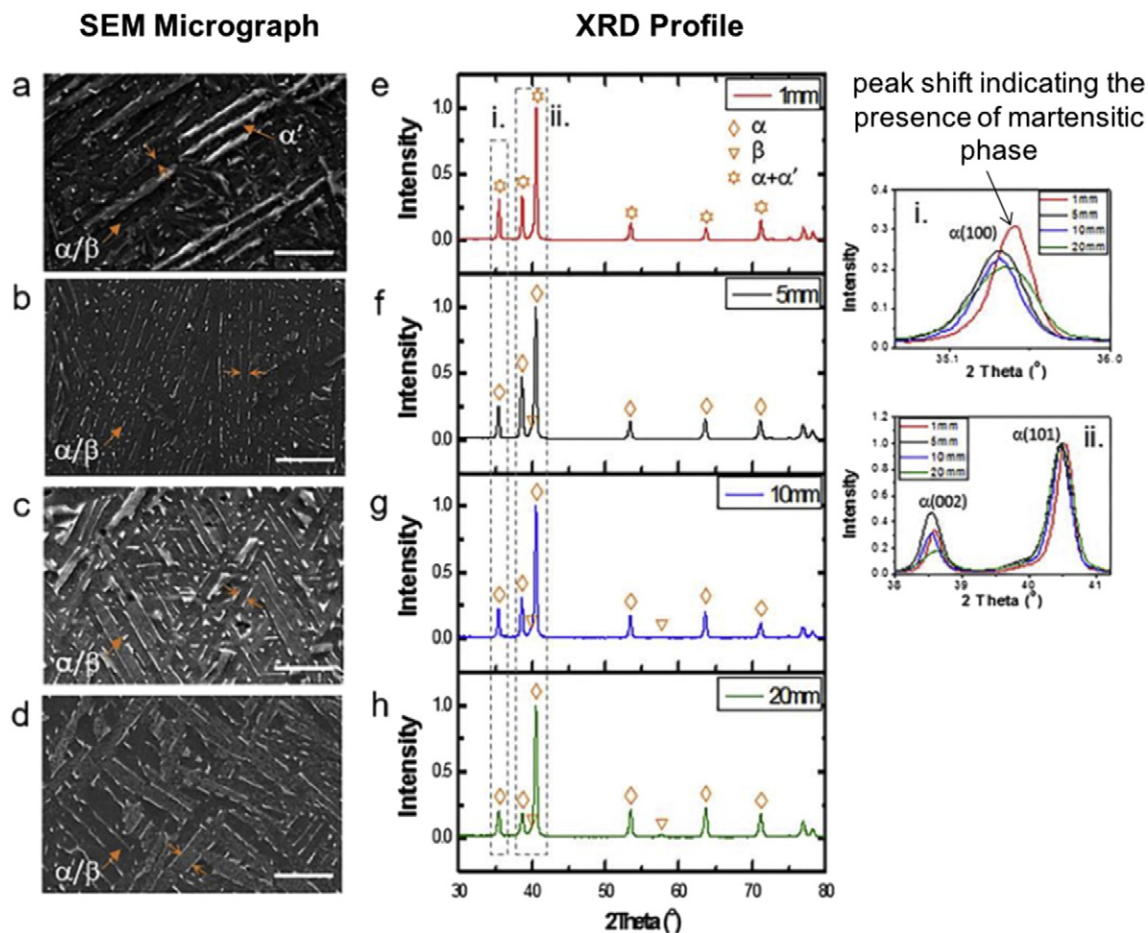


Fig. 13. SEM images showing the microstructure size with increasing cross-sectional thickness with their respective XRD profiles (a,e) 1 mm, (b,f) 5 mm, (c,g) 10 mm and (d,h) 20 mm [136] showing the heterogeneous microstructures in EBM-built Ti-6Al-4V.

an influence on the microhardness as well due to differences in heat flux. Studies have also been conducted on the effect of build height on the hardness [15,83,84]. However, such studies showed conflicting results. For example, a study by Hrabe et al. [83] reported no significant differences in Vickers microhardness values up to 25 mm from the substrate while the study from Tan et al. [84] showed that there were differences in the Vickers microhardness values with build height.

Tan et al. reported that Vickers microhardness decreased in value with increasing build height in EBM-built Ti-6Al-4V [84]. It was suggested that due to the higher cooling rate induced by the higher thermal conductivity of the stainless steel substrate. The microstructure at the bottom region was finer as compared to the top region. However, Wang et al. systematically examined the microhardness within an impeller component [15]. The study reported that microhardness value was increased with increasing build height. It must be noted that the part in Wang et al. work had a decreasing cross-sectional area with increasing build height. The difference in cross-sectional area may contribute to that result.

Many studies have thus concluded that heterogeneity in hardness values was dependent on the thermal input experience by the specific layer. A larger cross-sectional area would result in a higher thermal input as compared to a smaller cross-sectional area, resulting in different final microstructures. Future improvement on varying the process parameters with regards to the cross-sectional area could help alleviate such heterogeneity in hardness.

4.2.3. Fracture toughness

Location dependence in fracture toughness has been observed in EBM-built Ti-6Al-4V due to the heterogeneity in the microstructure

and defect distribution [9]. A related study also performed HIP process to investigate its effect on the heterogeneity in fracture toughness [23]. However, the measured fracture toughness was found to be lesser due to coarsening of the microstructure after the HIP process and the heterogeneity observed was not eliminated.

In summary, it can be deduced that anisotropy and heterogeneity in the mechanical properties of metal AM parts are due to the anisotropic and heterogeneous microstructure and material properties. Despite the anisotropy and heterogeneity in the mechanical properties, it can be concluded that the mechanical properties of post-processed metal AM parts are equivalent or better as compared to their cast equivalent. Further improvement regarding the optimization of heat treatment process parameters is highly demanded to produce end-use parts with fine microstructure in order to approach the static and dynamic mechanical properties of their wrought equivalent.

5. Modelling on anisotropy and heterogeneity

Numerical modelling of the thermal conditions of AM processes allows a better understanding of the anisotropic and heterogeneous microstructure which determines the final mechanical properties. An early study has developed a thermos-kinetic model of multilayer laser-based powder deposition, coupled FE heat transfer calculations, phase transformation data, and microstructure-property relationships, showing the increase in Vickers hardness with increasing build height and with minimizing substrate size [170]. Numerical modelling has also been used to simulate beam power-velocity (P-V) process maps and solidification maps in an effort to control the microstructure for various metal AM processes as shown earlier in Fig. 5c and d.

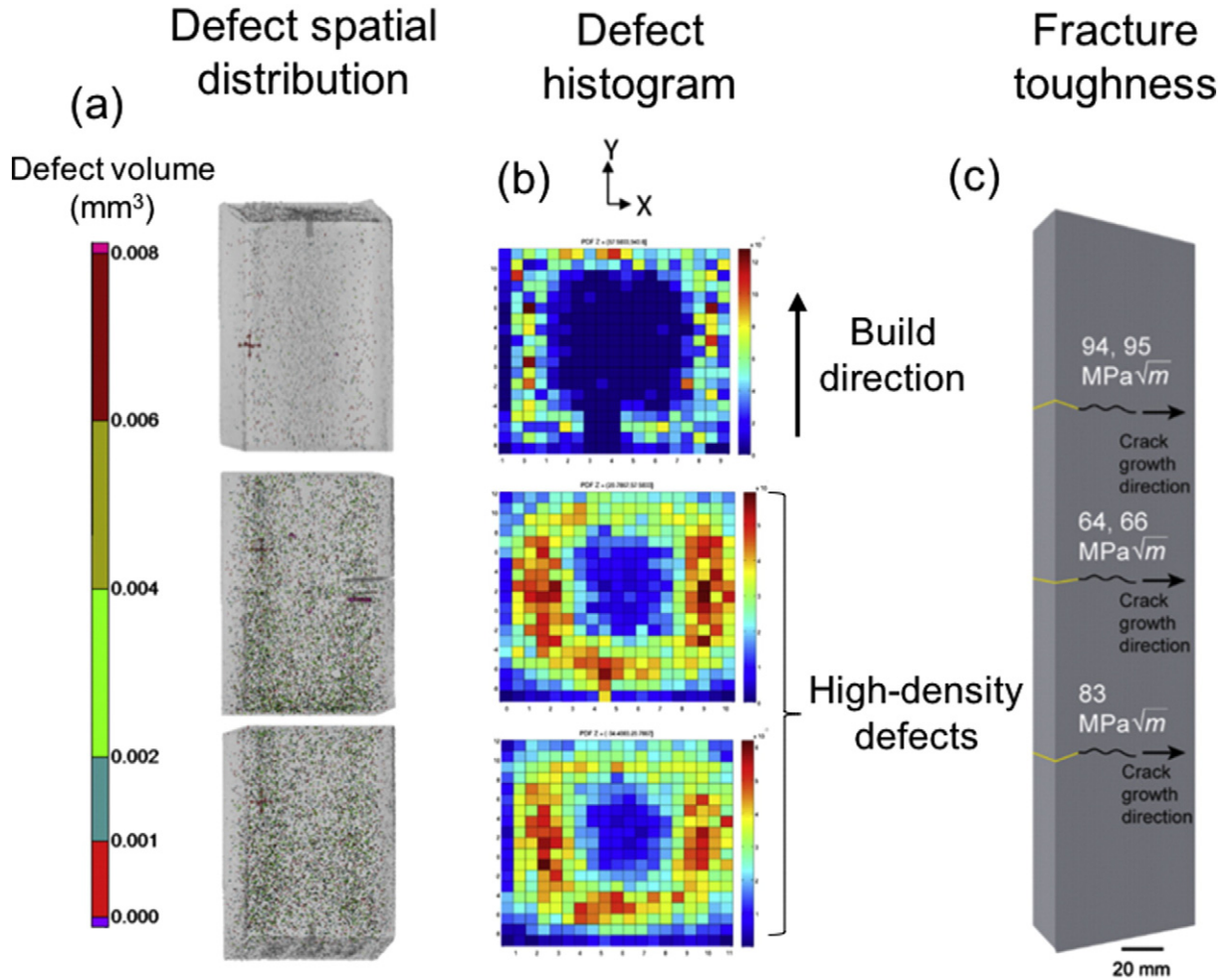


Fig. 14. (a) μCT scans showing defects spatial distribution in EBM-built Ti-6Al-4V (b) defect histogram for the EBM-built Ti-6Al-4V at bottom, middle and top region (c) fracture toughness variation at the bottom, middle and top region respectively [23] showing the heterogeneity in fracture toughness correlates with the defect density.

Other studies have also developed heat transfer and microstructural evolution equations for EBM-built Ti-6Al-4V showing that the heat transfer arising from the selective melting was sufficient to induce microstructure evolution through several layers below. Fig. 16 shows an FEM model of the temperature variation of metal AM parts with varying thicknesses along the build height and the evolution of volume fraction of α phase due to the variations in the temperature field within the metal AM part [134,171]. It provides a firm support to experimental works regarding the phase constitution and microstructural coarsening [142,171].

A recent study has also developed a model that was capable of calculating fraction, morphology and size of phases, with a measured or modelled thermal history in AM-processed Ti-6Al-4V [172]. With the more research focusing on modelling metal AM processes, a better understanding of the interrelationship between process-microstructure-mechanical properties can be achieved.

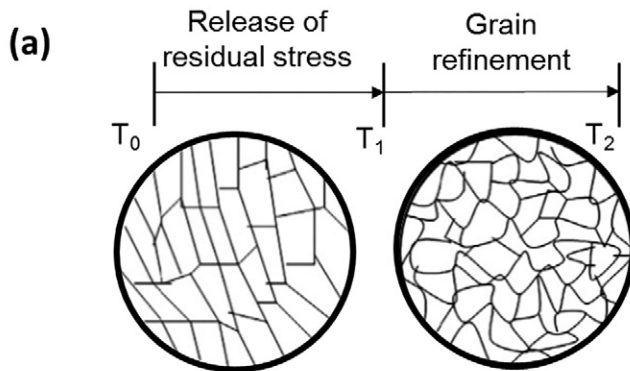
Concluding remarks

Metal AM became a competitive manufacturing process to conventional manufacturing techniques such as machining and casting with regards to the fabrication of components with complex geometries out of hard to process materials (e.g. titanium alloys). Metal AM processes could be broadly categorized as powder-bed fusion (PBF), directed energy deposition (DED) and sheet lamination (SL). During

the layer-by-layer fabrication, the metallic part was subjected to processing variables such as deposition rate, beam power, build environment and processing temperature which have an influence towards its final microstructure and mechanical properties. In general, despite the reported anisotropy and heterogeneity, the quasi-static mechanical properties (e.g. tensile strength and hardness) of metal AM parts often could meet the minimum requirements in comparison with their cast and wrought equivalents. However, post processing of metal AM parts must be implemented to obtain comparable dynamic mechanical properties (e.g. fatigue properties) as conventionally produced parts. Such post processing techniques are currently a costly means to control the anisotropic and heterogeneous microstructure within metal AM parts.

It can be deduced via the published datum summarized in this article that the cause for the anisotropic and heterogeneous microstructure and mechanical properties of metal AM parts was due to either microstructural features or defects. The influencing factors for the anisotropy and heterogeneity in the microstructure include: (1) grain morphology; (2) crystallographic texture; (3) lack-of-fusion defects; (4) phase transformation; (5) heterogeneous recrystallization; (6) layer banding and (7) microstructural coarsening. These factors were systematically discussed in terms of the processing variables within the metal AM process. Given the current state-of-the-art in metal AM, it is difficult to vary the processing variables in-situ with respect to a part's geometry and size so as to control its microstructure. However, with continued

Homogenous grain evolution during recrystallization



Heterogenous grain evolution during recrystallization

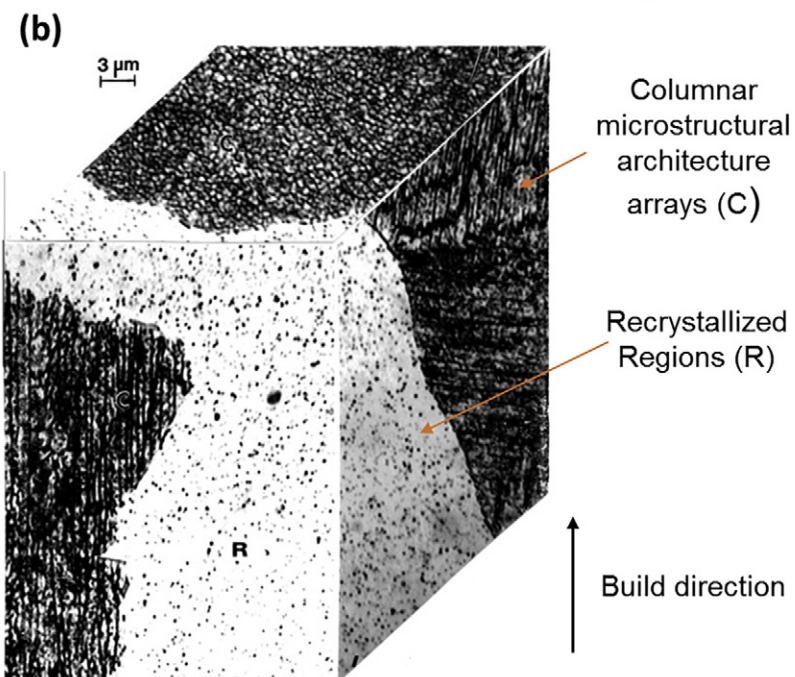


Fig. 15. (a) Schematic diagram of typical homogenous grain evolution during the grain recrystallization phenomenon [155]. (b) 3D Optical Micrograph (OM) composite view of the SLM-built IN718 microstructure [156] showing the heterogeneity in microstructure caused by heterogeneous recrystallization.

development in this technology, it is likely that better control over the processing variables during the fabrication process can be achieved.

Literatures have shown that microstructural modification of AM metallic materials can be achieved via the use of a roller mechanism that applied a load after each deposited layer or through the use of

Table 6
Summary of tensile properties of various metal AM parts.

Material	Condition	Process	Position	Yield strength (MPa)	Ultimate tensile strength (MPa)	Elongation (%)	Ref.
Ti-6Al-4V	Machined	DED	Upper half	945	1041	14.5	[10]
			Lower half	970	1087	13.6	
Ti-6Al-4V	Machined	EBM	Upper half	859.3	942.4	18.8 ± 2.5	[11,99]
			Lower half	898.9	976.6	17.9 ± 0.7	
Ti-6Al-4V ELI	Machined	EBM	Upper half	823–827	940–944	13.2	[84]
			Lower half	836–851	953–964	16.3	
Ti-6Al-4V ELI	Machined	EBM	Upper half	903.6 ± 24.6	991.8 ± 21.7	16.4 ± 0.8	[158]
			Lower half	911.9 ± 34.3	995.5 ± 28.5	13.5 ± 0.4	
Ti-6Al-4V ELI	Machined	EBM	Upper half	986.5	1050.5	14.3	[159]
			Lower half	987.5	1056.5	12.7	
Ti-6Al-4V	Machined	EBM	Upper half	991.1 ± 9.3	1065.9 ± 10.2	14.6 ± 0.1	[160]
			Lower half	990.9 ± 22.5	1056 ± 24.2	16.7 ± 1.0	
Ti-6Al-4V	Machined	DMLS	Upper half	1059	1221	4.8	[161]
			Lower half	~1167	~1281	~2.6	

Table 7

Summary of hardness properties of various metal AM parts.

Material	Process/model	Microhardness (Hv)	Distance measured from the substrate (mm)	Ref.
Ti-6Al-4V	EBM/Arcam S400	~460–360	~68	[146]
Ti-6Al-4V	EBM/Arcam S12	347	2–25	[83]
Ti-6Al-4V ELI	EBM/Arcam A2XX	319 ± 5–327 ± 5	24	[84]
Ti-6Al-4V	EBM/Arcam A2X	343–365	4–35	[15]
Ti-6Al-4V	EBM/Arcam A2X	380	0–4.5	[43]
Ti-6Al-4V ELI	EBM/Arcam A2	~368	0–110	[159]
Ti-6Al-4V	EBM/Arcam A2X	~340	~13	[11]
Pure Cu	EBM/Arcam A2	57–88	N.A.	[163]
AlCoCrFeNi	EBM/Arcam A2X	400–500	0–16	[164]
SS316L	EBM/Arcam S12	184 ± 11	2	[165]
IN718	EBM/Arcam S12	241 ± 12	2	[165]
Al-8.5Fe-1.3V-1.7Si	EBM/Arcam A2X	153 ± 2.5	N.A.	[166]
Ti-6Al-4V	SLM/Concept Laser M2	360	N.A.	[167]
SS316L	SLM/SLM 250 HL	213–220	N.A.	[47]
IN718	SLM/LSNF-I	365	1.3–2.4	[168]
Al-8.5Fe-1.3V-1.7Si	SLM/DEYU LM 200 SLM	135–175	N.A.	[169]

in-situ printed heat sink. Traditionally, adjusting the build orientation and specifying a minimum cross-sectional thickness were ways to reduce the effect of the anisotropy and heterogeneity in material properties. Moreover, it was widely shown that horizontally orientated AM parts typically had a higher mechanical strength as

compared to vertically orientated ones. As such if the build part is horizontally orientated along the load direction and that fine geometrical features are scaled up to increase mechanical strength, the anisotropy and heterogeneity might be effectively minimised or even eliminated.

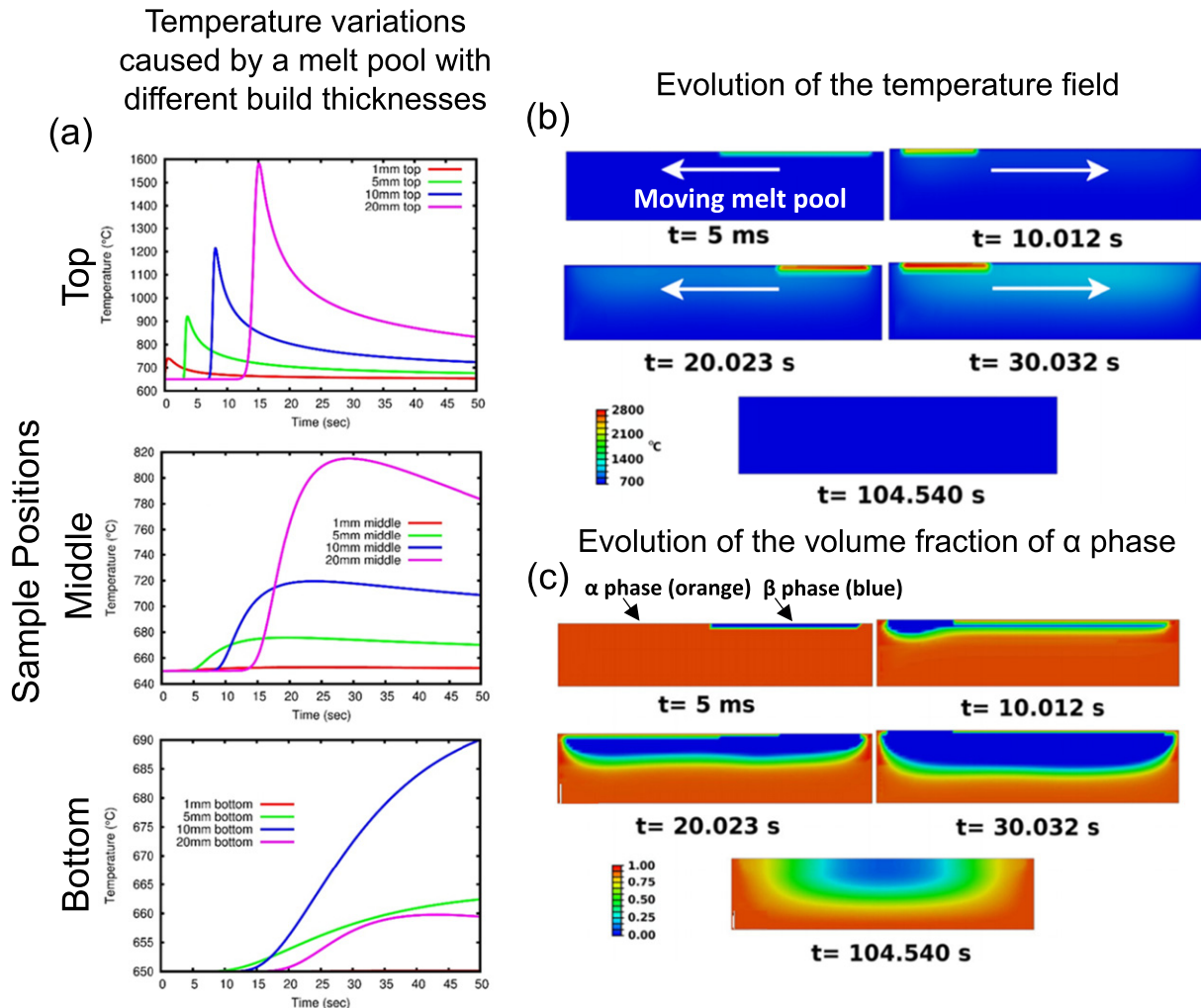


Fig. 16. Temperature evolution curves with respect to time for the positions of (a) top, (b) middle, and (c) bottom of the sample. Evolution of the (d) temperature field and (e) volume fraction of α phase after deposition of 4 layers of powder [134,171] showing the possibility of using numerical simulations to model the anisotropic and heterogeneous microstructure that is formed in metal AM parts.

Acknowledgements

The authors are grateful for financial support provided by A*STAR Industrial Additive Manufacturing Program: Work Package 3 (Electron Beam Melting, Grant No. 1325504103). We also acknowledge the financial support from Singapore Centre for 3D Printing funded by the National Research Foundation.

References

- [1] C.K. Chua, K.F. Leong, *3D Printing and Additive Manufacturing: Principles and Applications*, 2015.
- [2] I. Gibson, D.W. Rosen, B. Stucker, *Additive Manufacturing Technologies*, Springer, 2010.
- [3] J.D. Strickland, *Applications of Additive Manufacturing in the Marine Industry*, 8th ed., Proceedings of PRADS2016, 2016.
- [4] N. Patil, D. Pal, B. Stucker, A new finite element solver using numerical Eigen modes for fast simulation of additive manufacturing processes, *Proceedings of the Solid Freeform Fabrication Symposium*, Austin, TX, Aug, 2013 12–14.
- [5] X.P. Tan, Y.J. Tan, C.S.L. Chow, S.B. Tor, W.Y. Yeong, Metallic powder-bed based 3D printing of cellular scaffolds for orthopaedic implants: a state-of-the-art review on manufacturing, topological design, mechanical properties and biocompatibility, *Mater. Sci. Eng. C* 76 (2017) 1328–1343.
- [6] T. Wohlers, *Wohlers Report 2016*, Wohlers Associates, Inc., 2016.
- [7] K. Vartanian, T. McDonald, Accelerating industrial adoption of metal additive manufacturing technology, *JOM* 68 (3) (2016) 806–810.
- [8] C.Y. Yap, C.K. Chua, Z.L. Dong, Z.H. Liu, D.Q. Zhang, L.E. Loh, S.L. Sing, Review of selective laser melting: Materials and applications, *Appl. Phys. Rev.* 2 (4) (2015), 041101..
- [9] J.J. Lewandowski, M. Seifi, Metal additive manufacturing: a review of mechanical properties, *Annu. Rev. Mater. Res.* 46 (1) (2016) 151–186.
- [10] B.E. Carroll, T.A. Palmer, A.M. Beese, Anisotropic tensile behavior of Ti–6Al–4V components fabricated with directed energy deposition additive manufacturing, *Acta Mater.* 87 (2015) 309–320.
- [11] P. Wang, M.L.S. Nai, X.P. Tan, W.J. Sin, S.B. Tor, J. Wei, Anisotropic Mechanical Properties in a Big-Sized Ti-6Al-4V Plate Fabricated by Electron Beam Melting, *TMS 2016 145th Annual Meeting & Exhibition: Supplemental Proceedings*, Springer International Publishing, Cham, 2016 5–12.
- [12] Z. Wang, T.A. Palmer, A.M. Beese, Effect of processing parameters on microstructure and tensile properties of austenitic stainless steel 304L made by directed energy deposition additive manufacturing, *Acta Mater.* 110 (2016) 226–235.
- [13] Y. Tian, D. McAllister, H. Colijn, M. Mills, D. Farson, M. Nordin, S. Babu, Rationalization of microstructure heterogeneity in INCONEL 718 builds made by the direct laser additive manufacturing process, *Metall. Mater. Trans. A* 45 (10) (2014) 4470–4483.
- [14] N. Sridharan, M. Gussev, R. Seibert, C. Parish, M. Norfolk, K. Terrani, S.S. Babu, Rationalization of anisotropic mechanical properties of Al-6061 fabricated using ultrasonic additive manufacturing, *Acta Mater.* 117 (2016) 228–237.
- [15] P. Wang, X.P. Tan, M.L.S. Nai, S.B. Tor, J. Wei, Spatial and geometrical-based characterization of microstructure and microhardness for an electron beam melted Ti-6Al-4V component, *Mater. Des.* 95 (2016) 287–295.
- [16] Y. Zhu, X. Tian, J. Li, H. Wang, The anisotropy of laser melting deposition additive manufacturing Ti–6.5Al–3.5Mo–1.5Zr–0.3Si titanium alloy, *Mater. Des.* 67 (2015) 538–542.
- [17] R.R. Dehoff, C. Tallman, C.E. Duty, W.H. Peter, Y. Yamamoto, W. Chen, C.A. Blue, Case study: additive manufacturing of aerospace brackets, *Adv. Mater. Process.* 171 (3) (2013).
- [18] J.K. Patel, B. Wilshire, The challenge to produce consistent mechanical properties in Nb-HSLA strip steels, *J. Mater. Process. Technol.* 120 (1–3) (2002) 316–321.
- [19] J.J. Sobczak, L. Drenchev, Metallic functionally graded materials: a specific class of advanced composites, *J. Mater. Sci. Technol.* 29 (4) (2013) 297–316.
- [20] W.J. Sames, F.A. List, S. Pannala, R.R. Dehoff, S.S. Babu, The metallurgy and processing science of metal additive manufacturing, *Int. Mater. Rev.* 61 (5) (2016) 315–360.
- [21] W.E. Frazier, Metal additive manufacturing: a review, *J. Mater. Eng. Perform.* 23 (6) (2014) 1917–1928.
- [22] S.L. Sing, J. An, W.Y. Yeong, F.E. Wiria, Laser and electron-beam powder-bed additive manufacturing of metallic implants: a review on processes, materials and designs, *J. Orthop. Res.* 34 (3) (2016) 369–385.
- [23] M. Seifi, A. Salem, D. Satko, J. Shaffer, J.J. Lewandowski, Defect distribution and microstructure heterogeneity effects on fracture resistance and fatigue behavior of EBM Ti-6Al-4V, *Int. J. Fatigue* 94 (Part 2) (2017) 263–287.
- [24] M. Seifi, M. Dahar, R. Aman, O. Harrysson, J. Beuth, J.J. Lewandowski, Evaluation of orientation dependence of fracture toughness and fatigue crack propagation behavior of as-deposited ARCAM EBM Ti-6Al-4V, *JOM* 67 (3) (2015) 597–607.
- [25] A. Basak, S. Das, Epitaxy and microstructure evolution in metal additive manufacturing, *Annu. Rev. Mater. Res.* 46 (2016) 125–149.
- [26] S.M. Kelly, S.L. Kampe, Microstructural evolution in laser-deposited multilayer Ti-6Al-4V builds: Part II. Thermal modeling, *Metall. Mater. Trans. A* 35 (6) (2004) 1869–1879.
- [27] M.-W. Wu, P.-H. Lai, J.-K. Chen, Anisotropy in the impact toughness of selective laser melted Ti-6Al-4V alloy, *Mater. Sci. Eng. A* 650 (2016) 295–299.
- [28] B. Zhang, X. Lee, J. Bai, J. Guo, P. Wang, C.-N. Sun, M.L. Nai, G. Qi, J. Wei, Study of selective laser melting (SLM) Inconel 718 part surface improvement by electrochemical polishing, *Mater. Des.* 116 (2017) 531–537.
- [29] ASTM, Standard Terminology for Additive Manufacturing Technologies, ASTM F2792-12a, ASTM International, West Conshohocken, PA, 2010.
- [30] H. Bikas, P. Stavropoulos, G. Chrissoulis, Additive manufacturing methods and modelling approaches: a critical review, *Int. J. Adv. Manuf. Technol.* 83 (1) (2016) 389–405.
- [31] M.F. Zäh, S. Lutzmann, Modelling and simulation of electron beam melting, *Prod. Eng.* 4 (1) (2010) 15–23.
- [32] S.M. Thompson, L. Bian, N. Shamsaei, A. Yadollahi, An overview of direct laser deposition for additive manufacturing: part I: transport phenomena, modeling and diagnostics, *Additive Manufacturing* 8 (2015) 36–62.
- [33] K.P. Karunakaran, S. Suryakumar, V. Pushpa, S. Akula, Low cost integration of additive and subtractive processes for hybrid layered manufacturing, *Robot. Comput. Integrat. Manuf.* 26 (5) (2010) 490–499.
- [34] M. Hedges, N. Calder, Near-net-shape rapid manufacture and repair by LENS®, *Rapid Prototyping* 12 (4) (2006) 1.
- [35] P. Muller, P. Mognol, J.-Y. Hascoet, Modeling and control of a direct laser powder deposition process for functionally graded materials (FGM) parts manufacturing, *J. Mater. Process. Technol.* 213 (5) (2013) 685–692.
- [36] R.R. Dehoff, S.S. Babu, Characterization of interfacial microstructures in 3003 aluminum alloy blocks fabricated by ultrasonic additive manufacturing, *Acta Mater.* 58 (13) (2010) 4305–4315.
- [37] R.J. Friel, R.A. Harris, Ultrasonic additive manufacturing — a hybrid production process for novel functional products, *Procedia CIRP* 6 (2013) 35–40.
- [38] X.P. Tan, P. Wang, Y. Kok, W.Q. Toh, Z. Sun, S.M.L. Nai, M. Descoins, D. Mangelinck, E. Liu, S.B. Tor, Carbide precipitation characteristics in additive manufacturing of Co-Cr-Mo alloy via selective electron beam melting, *Scr. Mater.* 143 (2018) 117–121.
- [39] Y. Kok, X.P. Tan, S.B. Tor, C.K. Chua, Fabrication and microstructural characterisation of additive manufactured Ti-6Al-4V parts by electron beam melting, *Virtual and Physical Prototyping* 10 (1) (2015) 13–21.
- [40] J.K. Algardh, T. Horn, H. West, R. Aman, A. Snis, H. Engqvist, J. Lausmaa, O. Harrysson, Thickness dependency of mechanical properties for thin-walled titanium parts manufactured by electron beam melting (EBM)®, *Additive Manufacturing* 12 (Part A) (2016) 45–50.
- [41] P. Wang, W. Sin, M. Nai, J. Wei, Effects of processing parameters on surface roughness of additive manufactured Ti-6Al-4V via electron beam melting, *Materials* 10 (10) (2017) 1121.
- [42] M. Todai, T. Nakano, T. Liu, H.Y. Yasuda, K. Hagihara, K. Cho, M. Ueda, M. Takeyama, Effect of building direction on the microstructure and tensile properties of Ti-48Al-2Cr-2Nb alloy additively manufactured by electron beam melting, *Additive Manufacturing* 13 (2017) 61–70.
- [43] P. Wang, M.L.S. Nai, S. Lu, J. Bai, B. Zhang, J. Wei, Study of direct fabrication of Ti-6Al-4V impeller on a wrought Ti-6Al-4V plate by electron beam melting, *JOM* (2017) in press.
- [44] M. Seifi, A. Salem, D.P. Satko, U. Ackelid, S.L. Semiatin, J.J. Lewandowski, Effects of HIP on microstructural heterogeneity, defect distribution and mechanical properties of additively manufactured EBM Ti-48Al-2Cr-2Nb, *J. Alloys Compd.* 729 (2017) 1118–1135.
- [45] D. Deng, J. Moverare, R.L. Peng, H. Söderberg, Microstructure and anisotropic mechanical properties of EBM manufactured Inconel 718 and effects of post heat treatments, *Mater. Sci. Eng. A* 693 (2017) 151–163.
- [46] Y. Zhai, H. Galarraga, D.A. Lados, Microstructure, static properties, and fatigue crack growth mechanisms in Ti-6Al-4V fabricated by additive manufacturing: LENS and EBM, *Eng. Fail. Anal.* 69 (2016) 3–14.
- [47] Z. Sun, X.P. Tan, S.B. Tor, W.Y. Yeong, Selective laser melting of stainless steel 316L with low porosity and high build rates, *Mater. Des.* 104 (2016) 197–204.
- [48] X. Wang, K. Chou, Electron backscatter diffraction analysis of Inconel 718 parts fabricated by selective laser melting additive manufacturing, *JOM* 69 (2) (2017) 402–408.
- [49] X. Wang, K. Chou, Effects of thermal cycles on the microstructure evolution of Inconel 718 during selective laser melting process, *Additive Manufacturing* 18 (2017) 1–14.
- [50] X. Wang, T. Keya, K. Chou, Build height effect on the Inconel 718 parts fabricated by selective laser melting, *Procedia Manufacturing* 5 (2016) 1006–1017.
- [51] K. Graff, M. Short, M. Norfolk, Very High Power Ultrasonic Additive Manufacturing (VHP UAM) for Advanced MaterialsInternational Conference on Additive Manufacturing, 2010.
- [52] M.R. Sriraman, S.S. Babu, M. Short, Bonding characteristics during very high power ultrasonic additive manufacturing of copper, *Scr. Mater.* 62 (8) (2010) 560–563.
- [53] T. Wang, Y.Y. Zhu, S.Q. Zhang, H.B. Tang, H.M. Wang, Grain morphology evolution behavior of titanium alloy components during laser melting deposition additive manufacturing, *J. Alloys Compd.* 632 (2015) 505–513.
- [54] J. Gockel, J. Beuth, K. Taminger, Integrated control of solidification microstructure and melt pool dimensions in electron beam wire feed additive manufacturing of Ti-6Al-4V, *Additive Manufacturing* 1–4 (2014) 119–126.
- [55] K. Iwasaki, S. Ohkawa, M. Uo, T. Akasaka, F. Watari, Laser welding of titanium and dental precious alloys, *Mater. Trans.* 45 (4) (2004) 1140–1146.
- [56] P. Heinl, L. Müller, C. Körner, R.F. Singer, F.A. Müller, Cellular Ti-6Al-4V structures with interconnected macro porosity for bone implants fabricated by selective electron beam melting, *Acta Biomater.* 4 (5) (2008) 1536–1544.
- [57] S. Biamino, A. Penna, U. Ackelid, S. Sabbadini, O. Tassa, P. Fino, M. Pavese, P. Gennaro, C. Badini, Electron beam melting of Ti-48Al-2Cr-2Nb alloy: microstructure and mechanical properties investigation, *Intermetallics* 19 (6) (2011) 776–781.

- [58] B. Ferrar, L. Mullen, E. Jones, R. Stamp, C.J. Sutcliffe, Gas flow effects on selective laser melting (SLM) manufacturing performance, *J. Mater. Process. Technol.* 212 (2) (2012) 355–364.
- [59] W.J. Sames, K.A. Unocic, R.R. Dehoff, T. Lolla, S.S. Babu, Thermal effects on microstructural heterogeneity of Inconel 718 materials fabricated by electron beam melting, *J. Mater. Res.* 29 (17) (2014) 1920–1930.
- [60] X. Zhao, S. Li, M. Zhang, Y. Liu, T.B. Sercombe, S. Wang, Y. Hao, R. Yang, L.E. Murr, Comparison of the microstructures and mechanical properties of Ti-6Al-4V fabricated by selective laser melting and electron beam melting, *Mater. Des.* 95 (2016) 21–31.
- [61] X. Wang, K. Chou, Residual Stress in Metal Parts Produced by Powder-bed Additive Manufacturing ProcessesProceedings of the 26th International Solid Freeform Fabrication Symposium 2015, pp. 1463–1474.
- [62] W.U.H. Syed, A.J. Pinkerton, L. Li, Combining wire and coaxial powder feeding in laser direct metal deposition for rapid prototyping, *Appl. Surf. Sci.* 252 (13) (2006) 4803–4808.
- [63] N.T. Aboulkhair, N.M. Everitt, I. Ashcroft, C. Tuck, Reducing porosity in AlSi10Mg parts processed by selective laser melting, *Additive Manufacturing* 1–4 (2014) 77–86.
- [64] L. Thijis, F. Verhaeghe, T. Craeghs, J.V. Humbeeck, J.-P. Kruth, A study of the microstructural evolution during selective laser melting of Ti-6Al-4V, *Acta Mater.* 58 (9) (2010) 3303–3312.
- [65] L.N. Carter, C. Martin, P.J. Withers, M.M. Attallah, The influence of the laser scan strategy on grain structure and cracking behaviour in SLM powder-bed fabricated nickel superalloy, *J. Alloys Compd.* 615 (2014) 338–347.
- [66] M.F. Zaeh, M. Kahnert, The effect of scanning strategies on electron beam sintering, *Prod. Eng.* 3 (3) (2009) 217–224.
- [67] T. Ishimoto, K. Hagiwara, K. Hisamoto, S.-H. Sun, T. Nakano, Crystallographic texture control of beta-type Ti-15Mo-5Zr-3Al alloy by selective laser melting for the development of novel implants with a biocompatible low Young's modulus, *Scr. Mater.* 132 (2017) 34–38.
- [68] L. Thijis, K. Kempen, J.-P. Kruth, J. Van Humbeeck, Fine-structured aluminium products with controllable texture by selective laser melting of pre-alloyed AlSi10Mg powder, *Acta Mater.* 61 (5) (2013) 1809–1819.
- [69] L. Thijis, M.L. Montero Sistiaga, R. Wauthle, Q. Xie, J.-P. Kruth, J. Van Humbeeck, Strong morphological and crystallographic texture and resulting yield strength anisotropy in selective laser melted tantalum, *Acta Mater.* 61 (12) (2013) 4657–4668.
- [70] P. Kobryn, S. Semiatin, Mechanical Properties of Laser-deposited Ti-6Al-4V, Solid Freeform Fabrication Proceedings, Austin, 2001 6–8.
- [71] H. Helmer, A. Bauereiß, R.F. Singer, C. Körner, Grain structure evolution in Inconel 718 during selective electron beam melting, *Mater. Sci. Eng. A* 668 (2016) 180–187.
- [72] R.R. Dehoff, M.M. Kirka, W.J. Sames, H. Bilheux, A.S. Tremsin, L.E. Lowe, S.S. Babu, Site specific control of crystallographic grain orientation through electron beam additive manufacturing, *Mater. Sci. Technol.* 31 (8) (2015) 931–938.
- [73] A.B. Spierings, M. Voegtlin, T. Bauer, K. Wegener, Powder flowability characterisation methodology for powder-bed-based metal additive manufacturing, *Prog. Addit. Manuf.* 1 (1) (2016) 9–20.
- [74] N. Karapatis, G. Egger, P. Gygax, R. Glardon, Optimization of powder layer density in selective laser sintering, Proc. of Solid Freeform Fabrication Symposium 1999 (1999) 255–263.
- [75] A. Spierings, G. Levy, Comparison of Density of Stainless Steel 316L Parts Produced With Selective Laser Melting Using Different Powder Grades, Proceedings of the Annual International Solid Freeform Fabrication Symposium, Austin, TX, 2009 342–353.
- [76] F. Wang, S. Williams, P. Colegrove, A.A. Antonysamy, Microstructure and mechanical properties of wire and arc additive manufactured Ti-6Al-4V, *Metall. Mater. Trans. A* 44 (2) (2013) 968–977.
- [77] S.H. Mok, G. Bi, J. Folkes, I. Pushby, J. Segal, Deposition of Ti-6Al-4V using a high power diode laser and wire, part II: investigation on the mechanical properties, *Surf. Coat. Technol.* 202 (19) (2008) 4613–4619.
- [78] E. Brandl, B. Baufeld, C. Leyens, R. Gault, Additive manufactured Ti-6Al-4V using welding wire: comparison of laser and arc beam deposition and evaluation with respect to aerospace material specifications, *Phys. Procedia* 5 (2010) 595–606.
- [79] N. Hrabe, T. Quinn, Effects of processing on microstructure and mechanical properties of a titanium alloy (Ti-6Al-4V) fabricated using electron beam melting (EBM), part 2: energy input, orientation, and location, *Mater. Sci. Eng. A* 573 (2013) 271–277.
- [80] V. Cain, L. Thijis, J. Van Humbeeck, B. Van Hooreweder, R. Knutsen, Crack propagation and fracture toughness of Ti6Al4V alloy produced by selective laser melting, *Additive Manufacturing* 5 (2015) 68–76.
- [81] P. Edwards, A. O'Conor, M. Ramulu, Electron beam additive manufacturing of titanium components: properties and performance, *J. Manuf. Sci. Eng.* 135 (6) (2013), 061016.
- [82] B. Baufeld, Effect of deposition parameters on mechanical properties of shaped metal deposition parts, *Proc. Inst. Mech. Eng. B J. Eng. Manuf.* 226 (1) (2012) 126–136.
- [83] N. Hrabe, T. Quinn, Effects of processing on microstructure and mechanical properties of a titanium alloy (Ti-6Al-4V) fabricated using electron beam melting (EBM), part 1: distance from build plate and part size, *Mater. Sci. Eng. A* 573 (2013) 264–270.
- [84] X.P. Tan, Y. Kok, Y.J. Tan, M. Descoins, D. Mangelinck, S.B. Tor, K.F. Leong, C.K. Chua, Graded microstructure and mechanical properties of additive manufactured Ti-6Al-4V via electron beam melting, *Acta Mater.* 97 (2015) 1–16.
- [85] S.S. Al-Bermani, M.L. Blackmore, W. Zhang, I. Todd, The origin of microstructural diversity, texture, and mechanical properties in electron beam melted Ti-6Al-4V, *Metall. Mater. Trans. A* 41 (13) (2010) 3422–3434.
- [86] L. Qian, J. Mei, J. Liang, X. Wu, Influence of position and laser power on thermal history and microstructure of direct laser fabricated Ti-6Al-4V samples, *Mater. Sci. Technol.* 21 (5) (2005) 597–605.
- [87] A. Takaichi, T. Suyalatu, N. Nakamoto, N. Joko, Y. Nomura, S. Tsutsumi, H. Migita, S. Kurosu Doi, A. Chiba, N. Wakabayashi, Y. Igarashi, T. Hanawa, Microstructures and mechanical properties of Co-29Cr-6Mo alloy fabricated by selective laser melting process for dental applications, *J. Mech. Behav. Biomed. Mater.* 21 (2013) 67–76.
- [88] L. Ladani, J. Razmi, S.F. Choudhury, Mechanical anisotropy and strain rate dependency behavior of Ti6Al4V produced using e-beam additive fabrication, *J. Eng. Mater. Technol.* 136 (3) (2014) 031006.
- [89] J. Donoghue, A.A. Antonysamy, F. Martina, P.A. Colegrove, S.W. Williams, P.B. Prangnell, The effectiveness of combining rolling deformation with wire–arc additive manufacture on β -grain refinement and texture modification in Ti-6Al-4V, *Mater. Charact.* 114 (2016) 103–114.
- [90] A.A. Antonysamy, J. Meyer, P.B. Prangnell, Effect of build geometry on the β -grain structure and texture in additive manufacture of Ti6Al4V by selective electron beam melting, *Mater. Charact.* 84 (2013) 153–168.
- [91] L. Bian, S.M. Thompson, N. Shamsaei, Mechanical properties and microstructural features of direct laser-deposited Ti-6Al-4V, *JOM* 67 (3) (2015) 629–638.
- [92] S. Tammas-Williams, H. Zhao, F. Léonard, F. Derguti, I. Todd, P. Prangnell, XCT analysis of the influence of melt strategies on defect population in Ti-6Al-4V components manufactured by selective electron beam melting, *Mater. Charact.* 102 (2015) 47–61.
- [93] S.K. Everton, M. Hirsch, P. Stravroulakis, R.K. Leach, A.T. Clare, Review of in-situ process monitoring and in-situ metrology for metal additive manufacturing, *Mater. Des.* 95 (2016) 431–445.
- [94] ASTM, Standard Terminology for Additive Manufacturing–Coordinate Systems and Test Methodologies, ISO/ASTM52921-13, ASTM International, West Conshohocken, PA, 2013.
- [95] F. Froes, B. Dutta, The additive manufacturing (AM) of titanium alloys, advanced materials research, *Trans. Tech. Publ.* (2014) 19–25.
- [96] J. Alcristo, A. Enriquez, H. Garcia, S. Hinkson, T. Steelman, E. Silverman, P. Valdovino, H. Gigerenzer, J. Foyos, J. Ogren, J. Dorey, K. Karg, T. McDonald, O.S. Es-Said, Tensile properties and microstructures of laser-formed Ti-6Al-4V, *J. Mater. Eng. Perform.* 20 (2) (2011) 203–212.
- [97] M. Simonelli, Y.Y. Tse, C. Tuck, Effect of the build orientation on the mechanical properties and fracture modes of SLM Ti-6Al-4V, *Mater. Sci. Eng. A* 616 (2014) 1–11.
- [98] C. Qiu, N.J.E. Adkins, M.M. Attallah, Microstructure and tensile properties of selectively laser-melted and of HIPed laser-melted Ti-6Al-4V, *Mater. Sci. Eng. A* 578 (2013) 230–239.
- [99] P. Wang, M.L.S. Nai, W.J. Sin, J. Wei, Effect of building height on microstructure and mechanical properties of big-sized Ti-6Al-4V plate fabricated by electron beam melting, MATEC Web of Conferences 30 (2015), 02001.
- [100] S. Raghavan, M.L.S. Nai, P. Wang, W.J. Sin, T. Li, J. Wei, Heat treatment of electron beam melted (EBM) Ti-6Al-4V: microstructure to mechanical property correlations, *Rapid Prototyp. J.* (2017) in press.
- [101] T. Vilaro, C. Colin, J.D. Bartout, As-fabricated and heat-treated microstructures of the Ti-6Al-4V alloy processed by selective laser melting, *Metall. Mater. Trans. A* 42 (10) (2011) 3190–3199.
- [102] M. Svensson, U. Ackelid, A. Ab, Titanium alloys manufactured with electron beam melting mechanical and chemical properties, Proceedings of Materials & Processes for Medical Devices Conference (2010) 189–194.
- [103] H. Rafi, N. Karthik, H. Gong, T.L. Starr, B.E. Stucker, Microstructures and mechanical properties of Ti6Al4V parts fabricated by selective laser melting and electron beam melting, *J. Mater. Eng. Perform.* 22 (12) (2013) 3872–3883.
- [104] A. Christensen, R. Kircher, A. Lippincott, Qualification of electron beam melted (EBM) Ti6Al4V-ELI for orthopaedic applications, Medical Device Materials IV: Proceedings of the Materials and Processes for Medical Devices Conference (2008) 48–53.
- [105] R. Kircher, A. Christensen, K. Wurth, Electron beam melted (EBM) Co-Cr-Mo alloy for orthopaedic implant applications, Solid Freeform Fabrication Proceedings (2009) 428–436.
- [106] J. Strößner, M. Terock, U. Glatzel, Mechanical and microstructural investigation of nickel-based superalloy IN718 manufactured by selective laser melting (SLM), *Adv. Eng. Mater.* 17 (8) (2015) 1099–1105.
- [107] I. Rosenthal, A. Stern, N. Frage, Microstructure and mechanical properties of AlSi10Mg parts produced by the laser beam additive manufacturing (AM) technology, *Metallography, Microstructure, and Analysis* 3 (6) (2014) 448–453.
- [108] J. Suryawanshi, K.G. Prashanth, S. Scudino, J. Eckert, O. Prakash, U. Ramamurty, Simultaneous enhancements of strength and toughness in an Al-12Si alloy synthesized using selective laser melting, *Acta Mater.* 115 (2016) 285–294.
- [109] N. Read, W. Wang, K. Essa, M.M. Attallah, Selective laser melting of AlSi10Mg alloy: process optimisation and mechanical properties development, *Mater. Des.* 65 (2015) 417–424.
- [110] K. Kempen, L. Thijis, J. Van Humbeeck, J.-P. Kruth, Mechanical properties of AlSi10Mg produced by selective laser melting, *Phys. Procedia* 39 (2012) 439–446.
- [111] C. Song, Y. Yang, Y. Wang, D. Wang, J. Yu, Research on rapid manufacturing of CoCrMo alloy femoral component based on selective laser melting, *Int. J. Adv. Manuf. Technol.* 75 (1) (2014) 445–453.
- [112] C. Qiu, G.A. Ravi, C. Dance, A. Ranson, S. Dilworth, M.M. Attallah, Fabrication of large Ti-6Al-4V structures by direct laser deposition, *J. Alloys Compd.* 629 (2015) 351–361.

- [113] Q. Zhang, J. Chen, Z. Zhao, H. Tan, X. Lin, W. Huang, Microstructure and anisotropic tensile behavior of laser additive manufactured TC21 titanium alloy, *Mater. Sci. Eng. A* 673 (2016) 204–212.
- [114] ASTM International, ASTM F1472-14, Standard Specification for Wrought Titanium-6Aluminum-4Vanadium Alloy for Surgical Implant Applications (UNS R56400), West Conshohocken, PA, 2014.
- [115] ASTM International, ASTM F1108-14, Standard Specification for Titanium-6Aluminum-4Vanadium Alloy Castings for Surgical Implants (UNS R56406), West Conshohocken, PA, 2014.
- [116] ASTM International, ASTM F75-12, Standard Specification for Cobalt-28 Chromium-6Molybdenum Alloy Castings and Casting Alloy for Surgical Implants (UNS R30075), West Conshohocken, PA, 2012.
- [117] ASTM International, ASTM F1537-11, Standard Specification for Wrought Cobalt-28Chromium-6Molybdenum Alloys for Surgical Implants (UNS R31537, UNS R31538, and UNS R31539), West Conshohocken, PA, 2011.
- [118] J.G. Kaufman, Properties of Aluminum Alloys: Tensile, Creep, and Fatigue Data at High and Low Temperatures, ASM International, 1999.
- [119] M.M. Kirka, F. Medina, R. Dehoff, A. Okello, Mechanical behavior of post-processed Inconel 718 manufactured through the electron beam melting process, *Mater. Sci. Eng. A* 680 (2017) 338–346.
- [120] L.A. Pruitt, Deformation, yielding, fracture and fatigue behavior of conventional and highly cross-linked ultra high molecular weight polyethylene, *Biomaterials* 26 (8) (2005) 905–915.
- [121] K.-H. Schwalbe, On the influence of microstructure on crack propagation mechanisms and fracture toughness of metallic materials, *Eng. Fract. Mech.* 9 (4) (1977) 795–832.
- [122] P.O. Judt, A. Ricoeur, G. Linek, Crack paths at multiple-crack systems in anisotropic structures: simulation and experiment, *Procedia Materials Science* 3 (2014) 2122–2127.
- [123] G. Welsch, R. Boyer, E. Collings, *Materials Properties Handbook: Titanium Alloys*, ASM International, 1993.
- [124] D. Cameron, D. Hoeppner, *Fatigue Properties in Engineering*, ASM International, ASM Handbook, 19, 1996 15–26.
- [125] P. Edwards, M. Ramulu, Effect of build direction on the fracture toughness and fatigue crack growth in selective laser melted Ti-6Al-4V, *Fatigue Fract. Eng. Mater. Struct.* 38 (10) (2015) 1228–1236.
- [126] X. Gong, T. Anderson, K. Chou, Review on powder-based electron beam additive manufacturing technology, *Manuf. Rev.* 1 (2014) 2.
- [127] N. Ikeyo, T. Ishimoto, A. Serizawa, T. Nakano, Control of mechanical properties of three-dimensional Ti-6Al-4V products fabricated by electron beam melting with unidirectional elongated pores, *Metall. Mater. Trans. A Phys. Metall. Mater. Sci.* 45 (10) (2014) 4293–4301.
- [128] R. Wauthle, B. Vrancken, B. Beynaerts, K. Jorissen, J. Schrooten, J.-P. Kruth, J. Van Humbeeck, Effects of build orientation and heat treatment on the microstructure and mechanical properties of selective laser melted Ti6Al4V lattice structures, *Additive Manufacturing* 5 (2015) 77–84.
- [129] O. Cansizoglu, O. Harrysson, D. Cormier, H. West, T. Mahale, Properties of Ti-6Al-4V non-stochastic lattice structures fabricated via electron beam melting, *Mater. Sci. Eng. A* 492 (1–2) (2008) 468–474.
- [130] P. Li, D.H. Warner, A. Fatemi, N. Phan, Critical assessment of the fatigue performance of additively manufactured Ti-6Al-4V and perspective for future research, *Int. J. Fatigue* 85 (2016) 130–143.
- [131] B.L. Boyce, R.O. Ritchie, Effect of load ratio and maximum stress intensity on the fatigue threshold in Ti-6Al-4V, *Eng. Fract. Mech.* 68 (2) (2001) 129–147.
- [132] J. Ding, R. Hall, J. Byrne, Effects of stress ratio and temperature on fatigue crack growth in a Ti-6Al-4V alloy, *Int. J. Fatigue* 27 (10–12) (2005) 1551–1558.
- [133] R. Hague, S. Mansour, N. Saleh, Material and design considerations for rapid manufacturing, *Int. J. Prod. Res.* 42 (22) (2004) 4691–4708.
- [134] X.P. Tan, Y. Kok, Y.J. Tan, G. Vastola, Q.X. Pei, G. Zhang, Y.-W. Zhang, S.B. Tor, K.F. Leong, C.K. Chua, An experimental and simulation study on build thickness dependent microstructure for electron beam melted Ti-6Al-4V, *J. Alloys Compd.* 646 (2015) 303–309.
- [135] M. Seifi, A. Salem, J. Beuth, O. Harrysson, J.J. Lewandowski, Overview of materials qualification needs for metal additive manufacturing, *JOM* 68 (3) (2016) 747–764.
- [136] X.P. Tan, Y. Kok, W.Q. Toh, Y.J. Tan, M. Descoins, D. Mangelinck, S.B. Tor, K.F. Leong, C.K. Chua, Revealing martensitic transformation and α/β interface evolution in electron beam melting three-dimensional-printed Ti-6Al-4V, *Sci. Rep.* 6 (2016) 26039.
- [137] P. Wang, M.L.S. Nai, X.P. Tan, G. Vastola, R. Srinivasan, W.J. Sin, S.B. Tor, Q.X. Pei, J. Wei, Recent Progress of Additive Manufactured Ti-6Al-4V by Electron Beam Melting, 2016 Annual International Solid Freeform Fabrication Symposium (SFF Symp 2016), Austin, Texas, USA, 2016 691–704.
- [138] W. Xu, M. Brandt, S. Sun, J. Elambariseril, Q. Liu, K. Latham, K. Xia, M. Qian, Additive manufacturing of strong and ductile Ti-6Al-4V by selective laser melting via in situ martensite decomposition, *Acta Mater.* 85 (2015) 74–84.
- [139] S.-H. Sun, Y. Koizumi, S. Kurosu, Y.-P. Li, H. Matsumoto, A. Chiba, Build direction dependence of microstructure and high-temperature tensile property of Co-Cr-Mo alloy fabricated by electron beam melting, *Acta Mater.* 64 (2014) 154–168.
- [140] S.-H. Sun, Y. Koizumi, S. Kurosu, Y.-P. Li, A. Chiba, Phase and grain size inhomogeneity and their influences on creep behavior of Co-Cr-Mo alloy additive manufactured by electron beam melting, *Acta Mater.* 86 (2015) 305–318.
- [141] Y.H. Kok, X.P. Tan, N.H. Loh, S.B. Tor, C.K. Chua, Geometry dependence of microstructure and microhardness for selective electron beam-melted Ti-6Al-4V parts, *Virtual and Physical Prototyping* 11 (3) (2016) 183–191.
- [142] S.M. Kelly, S.L. Kampe, Microstructural evolution in laser-deposited multilayer Ti-6Al-4V builds: part I. Microstructural characterization, *Metall. Mater. Trans. A* 35 (6) (2004) 1861–1867.
- [143] F. Martina, P.A. Colegrove, S.W. Williams, J. Meyer, Microstructure of interpass rolled wire + arc additive manufacturing Ti-6Al-4V components, *Metall. Mater. Trans. A* 46 (12) (2015) 6103–6118.
- [144] J.Y. Guédou, C. Körner, H. Helmer, A. Bauereiß, R.F. Singer, J. Choné, Tailoring the grain structure of IN718 during selective electron beam melting, *MATEC Web of Conferences* 14 (2014), 08001.
- [145] K. Hagihara, T. Nakano, M. Suzuki, T. Ishimoto, S.-H. Suyalatu, Sun, Successful additive manufacturing of MoSi₂ including crystallographic texture and shape control, *J. Alloys Compd.* 696 (2017) 67–72.
- [146] L.E. Murr, E.V. Esquivel, S.A. Quinones, S.M. Gaytan, M.I. Lopez, E.Y. Martinez, F. Medina, D.H. Hernandez, E. Martinez, J.L. Martinez, S.W. Stafford, D.K. Brown, T. Hoppe, W. Meyers, U. Lindhe, R.B. Wicker, Microstructures and mechanical properties of electron beam-rapid manufactured Ti-6Al-4V biomedical prototypes compared to wrought Ti-6Al-4V, *Mater. Charact.* 60 (2) (2009) 96–105.
- [147] A.R. Nassar, J.S. Keist, E.W. Reutzel, T.J. Spurgeon, Intra-layer closed-loop control of build plan during directed energy additive manufacturing of Ti-6Al-4V, *Additive Manufacturing* 6 (2015) 39–52.
- [148] T. Machry, D. Eatock, J. Meyer, A. Antonysamy, A. Ho, P. Prangnell, Effect of microstructure on the tensile strength of Ti6Al4V specimens manufactured using additive manufacturing electron beam process, *Powder Metall.* 59 (1) (2016) 41–50.
- [149] T. Amine, J.W. Newkirk, F. Liou, Methodology for studying effect of cooling rate during laser deposition on microstructure, *J. Mater. Eng. Perform.* 24 (8) (2015) 3129–3136.
- [150] N. Yu, *Process Parameter Optimization for Direct Metal Laser Sintering (DMLS)*, Department of Mechanical Engineering, National University of Singapore, Singapore, 2005.
- [151] W. Toh, P. Wang, X.P. Tan, M. Nai, E. Liu, S. Tor, Microstructure and wear properties of electron beam melted Ti-6Al-4V parts: a comparison study against as-cast form, *Metals* 6 (11) (2016) 284.
- [152] M. Jamshidinia, M.M. Atabaki, M. Zahiri, S. Kelly, A. Sadek, R. Kovacevic, Microstructural modification of Ti-6Al-4V by using an in-situ printed heat sink in Electron Beam Melting® (EBM), *J. Mater. Process. Technol.* 226 (2015) 264–271.
- [153] C. He, P. Wang, M.L.S. Nai, J. Wei, Distribution of Porosity in Electron Beam Melting Additive Manufactured Ti-6Al-4V Component, The Ninth Pacific Rim International Conference on Advanced Materials and Processing (PRICM9), The Japan Institute of Metals and Materials, 2016 385–387.
- [154] R. Cunningham, S.P. Narra, T. Ozturk, J. Beuth, A.D. Rollett, Evaluating the effect of processing parameters on porosity in electron beam melted Ti-6Al-4V via synchrotron X-ray microtomography, *JOM* 68 (3) (2016) 765–771.
- [155] B. Song, S. Dong, Q. Liu, H. Liao, C. Coddet, Vacuum heat treatment of iron parts produced by selective laser melting: microstructure, residual stress and tensile behavior, *Mater. Des.* 54 (2014) 727–733.
- [156] K.N. Amato, S.M. Gaytan, L.E. Murr, E. Martinez, P.W. Shindo, J. Hernandez, S. Collins, F. Medina, Microstructures and mechanical behavior of Inconel 718 fabricated by selective laser melting, *Acta Mater.* 60 (5) (2012) 2229–2239.
- [157] E. Brandl, D. Greitemeier, Microstructure of additive layer manufactured Ti-6Al-4V after exceptional post heat treatments, *Mater. Lett.* 81 (2012) 84–87.
- [158] S.L. Lu, H.P. Tang, Y.P. Ning, N. Liu, D.H. StJohn, M. Qian, Microstructure and mechanical properties of long Ti-6Al-4V rods additively manufactured by selective electron beam melting out of a deep powder bed and the effect of subsequent hot isostatic pressing, *Metall. Mater. Trans. A* (2015) 1–11.
- [159] H. Galarraga, D.A. Lados, R.R. Dehoff, M.M. Kirka, P. Nandwana, Effects of the microstructure and porosity on properties of Ti-6Al-4V ELI alloy fabricated by electron beam melting (EBM), *Additive Manufacturing* 10 (2016) 47–57.
- [160] Y.Y. Sun, S. Gulizia, D. Fraser, C.H. Oh, S.L. Lu, M. Qian, Layer additive production or manufacturing of thick sections of Ti-6Al-4V by selective electron beam melting (SEBM), *JOM* 69 (10) (2017) 1836–1843.
- [161] S. Palanivel, A.K. Dutt, E.J. Fairson, R.S. Mishra, Spatially dependent properties in a laser additive manufactured Ti-6Al-4V component, *Mater. Sci. Eng. A* 654 (2016) 39–52.
- [162] S. Das, M. Wohler, J.J. Beaman, D.L. Bourell, Processing of titanium net shapes by SLS/HIP, *Mater. Des.* 20 (2–3) (1999) 115–121.
- [163] D.A. Ramirez, L.E. Murr, E. Martinez, D.H. Hernandez, J.L. Martinez, B.I. Machado, F. Medina, P. Frigola, R.B. Wicker, Novel precipitate-microstructural architecture developed in the fabrication of solid copper components by additive manufacturing using electron beam melting, *Acta Mater.* 59 (10) (2011) 4088–4099.
- [164] H. Shiratori, T. Fujieda, K. Yamamoto, Y. Koizumi, K. Kuwabara, T. Kato, A. Chiba, Relationship between the microstructure and mechanical properties of an equiatomic AlCoCrFeNi high-entropy alloy fabricated by selective electron beam melting, *Mater. Sci. Eng. A* 656 (2016) 39–46.
- [165] A. Hinojosa, J. Mireles, A. Reichardt, P. Frigola, P. Hosemann, L.E. Murr, R.B. Wicker, Joining of Inconel 718 and 316 stainless steel using electron beam melting additive manufacturing technology, *Mater. Des.* 94 (2016) 17–27.
- [166] S. Sun, L. Zheng, H. Peng, H. Zhang, Microstructure and mechanical properties of Al-Fe-V-Si aluminum alloy produced by electron beam melting, *Mater. Sci. Eng. A* 659 (2016) 207–214.
- [167] G. Kasperovich, J. Hausmann, Improvement of fatigue resistance and ductility of TiAl6V4 processed by selective laser melting, *J. Mater. Process. Technol.* 220 (2015) 202–214.
- [168] Z. Wang, K. Guan, M. Gao, X. Li, X. Chen, X. Zeng, The microstructure and mechanical properties of deposited-IN718 by selective laser melting, *J. Alloys Compd.* 513 (2012) 518–523.
- [169] L. Zheng, Y. Liu, S. Sun, H. Zhang, Selective laser melting of Al-8.5Fe-1.3V-1.7Si alloy: investigation on the resultant microstructure and hardness, *Chin. J. Aeronaut.* 28 (2) (2015) 564–569.

- [170] L. Costa, R. Vilar, T. Reti, A.M. Deus, Rapid tooling by laser powder deposition: process simulation using finite element analysis, *Acta Mater.* 53 (14) (2005) 3987–3999.
- [171] G. Väistöla, G. Zhang, Q. Pei, Y.-W. Zhang, Modeling the microstructure evolution during additive manufacturing of Ti6Al4V: a comparison between electron beam melting and selective laser melting, *JOM* 68 (5) (2016) 1370–1375.
- [172] J. Irwin, E.W. Reutzel, P. Michaleris, J. Keist, A.R. Nassar, Predicting microstructure from thermal history during additive manufacturing for Ti-6Al-4V, *J. Manuf. Sci. Eng.* 138 (11) (2016) 111007.



A critical review of powder-based additive manufacturing of ferrous alloys: Process parameters, microstructure and mechanical properties



Haniyeh Fayazfar ^a, Mehrnaz Salarian ^a, Allan Rogalsky ^a, Dyuti Sarker ^a, Paola Russo ^a, Vlad Paserin ^b, Ehsan Toyserkani ^{a,*}

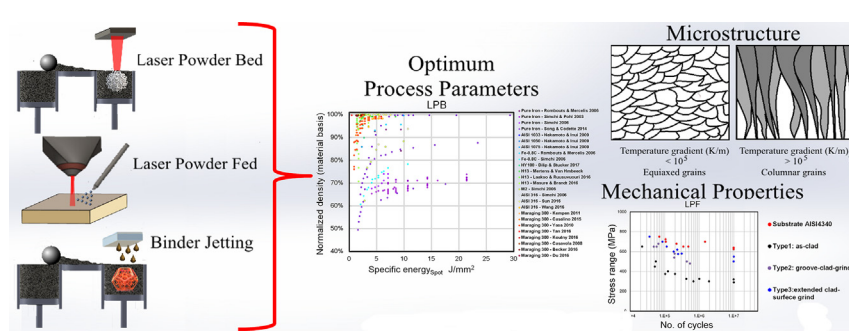
^a Multi-Scale Additive Manufacturing Lab, Department of Mechanical and Mechatronics Engineering, University of Waterloo, Waterloo, Ontario N2L 3G1, Canada

^b Rio Tinto Metal Powders, 1655 Route Marie-Victorin, Sorel-Tracy, Quebec J3R 4R4, Canada

HIGHLIGHTS

- Critical overview of different additive manufacturing (AM) process parameters on the quality of ferrous alloys.
- Introduction of new effective energy density numbers combined with the penetrated heat depth, hatch spacing and spot size.
- Critical overview of solidification and phase transformation of AM-processed ferrous alloys with mechanical properties.

GRAPHICAL ABSTRACT



ARTICLE INFO

Article history:

Received 28 October 2017

Received in revised form 2 February 2018

Accepted 6 February 2018

Available online 7 February 2018

Keywords:

Additive manufacturing

Laser powder-bed

Laser powder-fed

Binder jetting

Selective laser melting

Ferrous alloys

Steels

Process parameter

Microstructure

ABSTRACT

Additive manufacturing (AM) is an advanced manufacturing technology, enabling production of complex shapes by adding material layer-upon-layer, as distinct from conventional subtractive, forming and other manufacturing approaches. Thus far, several metallic materials including different types of ferrous alloys have been additively manufactured to full density with better or equivalent properties compared to counterparts made by conventional methods. In this perspective, this review article presents different powder-based additive manufacturing processes deployed to ferrous alloys, their key process parameters, phase transformation and microstructure development during solidification, all of which impact on mechanical behavior. The article enlightens the basics of Laser Powder-Bed (LPB), also known as selective laser melting), Laser Powder-Fed (LPF) and Binder Jetting (BJ) AM processes. These processes involve a sequence of complex/rapid thermal cycle and solidification behavior that influence the development of microstructure and eventually control the mechanical properties. A thorough discussion on mechanical behaviors, i.e., hardness, tensile, and cyclic/fatigue properties of AM manufactured steels is also presented based on several combined process parameters.

© 2018 Elsevier Ltd. All rights reserved.

1. Introduction

AM is a rapidly growing technique, where digital 3D design data is used to directly build up a product in a layer-by-layer process following

deposition, melting, fusion and binding of the successive material layers [1]. It is a direct manufacturing technology that enables to fabricate components composed of metal, polymer, ceramic, and composites with intricate features through external and internal layout, and reduce material consumption [2,3]. Metal AM technology has attracted industry/researchers where it offers unique applications in various industries for replacement or customization of parts with complex geometries,

* Corresponding author.

E-mail address: ehsan.toyserkani@uwaterloo.ca (E. Toyserkani).

Nomenclature

A	spot size area
c_p	specific heat capacity
d	laser spot diameter
g	acceleration of gravity
G	temperature gradient
H	capillary rise
k	thermal conductivity
l	layer thickness
\dot{m}	powder flow rate
P	laser power
q	laser energy flux
s	hatch spacing
t_d	drying time
T_m	melting temperature
T_0	room temperature
v	laser scan speed
V_s	solidification velocity
Z	normalized powder feed rate
α	thermal diffusivity
β	thermal absorptivity
ρ	Density
μ	dynamic viscosity of the melt pool
θ_s	melt pool transverse angle with respect to the substrate
γ	surface tension
ω	spacing between the walls
CE	carbon equivalent
$d\gamma/dT$	thermal surface tension gradient
HDR	heating depth ratio
VED	Volumetric Energy Density

internal structures and functionally graded properties [4–6]. Additional advantages of AM are: enabling consolidated parts for complex assembly, rapid production of prototypes and reduced design iterations, and faster market introduction of new products [7].

In contrast to the conventional cast and thermo-mechanical technique of material processing, in AM, there are limited options to modify the microstructures after manufacture, mostly because products are fabricated to near-net shape. Also, in the AM fabrication process, parts normally show significant anisotropy in properties along and perpendicular to the deposited layers. Samples deposited parallel (e.g. horizontal) or perpendicular (e.g. vertical) to the substrate undergo a different thermal history resulting in anisotropic mechanical properties [8,9]. The exact impact of process design parameters on physical and mechanical behaviors, and thus conformity of engineering parts fabricated via AM is still not well understood. Therefore, determination of the mechanical behaviors and also the influence of process design parameters for AM parts are of vital importance to predict their performance in service [10].

The goal of this paper is not to include all the existing studies related to AM of ferrous alloys but to provide an overview for researchers to understand significant and imminent research problems or opportunities as well as the R&D trend in this area. To this end, the most common mechanical properties reported in the literature for various ferrous alloys as well as process parameters control to achieve high density, near-net shape AM parts are investigated and reported for three AM techniques; Laser Powder-Bed (LPB), Laser Powder-Fed (LPF) and Binder Jetting (BJ) that are mainly used for the fabrication of parts composed of ferrous alloys. Electron-beam powder-bed fusion (EPBF) has also been used for the fabrication of parts composed of ferrous alloys; however, due to a very limited number of papers in the literature, the detail of this process is not included in the critical analysis. In addition, AM of

Metal Matrix Composites (MMCs) with ferrous alloys reinforcement elements, their process types and parameters, microstructural and mechanical properties are briefly summarized.

2. Additive manufacturing processes

2.1. Laser powder-bed (LPB)

LPB falls under powder-bed fusion AM according to ASTM committee F42 standard. LPB, also known as laser powder-bed fusion or selective laser melting (SLM), is a layer-upon-layer AM technique, where powder is spread in a layer and melted using a focused laser beam as shown in Fig. 1, to produce dense metallic parts. In this process, the obtainable geometric tolerance and minimum feature sizes are between 40 and 200 μm [11]. The overhanging geometry is supported by unmelted powder from previous layers. The main limitations for LPB are low build rate and the need to clear unmelted powder from internal geometry. A review with typical process applications can be found in [12]. LPB is widely used in multidisciplinary arenas such as, (1) in engineering to manufacture light weight machine parts, complex geometrical components, fuel cell, architectural design etc., (2) it also has demand in medical and dental applications because of some unique properties. The review identified two LPB topics generally applicable to any alloy, namely: (i) process optimization to maximize build rate at full density, (ii) microstructure control versus mechanical properties.

The operating design of LPB is schematically illustrated in Fig. 1a. In this technique, a numerically developed hatch stripe pattern is used over which the laser beam is scanned to melt the deposited powder layer as shown in Fig. 1b [13]. The main process parameters used in LPB are schematically shown in Fig. 1b, where the area is divided into stripes; comprising of several tracks detached by hatch spacing. The track is fabricated using laser beam with a fixed scan speed. During laser scanning process, an inert gas such as argon or nitrogen is introduced into the chamber to minimize oxidation. The platform is heated to about 80 °C before depositing and melting of the powder. After completing the process, the left-over powder is vacuumed and screened to be reused.

2.2. Laser powder-fed (LPF)

LPF falls under Directed Energy Deposition (DED) based on ASTM committee F42 standard. It is a class of laser-based additive manufacturing processes to synthesize full-density and high-performance complex metallic functional components. It is also known as laser consolidation, laser direct metal fabrication, laser cladding with blown powder, etc. This technique is based on a laser beam, focused on a specific area of a part where the powder is simultaneously supplied through a nozzle pointing to the same area, layer by layer. In contrast to the LPB process, which employs a bed of powder metal that is 'selectively' melted by a laser, LPF is accomplished by simultaneously delivering metallic powder and focused laser energy, as schematically shown in Fig. 2.

In LPF, a high power laser (e.g., Fiber, Disk, Nd:YAG or CO₂) is used to fabricate a melt zone on a substrate within an inert atmosphere; simultaneously, powder is injected to the melt through the laser beam. Subsequently, parts are made layer by layer using a 3D CAD file with each layer assembled track-upon-track via a controlled tool-path.

Advantages of the LPF process include the production of near-net-shape, full density parts with good mechanical properties and minimal imperfections (e.g. micro-cracking, distortion) [10,15]. A broad range of LPF applications was observed to various areas, including: 1) net shaped solid metallic parts, 2) functionally graded materials, 3) cellular solids, 4) in-situ alloyed parts, and 5) parts with conformal/internal features. However, predicting the properties of fabricated parts is very complicated due to the many process variables involved. Therefore, a better understanding regarding the microstructural evolution and

resulting materials properties is needed to achieve more consistency in the properties of the deposited parts.

2.3. Binder jetting (BJ)

In the binder jetting AM process (one of the AM classes based on ASTM standard), complex metal parts are fabricated using different materials by selectively injecting liquid binder agent into a powder bed. The BJ process is schematically shown in Fig. 3. After one layer is printed, a counter-rotating roller or a wiping blade spreads a new layer of powder on the surface of the prior layer, which is subsequently printed and stitched with the earlier one through jettied binder. This procedure is repeated to finish the green part formation. The BJ printing process is completed by post-sintering of 3D printed green parts in a high-temperature furnace, where the polymeric binder is burned off and the powder particles are sintered together through atomic diffusion to achieve final density and strength [16,17].

The main advantages of the BJ technique are: (1) the prevention of residual stresses in the printed parts due to the absence of rapid heating and cooling of the melt pool, (2) no need to support structure and build substrate, (3) no need for environmentally controlled chamber during the green parts fabrication, (4) compatible with highly reflective materials in contrast to LPB [16]. However, one of the major drawbacks of the BJ process is the difficulty to reach full density parts after the post-sintering, leading to reduced mechanical performance of the BJ-made parts compared to conventional manufactured ones [18]. Moreover, BJ is usually unable to process ultra-fine and loosely packed powders. Ultra-fine powders are difficult to spread owing to low flowability and potential powder agglomeration due to humidity, creating defects in the green parts. The sintered products will experience a significant dimensional change and reduction in mechanical properties [19].

Within the steel family, the use of metal BJ process has been limited to the fabrication of end-use products from stainless steel (SS) powders. Binder jetted SS materials have shown applications in the area of aerospace, energy, automotive, prosthetics [21,22], microwave circuits and antennas [23], art, and design industry as rotors, stators, impellers, etc. offering a significant manufacturing time reduction and impactful weight and cost savings [24]. For example, meshed Ku band waveguides of 420 SS are fabricated using the BJ process, which reduces the material usage and weight by 22% while obtaining the low loss characteristic of metallic waveguides [23].

2.4. Electron-beam powder-bed fusion (EPBF)

EPBF falls under the class of powder-bed fusion AM as per the ASTM standard F3001-14 [25], which is a layer-by-layer process with similar

capabilities to LPB [26], as schematically shown in Fig. 4. Electrostatic charge is a consideration, leading to use of slightly larger powder (<40 µm fraction excluded [27]). The main process differences are the need for high vacuum and the use of the electron beam to pre-heat the powder bed. Use of vacuum is beneficial in eliminating impurities such as oxygen; however, it can also strip out low boiling point alloying agents such as Mn [28]. Electron beam heating provides interesting design capabilities for microstructure control [29], but its capabilities appear to be largely unstudied in ferrous alloys. Work with ferrous alloys is limited to two reports, which note that the cooling rate in the build chamber was insufficient to harden H13 tool steel [28]. This is disadvantageous for less hardenable low alloy materials but may lead to more consistent microstructure for higher alloy materials where post processing heat treatment is necessary. Arcam AB (A GE Additive company) is the only commercial equipment supplier for EPBF equipment and holds the process under patent until 2022 [25]. This causes limited new material development from this process [25,30]. However, it is reasonable to expect the field to open up as Arcam's patents expire.

3. Reflection on the number of relevant papers covering ferrous alloys

Fig. 5a, b illustrate the volume of papers associated with different kinds of steels processed by various AM processes. Among them, majority of the work is reported using the LPB process (155 papers) followed by the LPF process (54 papers), to the best knowledge of the authors and as of August 2017.

In the literature, the BJ process (15 papers) is limited to 420 SS and 316 SS. However, compared to others, the EPBF process (2 papers) is only available for limited work on H13 tool steel. Therefore, based on the literature, sufficient study is not available to do a critical review of the EPBF process.

For various AM processes of LPB, LPF and BJ, the pie charts in Fig. 6a–c represent the detail studies for each technique that have used steel powders of various compositions. In the LPB process, as shown in Fig. 6a, almost equal amount of work has been done on H13 tool steel, maraging steel and M2 HSS.

For other SS, i.e. 316 SS, 420 SS, 17-4 PH SS and low alloy steels, very limited work has been reported using LPB. From Fig. 6b, it was observed that in LPF, the most researched steel powders were 316 L SS and H13 tool steel followed by low alloy steels. However, only a limited amount of LPF studies have been reported on using 420 SS, 304 SS and maraging steel. In contrast to LPB, in BJ as shown in Fig. 6c, most of the work has been done with 316 SS and 420 SS. Also, the process covers a small quantity of work on pure iron, 430 SS and 410 SS.

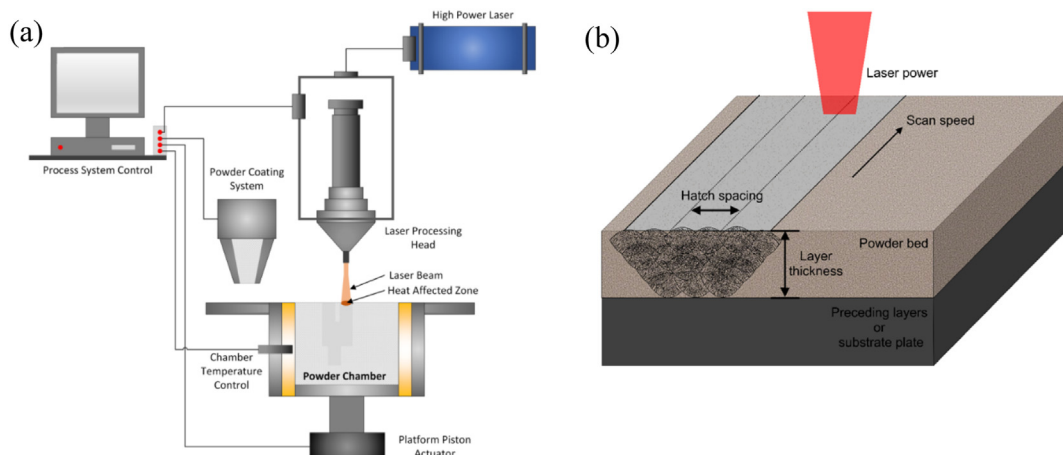


Fig. 1. (a) Schematic of operating process design in LPB, (b) close up of the LPB process zone [13].

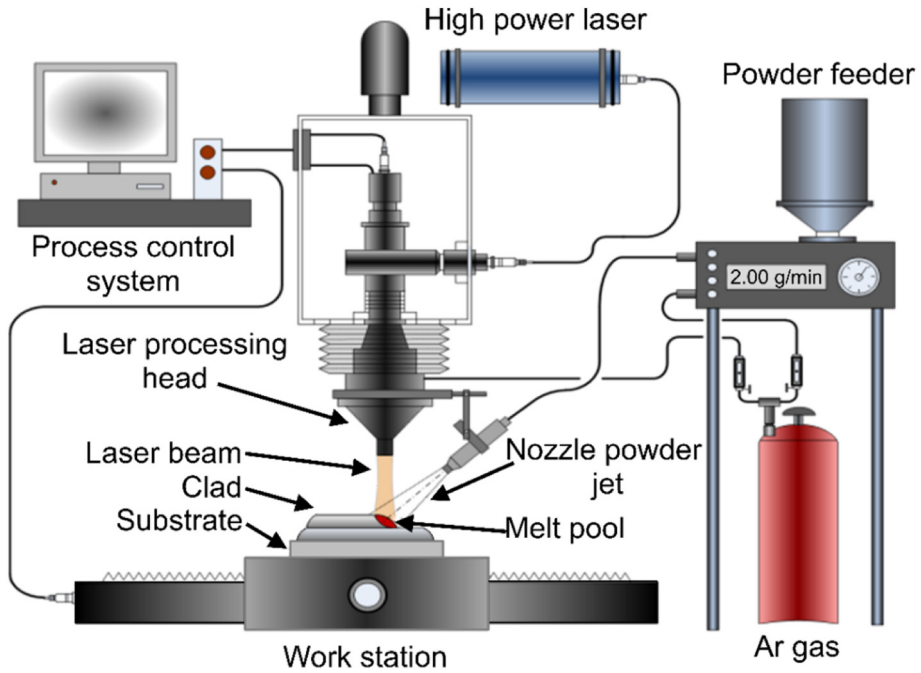


Fig. 2. Schematic presentation of the LPF technique (reproduced with permission from Elsevier) [14].

4. General process parameters

A wide range of process parameters as well as physical phenomena control the quality of AM products. Fig. 7 summarizes these parameters grouped as input parameters, process physics, and outputs. Commonly, the input parameters are as follows: laser energy, motion device, powder feeder set points, material, binder and ambient properties. In the design parameter chart, the output signifies the quality of the final product, listed as geometry, microstructure, hardness, cracks, porosity, residual stresses, surface roughness, and dilution [32]. Among the detail listed parameters in the chart (Fig. 7), some of the significant

parameters and their impact on physical and mechanical behaviors are discussed here.

As shown in Fig. 7, there are many common parameters for all three processes; however, each process has its own specific parameters too. With this point in mind, in the following, the role of common process parameters and process specific parameters are discussed. In addition, the authors intend to combine several parameters together to ease the critical review of results. To this extent a few new combined process parameters are proposed for the first time in this review paper. It has to be noted that some of the parameters are inherently important for a specific AM process and may not be relevant to other AM processes covered

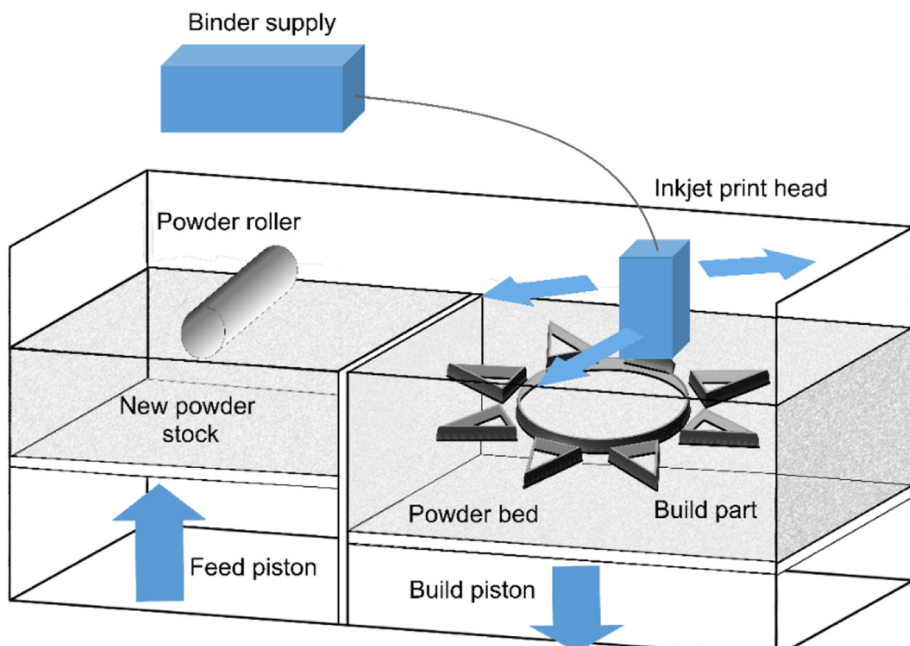


Fig. 3. Representation of binder jet 3D printing process [20].

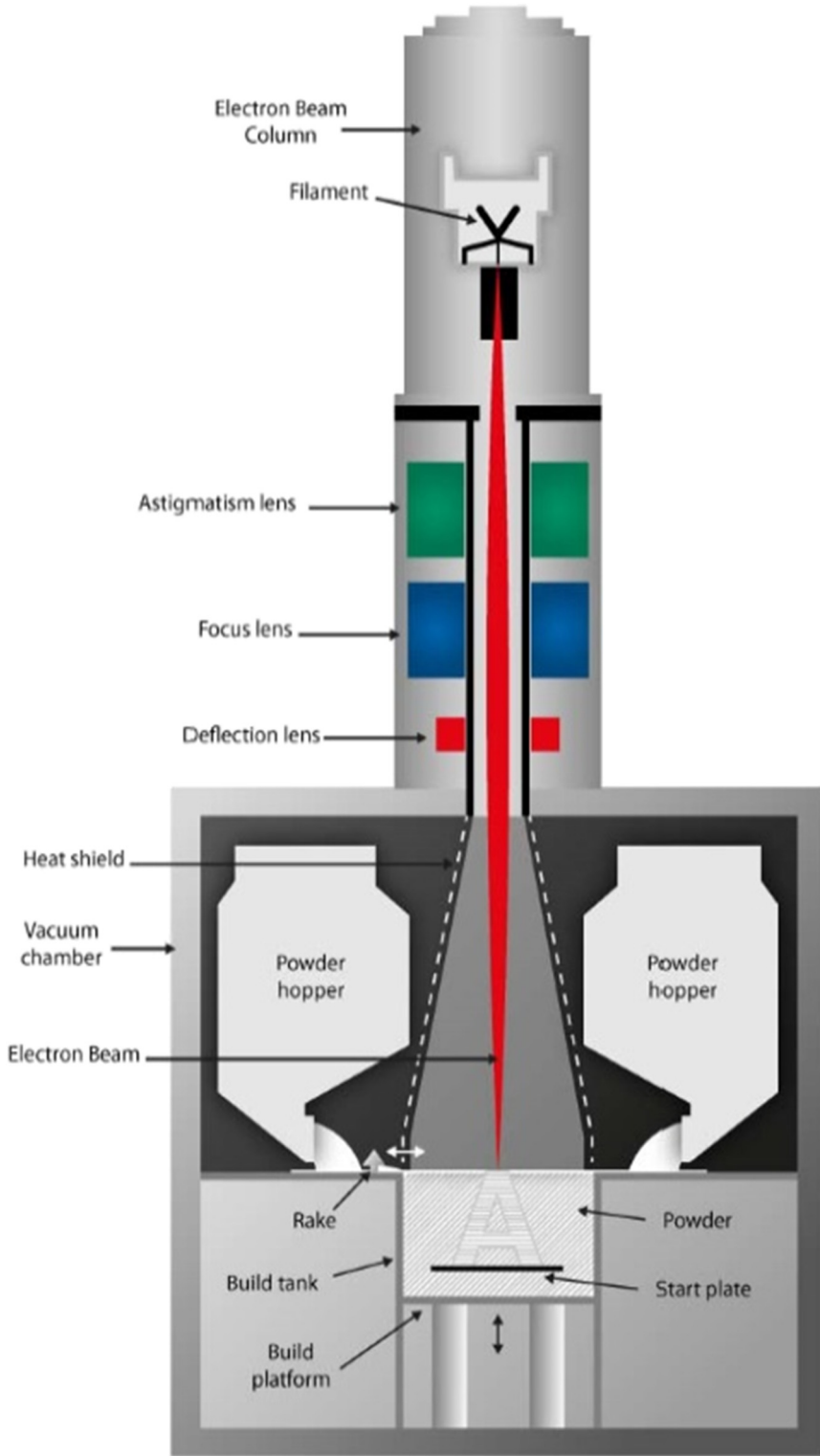


Fig. 4. Schematic of EPBF process; available on internet [25,31].

in this paper. For each process parameter set, therefore, the corresponding AM process is labelled accordingly.

4.1. Key process parameters and their effects on relative density

4.1.1. Hatch spacing to spot size ratio

The ratio between hatch spacing and spot size has major effects on process stability and the regular density when LPB is used [33]. As

seen in literature summary represented in Fig. 8, the majority of the work uses hatch spacing and spot size for analysis. According to Nakamoto et al. [34], highly dense part is obtained while hatch spacing is atypically low and heating depth is high at low energy density. Also, Mertens et al. [35] achieved good results with large hatch spacing and unusually high energy density, while increasing process speed with the available laser power. When hatch spacing is reduced, re-melting of solidified region is a strategy to maintain density despite high scan

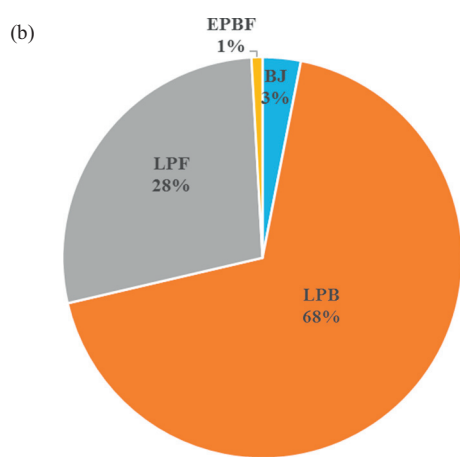
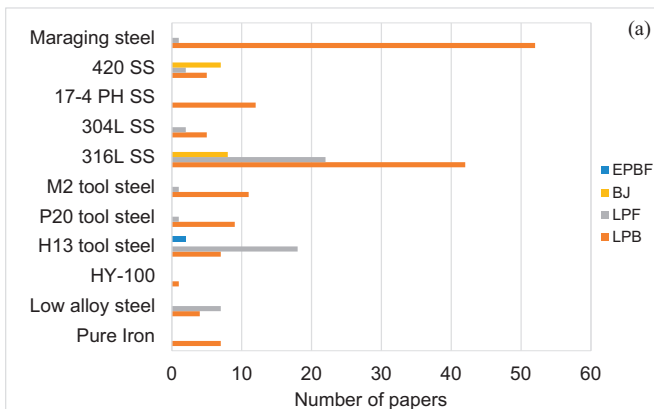


Fig. 5. (a,b) Relative emphasis of steels reported in the literature using various AM processes.

speed [36]. Fig. 8 indirectly explains the role of laser beam tracing overlap through the ratio between hatch space to spot size and its role on the relative density. Although the plot does not represent other main process parameters used for generating the densities, it implies that a wide range of densities is achievable while the average hatch spacing to spot size ratio is mainly set from 0.6 to 1.5.

4.1.2. Energy ratio

A consensus in the literature is that some measure of energy density is one of the best predictors for parts relative density for both LPB and LPF. A variety of energy density measures are used in the literature with a volumetric density approach. Volumetric density may have the advantages that it can be normalized against material enthalpy to be used for the comparison of multiple materials. However, some arguments have been made that the melting of multiple layers and also key-hole shape of the melt pool invalidates the use of layer thickness for the vertical length scale parameter [43]. This is backed by the observation in the next section that the layer thickness is highly correlated with optimum heat pulse depth. It is expected that the melted volume does not directly correspond to the cube defined by Volumetric Energy Density (VED), but that melted volume will scale fairly linearly with the volume of this cube for successful recipes [44,45]. However, the specific energy used mainly for LPF [32] and also used for LPB [43], [46–49] is more indicative of input energy from the surface irradiated by the laser beam [50].

$$E_{\text{specific}} = \frac{P}{v d} \quad (3.1)$$

where P is laser power, v is process speed and d is the spot size.

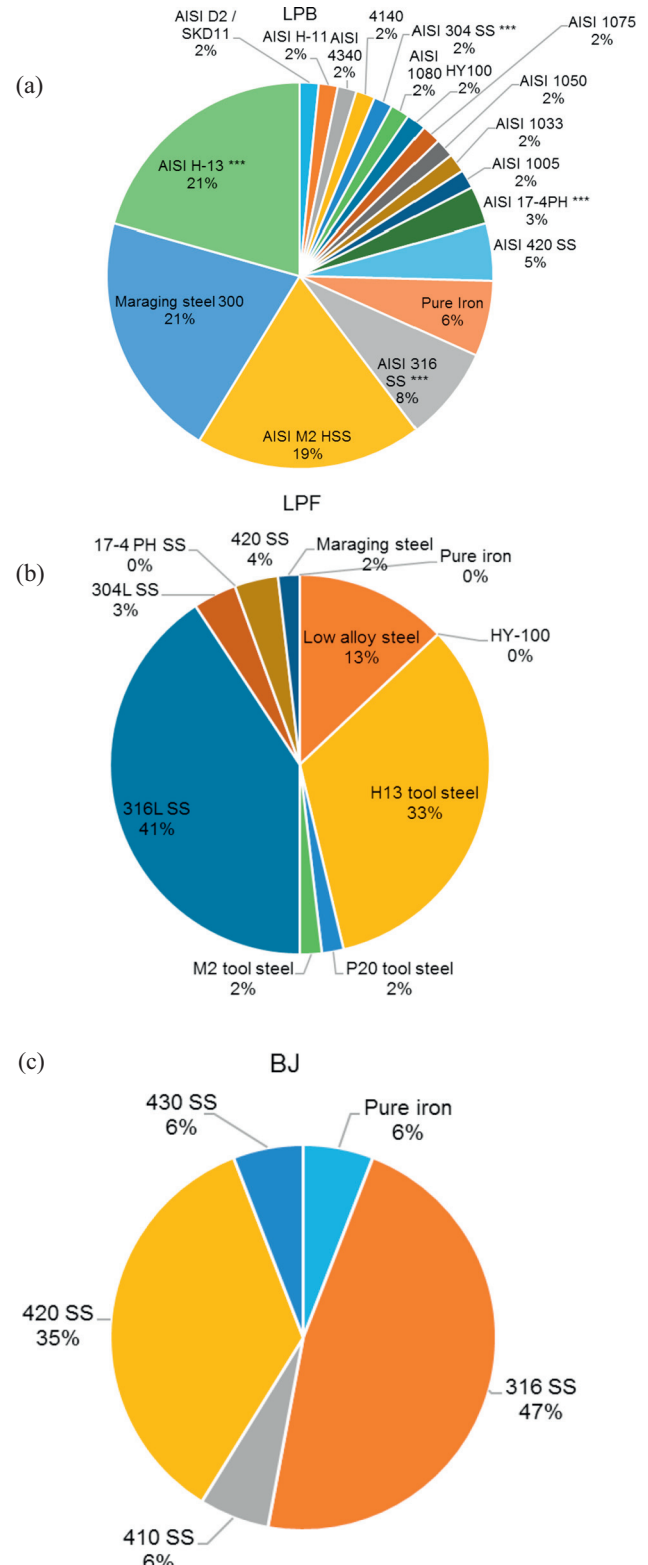


Fig. 6. Relative emphasis of steels reported in the literature using (a) LPB, (b) LPF and (c) BJ processes.

VED is more widely used for LPB techniques [27], [34], [39–42], [50–57], where three most important parameters are combined and justified based on the volumetric heat adsorption in powder bed; as defined below [58]:

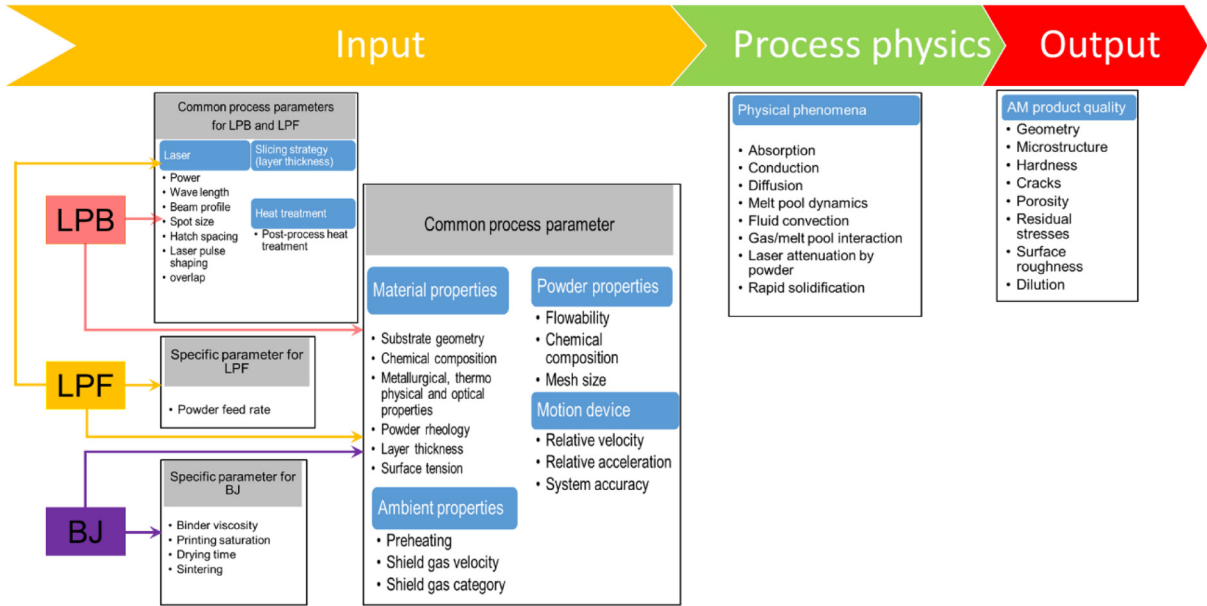


Fig. 7. A detail process design parameters for AM techniques.

$$VED_{Hatch} = \frac{P}{v s l} \quad (3.2)$$

where s is hatch spacing and l is layer thickness.

Spot size d provides an alternative definition more similar to specific energy,

$$VED_{Spot} = \frac{P}{v d l} \quad (3.3)$$

This is presumably related to energy requirements for fully melted materials within the proposed cube cells represented by hatch spacing, spot size and interaction length (i.e., speed/interaction time) [40,59]. Therefore, to compare across materials normalized VED, estimated enthalpy difference is used between room temperature (T_0) and the materials melting point (T_m).

$$\frac{VED_{Spot}}{\Delta H} = \frac{P}{v d l} \cdot \frac{\beta}{C_p,100^\circ C (T_m - T_0)} \quad (3.4)$$

where β is absorption factor, and C_p is heat capacity.

With the above four combined numbers, Fig. 9a–d are generated. This exercise has used C_p at 100 °C, which is readily available for all

materials and neglected the latent heat of fusion that normally covers small amount of total energy required for melting.

All plots, as shown in Fig. 9a–d, regarding density vs. energy, show similar trend; they reproduce well known result that energy input should be above the minimum threshold to achieve full density part. Normalized figure allows prediction that $VED_{Spot}/\Delta H$ should be >30 for full density part in steels. Based on the observed scatter, it is apparent that other factors are significant. Elevated value for enthalpy ratio suggests that heat transfer is very significant for the chosen process parameters. Also, precise value for required energy density is influenced by powder particle size distribution [51,52,60]. Moreover, from the literature, it is evident that high energy density reduces dimensional control making a hard process optimization procedure to compromise between specimen dimensionality and porosity [42].

4.1.3. Surface tension

In both LPB and LPF, surface tension plays an important role as it dictates capillary and wetting forces and also represent if the AM process is a diffusion based process or convention based. From [32], surface tension number is defined as,

$$S = \frac{(d\gamma/dT)qd}{\mu v k} \quad (3.5)$$

where $(d\gamma/dT)$ is the thermal surface tension gradient, q is the laser flux, d is the spot size, μ is the dynamic viscosity of the melt, v is the scan speed and k is the material thermal conductivity near its melting point.

For $S \leq 45,000$, surface tension is negligible. This is one of the recommended non-directional parameters which is closely related to Marangoni number [38,61]. In the literature, surface tension gradient and melt viscosity data is only readily available for pure iron, whereas viscosity estimates may be available for alloys via a generalization of the Andrade equation [62–64]. A tenuous approximation of surface tension is possible via thermodynamic approaches [65], however as atmospheric interaction is expected to be very significant (for both O₂ & N₂) [38,61,65,66], accurate estimations should include atmosphere data which is not readily available. Unfortunately, significance of surface tension cannot be adequately/comprehensively evaluated from the literature due to the factors mentioned above.

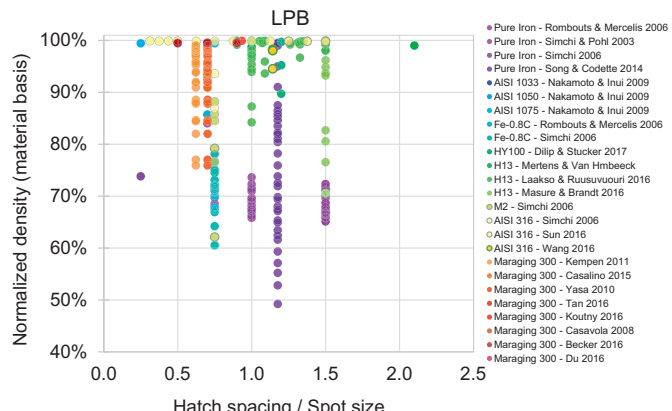


Fig. 8. Effect of hatch spacing/spot size on the density of ferrous alloys in LPB process [33–35], [37–42].

4.1.4. Dimensionless heating depth ratio (HDR)

To incorporate material properties and the heat penetration depth that would represent the keyhole depth into the analysis, the authors propose a new combined number called “dimensionless depth”. The one dimensional transient model is formulated as: [67,68],

$$T(z, t) = \frac{P\beta}{Ak} \sqrt{4\alpha t} \text{iefc} \left[\frac{z}{\sqrt{4\alpha t}} \right] \quad (3.6)$$

where A is spot area, z is distance from surface, t is laser interaction time, α is thermal diffusivity, z is vertical axis, P is laser power, k is thermal conductivity and β is absorption factor. While, 90% of temperature change occurs within 1 scaling parameter of surface [67], the interaction time can be expressed by d/v where d is the spot size diameter [61]. The heating depth can be obtained when the limit of Eq. (3.6) approaches zero. This results in the following equation representing the heat penetration depth:

$$\text{HeatedDepth} = \sqrt{4\alpha \frac{d}{v}} \quad (3.7)$$

A logical dimensionless combined process parameter may be proposed through a ratio of the above equation and layer thickness, leading to a parameter so-called heating depth ratio (HDR).

$$HDR = \frac{\sqrt{4\alpha \frac{d}{v}}}{l} \quad (3.8)$$

The relative density versus HDR data from the literature is plotted in Fig. 10a. From the data available in the literature, it is apparent that, all successful authors are operating with heating depth greater than layer

thickness. Therefore, an HDR of 1.5 appears to be a good guideline for full density parts, as shown in Fig. 10a. Also the low part density at high VED generally correlates with large HDR (long interaction times) as seen in Fig. 10b and c. Fig. 10c zooms into a narrower range of HDR. From the Fig. 10b and c, it is seen that the central trend VED requirement appears to increase with increasing HDR [37]. There are however, a few outliers (reported density approximately above 99%) that may be attributed to the fact that the operating in a significantly different mode with respect to hatch spacing [26].

4.1.5. Drying time (BJ process)

In the BJ process, after printing of each powder layer, the print bed needs some time to be dried using resistive heater, known as ‘drying time’. To prevent blocking at the print head, it simultaneously shifts to a clean tank to remove extra binder materials. If the drying time is not adequate, print head may be blocked, which significantly reduces the surface quality of the final part [24]. Moreover, as demonstrated in Fig. 11, at short drying time, binder infiltrates only into the top thin layer leaving more pores in the green part, which leads to a higher porosity and a higher shrinkage in the sintering process [24]. Drying time should be long enough to achieve satisfactory green strength [69].

As depicted in Fig. 12, a drying time ranging from 10 to 20s is adequate to promote sufficient green strength and higher relative densities compared to the 60s drying time. Moreover, excessive drying time causes higher solidification and shrinkage rate, which eventually increases the production time and electric power consumption [24].

However, drying time is also determined by the choice of binder. For example, diethylene glycol (DEG) binders have a longer drying time of about 30s/layer, while phenolic binders do not require drying. Therefore, drying time (t_d) is defined as a function of powder thermal conductivity (k), binder saturation (S), and surface area (A), as expressed in

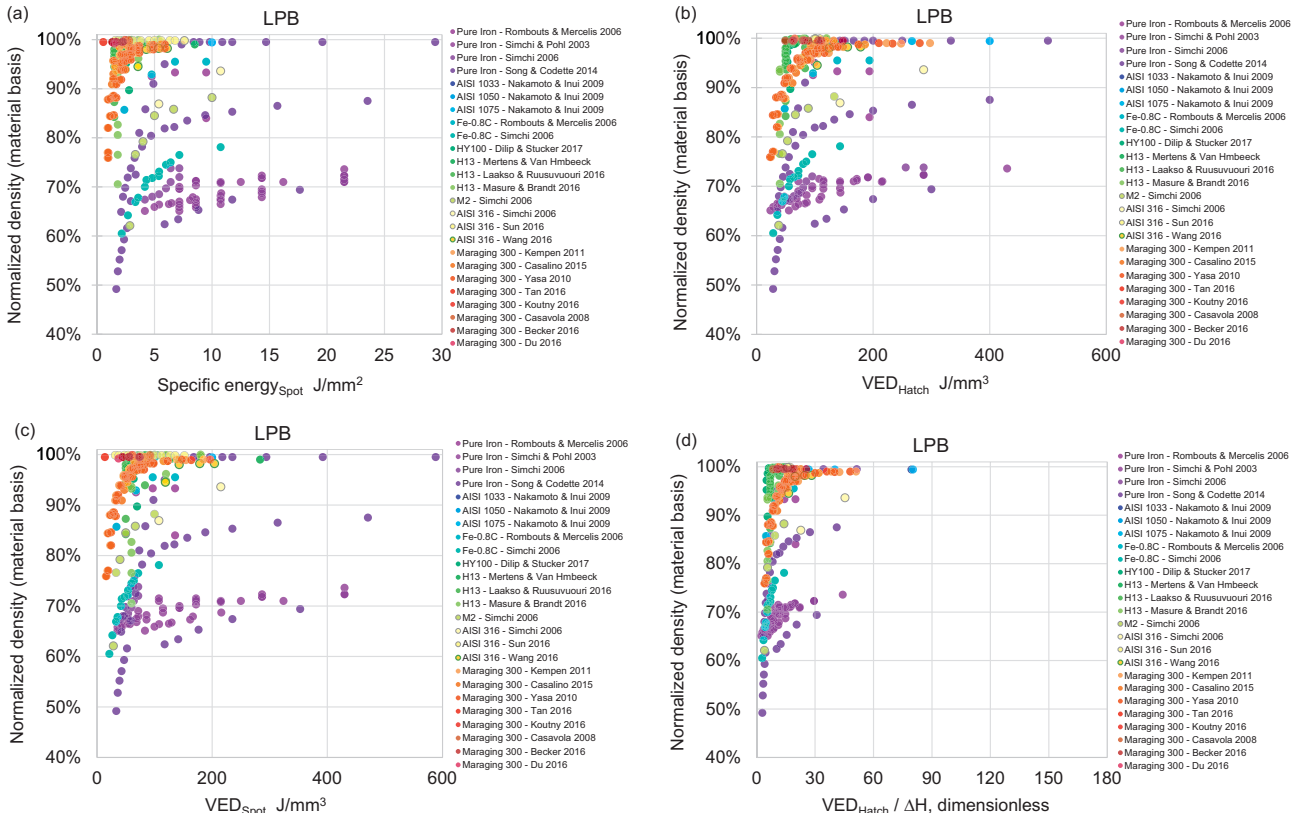


Fig. 9. Relative density vs. energy for various ferrous alloys, (a) relative density vs. specific energy, (b) relative density vs. hatch based VED, (c) relative density vs. spot based VED, (d) VED/ ΔH [33–35], [37–42].

Eq. (3.9). Thus, powders with poor thermal conductivity, higher binder saturation, and larger surface area need longer drying time (t_d) [70].

$$t_d \propto \frac{SA}{k} \quad (3.9)$$

4.1.6. Printing saturation (BJ process)

Printing saturation or binder saturation in BJ is the ratio of air space between powder particles (V_{air}) and binder volume (V_{binder}) [24,72]. In simple words, saturation explains the amount of binder to be deposited in the period of printing, and it determines the printing quality and final

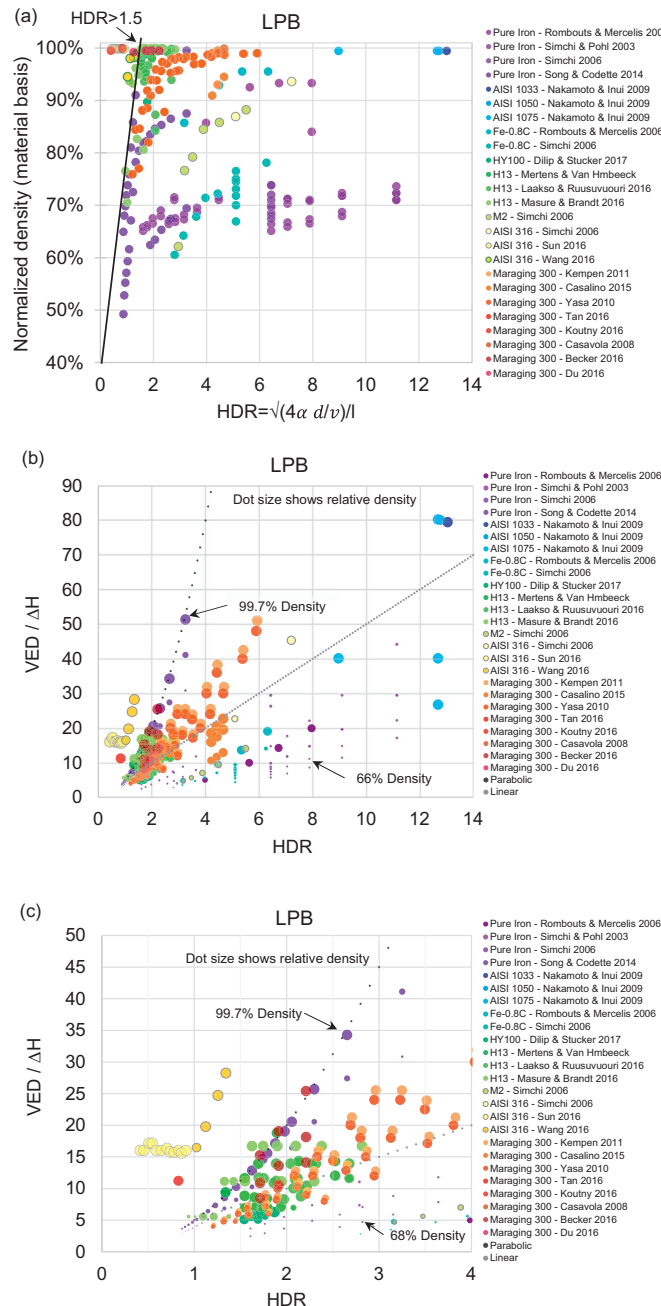


Fig. 10. Relative density vs. heating depth ratio for various ferrous alloys, (a) normalized density vs. dimensionless depth, (b) VED/ΔH vs. heating depth ratio, (c) zoom in the plot of (b) [33–35], [37–42].

sintered density, which is defined by the following equations [24,72].

$$S = V_{binder}/V_{air} \quad (3.10)$$

$$V_{air} = \left(1 - \frac{PR}{100}\right) \times V_{solid} \quad (3.11)$$

where V_{solid} is the volume of solid particles in a defined envelope. Here, PR is the packing density of the powder bed, as defined below, [24].

$$PR = \frac{V_{powder}}{V_{powder} + V_{air}} \quad (3.12)$$

Therefore, optimal binder saturation is selected based on powder packing factor and wettability [70]. In order to yield sufficient green part strength and quality, satisfactory binder saturation is needed [72]. If not satisfactory, some powders fall off from the part, leading to a bad surface quality (zigzag surface), as shown in Fig. 13a [24]. On the other hand, low level saturation can result in inaccurate geometry and low sintered density leaving porosity after binder burn-out. The excessive powder bonded to the surface makes some swells on the surface leading to bad surface roughness as depicted in Fig. 13b.

Oversaturation also leads to unwanted wetting of the bed, thus sticking powders to the roller and subsequent inhomogeneous powder bed [70,72]. It has been shown that spherical particles use binders more efficiently by having small necking area between particles leading to comparatively low binder saturation levels [72]. Our review shows that compared to the 3D printed bio-implants, which are designed to possess higher porosity, lower binder saturation level gives rise to higher relative density for ferrous alloys. The effect of printing saturation on relative density for the 3D printed parts is shown in Fig. 14; however, we do not have enough data points to be able to draw a concrete conclusion for ferrous alloys.

4.2. Common key process parameters for all three AM processes

4.2.1. Powder characteristics

Powder properties such as flowability, compressibility, tap density, size, shape, distribution, etc. have significant effects on the final AM made parts [73,74]. Most research studies on the LPB processing of maraging steels have been focused on the use of gas atomized powders that are usually expensive. Hoeges et al. [75] investigated the impact of different atomization methods on the quality of LPB processed parts. They employed high-pressure water atomization to produce maraging steel (Ni 17–19, Co 8.5–9.5, Mo 4.5–5.2, Ti 0.6–0.8, Al 0.05–0.15, C ≤ 0.03, Cr, Cu ≤ 0.5, Si, Mn ≤ 0.1, S,P ≤ 0.01 wt%) with niobium instead of titanium. It is beneficial to replace titanium with niobium, because of its lower affinity to oxygen preventing the formation of stable solid oxides which tend to adhere to the pouring nozzle. Moreover, it optimizes the flowability of maraging steel, and minimizes oxide inclusions during the LPB process. The detail of the formation of oxide inclusions due to the oxide contamination of the powder is focused in LPB processed 17-4

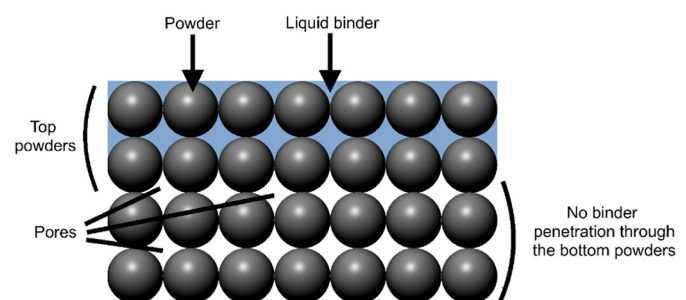


Fig. 11. Short drying time leads to thin binder penetration [24].

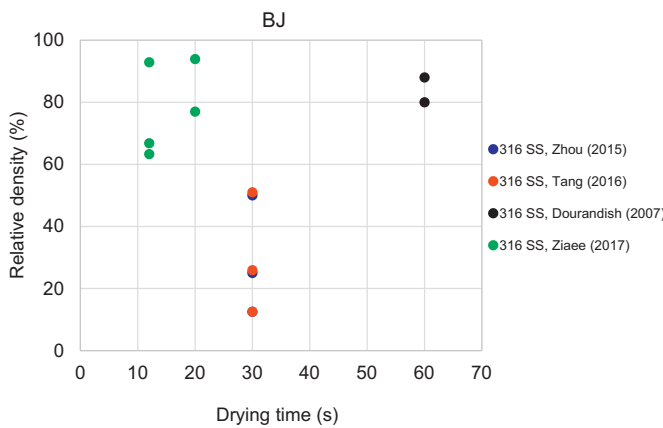


Fig. 12. Effect of drying time on relative density of 3D printed parts [21,22,69,71].

PH steel [76]. The researchers addressed the major drawbacks associated with water atomized powder characteristics including irregular particle shape, lower tap densities, and oxidized surfaces. More importantly, there is a slight difference in the avalanche angle between water atomized and gas atomized maraging steel powder (1°). The smaller the avalanche angle, the better the processability of the powder; therefore, the powder will spread more smoothly during the deposition of a thin powder layer [75]. It should be noted that water atomized pure iron powder (WA-Fe-Powder) with avalanche angle of $\sim 54^\circ$ has shown sufficient flowability to be processed with additive manufacturing machines, and is documented as a minimum requirement for the processability in LPB. In addition, Latenieur et al. [73], worked on WA-Fe based powder using the LPB process, where process parameters were optimized to improve density and mechanical properties of the 3D printed parts. While gas atomized maraging steel has been most widely used for additive manufacturing [75,77], there are not many papers associated with water atomized powders. Nevertheless, the mechanical properties of the water as well as gas-atomized powders for a few steel alloys are compared in Table 1 [75].

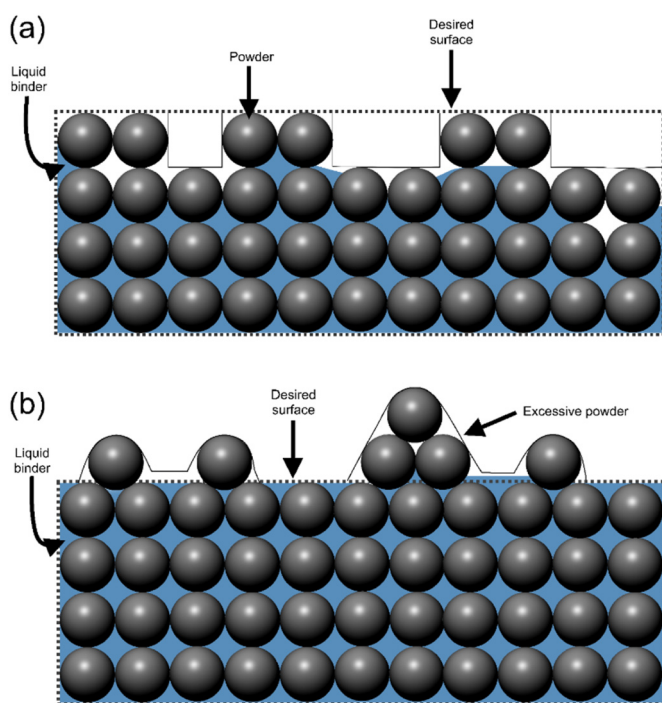


Fig. 13. (a) Low-level saturation leads to powder loss, and (b) over-saturation leads to excessive powder bond [24].

In the BJ process, powder characteristics such as particle size, morphology, density, tap density, and flowability affect the final properties of the AM components. For example, spherical particles are mostly preferred, although irregular particles are able to improve green strength without achieving uniform density. Furthermore, in order to reach good packing of powder layers and high green density, tap density of the powder should be satisfactory. Insufficient tap density leads to high porosity levels in the green components and subsequent high shrinkage during sintering, which makes it difficult to reach desired density and tolerances of the final component [78].

The powder particle size distribution (PSD) has a significant influence on the entire BJ process from making green parts to post processing. Dourandish et al. [69] showed that sintering behavior of complex-shaped biomedical parts of 316 L SS significantly depends on the PSD. Solid state sintering governs the densification of 316 L SS powders. However, using fine 316 L powder, after sintering the total amount of porosity is low (~12%) with relatively small pores. When coarse 316 L particles are used, a higher total porosity (~20%) with a significant amount of large (~100–300 μm) pores is observed. Moreover, the amount of carbon pick-up during de-bonding and sintering depends on the powder particle size. The amount of carbon pick-up for fine powder is 0.2 wt% compared to 0.07 wt% for coarse powders, which is attributed to the lower layer thickness and lower amount of binder used for 3D printing [69].

4.2.2. Layer thickness/layer slicing strategy

In steel alloys fabricated by LPB, higher layer thickness causes a decrease in relative density as extracted from published sources and shown in Fig. 15. Consequently, layer thickness influences the macro-hardness together with the scan speed [77,79,80]. To make the plot more representative, different color is used to focus different laser power, scanning speed, etc.; however, the plot is normalized around layer thickness.

Some studies have been carried out to control the three-dimensional deposition by the LPF technique [32,89–91]. It is known that if the process parameters are not completely optimized, the final layer thickness might be dissimilar to the original setting value, even with the use of height control device. To find out the impact of process design parameters on the layer thickness of H13 tool steel, actual layer thickness was measured. The dissimilarity in the final layer thickness from the setting values in terms of thickness error distribution is shown in Fig. 16a. It is seen that to achieve a good dimensional accuracy in H13 tool steel, layer thickness might be fixed as 0.254 or 0.381 mm. Also according to results shown in Fig. 16b, superior dimensional accuracy can be obtained by high powder mass feed rate. Therefore, in this process, both layer thickness and porosity greatly depend on powder mass feed rate and overlap percentages with a constant laser input power.

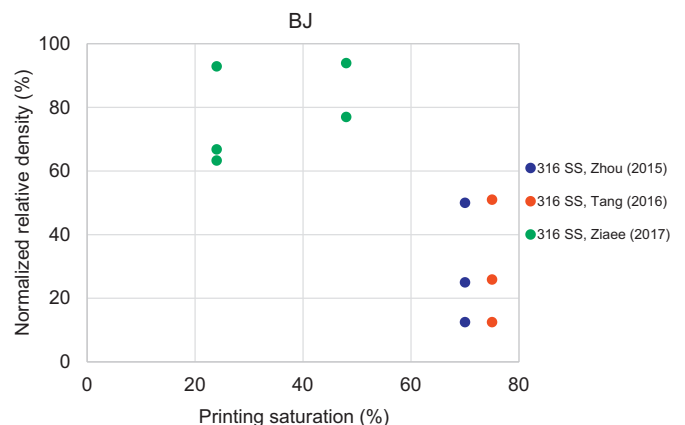


Fig. 14. Effect of printing saturation on relative density of 3D printed steel parts [21,22,71].

Table 1

Average avalanche angle of water and gas atomized powder and mechanical properties of LPB processed maraging steel after age hardening at 490 °C for 6 h [75].

Material	Avalanche angle (°)	Density (g/cm ³)	UTS (MPa)	Elongation at break (%)	Hardness (HRC)	Impact energy (J)
GA-maraging 300	47.5	8	2006	3.1	52	7
WA-maraging 300	48.5	8.04	1793	1.4	43	5

The larger powder mass feed rate causes greater porosity, but the possibility of actual layer thickness formation is enhanced [90]. However, in case of deficiency of energy input, the overlap of the melted track should be >50% [90]. By contrast, in another research, it is claimed that 40% overlap in H13 tool steel gives the best combination of layer thickness and maximum volume of deposition rate [91]. It has been reported that the layer thickness in LPF fabricated products shows a key role in the final parts microstructure. In particular, for H13, by increasing the layer thickness or specific energy, the primary dendrite widths are enhanced. In addition, the finer grain and the higher cooling rates can be obtained by a lower specific energy, lower layer thickness but by a higher speed [91]. For H13 tool steel, it is then shown a progressive relationship among the outputs of layer thickness and specific energy with powder mass feed rate [91].

An interesting strategy to achieve dimensional accuracy is by layer slicing. In the LPF process, the CAD design part is sliced into parallel layers and synthesized in a layer-wise method. This method is only applicable to surfaces where normal vectors are not aligned to 0° or 90° with the process direction. Therefore, in spite of a feasible solution of this method, the staircase effect (a surface with step-like features) still remains [92]. There are some studies reflecting on the slicing procedure to reduce staircase effects, such as the volumetric difference between layers [93] and controlling layer thickness [94]. However, these methods are considered for fixed direction deposition processes and do not entirely remove the staircase effect. There are other methodologies such as, multi-axis processing to minimize the staircase effect. In this method the slicing direction rotates to 90°, in case of an overhang structure instead of taking the classical parallel slicing procedure [95,96].

It has been reported that layer thickness in BJ is the most critical factor that affects the integrity of the part. It also determines the possibility to design of smallest feature size [24]. High layer thickness results in unbounded layers, while applying a thin layer leads to pushing away of the printed layers during spreading of the next powder layer [69]. Generally, it is believed that better end-product properties are achieved when applying a low layer thickness, while building time will considerably increase as a tradeoff [24]. It is also reported that layer thickness must be bigger than the diameter of the largest particle [70] or at least one diameter of the largest particle in the powder feedstock [15]. In this review, layer thickness/average particle size is defined as one of

the key parameters that need to be identified and controlled; however, the capability of the BJ machine constrains the choice of the layer thickness. Our review shows that higher relative densities are attained when the ratio of layer thickness to average particle size is in the range of 2.3 to 3.3, as shown in Fig. 17. It should be noted that to reach a firm conclusion more data points are necessary.

4.3. Specific process parameter for BJ

4.3.1. Binder burnout and sintering

The binder used in BJ AM technique is typically a glycerol based binder, which mainly occupies the interstitial spaces among the powder particles to hold the powder together in the desired shape. In the post-processing step, green part is subjected to binder burnout followed by sintering process, normally in a single step. Particle size distribution and alloy chemistry have a direct impact on sintering kinetics. In solid-state sintering, particle diameter is the main governing factor [70]. Conversely, in super solidus liquid-phase sintering regime, both particle diameter and liquid volume fraction control the sintering kinetics. Liquid volume fraction is the overriding factor. The alloy chemistry is a significant factor in selecting the optimized process temperature [70]. It is important to determine a correct sintering set temperature to obtain full density and sufficient mechanical properties. Frykholm et al. [78] suggest that 316 L SS green parts are required to be sintered at a temperature close to solidus temperature (1360–1380 °C) and in

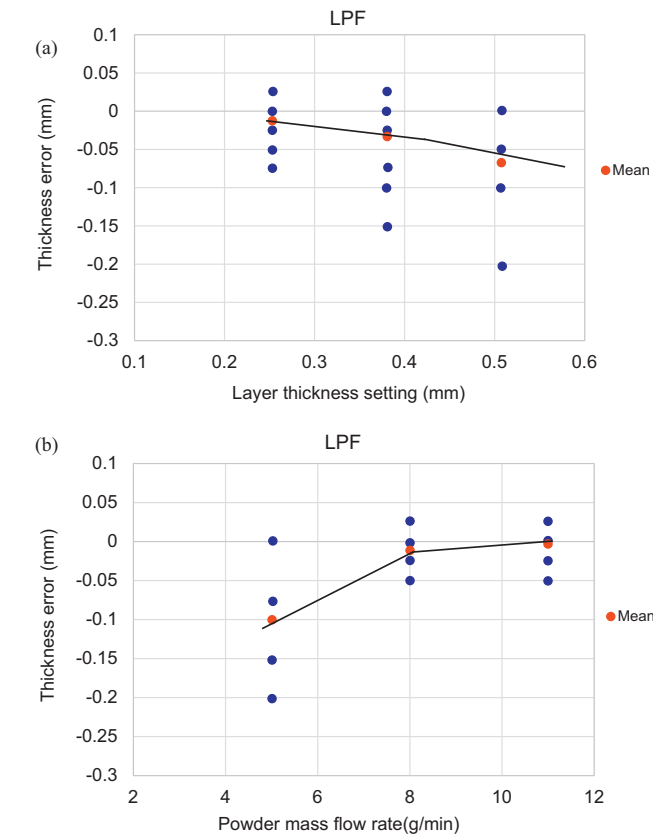
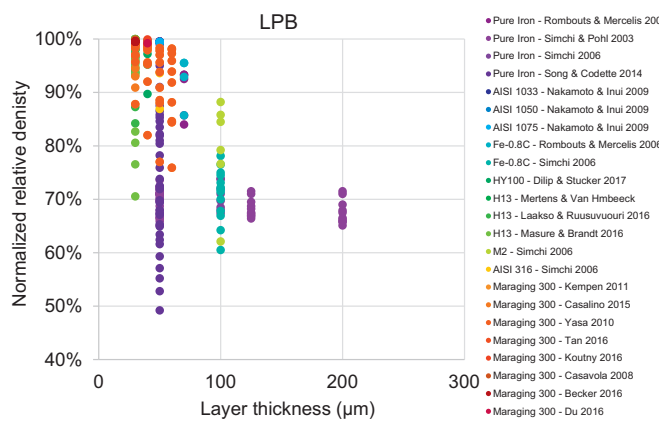


Fig. 15. Influence of layer thickness on relative density in LPB for different steel alloys [56,77,81–88].

Fig. 16. Impact on layer thickness error, in relation with, (a) layer thickness value, and (b) powder mass flow rate for H13 tool steel processed with LPF, adopted from [90].



vacuum with a partial pressure of Ar. This setting decreases the level of Cr loss from the surface, and preserves the corrosion resistance of the steel. In addition, sintering at high temperature leads to the formation of delta-ferrite, which is favorable for mechanical performance and corrosion resistance. After cooling, some residues of ferrite remain in the material; however, the impact of the low amount of delta-ferrite (up to 8%) is somewhat negligible. To yield higher densities, the sintering temperature could be increased, but this is not generally recommended as the higher temperature might affect tolerances. In this review, sintering temperature/melting temperature (T/T_m) is defined as a key parameter for post-processing of components processed through binder jetting 3D printing. From the review work as plotted in Fig. 18; it is stated that higher relative densities are achieved when the T/T_m is in the range of 0.8–1, with the highest relative density of 99.8 attained at $T/T_m = 0.89$. Vacuum sintering is another option to improve the final density by eliminating trapped air inside the samples [98].

4.3.2. Sintering additives

In BJ, it is known that incorporation of sintering additives into the base material enhances the densification and final structural integrity [97]. Sun et al. [99] demonstrated the effectiveness of adding silicon nitride (Si_3N_4) on density, dimensional accuracy, and mechanical properties for 3D printing processed 420 SS in a series of sintering conditions. From their work, it is evident that the 3D printed parts with additives can achieve a high relative density (~98%) and excellent mechanical properties (~200 GPa) with a slight distortion after sintering at 1300 °C. However, because of the large amount of silicon nitride (12.5 wt% ~28 vol%), the part is not considered to be a 420 SS anymore.

Among the various sintering additives, boron (B), carbon (C), and nitrogen (N) are the most effective elements to reduce the liquidus temperature, as shown in Fig. 19 [98]. For example, addition of 4 wt% B in iron (Fe) can reduce the eutectic point to 1174 °C in Fe-B phase diagram [98]. The sintering process is enhanced by the transformation of a solid to a liquid phase. With the adequate volume of liquid phase in the green part, sintering temperature is reduced and the sample density is improved whereas the excessive formation of liquid phase substantially destroys the sample shape. In powder mixture of SS and B, the liquid phase starts to occur from the location of high concentration of B and dissolves the neighboring SS powders as the liquidus temperature lowers the sintering temperature. However, the higher concentration of sintering additives causes the formation of extensive liquid phase to lose the intended sample shape and can lead to the formation of pores [97].

4.3.3. Infiltration of nanoparticles into porous BJ printed parts

Another strategy to improve the density of BJ parts involves the incorporation of nanoparticles into the inkjet fluid to fill the void spaces

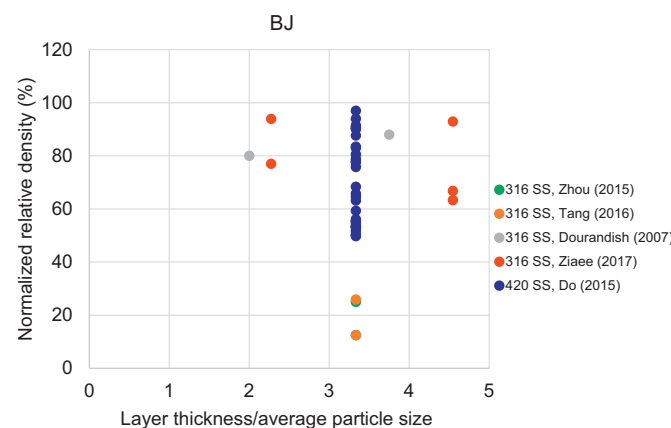


Fig. 17. Effect of layer thickness/average particle size on relative density of BJ 3D printed parts [21,22,69,71,97].

between the powder particles. However, nanoparticles may have impact on viscosity of the binder being jetted to make inkjet deposition challenging or impossible [18]. Following this approach where nanoparticles behave as a sintering additive, objects with densities up to 86.8% are achieved as void filled nanoparticles increases the packing factor of the powder bed [101]. Addition of metal nanoparticles will improve mechanical properties and dimensional accuracy, decrease the sintering temperatures, and offer multi-functional aspects to 3D printed parts; for example, thermal and electrical conductivity [101].

The chosen nanoparticles should be compatible with the composition of final parts, thus not negatively impacting the final material properties. Increasing the packing factor of the powder bed by incorporating nanoparticles was first adopted by Crane et al. [102], where iron nanoparticles dispersed in an organic solvent were employed to improve the quality of 3D printed 410 SS. Iron nanoparticles are excellent candidate for steel parts since addition of several percent more iron nanoparticles impacts slightly on the part composition.

During heating, the nanoparticle deposits, and sintering of nanoparticle toughens the bonds between particles, followed by shrinkage of deposits, which is schematically shown in Fig. 20. The differences in shrinkage kinetics between the associated powder and the products can cause cracks, which can be repaired by reapplying the nanoparticles, then the newly formed cracks are smaller than the previous ones.

In another attempt, Elliott et al. [101] infiltrated 316 L stainless steel 3D parts by 316 nanoparticles. The nanoparticles were suspended in water mixed with two liquid polymer carriers, diethylene glycol (DEG) or ethylene glycol (EG), and deposited drop-wise to a sintered 3D printed binder jetted part. This process depends on pH and molar ratio of water and polymers. The higher polarity of DEG compared to EG at a pH level of 11 and a DEG/H₂O molar ratio of 1:4 leads to the enhancement of dispersion and infiltration of nanoparticles in the 3D parts and subsequent increase in mass and density followed by sintering.

Bailey et al. [18] produced a nanoparticle, binder, and powder system that is more comparable to the BJ process by suspending copper nanoparticles in binder and adding the mixture to the 430 SS powder. Nano copper was selected only because it provides contrast with powder particles, which helps to distinguish the location of the nanoparticles inside the part. The quantity of nanoparticle parent solution is determined based on the parent solution's packing factor and targeted fraction of void space between skeleton particles [18].

However, incorporation of nanoparticles introduces dimensional instability, because of shrinkage and creep; especially at high infiltration temperature of steel [102]. To minimize creep deflections during infiltration, parts were packed with refractory powder; which is also challenging for complex shaped parts. Also, the shrinkage difference between the packing powder and parts may cause tearing during sintering. Moreover, at higher nanoparticle contents, a substantial foaming or void expansion occurs during curing. This is because the

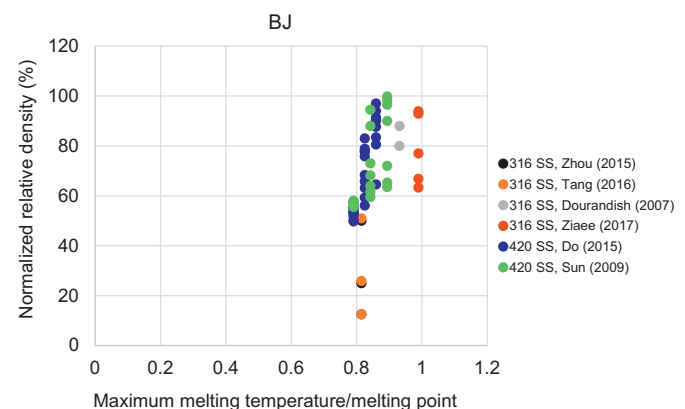


Fig. 18. Influence of maximum sintering temperature/melting point on relative density of 3D printed parts by BJ [21,22,69,71,97,99].

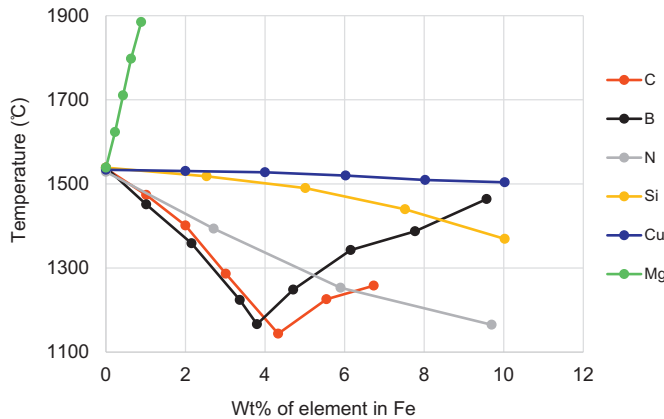


Fig. 19. The liquidus lines for various elements in Fe [100].

nano-particles occupy the voids in between the bigger particles and prevent the solvent in the binder from escaping, thus creating large cavities/visible porosities in the parts. On the other hand, the presence of nano-particles becomes more evident between the larger SS particles leading to an increase in the sintering of SS due to the nano-copper behaving as a sintering aid [18].

4.3.4. Liquid metal infiltration

Another route of densification is by the infiltration of liquid-metal, with negligible dimensional changes. Therefore, in BJ technique, metal parts are usually infiltrated with a low melting point material such as bronze in order to remove residual porosity and obtain full density [97,103]. This manufacturing process counts on capillarity of the infiltrant material to be absorbed by pores on the surface [103]. Infiltration changes the nature of the material while filling the pores of the printed material which slightly enhances the mechanical properties including hardness, elastic modulus, yield strength, etc. [17,97].

Sachs et al. [103] made an attempt to fabricate injection molding tooling of 316 SS, where cooling channels were conformal with the molding cavity. They introduced a new technique called “stilt infiltration” which assures that the channels would be free of infiltrant with almost no under-infiltration or over-infiltration of the part and clogged passages. Also in the process, the sample was raised on the top of the infiltrant surface, which created a negative pressure in the infiltrant causing the infiltrant to be kept out of the cooling channels. From this approach, it is assured that passages will not be filled above some

critical range. During infiltration, channels should be placed horizontally, in a way to maintain the capillary rise between parallel walls. If the infiltrant angle with respect to the walls is close to zero, then the capillary rise is given by the following [103],

$$h = \frac{2\gamma}{\rho g \omega} \quad (3.15)$$

where ω is the spacing between the walls, for the molten infiltrant, h is the capillary rise, γ is the surface tension, ρ is the density, and g is the acceleration of gravity.

Cordero et al. [104], also fabricated a dense ferrous alloy by infiltration of molten bronze, which showed higher rupture strength by eliminating stress concentration between the particle necks.

The optimum saturation of infiltrant liquid is significantly important to manufacture a standard green product. If the liquid infiltrant exceeds the saturation level, dimensional accuracy will be destroyed by the migration of excess infiltrant. On the other hand, lack of infiltrant can cause weak bonding between particles. Therefore, precise estimation of infiltrant saturation is vital for the design of BJ printed parts.

5. Potential defects

5.1. Cold and segregation cracking

Cold cracking susceptibility is proportional to hardenability, where carbon equivalent (CE) is defined as [105]:

$$CE = \%C + \left(\frac{\%Mn + \%Si}{6} \right) + \left(\frac{\%Cr + \%Mo + \%V}{5} \right) + \left(\frac{\%Cu + \%Ni}{15} \right) \quad (4.1)$$

The high carbon steel contains a continuous phase like martensite, whereas in SS, continuous phase is often retained austenite, which prevents cracking. Cracking is worst in M2 and H13 steel that can be blocked by preheating to partially or fully suppress martensite formation. In LPB, rapid solidification is insufficient to suppress segregation but generally results in fine microstructure. Also, low melting phase is sufficiently discontinuous to avoid segregation cracking. This type of phenomena is observed in high copper alloy 17-4 PH SS [106]. The crack formation is also reported in the LPB processed high silicon steel (6.9 wt%), which was influenced by higher laser energy input [45].

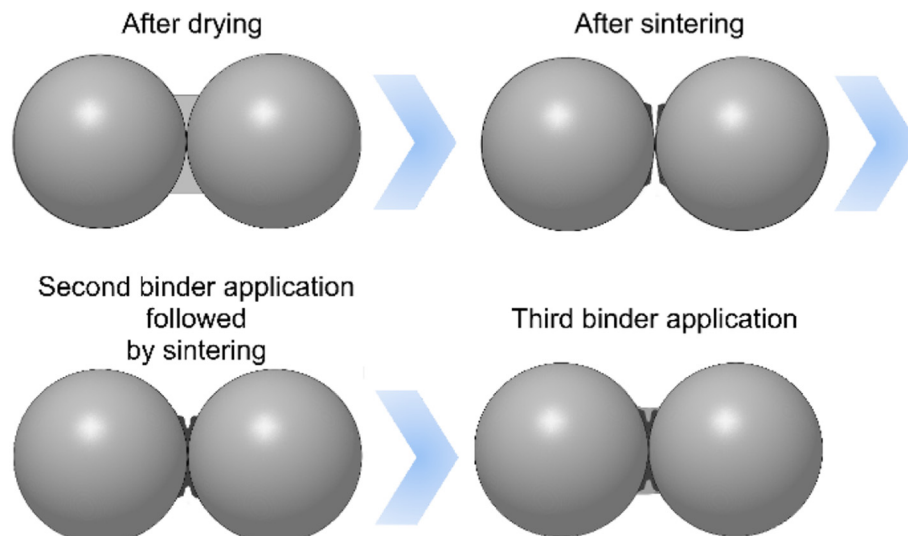


Fig. 20. Multiple application of nano-binder to enlarge the bonds and disappear the cracks generated during sintering [102].

The faster melting and solidifying rates in both LPB and LPF techniques result in a deposited layer with higher residual stresses and consequently cracking [107]. LPB introduces tensile residual stresses because of the localized input of high laser energy in a very short period of time, and together with the lower thermal conductivity of the powder, a higher temperature gradient is developed near the laser spot [45]. Consequently, the expansion of the heat affected zone is repressed by the neighboring material, which usually causes plastic compression. Again, during the cooling, the contraction affinity of the upper layers is neutralized by the subsequent layers, which cause tensile stresses that are major source of cracking.

In comparison between austenitic SS and low-carbon steels, the former is more sensitive to solidification cracking than the later one because of their lower thermal conduction and higher thermal expansion coefficients. Moreover, some contaminants like sulfur and phosphorous have a profound impact on cracking in SS. Table 2 shows the cracking behavior of different water/gas atomized 316 SS powders linked with impurity amount. The cracking sensitivity becomes less by decreasing S + P + Si content. It is also claimed that, a considerable nitrogen value is harmful to solidification cracking [108].

5.2. Porosity

Generally, in AM, it is believed that the tendency of pore formation can be diminished (or controlled) by optimizing the process parameters, i.e. laser scan speed or laser power [109,110]. There are various reasons behind the formation of interlayer porosity including; (i) mismatch between mechanical properties of the underlying layer, (ii) mismatch between thermal elongation due to sharp temperature distribution in the deposited material, (iii) enclosed gas entrapped in the melt, (iv) chemical reaction between different feedstock etc. [111–113]. It was observed that low ductile materials show a greater tendency to interlayer porosity [112]. A recent study suggests that specified critical level of porosity and gas content in the starting powder has a profound impact on the interlayer porosity formation. Choi et al. [90] statistically investigated the pore formation in AISIH13 tool steel and concluded that the powder feed rate is a considerable factor, influencing porosity [114].

Primarily two types of porosity are considered: (1) gas porosity; resulted from encapsulated gas due to incomplete melting of particles with internal-porosity, and (2) lack of fusion (LOF) porosity due to voids that create among unmelted or incompletely melted powder particles. The former can be resolved by using powders free of gas porosity, while the latter can be prevented by complete melting of the powder [115]. It is worth considering that LOF is the most detrimental flaw as it may act as a crack initiator as well as lead to a complete failure. Careful selection of process parameters should be considered in order to diminish crack formation and propagation [111,116].

Table 3 represents the impact of both laser power and powder feeding rate of H13 tool steel on pore formation in the LPF process. The results indicate that only powder feed rate is a crucial factor for the porosity formation in H13 tool steel. Also, as seen, in case of higher powder feed rate, porosity level can be reduced with increasing the laser power input. It should be noticed that achieving a desirable quality can be challenging. For example, obtaining actual layer thickness is more probable at a higher powder mass flow rate, but on the other hand, chance of pore formation is increased [90]. By optimizing the layer thickness of single clad tracks with adequate energy input, the porosity may be eliminated. In addition, choosing a suitable overlap between tracks can be another effective solution to reduce porosity.

A research work on H13 tool steel demonstrated that with a lower energy input, the overlap should be >50% [90]. In another work on H13, it is pointed out that acceptable layer thickness is <0.7 mm, and the ratio of energy/mass must be higher than 40 KJ/g to avoid pore formation [91]. In addition, the higher nominal specific energy can result in the lower pore/void formation. Also, Fig. 21 represents the specific

Table 2

In LPF, cracking behavior of various 316 SS powders related to impurity content, adopted from [108].

Different 316 SS powders	Fabrication method	S + P (Wt %)	S + P + Si (wt%)	N content	Cracking
316 SS-1	WA ^a	0.02	2.25	0.047	✓
316 SS-2	WA	0.125	1.445	–	✓
316 SS-3	GA ^b	0.023	0.553	0.062	✗
316 SS-4	GA	0.041	0.541	0.09	✓
316 SS-5	GA	0.035	0.475	–	✗
316 SS-6	GA	0.044	0.384	–	✗

^a Water atomized.

^b Gas atomized.

energy vs. porosity obtained from the literature on H13 tool steel with relevant normalized powder feed rate [117]. The normalized powder feed rate (ζ) is defined as:

$$\zeta = \frac{4m}{\pi d^2} \quad (7.1)$$

where, m is powder feed rate (g/s) and d is laser spot diameter on the substrate surface.

Table 4 shows the summary of the effect of various parameters on porosity level in different steels. The behavior of porosity in both 420 and 4140 low alloy steel has been investigated in several experiments.

For 420 SS, the linear mass density ($\frac{m}{d}$) which is the ratio of powder flow rate (m) divided by the laser traverse velocity ($v = \frac{d}{t}$) has been used to identify a proper combination of powder feed rate and laser traverse velocity to result in a fully dense part.

Fig. 22a shows that there is an optimal linear mass density, ($\frac{m}{d}$)*. At a lower value, no porosity is observed, and at a higher value, the porosity increases linearly with increasing linear mass density. For the 420 SS deposited on a 420 SS substrate, the critical linear mass density is 0.0115 g/mm to arrive at a full density part [115]. This optimal amount for 4140 SS on a 1045 steel substrate is approximately 0.018 g/mm, as shown in Fig. 22b. It can be seen that there are many combinations of powder flow rates and laser speeds to obtain a fully dense specimen. Values out of the optimal mass density range lead to lack of fusion porosity [115].

6. Microstructure development

6.1. General microstructural characteristics in AM ferrous alloys

In both LPB and LPF processes, the manufactured parts are usually pass through the complex thermal cycles; (i) rapid heating due to the absorption of laser energy, (ii) fast solidification of the melted region in the absence of heat source, (iii) substantial temperature gradients, (iv) accumulated heat and (v) reheating/recooling due to the laser energy in the adjacent layers/tracks. The frequent re-melting and re-solidifying progressions are continued when the subsequent layers are exposed to heat [10,120,121]. While non-equilibrium thermodynamics govern the physics of the microstructure formation in LPF and LPB, thermal cycle depends upon many process variables, hence predicting the microstructural characteristics of AM components, and the impact of process parameters on them, is still poorly understood.

Table 3

Influence of powder mass feed rate and laser power on porosity in H13 tool steel made by LPF [90].

Laser power (W)	1400			1200			1000		
Powder feed rate (g/min)	5	8	11	5	8	11	5	8	11
Porosity (%)	0.08	1	1.8	1.3	1.1	3	1	2.5	11

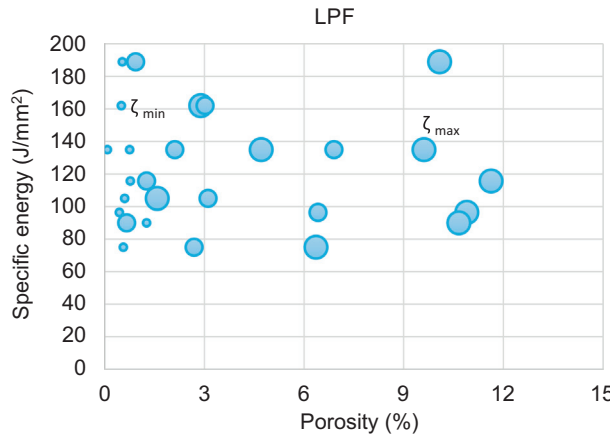


Fig. 21. Specific energy versus porosity in H13 tool steel with relevant normalized powder feed rate for LPF [117].

In general, the microstructure in AM is developed based on the above defined thermal history, where three main grain morphologies are observed in steel processed by AM: (i) columnar, (ii) mixture of columnar and equiaxed, and (iii) equiaxed. In other words, the AM processed steel typically show three different regions; (i) interface region, (ii) columnar grain region and (iii) equiaxed grain region. The predilection of microstructure is governed by a crucial control parameter proposed by Hunt [122], based on related solidification theory; the ratio of temperature gradient G and the solidification velocity V_s , i.e. G/V_s . In an extremely large G/V_s , when V_s tends to zero, the solidification microstructure contains planar grains. In a relatively high value, the predominant solidification microstructure would be columnar dendrites and smaller G/V_s value gives rise to equiaxed grains. In LPB, the heat is mostly transmitted through the formerly deposited layers, and develops the highest temperature gradient in that direction, which eventually influences the formation of directional columnar dendrites.

However, this may not be the case for LPF as the melt pool transverse angle with respect to the substrate (θ_s) can vary from 30 to 70° that can change the solidification rate by a factor of $\cos(\theta_s)$ [32]. If the temperature gradient becomes alike in some directions, grains tend to grow in that directions and become equiaxed. A schematic of solidified melt pool with different zones is shown in Fig. 23a. The melt pool consists of equiaxed grains in Zone I and columnar grains in Zone II, also shown in Fig. 23b. The shape and growth of dendrites are different at different layers based on the heat dissipation, as depicted in Fig. 23b.

During the LPF process, bottom layer is heated for a long time which may cause tempering effect and the accumulated heat can result in dendritic growth. On the other hand, at the top layer because of rapid cooling rate dendrites solidify very quickly and have no time to grow coarsely. Also in the LPB process, the microstructure developed is complex because of continuous re-melting process and the Marangoni effect that causes different heat flow directions in the same melt pool. This phenomenon eventually creates different grain growth orientations [123]. The higher thermal gradient, i.e. 10^6 K/m in the LPB process causes columnar microstructure in most of the materials [124]. Moreover, in LPB, the temperature gradients are interrupted by thermal

conductivity of powder as well as solidified zone [125]. As the heat dissipation through the build direction is higher compared to the other directions, solidification in that direction results in anisotropy in grain morphology and mechanical properties. Also in LPB and LPF, cooling rates tend to be high because the area that laser beam heats up is relatively small. Therefore, small heat affected zones and finer microstructures can be obtained in comparison with conventionally cast samples [122,126]. Yadroitsev et al. [127] explored that the 316 L SS processed with LPB presented higher yield strength compared to the forged materials. This statement is supported by Song et al. [37], where he stated that, the better mechanical property of LPB processed samples was due to the presence of smaller grains and higher dislocation density, associated with rapid solidification.

6.2. Solidification and phase transformation in AM steels

The phase transformation and microstructure development in AM processed steels are completely different compared to the conventional cast steels, which pass through slower cooling rates as well as gradual/equilibrium thermo-mechanical processes after casting to obtain more homogeneous material properties. Austenitic SS, (e.g. 316 L and 304) usually shows a completely austenitic microstructure in AM processed steel. Sun et al. [128] employed a detail microstructural characterization in LPB processed austenitic SS 316 L, where two main phases were identified as primary austenite (fcc γ) and small amount of retained ferrite (bcc δ) without any formation of martensite. However, Tucho et al. [129] identified traces of martensite and/or ferrite phases in austenite matrix in LPB processed 316 SS. Zhang [126] observed complete austenite phases in LPF of SS 316 L, but some ferrite phase was also observed by Yadollahi et al. [130]. Also, in LPB processed austenitic SS 304, similar elongated grains in building direction and complete austenite phase with no carbide precipitates were observed [131]. Similar austenitic phase with columnar structure is reported by Yu et al. [132], in LPB processed 304 SS. In this work, the mechanical anisotropy was compared between LPB processed 304 SS and Ti-6Al-4 V alloy, which is related to microstructure morphology governed by directional solidification. During the fast cooling stage involved in LPB processed SS 316 L, the high-temperature ferrite phase was not transformed to a low-temperature austenite phase. This retained ferrite phase eventually strengthens the austenitic matrix. For similar composition of Cr and Ni in SS up to Cr/Ni ratio of about 1.5, the solidification microstructure mainly contains austenite phases [133].

The microstructure of the conventional martensitic SS fabricated in the AM process is found to form some austenite phases together with martensite, which is stated for 17-4 PH SS, maraging steel (18Ni300), and also for the martensitic SS grade AISI420. 17-4 PH steel fabricated through the LPB process contains a significant amount of retained austenite with body centered cubic (bcc)/martensite and fine niobium carbides (NbC) favorably arranged through dendritic boundaries [106]. According to Cheruvathur et al. [106] during solidification of AM 17-4 steel, from the liquid the first phase is formed as: bcc/ferrite followed by bcc + fcc/austenite. Also, some MC phases enriched with Nb is formed. When solidification is roughly completed, the fcc turns as the major phases, and at the end of solidification, approximately equivalent amounts of bcc and fcc phases and small amount of NbC are detected.

Table 4

Influence of some process parameters on porosity of steels made by LPF.

Material	Resulting porosity	Mass flow rate	Laser power	Specific energy	Thickness	Stability of flow rate	Scan speed	Linear mass density
H13 tool steel [90]	↑							
H13 tool steel [90]	↓	↑						
H13 tool steel [117]	↓		↑					
316 SS [118]	↓				↑			
316 SS [114]	↓					↑		
316 SS [119]	↓						↑	
420 SS [116]	↑							↑

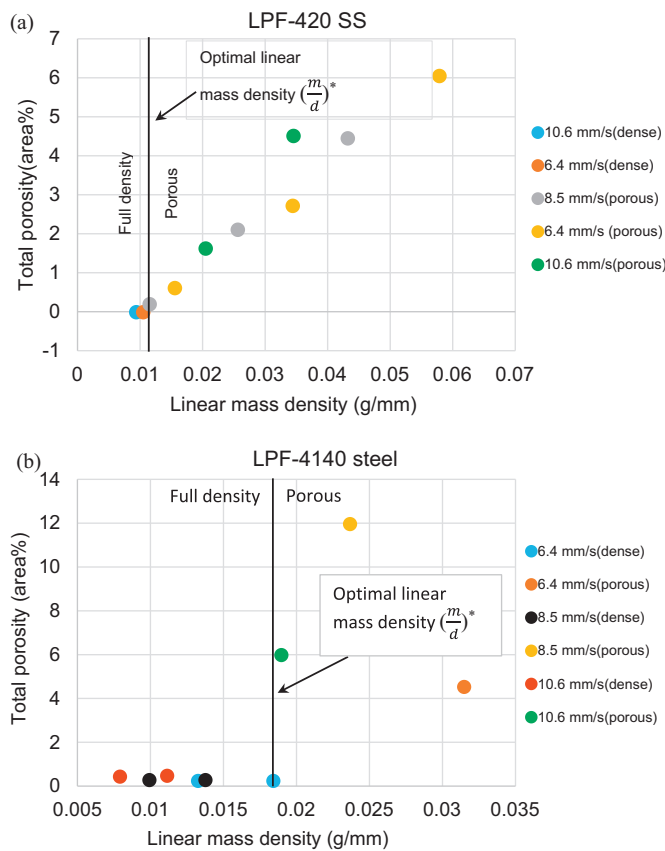


Fig. 22. Variation of total porosity with (a) linear mass density for various laser velocities in 420 SS, and (b) in 4140 steel made by LPF, adopted from [115].

Facchini et al. [134] worked on LPB of 17-4 PH steel and reported a microstructure consisting of austenite and martensite phases, with both twinned and un-twinned regions adjacent to the martensitic grains. The retained austenite is observed among the martensite plates. Kudzal et al. [135] and LeBrun et al. [136] examined the same phenomenological phase structure in 17-4 PH SS. During the cooling stages in LPB, the residual thermal stresses in the material cannot transfer all austenite to martensite, which result in retained austenite [136]. Mainly retained austenite forms at grain boundaries, because of the irregular atomic arrangement, which stops further growth of martensite [137]. Therefore, finer grain sizes enclosing more grain boundaries may influence the occurrence of more retained austenite in LPB of 17-4 PH SS. Al-Mangour et al. [138–140] worked on the LPF processed 17-4 SS, and reported on the microstructural phase transformation during shot-peening (SP) and heat-treatment. From their experiment, the retained austenite of

as-built sample passed through the SP process and possessed martensite phase transformation [139]. Their another study also explored microstructure development at different aging temperatures, where fractions of retained austenite was observed at 866 K but showed fully martensite at lower temperature of 755 K [138].

For both LPB and LPF processes, maraging steel grade 18Ni-300 shows similar tendency to form cellular/dendritic structure and epitaxial growth of the solidified grains [77,141]. This martensitic SS has a considerable amount of retained austenite and upon aging precipitation, together with austenite reversion is occurred [77,141,142]. The austenite reversion is expected during long period of aging, because the metastable martensite converts to stable austenite. During the aging process, Ni is released into the Fe matrix and convoys the conversion from Ni₃ (Mo, Ti) to further steady Fe₂Mo precipitates, which stimulates austenite reversion [143]. Campanelli et al. [144] investigated the microstructural morphology in 18Ni (300) maraging steel clad produced on AISI 304 substrate in the LPF process. The presence of equiaxed and elongated grains also with dendrite morphology were alike to that observed by Casalino et al. [88] in the LPB process of maraging steel. Their work revealed a microstructure with fine martensite phases and a transformation of austenite to Fe-Ni martensite. Austenite reversion is also explored by Krakhmalev et al. [145] in LPB processed AISI 420 martensitic SS. The top layer revealed martensite and retained austenite in contrast to inner layer where tempered martensite was present with higher volume of austenite. The LPB process is a multi-step technique containing repeated thermal cycles (melting-solidifying), which then believed to cause stabilization of austenite by rearrangement of carbon between martensite and austenite. Their selective diffusion result in the austenite reversion and consequent growth of retained austenite. In another investigation of martensitic SS SC420 processed in LPF [146], showed tempered martensite with fine carbides and ferrite along the grain boundary.

Mertens et al. [35] worked on LPB processed H13 tool steel, and reported a significant observation in microstructure development with different powder bed pre-heating temperatures. The microstructure after preheating at 200 °C, is comparable to the microstructure obtained without preheating which constitutes a martensitic phase as well as retained austenite. After preheating at 400 °C, which is above the martensite transformation temperature will produce bainite; an intermediate form between martensite and pearlite. Yan et al. [132] also reported martensitic phases decomposed into α-Fe and Fe₃C with retained austenite in the LPB processed H13 tool steel. During LPF of H13 tool steel, the microstructure morphology is columnar to equiaxed grains and most of the grains contain martensite phases [90,91].

During LPB of a high strength low alloy steel, e.g. HY100 [39], the microstructure in the molten region after solidification is fully austenitic; that completely converts to martensite (untempered) by rapid solidification. It is already reported in many work [147,148] that HY100 steel with lower carbon content and higher Ms. (406 °C) and Mf (221 °C)

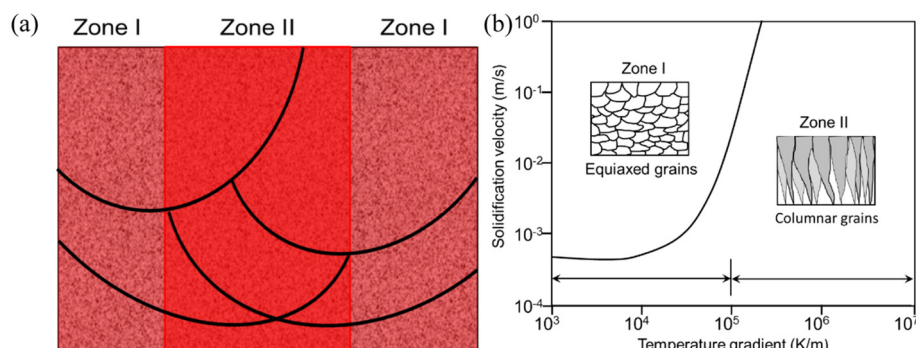


Fig. 23. (a) Schematic of the melting (Zone I) and re-melting zones (Zone II) in the melt pool, (b) the plot shows different temperature gradient regions to form columnar and equiaxed grains, with relation to solidification velocity for 316 SS [126].

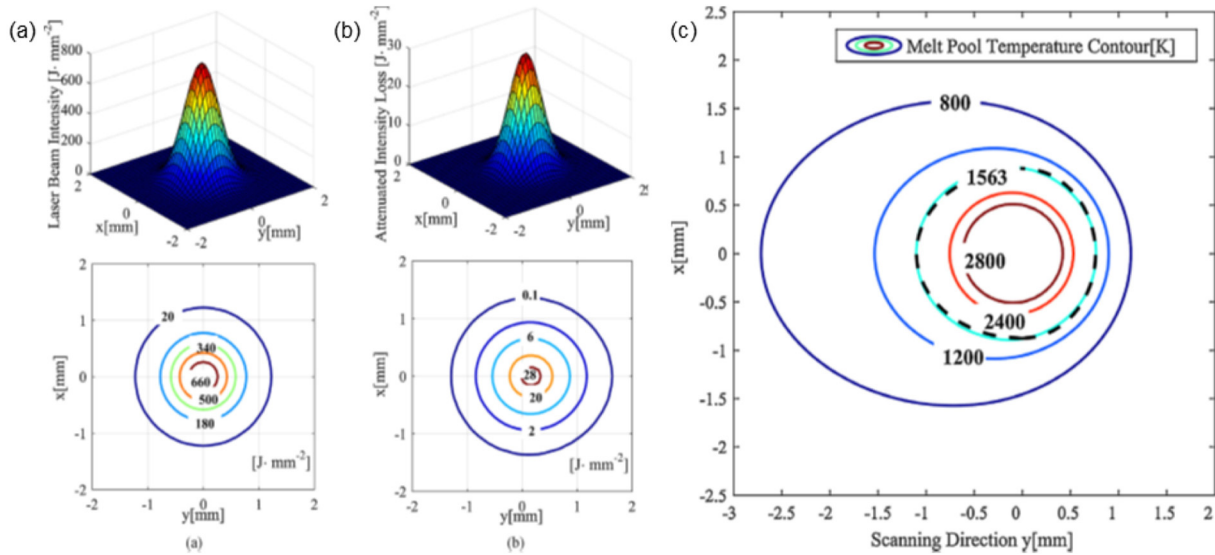


Fig. 24. Laser beam intensity distribution on the substrate surface (a) without attenuation (b) attenuated laser intensity loss by the powder and (c) temperature distribution in the melt pool on the Inconel 625 substrate surface [157] [reproduced with permission from Elsevier].

temperatures produces lath martensite and complete transformation of austenite to martensite. The standard heat treatment at austenizing temperature followed by quenching and tempering form tempered

martensite with variation in lath size. In steel, tempering causes carbon to diffuse out of supersaturated martensite, and reacts with Fe, Cr, and Mo to form carbides in the matrix of martensite.

Table 5

A summary of the input parameters and outputs employed for the modeling of different AM processes where ferrous alloys are used.

Materials/process	Input parameters	Output	Max. percentage difference
SS 303 L/LPF [155]	<ul style="list-style-type: none"> - Laser pulse energy - Laser pulse frequency - Laser pulse width - Laser beam diameter - Thermal conductivity - Specific heat capacity - Melting temperature - Density 	<ul style="list-style-type: none"> - Temperature field, - Melt pool depth and dilution 	In agreement with the experimental results
AISI 4340//LPF [165]	<ul style="list-style-type: none"> - Powder feed rate - Laser power on the substrate - Ambient temperature - Radius of the powder jet - Melting temperature - Radius of the laser beam - Process speed - Absorption factor 	<ul style="list-style-type: none"> - Shape of each deposited layer - Temperature distribution across the part 	In agreement with the experimental results (~23% between the third and fourth layers)
AISI-D2 AISI-316 L/LPF [166]	<ul style="list-style-type: none"> - Mass flow - Particle shape - Size distribution 	Particle flux	<15%
SS 304 L/LPB [167]	<ul style="list-style-type: none"> - Laser power - Hatch spacing - Point distance - Laser exposure time - Effective scan speed - Laser diameter - Optical penetration depth - Reflectance of SS304 L - Number of laser tracks 	<ul style="list-style-type: none"> - Temperature history - Melt pool size prediction - Microstructure formation 	Max error: 4% in width Max error: 30% in depth (Dependent on laser power)
316 SS/LPB [168]	<ul style="list-style-type: none"> - Laser power - Melting point - Latent heat of melting - Specific heat of the solid phase - Specific heat of the liquid phase - Thermal conductivity of dense material - Thermal conductivity of powder 	Local temperature distribution in the laser-powder interaction zone	
316 SS/LPB [169]	<ul style="list-style-type: none"> - Laser power - Scan speed - Energy density 	<ul style="list-style-type: none"> - Melt pool cross section and dimensions 	<ul style="list-style-type: none"> - 8.2% in width - 2.9% in depth

For high carbon steel 4140 in the LPB process [149], the microstructure constituents are obviously finer compared to the wrought 4140 steel and show martensite and bainite dominate phases. Because of the rapid solidification of the melt pools, similar martensitic phases with fine microstructure are observed in 4340 high-strength low alloy steel [53].

7. AM modeling for ferrous alloys

Modeling of AM processes is extremely important for the process parameters optimization and to provide prediction of residual stresses and microstructure evolution in 3D printed parts. Three categories of models can be found in literature: numerical, analytical and empirical. In LPB and LPF processes, melt pool formation [150], laser particle interaction process [151], temperature, velocity and thermal stress field distributions over the process, can be simulated by numerical models [152–154]. Analytical models take into consideration the physics of the processes and the process optimization. In the literature, analytical models have been employed to predict the melt pool depth, dilution and the temperature field with known values of clad height and width [155]. In their work Fathi et al., used a parabolic equation to build the melt pool's top surface and the temperature field was predicted solving the heat conduction in substrate based on an infinite moving point heat source [155]. Tan et al. [156], estimated the clad layer geometry based on a moving disc heat source model. An ellipse was used to fit the melt pool and the powder catchment efficiency was calculated as the ratio of melt pool and the powder stream area. Most of these models have different prediction accuracy, since they have either decoupled the heat and mass flow interactions in the LPF process or did not take into consideration the changes of the laser power absorptivity [157]. Huang et al. have developed an analytical model for LPF that combines the main physical changes of the whole process with the attenuated laser power, the heated powder stream and the semi-infinite substrate taking in consideration their intensity spatial distribution and concentration [157]. The original laser beam intensity distribution on substrate is shown in Fig. 24a, with maximum value of 660 J/mm², while the attenuated laser intensity loss of around 28 J/mm², by the powder is shown in Fig. 24b [157].

The temperature field on substrate surface, shown in Fig. 24c, was obtained coupling the attenuated laser beam and the heated powder stream that is considered the moving heat source. Two half ellipses were used to approximate the melt pool projection geometry on the substrate surface, and are displayed as dashed lines in Fig. 24c.

The modeling and simulation of LPB-AM are mostly based on numerical models, which incorporate multi-physics by means of Lattice Boltzmann method [158] or the Lagrangian-Eulerian method [159] and cover either the hydrodynamic or the thermodynamic aspects.

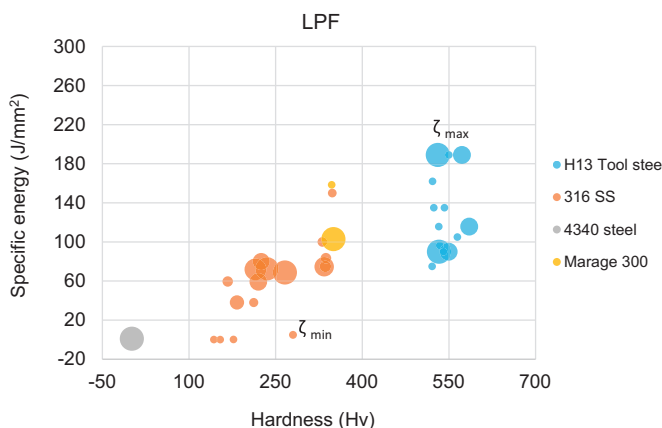


Fig. 25. Specific energy versus hardness of steels shown with equivalent normalized powder feed rate values with, $\xi_{\min} = 218,269.6$ and $\xi_{\max} = 478,114.4$. [176–179].

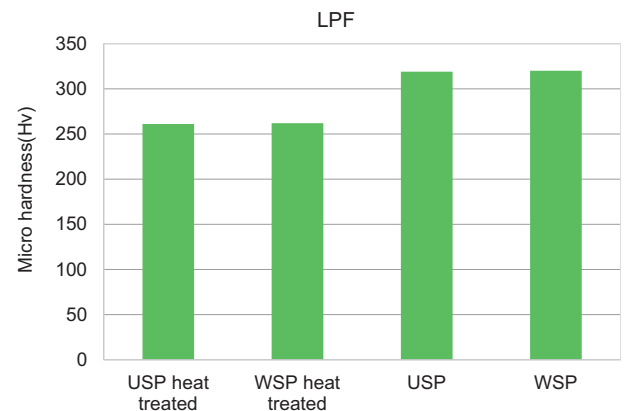


Fig. 26. Hardness distribution of 316 SS at different laser scanning strategies (unidirectional (USP) and weaving scanning path (WSP)) [184].

Empirical modeling are more time-efficient [160] compared to the numerical models, but are case sensitive, while numerical models requires high computation to capture the complex phenomena in the molten pool [157]. Numerical modeling of the LPB process consists of simulations at the micro level (melt-pool modeling) and at the macro level (part-level simulation). At the melt-pool modeling level, multiple physics phenomena should be considered: heat conduction, heat convection and radiation, capillary effects, Marangoni effect, photon absorption by particles [161]. Panwisawas and coworkers [161], taking into consideration most of the interfacial phenomena in their model, they derived the temperature distribution of single-track molten zones. It was demonstrated that the irregularity of the single tracks increased as the laser-scan speed increased. Regarding part level simulations, analytical and numerical modeling has been used to study the residual stresses in the LPB processes [162] and to investigate the temperature and stress distributions in one single layer in LPB [163]. Analytical models, do not incorporate the multi-physics, and are less common due to the more complex physics behind the LPB AM process. For instance, the model proposed by Knol [164] describes the process parameters effect on the residual stresses and the porosity through a semi-analytical thermal model. In their model, the authors build the powder bed temperature field adding the analytical temperature solution together with the numerical boundary correction solution.

Although there are many modeling papers for LPF and LPB, the number of modeling papers in which the target materials are ferrous alloys is limited. A summary of the input parameters and outputs employed for the modeling of different AM process, where ferrous alloys used for model verification and process parameters prediction, is presented in Table 5.

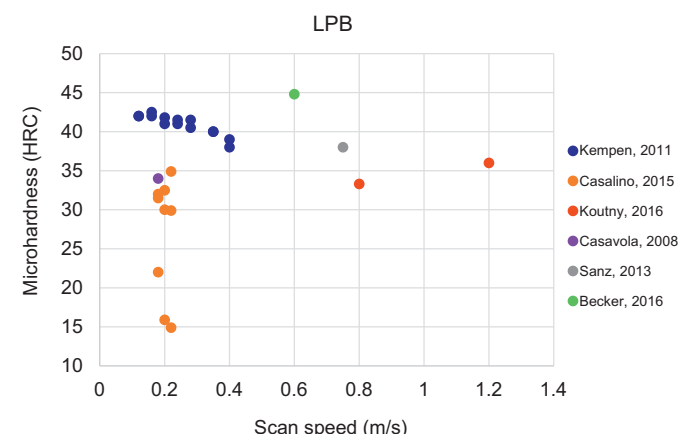


Fig. 27. Influence of scan speeds on microhardness [77,84,85,87,88,189].

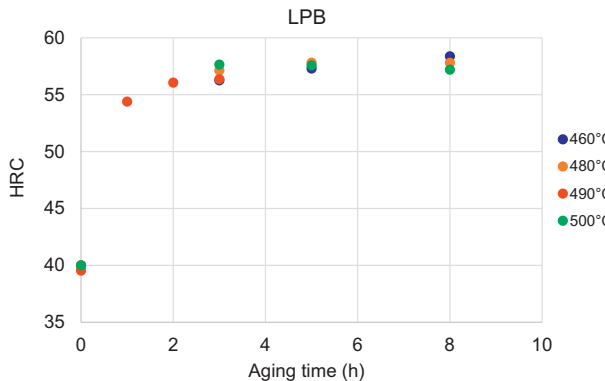


Fig. 28. Influence of different aging parameters on micro-hardness [77,80].

8. Mechanical characteristics

8.1. Hardness

8.1.1. Hardness for LPF processed parts

In the literature, clearly distinguished microstructure zones with micro-hardness have been reported for LPF processed AISI P20 tool steel [170], AISIH13 tool steel [91,171,172], AISI 420 tool steel [173], AISI 4140 steel [174], AISI 410 SS [109] and AISI 316 L SS [118]. It has been stated that for steels, the micro-hardness values of multilayers decreases from the first deposited layer and then increases towards the top layers [118,174,175] due to the heating up of the previous layers and giving them time to be slightly annealed [91]. Furthermore, this inhomogeneity can be ascribed to the time-changing solidification rate in the melt zone and a relatively slower rate in the central area. As a result, higher micro-hardness has generally been recognized at the top and bottom of LPF parts in comparison with the middle region [10].

In Fig. 25 for different kind of steels, the data for specific energy vs. the average micro-hardness is presented, as obtained from the literatures. From the Fig. 25, shown that, H13 tool steel has the highest hardness among the other steels included in these studies, as expected.

Between the low alloy steels; ASTM/SAE 4140, 4130, and 1045 are anticipated to be the hardest steel because of the higher content of alloying elements, as well as higher carbon content in 4140 and 4130 [180]. In another research work on 4140 steel, hardness was measured at different regions of the clad. The hardness value near the substrate surface was an average of 375 HK500, in the middle of the sample was

330 HK500 and the very last layer showed the hardness of 386 HK500. These hardness values were comparable to other works available in the literature, which associated with the formation of bainite and tempered martensitic [181,182]. In other publication, the hardness values of the deposited 18Ni (300) maraging steel was found between 347 and 350 HV [176–179]. These values are in agreement with the usual microhardness of 18Ni (300) steel after solution annealing heat treatment, as referred in the ASM Handbook [144,183].

In H13 tool steel, the internal part hardness somewhat diminished towards the center and bottom of the sample because of re-heating during the process [91]. Similar behavior was observed for 316 SS, where the Vickers microhardness values of clad surface intensified compared to the inside of the clad, as the clad surface experiences the cooling effect of shielding gas. In addition, for H13 tool steel, hardness values were similar to that of wrought material. However, for 316 SS clad, the hardness is much greater than that of conventional cold-rolled material because of the rapid solidification throughout the LPF process [126].

The impact of inter-layer time interval on microhardness values for 316 LSS was obtained according to the longitudinal axis of the samples, where the hardness amounts represent that the single-built set has lower hardness values (185 HV) even in heat treated condition (157 HV) compared to the nine-built specimens (215 HV). According to this research, the inter-layer time interval and post heat treatment can have an effect on the microhardness values of 316 SS [118]. It is worth mentioning that unidirectional and weaving laser scanning path (USP and WSP respectively) do not extremely influence the microhardness of 316 SS, as evident in Fig. 26. The Vickers hardness values of USP and WSP samples do not show any significant differences. However, as-deposited samples have higher hardness values compared to the heat-treated (1050 °C for 1 h) ones, which is in agreement with other researches [184].

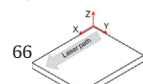
8.1.2. Hardness for LPB processed parts

A broad range of microhardness values for LPB processed 316 SS can be obtained by various scanning speeds and hatch spacing, as recently reported by Sun et al. [128]. The highest value of microhardness reported at an energy volume density of 101.33 J/mm³ was 220 HV [128], while, the annealed SS316 L samples showed a microhardness values between 150 and 160 HV. These microhardness values were lower than the ones reported by Saeidi [185] (320 HV). As reported by Sun [128], this difference might be attributed by the amount of amorphous nano-scale inclusions and the grain size. In particular, smaller

Table 6

Tensile properties of several 316 SS grades processed with LPF and conventional ones.

Ferrous alloys	Process	UTS (MPa)	YS (MPa)	EL (%)
316 SS [15]	Wrought or forged/and annealed bar	586	234	50
	LPF	758	434	46
	LPF-perpendicular building direction (Y)	793	448	
316 SS [193]	LPF-parallel building direction (X)	807	593	30
	Wrought or forged/and annealed bar	578	289	50
316 SS [194]	LPF	661	276	67
	LPF	579	296	41
316 L SS [191]	Wrought or forged/and annealed bar	480	170	40
	LPF	540–560	330–345	35–43
	LPF-parallel building direction (X)	586	241	50
316 SS [126]	Wrought or forged/and annealed bar	639	558	21
	LPF	352	536	46
	Perpendicular building direction (Y)	558	639	21
	Parallel building direction (X)	620–660	405–415	32–40
316SS,single-built(as-built) [130]	LPF	600–620	325–355	42–43
316SS,single-built(heat-treated) [130]	LPF	660–685	465–485	12–20
316SS,nine-built(as-built) [130]	LPF	540–625	330–395	35–85
316 SS [118,190]	LPF			



grain size and larger amount of inclusions lead to higher values of microhardness [128,185].

Another research conducted by Wang et al. [186], showed a correlation between the densification level, which depends on the volume energy density and the grain size. The researchers demonstrated higher hardness values (281.6 HV) at higher densification level, which resulted in more refined microstructures [186]. At increased energy density, a coarsening of the cellular dendrites occurs and leads to a decrease in the microhardness values (267.1 HV) [186]. Similar hardness value of 280 HV, is observed in LPB processed single tracks in 316 L austenitic SS [187].

Recently Rashid and coworkers reported the effect of scan strategy on microhardness of LPB processed 17-4 PH SS [188]. The highest hardness value (458 HV) was measured for the samples fabricated with a double scan strategy compared to the ones with a single scan strategy [193]. This phenomenon was due to the occurrence of lower percentage of retained austenite and a higher percentage of martensite [188]. However, for maraging steel, there is negligible effect of scan strategy on the hardness values, as plotted in Fig. 27, specifically at low scan speeds, and the same trend is reported for layer thickness [77,79,80]. However, at higher scan speeds, a small drop in micro-hardness values is observed.

Aging has a significant effect on the hardness values of LPB processed maraging steel, as shown in Fig. 28, where at 460 °C, the hardness and the aging time follow a linear relationship; micro-hardness continues to increase with time without showing over aging. However, the longer aging time has no significant effect to increase the micro-hardness values. On the other hand, at elevated temperatures and prolonged durations, micro-hardness starts to slightly decrease, which may be because of the austenite reversion and coarsening of the intermetallic precipitates. During laser melting, the surrounding material and the following layers are heated up leading to precipitation reactions, which may be promoted with micro-segregation accompanied with cellular growth. In LPB, the re-melting process is significantly pronounced to increase the micro-hardness of the parts, since a second round of aging takes place [77,80]. On the other hand, age hardening of LPB produced maraging steel causes an increase in the hardness up to 58 HRC, when optimal aging time and temperature (5 h and 480 °C) is selected.

8.2. Tensile properties

8.2.1. Tensile properties of LPF processed parts

Table 6 lists the ultimate tensile strength (UTS), yield strength (YS), and the elongation at failure (EL) for different grade steels processed by LPF along with reference properties of wrought steels, [15,118,190–192]. The UTS and YS of LPF parts are mostly greater than those synthesized from wrought counterparts, which can be ascribed to the higher cooling rate and grain refinements [15,190,192]. However, LPF processed steels show lower elongation-to-failure values, which is believed to be due to porosity and inclusions inside the products caused by the poor optimized process conditions.

Fig. 29a–c shows the specific energy vs. UTS, YS and EL values for various kinds of SS (316SS vs. 420SS) obtained from the literature. For comparison, different values of normalized powder feed rate (ζ) are also indicated.

Another interesting feature regarding the tensile properties of LPF steels is the building orientation of the parts, which affects the resultant tensile properties of the component. A summary of building orientation effects, e.g. parallel (X-direction) vs. perpendicular (Y-direction), on tensile properties of steels is listed in Table 6. It is believed that this anisotropic behavior is due to the occurrence of weak interfacial layers, both in Z- and Y-directions, which provides a simple path for shear bands [10,15]. Various cooling rates in these deposition directions might affect microstructure and mechanical properties.

The laser passing time between each subsequent layer is greater for X-direction compared to the materials built in the Y- or Z-directions.

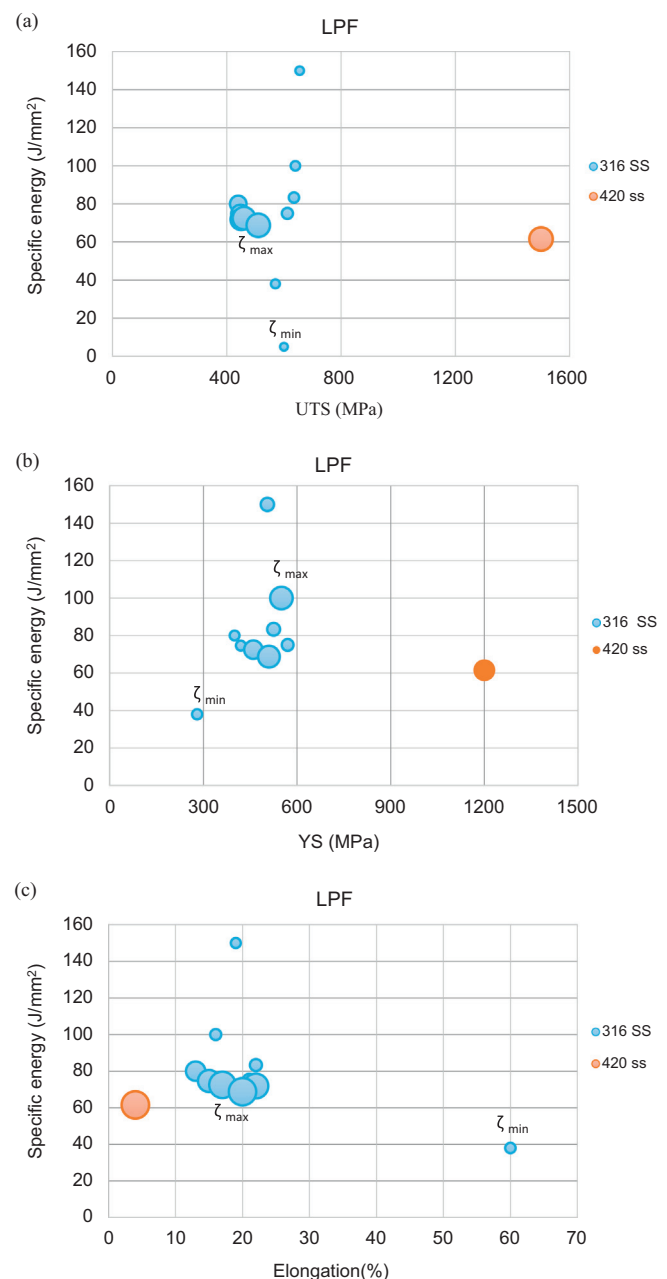


Fig. 29. Specific energy vs. (a) UTS, (b) YS and, (c) EL for different kinds of steels with relevant normalized powder feed rate (ζ) [89,108,118,126,146,195–198].

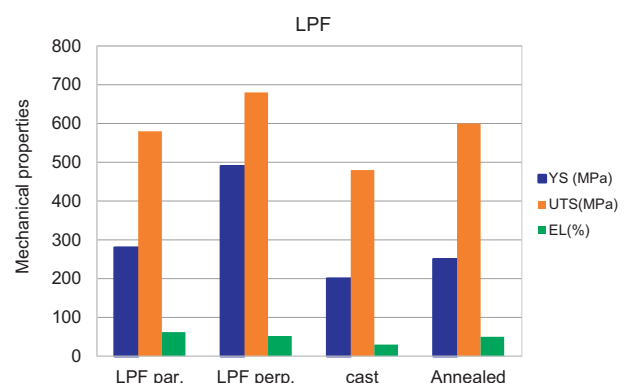


Fig. 30. Unusual behavior of YS, UTS and EL for LPF of 316 SS [110].

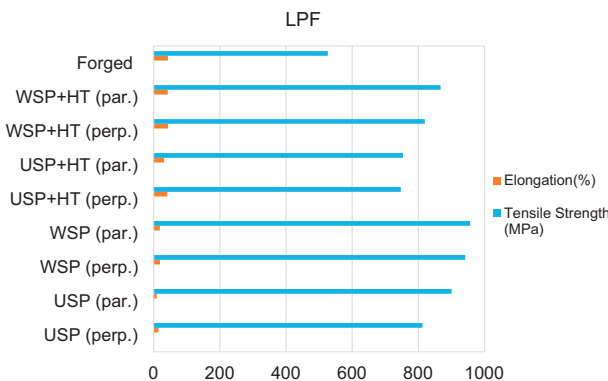


Fig. 31. Tensile properties of 316 SS, as-built, heat-treated and forged specimens with different scanning paths (unidirectional and weaving) in LPF [184].

Accordingly, higher cooling rates, and consequently, finer microstructures for specimens deposited in the X-direction can be obtained [199].

However, some authors describe different behavior for 316 SS in terms of anisotropy, as illustrated in Fig. 30, where the tensile properties for LPF steels in X and Y directions, as well as the results for cast and annealed steels are presented. The mechanical properties of LPF materials are superior to the cast and annealed wrought ones. Interestingly, specimens constructed perpendicular to build direction possess higher tensile strength and poorer elongation than the specimens build along the parallel direction. However, this is in contrast with other studies. According to the authors, this behavior was the result of the distinct positioning of grains along the tensile loading direction, together with the grain size and spacing between inclusions [108].

In addition to building orientation, there are other two factors affecting the tensile properties of LPF parts; (i) inter-layer time interval and (ii) the scanning path. The measured tensile properties for single-built, nine built 316 SS and their corresponding cast and wrought materials are listed in Table 6. It is stated that the YS and UTS of 316 L SS by LPF is higher than their cast/wrought alloys, whether or not heat treatment or process time interval are taken into consideration. In addition, yield and tensile strengths of the specimens have been increased by higher layer-to-layer time interval. However, heat treatment can

decrease yield/tensile strength. Nine-built specimens show significantly poor elongation to failure in comparison with the cast and wrought materials probably due to the reasons such as: flaws within the parts, finer microstructures and unsteady metallurgical bond between the layers, when the elongation to failures of one-built specimens is similar to the heat treated ones [130].

The impact of scanning path on tensile properties of 316 SS is of interest. Fig. 31 represents the tensile data in both as prepared and heat-treated condition for 316 SS; built by following unidirectional (USP) and weaving scanning path (WSP). From the plot, it is evident that the USP and WSP as-built specimens have higher tensile strength than the forged parts. However, elongations are significantly lower in comparison with forged counterparts. The reasons for this behaviour could be the presence of finer grains resulted from the rapid solidification of the material in the LPF process. In addition, inevitable internal stress, oxidation and porosity might be other disadvantages for ductility. As displayed in Fig. 31, the tensile properties are anisotropic for the USP. The parallel loading direction to the scanning path shows greater tensile strength compared to the perpendicular one, whereas the elongation is the opposite. Therefore, it seems that the samples deposited by WSP have higher performance than the USP and the conventional forging ones [184].

8.2.2. Tensile properties of LPB processed parts

In Table 7, the tensile properties are listed for different steel grades fabricated by LPB techniques along with the properties of the wrought materials [125]. Ahmadi and coworkers reported about the variation of the mechanical properties with laser input power, scanning speed and scanning strategy in 316 SS fabricated by LPB [200]. In particular the authors demonstrated that strain and toughness of the samples are remarkably affected by the laser power. The reason is that as the laser power increases, greater energy density and complete melting are reached due to the greater particle fusion. Moreover, the high energy density reduces the porosity and leads to bigger melt pools, and eventually the manufactured products density will be increased. The tensile strength, as well as other mechanical properties are influenced by porosity [200]. The authors also studied the variation of the mechanical properties with the scanning direction.

Table 7
Tensile properties of various steels, fabricated by LPB

Ferrous alloy	Process	UTS (MPa)	YS (MPa)	EL (%)
Iron (electrolytic, annealed) [201]	Wrought	240–280	70–140	40–60
Iron (0.004%) [202]	LPB	450	380	20
Iron (0.02%) [37]	LPB	350–410	240–300	10
AISI 1005 [203]	LPB	305	164	–
AISI 1033 [34]	LPB	–	650 ^a	–
AISI 1050 [34]	LPB	–	800 ^a	–
AISI 1075 [34]	LPB	–	1150 ^a	–
4130 – as built [149]	LPB	1503 ± 69	1344 ± 67	12 ± 2
17-4 PH SS ASTM A564 [125]	Wrought (ST + PA)	1310	1170	10
17-4 PH SS [136]	LPB	1255 ± 3	661 ± 24	16.2 ± 2.5
304 SS [204]	LPB (orthogonal to building direction)	715.5 ± 1.5	568 ± 2	41.7 ± 1.1
304 [205]	LPF longitudinal	710	448	59
	LPF transverse	324	655	70
18Ni-300 M [77]	Wrought	1000–1170	760–895	6–15
18Ni-300 M [77]	LPB	1290 ± 114	1214 ± 99	13.3 ± 1.9
18Ni-300 M [142]	LPB	1165 ± 7	915 ± 7	12.44 ± 0.14
4340 [53] 593 °C stress-relieved	LPB	1289–1310	1365	16–17
HY100 [39] as per MIL-S-16216	Wrought	Not specified	690–827	>18%
HY100 – as built (xy) [39]	LPB	1200 ± 15	1160 ± 15	6 ± 2
HY100 [39] direct temper 650 °C-2 h-AC (xy)	LPB	880 ± 10	710 ± 30	8 ± 3
HY100 [39] 900 °C-1 h-WQ + 650 °C-2 h-AC	LPB	780 ± 10	690 ± 10	18 ± 2
H13 [206]	LPB	1000–1200	–	0.9–1.9
H13 [207]	LPB	1370 ± 175.1	1003.0 ± 8.5	1.7 ± 0.6
M2 – heat treated [36]	Wrought	1611	–	1.3
M2 [36]	LPB	1286	–	0.6

^a Compressive, ST: solution treated, PA: peak aged.

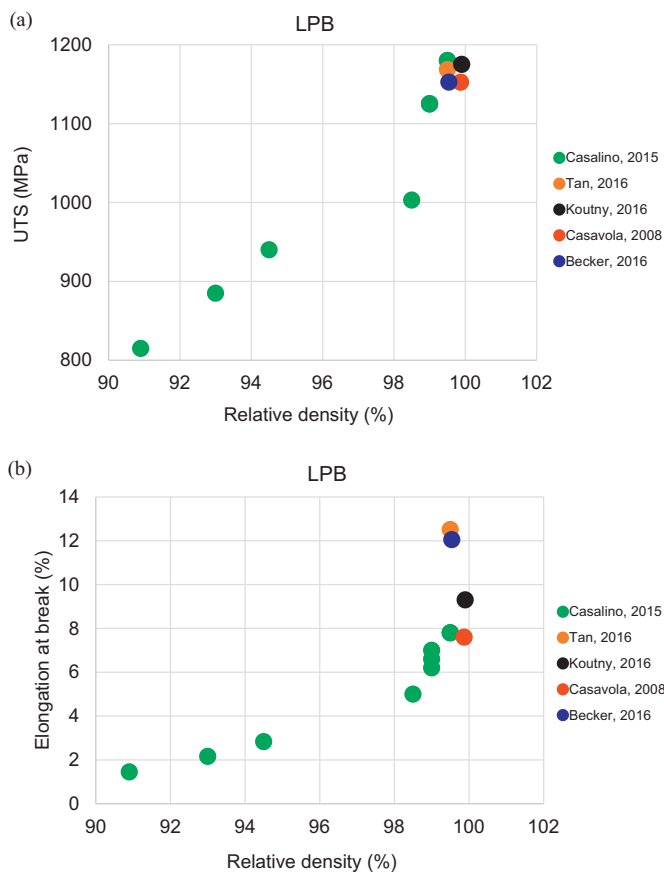


Fig. 32. Correlation between ultimate tensile strength (a) and elongation at break (b) and relative density [83–85,87,88].

In particular, it was demonstrated that the parts fabricated by cross-hatching with zig-zag scanning showed improved mechanical properties compared to the parts obtained by the unidirectional scanning [200]. The enhancement of the tensile strength and toughness is due to the reduction of porosity induced by the cross-hatching method.

Wang et al. [186] also showed that the tensile strength and elongation values of LPB manufactured 316 SS are influenced by the laser energy density ($\frac{P}{vsl}$, where P is laser power, v is process speed, s is hatching space and l is layer thickness). From their work, higher tensile strength is found in LPB processed 316 SS, compared to the wrought one. The strength properties vary with the processing method, processing parameters and the post-process heating, which affect the microstructure [125]. Nakamoto and coworkers [34], showed that steels with higher carbon content showed increased values of yield stress. Moreover, for fully dense SLS samples at a given carbon content, the yield stress is higher for those ones fabricated at a lower energy input.

The tensile property of maraging steels fabricated by the LPB process, correlates positively with relative density, as displayed in Fig. 32 (a,b). LPB processed parts show higher strength and hardness values compared to conventionally aged products, because of the melting and re-melting process. In addition, aging heat treatment leads to an

increase in ultimate tensile strength and Young's modulus through the precipitation of intermetallics. However, the elongation is significantly reduced by age hardening [77,79,83]. As relative density of the LPB processed parts increases, fracture behavior shifts from brittle to ductile. Ductile fracture results from the growth and joining of micro-cavities, while brittle fracture behavior is the result of macro-cavities, which generated throughout the sintering process without sufficient energy density.

8.2.3. Tensile properties of BJ printed parts

Binder jetted cellular lattice structures are less stiff with a smaller elastic modulus compared to the LPB/LPF processed lattice structures, which is due to the formation of a weak neck connection among the powder particles in BJ manufacturing process and partially sintered metal powders [21,22]. Consequently, these lattice structures are only suitable for tissue engineering scaffolds that necessitate micropores for nutrient diffusion [21]. Zhou et al. [22] introduced Instrumented Indentation Testing (IIT) to measure the Young's modulus of lattice structural parts made by BJ, and depicted a value of 1.50 and 0.446 GPa for grid lattice sizes of 1.5 and 1 mm, respectively, which are far from 200 GPa for a conventionally processed SS.

8.3. Fatigue property

8.3.1. Background

Fatigue is one of the critical failure modes for the effective design of many engineering materials. Cyclic loading normally initiates cracks by accumulating the plastic damage and subsequent propagation of the cracks [208]. Generally, cracks tend to initiate near the surface, where nominal stresses are often higher (e.g., in bending), and where geometric variations at surfaces (such as machining marks, surface flaws, notches, etc.) cause stress concentration. Also, material defects (such as inclusions, second-phase particles, voids, micro-cracks etc.) can produce stress concentrations to promote crack formation and failure. Thus, fatigue plays a significant role in the engineering design.

8.3.2. Fatigue strength in LPB processed steel

From the literature, it is already known that high cycle fatigue (HCF) properties of LPB steels are very sensitive to process-induced porosities which influence premature failure through the crack initiation mechanisms. Fatigue test parameters for some LPB processed steels are summarized in Table 8.

Zhang et al. [209] studied the fatigue properties of LPB processed 316 L SS and explored that within a $\pm 30\%$ tolerance limit, porosity does not invade the HCF properties. Within the optimum processing level, porosity driven cracking may be influenced by solidification defects caused by over-melting and under-melting and degrade fatigue resistance. In their experiment, laser powers were varied from 50%, 70%, 100%, 130% and 150%, samples were denoted as 0.5P, 0.7P, P, 1.3P and 1.5P respectively, as shown in Fig. 33.

A longer fatigue life is observed in 0.7P sample because of the internal grain growth morphology. Usually grains with less favorable orientation relative to the temperature gradient stop growing at melt pool boundary. The finer grain sizes with increased grain boundaries act as obstacles to dislocation motion and promote intergranular crack

Table 8

Heat treatment (HT) detail of LPB processed steels and their fatigue test parameters.

Substrate	Fabrication method	Clad-microstructure	Post-HT	Microstructure after post-HT	Fatigue test parameter
316 SS [209]	LPB	Austenite	–	–	R = 0.1, F = 5 Hz
17-4 PH SS [137]	LPB	Martensite + retained austenite	Solution annealing 1040 °C/30 m + AC + precipitation hardening 482 °C/1 h + AC	Precipitation of chromium nickel copper	R = -1, strain controlled
AISI18Ni300 [210]	LPB	Martensite	–	–	R = 0, F = 15–50 Hz

initiation and crack branching, which could result in higher ductility and longer fatigue life.

Yadollahi et al. [137] studied the strain-controlled fatigue behavior of LPB processed 17-4 PH SS, where four types of samples were considered; (i) as built horizontal, (ii) as built vertical, (iii) horizontal + heat treatment, and (iv) vertical + heat treatment. The strain amplitudes vs. fatigue lives of different LPB 17-4 PH SS is shown in Fig. 34. For LPB processed 17-4 PH SS, solution annealing and peak-aging heat treatment is favorable for low cycle fatigue (LCF), and unfavorable for HCF. This is because the associated impurities from the LPB process make 17-4 PH SS more sensitive and after heat treatment it became harder. However, as the defect sensitivity in LCF process was less obvious, after heat treatment specimens showed better fatigue property. Also the building direction showed significant impact on fatigue properties in LPB processed parts. In horizontally built sample, higher fatigue strength was mainly ascribed by their orientation along the loading axis. In case of vertical specimen, defects were more harmful as they generated stress concentration during loading.

The effect of scan speed, porosity and microstructure on fatigue properties of LPB processed maraging steel AISI 18Ni300 was investigated by Santos et al. [210]. The result shown in Fig. 35 indicated that for short lives, fatigue strength in both load control and displacement control is similar. However, for longer life, load control tests show higher fatigue strength.

8.3.3. Fatigue strength in LPF processed steel

Very few research works have been done on the fatigue properties of LPF processed steel, among them 300 M steel [211], AISI4340 steel [212,213] AerMet100 [214] steel are reported. The experimental detail of pre and post heat treatment of various laser cladded steels and their fatigue test parameters are listed in Table 9. The fatigue behaviour of the laser cladded material is not simple because of the formation of complex microstructures with different zones (cladding zone, interfacial zone, and heat affected zone) compared to the conventional microstructure in steel after heat treatment.

Chew et al. [212] characterized the axial fatigue failure of AISI4340 steel where three types of specimens were designed in: Type1: as-clad, Type2: groove-clad-grind, Type3: extended clad-surface grind. The fatigue behavior of the substrate together with the above mentioned cladded samples, is shown in Fig. 36. In general, laser cladding reduced the fatigue life, e.g. Type1 specimen has poor fatigue strength compared to Type2 and Type3. In Type1 specimen, the as-clad region acts as localized stress raiser to initiate crack propagation and failure. The surface grounded clad toe region in Type2 specimen also enables to initiate surface cracks with lower propagation rate because of lesser stress concentration, which results in longer fatigue life. Design of Type3 specimen reduced the cross-sectional area which improved fatigue behavior though it pass through the surface grinding of the extended clad.

AISI4340 steel was used as a substrate, where AISI4340 and AerMet100 clads were produced using laser cladding, and a poor fatigue life was reported in AISI4340 as-clad compared to AerMet100 clad [213]. Fig. 37 shows a comparison of fatigue life between AISI4340 as-clad and AerMet100 clad. The reasons for this degradation are summarized as: (1) the clad and HAZ region show high hardness and brittle properties, (2) generation of tensile residual stresses and (3) microstructural inhomogeneity, i.e. columnar grains in the clad area and grain growth in HAZ stimulating inter-granular fracture.

During laser cladding process, the conversion of ferrite from austenite is inhibited because of rapid solidification. As a result, a brittle phase martensite is formed from austenite. Bhattacharya et al. [215] stated a detailed microstructure development during DMD of AISI4340 steel powder. In their work, tempered lath martensite was formed in AISI4340 steel clad.

During laser processing of steel, heating produced by the successive overlapping tracks will not allow austenite in the earlier track to cool

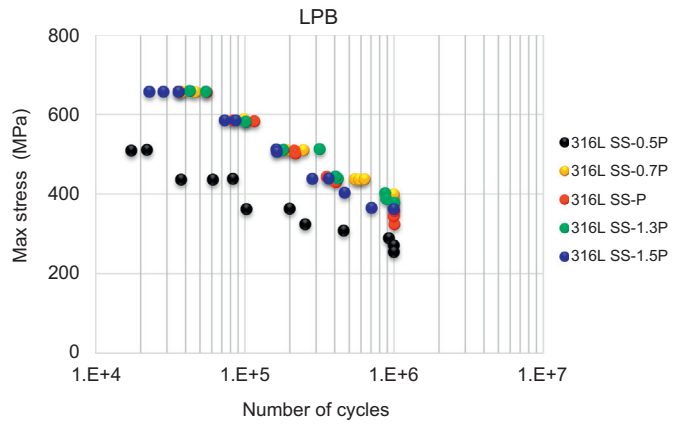


Fig. 33. S-N curves of LPB processed 316 L steel made with different laser powers in LPB, adopted from [209].

below Ms. temperature to form martensite. At the end of the cladding process, the substrate will solidify which results in the conversion of austenite to martensite. This brittle and untempered martensite degraded fatigue life and showed brittle failure mode in AISI4340 as clad steel [212,213].

On the other hand, AerMet100 showed increased fatigue life compared to AISI4340. This is because of the following reasons; (1) lower carbon content of the AerMet100 (0.25 wt%), compared to AISI4340 (0.4 wt%), resulting lower hardness in the clad region, and (2) high nickel content produced Fe-Ni lath-martensite which stimulate ductility. After post clad heat treatment (PCHT), the fatigue life is improved for both clad materials, which is because of the recovery of ductility and toughness in that region.

9. Metal matrix composites (MMC) in AM

Metal matrix composites (MMCs) are manufactured with metals or alloys, reinforced with particulates or fibers of other materials with the objective of high specific strength and stiffness, higher operating temperature/thermal stability, better wear resistance, improved fatigue strength and the capability to possess these properties for a particular applications [216–219]. The reinforcement of metal matrix using AM technology, opens up the possibility of their application in areas where light weight material and cost reduction has the priority, like in automotive, aerospace, and biomedical industries [216–218].

Generally, MMCs are manufactured using conventional techniques, i.e., casting and powder metallurgy, where some major problems are associated as follows: (1) In casting method, the required molds and the

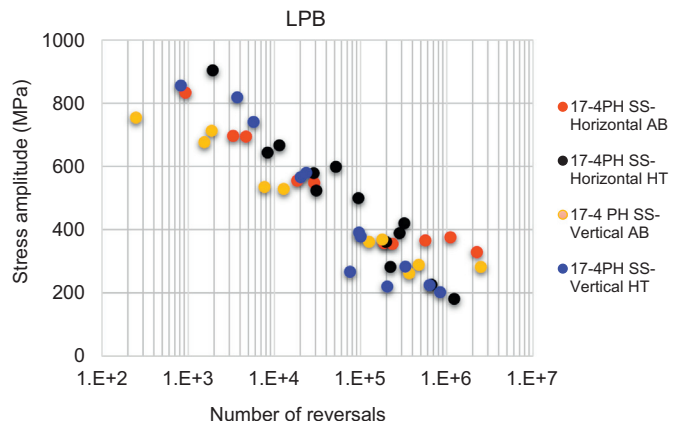


Fig. 34. S-N curves of LPB processed 17-4 PH SS at different sample orientation and heat treatment, adopted from [137].

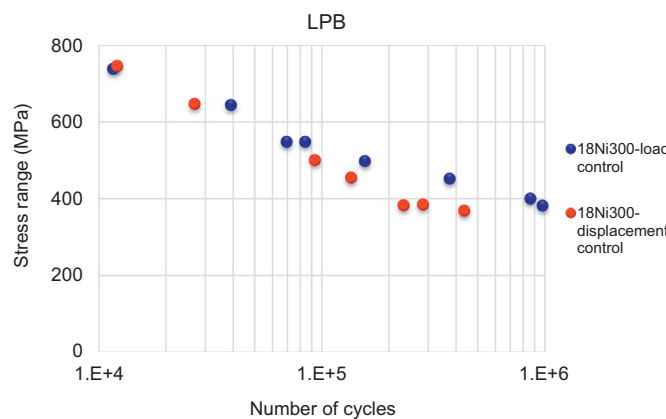


Fig. 35. S-N curves of LPB processed 18Ni300 steel in both load control and displacement control condition, adopted from [210].

post process machining make the technique expensive [216], (2) The low working temperature results weak interfacial bonding between reinforced particle and the matrix which may deteriorate the mechanical property of the composite [220], (3) Microstructural inhomogeneity is another problem due to the non-uniform distribution of reinforcing element throughout the matrix because of Van der Waals attraction forces between surrounding particles [221]. Compared to the conventional casting, in LPB and LPF AM, melt pool pass through a non-equilibrium solidification due to fast heating and cooling over a small melt pool area, which lead to finer microstructure and homogeneous distribution of reinforcing element [5,222]. Moreover, AM can reduce processing times and cost by fabricating near net shape with minimum machining and allow to manufacture products with complex geometry.

In MMC of ferrous alloys, the common reinforcing element includes phases of carbides (SiC, TiC, WC), nitrides (TaN, TiN), borides (TiB, TiB₂, WB), metal oxides (Al₂O₃), and carbon fibers [139], [217,223,224]. Addition of second-phase carbides into steel matrix can improve mechanical properties because of their slow growth rate and thermal stability compared to the cementite [217,225]. For example, reinforcement of thermodynamically stable TiC in martensitic steel matrix, has proven improved stiffness, hardness and wear property [217]. In laser based AM, the strong Marangoni convection brought by high thermal capillary forces caused instability in the melt pool. The liquid flow is generally obsessed by gravity force, buoyancy force and surface tension in the molten area. Consequently, the redisposition of reinforcing elements and their subsequent distributions are significantly influenced by the fluid flow.

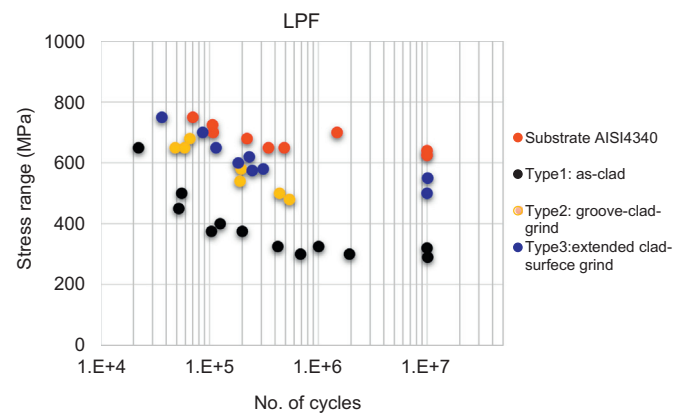


Fig. 36. A comparison between the fatigue behaviors of AISI4340 steel and the clad produced as Type1 (as-clad), Type2 (groove-clad-grind) and Type3 (extended clad-surface grind), adopted from [212].

9.1. LPB processed MMC

In literature, MMC manufactured using LPB process is limited to two steel matrix materials (316 L SS, H13 tool steel) and three reinforced materials or fillers: (titanium carbide (TiC), titanium diboride (TiB₂) and hydroxyapatite (HA)), as summarized in Table 10. The as printed relative density > 95% is achieved with TiC and TiB₂ but is not reported for HA [216,222,223,225–228]. Hot Isostatic Pressing (HIP) treatments allowed a relative density in the range of 99% + for TiB₂, however this decreased the wear resistance and hardness when compared to the as printed condition [225,226].

While filler is seen throughout the matrix, it is typically more concentrated at solidification cell boundaries forming a continuous network of high filler content regions with a honeycomb like appearance [216–218,221,223,225–230]. The presence of well dispersed high melting particulate fillers serves as a nucleating agent resulting in grain refinement. As expected from composites theory, well dispersed nanofillers produce the strongest effects (e.g. 316 L-15TiC [216,221,227]). Due to the increased nucleation, MMC matrix grains are also more equiaxed and exhibit weaker crystallographic texture when compared to unfilled material [217,222,227]. Unlike typical LPB builds, columnar grains in MMC do not extend though the layer due to increased nucleation [222,223].

In LPB produced MMC, the hardness and wear resistance follow the expected trends for particulate reinforced composites, namely they are proportional to filler volume fraction and inversely proportional to filler size. Despite the lower relative densities of MMC, their properties were consistently better than unfilled controls. The most successful filler

Table 9
Heat treatment detail of LPF processed steels and their fatigue test parameters.

Substrate	Pre-HT	Microstructure after Pre-HT	Fabrication method	Clad-microstructure	Post-HT	Microstructure after post-HT	Fatigue test parameter
AISI4340steel [212]	OQ 860 °C + TP 610 °C/160 m	Tempered martensite, coarse carbides	Laser cladding-6 kWIPG fiber laser	Martensite	–	–	R = 0, F = 15 Hz
Alloy steel 300 M [211]			LSF-IIIB laser solid forming	Martensite, bainite	925 °C/1 h + AC + 870 °C/1 h + OQ + 300 °C/2 h + AC	Martensite, bainite, retained austenite	R = 0.1,0.3,0.5
AerMet100 [214]	885 °C/1 h + cold treatment-73 °C/1 h + TP482°C/5 h	Ferrite and martensite	Laser cladding-TRUMPF TruLaser Cell 7020	Austenite and lath martensite	TP 482 °C/5 h	Ni-Fe lath martensite, M2C carbides (M = Cr,Mo,Fe)	R = 0.1, 0.7, F = 5 Hz
AISI 4340, cladding with AerMet100 and AISI4340 [213]	850 °C/1 h + OQ + TP 220 °C/4 h	Tempered martensite	2.5 kW ND:YAG laser	4340 clad microstructure is austenite	Annealing 830 °C/1 h + slow cooling, hardening 850 °C/1 h + OQ + TP 220 °C/4 h.	4340-fine tempered lath martensite, AerMet100-coarse microstructure	R = 0.1, F = 10 Hz

Heat treatment-HT, OQ-Oil Quenching, AC-Air Cooling, TP-tempering, Frequency = F.

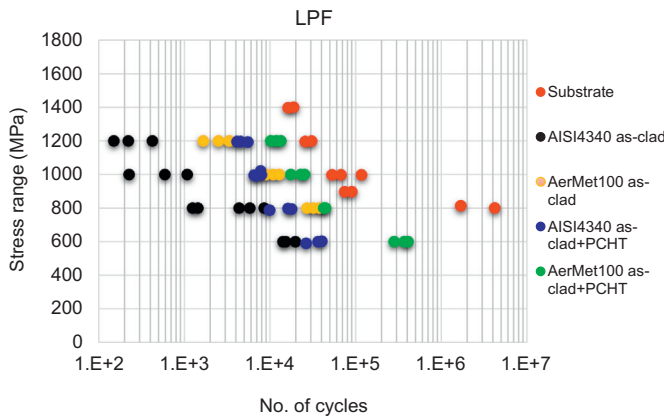


Fig. 37. Constant amplitude axial S-N fatigue curve using $R = 0.1$ and frequency of 10 Hz, adopted from [213].

appears to be TiB_2 , while the most successful preparation strategy appears to be in-situ filler formation during ball milling. The advantages of in-situ formation over the incorporation of an existing filler are the decreased filler size, clear and coherent filler/matrix interface [218] and the avoidance of an independent nano-particle production step. The primary disadvantage is the long-required reaction time (8–36 h) [218,228].

9.2. LPF processed MMC

In LPF, majority of researches have been considered TiC as the reinforcing material because of their high strength and better wear resistance properties, as summarized in Table 11. The amount of reinforced TiC has a significant effect on the size and morphology of the TiC in MMC. Also, various forms of TiC including, spherical, rod, flower-petal, cubic and dendrite shapes can be formed depending on the laser process parameters [231–234]. It is worth mentioning that TiC particles could be undissolved, partially dissolved and completely dissolved in the steel matrix relying on laser cladding parameters such as, laser power, powder feeding rate, and laser cladding speed. It is found that in most of the researches on Fe-TiC MMC, defects free coatings can be produced if TiC is completely dissolved in the steel matrix [234–236]. Also, in other

MMC, containing TiB_2 , SiC, VC, Cr_3C_2 , Al_2O_3 and ZrC as the reinforcing materials, defect free and favorable metallurgical bond between the clad and the substrate has been observed [237–240].

The microstructure of the composite coating is generally planar, cellular, dendritic or fine equiaxed grains [247,251]. So, laser process parameters show a critical role in the quality and microstructure of the composite clad and the interfacial strength between TiC reinforcing particle and the matrix [233,243]. Consequently, they can influence the wear resistance and hardness of the clad layer [232,242].

9.3. BJ printed MMC

The process detail of MMC manufactured in BJ technique and their properties are summarized in Table 12.

Kuldeep Agarwal's group at the Minnesota State University adopted BJ AM process to produce porous biocomposites based on SS and tricalcium phosphate (TCP) with tailored microstructure and mechanical properties to act as load bearing medical implants [254,255]. In their experiment, 316 SS and β -TCP were simply mixed in different volume fractions. After printing and sintering, β -TCP formed a coating on SS particles, with higher volume fraction of β -TCP covered more SS particles [254]. 316SS-20TCP and 316SS-40TCP composites represented an elastic modulus of 7–30 GPa, within the range of cortical and cancellous bones. Where, 316SS-40TCP was suited for scaffold applications and 316SS-20TCP composite found to be an excellent candidate for implant applications [254,255].

Scheithauer et al. [253] reported a thermoplastic 3D printing approach to produce metal-ceramic composites using high-filled iron chromium alloy/17-4 PH suspension and zirconia suspension in molten thermoplastic binder systems/dispersing agent with powder content of 50 vol% steel and 50 vol% zirconia. The process involved preparing suspensions in a heatable ball mill and printing of the suspensions in a layer-by-layer process, which then solidified and passed through the conventional de-binding and sintering [252,253]. Unwanted secondary phases such as oxides and carbides were formed and precipitated within the grain boundaries and the grown pore spaces, which could be avoided during heat treatment in inert atmosphere (Ar/H_2) [252]. This process can be adopted for any materials compositions, considering similar thermal expansion or shrinkage behavior of the materials, which leads to the formation of defectless parts with no delamination, structural changes, etc. [253].

Table 10
Properties of LPB processed MMCs.

Composite Matrix-Vol%	Mixing/heat treatment	Filler size	Hardness	Wear mm^3/Nm	YS (MPa)	Modulus (GPa)
316 L-15TiC	BM AP	45 μm [221]	–	–	710	–
		2–12 μm [227]	335–373 HV	–	987–1150	–
		1 μm [216]	385 HV	6.5×10^{-4}	–	–
		50 nm	406 HV [216]	6.1×10^{-4}	814 [221,222]	–
316 L-10TiC	IS AP	20 nm [218]	342–386 HV [228]	$1.4\text{--}2.3 \times 10^{-4}$ [218,228]	–	–
			318–415 HV [218]	–	–	–
316 L-10TiC [216]	BM AP	1 μm	339 HV	7.3×10^{-4}	–	–
		50 nm	364 HV	4.3×10^{-4}	–	–
316 L-2.5TiC [216]	BM AP	1 μm	293 HV	9.6×10^{-4}	–	–
		50 nm	295 HV	9.4×10^{-4}	–	–
316 L-15TiB ₂ [226]	PB AP	2–12 μm	568 HV	0.006×10^{-4}	–	–
		2–12 μm	617 HV	0.001×10^{-4}	–	–
		BM HIP	2–12 μm	1.0×10^{-4}	–	–
		BM 2xHIP	2–12 μm	1.6×10^{-4}	–	–
316 L-2.5TiB ₂ [226]	BM AP	2–12 μm	303 HV	–	–	–
316 L-15HA [229]	BM AP	<100 nm	2.52 NI	–	85	151
316 L-10HA [229]	BM AP	<100 nm	2.51 NI	–	162	167
316 L-5HA	BM AP	<100 nm [229]	2.36 NI	–	443	226
H13-15TiC	BM AP	5 μm [230]	241 HV	–	50–80	–
	BM AP	50 nm	306–858 HV [225], 811 HV [9]	3.6×10^{-6} [9]	–	256 [9]
	BM HIP [225]	50 nm	345 HV	–	–	–
H13-15 TB ₂ [223]	BM AP	2–12 μm	759 HV	1.24	–	–
	BM HIP	2–12 μm	833 HV	1.95	–	–

BM-Ball-Mill, IN-in-situ, PB-powder blend; AP-As Printed, HIP- Hot Isostatic Press; HV-Vikers, NI-Nano Indentation (GPa).

Table 11

Properties of LPF processed MMCs.

Composite Matrix-Vol% filler/substrate	Filler (cemented) particle size (μm)	Hardness	Weight loss by wear (mg)
Tool steel 90MnCrV8-TiC [232]	3	950 HV2	8
Heat treated samples:	–	890 HV2	17
As-quenched			
TP 180 °C	–	790 HV2	38
TP 300 °C	–	1060 HV2	–
OQ1000 °C + twofold refrigerating –196 °C			
OQ 1000 °C + twofold refrigerating –196 °C	50–100	600–860 HV	–
16NCD13(14NiCrMo13-4); low-carbon low alloy	–80 + 40	550 HV0.1	–
Steel-TiC/cast iron [234,241,242]		At 2.5 vol% TiC	
Pure Fe-30 wt% TiC [243,244]	40	1000–1400 HVN	–
Fe-TiC/1045 steel [236]	–	840–500 HV0.2	0.1 mm ³
AISI 304 L SS-TiC [245]	82	220–500 HV0.1	
Steel-20 wt%TiB2/low carbon steel substrate [240]	–	900 HV0.2	0.24 mm ³
Fe-TiB2composite coating/1010 steel [246]	100	700–1000 HV0.2	5
AISI 316 L SS-SiC (5, 20 wt%)/mild steel [239,247]	25–40	340 VHN (for 5% SiC) 800 VHN (for 20% SiC)	–
Fe based alloy-VC/H13 steel [248]	–	900HV0.2	–
Fe-VC/1020 low carbon steel [237]	–	300–800 HV0.2	0.2 mm ³
AISI316–33,50 vol%Cr3C2/SS [249]	–45 /+5	45–57HRC0.2 (for 33 vol%) 52–58HRC0.2 (for 50 vol%)	25–35 times improvement (33 vol%) 42–88 times improvement (50 vol%)
Fe-based alloy-10,20%Cr3C2/35CrMo steel [250]	30–50	650–680HV0.2 (for 20%) (20% Cr3C2) 18 (10% Cr3C2)	5 – 1.2
304SS-10wt.%Al2O3/45steel [251]	45–100	600 HV	–
Fe based alloy-ZrC0.7/medium carbon steel [238]	74–100	1000–1200 HV0.2	–

10. Challenges, trends and opportunities

Metal AM processes have the potential to produce complex near-net-shape steel components. Various examples were found in the literature, where dense steel parts with acceptable properties were fabricated. However, there are significant challenges associated with LPB, LPF and BJ processes; some of the most significant ones are mentioned below:

- 1- There is a large number of process/design parameters such as, laser power, powder feed rate, laser traverse speed, layer thickness, scanning pattern, etc. involved in LPB and LPF manufacturing processes. As mechanical properties, thermal gradient and consequent microstructure of laser fabricated parts depend on the process parameters and interaction among them, it is vital to optimize these parameters to achieve near-net-shape components with minimal defects such as pores and inclusions. Therefore, novel and effective statistical approaches are required to consider all interdependencies of parameters while a minimum number of experiments is conducted. Within the context of new statistical approaches, much attention must be given to such higher-order interaction effects, which lead to systematic uncertainty in the resulting models and experimental achievements. In this regard, choosing the appropriate combined parameters is of vital importance for the statistical analysis as it is easier to consider their effect on porosity and mechanical properties of the AM parts instead of using individual parameters.
- 2- A vast majority of existing studies only investigate optimal process parameters for steels using simulation and/or experimental approach. A significant limitation is that, by changing the experimental conditions (e.g., material, process, system, or environmental conditions), the resulting optimal process parameters might no longer be applicable. Consequently, new experiments are needed to be

Table 12

Composite detail, process parameters, and properties of MMCs, manufactured in BJ process.

Composite Matrix-Vol% filler (method/substrate)	Filler (cemented) particle size (μm)	Heat treatment	YS (MPa)	Modulus (GPa)
17-4 PH SS-45 TZ-3Y-SE zirconia (suspensions based on heated binder mixture/dispersing agent) [252]	d50 = 0.3	Two-step de-binding: 270 °C (Air), 800 °C (Ar), Sintering-1350 °C (Ar)		
Crofer22APU/17-4 PH SS-50 TZ-3Y-SE/TZ-3Y-E (suspensions based on heated binder mixture/dispersing agent) [253]	d50 (TZ-3Y-SE) = 0.180 d50 (TZ-3Y-E) = 0.105	Two-step de-binding: 270 °C (Air), 900 °C (Ar) Sintering-1400 °C (Ar/H ₂)	–	–
316 SS-20 TCP (mechanical mixing) [254,255] Layer thickness: 50 μm	–	Curing-150 °C, Sintering-1200 °C/8 h	798.713	–
316 SS-20 TCP (mechanical mixing) [254,255] Layer thickness: 200 μm	–	Curing-150 °C, Sintering-1200 °C/8 h	786.513	–
316 SS-20 TCP (mechanical mixing) [254] Layer thickness: 50 μm	5	Curing-175 °C, Sintering-1200 °C/4 h (Ar)	238.16	32.4
316 SS-20 TCP (mechanical mixing) [254] Layer thickness: 100 μm	5	Curing-175 °C, Sintering-1200 °C/4 h (Ar)	89.39	29.8
316 SS-40 TCP (mechanical mixing) [254] Layer thickness: 50 μm	5	Curing-175 °C, Sintering-1200 °C/4 h (Ar)	48.8	13.6
316SS-40 TCP (mechanical mixing) [254] Layer thickness: 100 μm	5	Curing-175 °C, Sintering-1200 °C/4 h (Ar)	31.7	15.7

- done from scratch. It is obvious from the data in the literature that it is extremely challenging to consolidate the data available due to the inconsistencies in the procedures and methodologies used for extracting data. As the AM community grows, the development of standard procedures is inevitable to help the community to interpret the data more effectively and prevent experimental duplication as much as possible.
- 3- Building orientation of steel parts fabricated via LPB and LPF may affect their thermal history. This is because of the anisotropic heat conduction along the built direction. As a result inhomogeneity in microstructure with elongated grains is formed that eventually leads to anisotropic mechanical properties. Post process heat treatment may eliminate the anisotropic property, but further investigation and validation of this approach is required. For example, Hot Isostatic Pressing (HIP) can significantly decrease the anisotropy in the building orientation by removing directional porosities; however, the HIP may cause a detrimental dimensional shrinkage. Another possible solution that to the best of our knowledge has not been considered yet in the literature is cooling of the substrate, for the sake of tempering, as soon as the AM process is completed. This would need to be carefully examined and effectively controlled.
- 4- Last but not least, the number of ferrous alloys deployed to AM processes is extremely limited. While there are >1000 steel alloys for conventional manufacturing (casting, forging, machining, etc.), there have not been many steel alloys deployed to AM by researchers and industry to-date. It becomes a more limiting factor when the number of qualified steel alloys offered by the AM Original Equipment Manufacturers (OEMs) is <10. Further efforts must be made to develop new steel alloys, which are better tailored to AM and also to deploy existing alloys to AM processes, for which imminent market opportunities are expected.

Acknowledgement

This study was carried out under the project, 'Additive manufacturing of ferrous alloys'. The authors gratefully acknowledge the financial support from the Federal Economic Development Agency for Southern Ontario (FedDev Ontario), Ontario Research Fund–Research Excellence, and Rio Tinto Metal Powders. The authors would also like to thank Zhidong Zhang, PhD student, for his contributions to the modeling section.

References

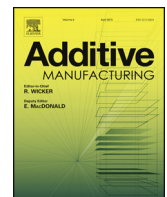
- [1] J.G.S.J. Laeng, F.W. Liou, Laser metal forming processes for rapid prototyping - a review, *Int. J. Prod. Res.* 38 (2000) 3973–3996, <https://doi.org/10.1080/00207540050176111>.
- [2] W.E. Frazier, Metal additive manufacturing: a review, *J. Mater. Eng. Perform.* 23 (2014) 1917–1928, <https://doi.org/10.1007/s11665-014-0958-z>.
- [3] L.E. Murr, E. Martinez, S.M. Gaytan, D.A. Ramirez, B.I. Machado, P.W. Shindo, J.L. Martinez, F. Medina, J. Wooten, D. Ciscl, U. Ackelid, R.B. Wicker, Microstructural architecture, microstructures, and mechanical properties for a nickel-base superalloy fabricated by electron beam melting, *Metall. Mater. Trans. A* 42 (2011) 3491–3508, <https://doi.org/10.1007/s11661-011-0748-z>.
- [4] L.E. Murr, S.M. Gaytan, D.A. Ramirez, E. Martinez, J. Hernandez, K.N. Amato, P.W. Shindo, F.R. Medina, R.B. Wicker, Metal fabrication by additive manufacturing using laser and electron beam melting technologies, *J. Mater. Sci. Technol.* 28 (2012) 1–14, [https://doi.org/10.1016/S1005-0302\(12\)60016-4](https://doi.org/10.1016/S1005-0302(12)60016-4).
- [5] D.D. Gu, W. Meiners, K. Wissenbach, R. Poprawe, Laser additive manufacturing of metallic components: materials, processes and mechanisms, *Int. Mater. Rev.* 57 (2012) 133–164, <https://doi.org/10.1179/1743280411Y.0000000014>.
- [6] I. Gibson, D. Rosen, B. Stucker, *Additive Manufacturing Technologies*, Springer New York, New York, NY, 2015, <https://doi.org/10.1007/978-1-4939-2113-3>.
- [7] L.E. Murr, E. Martinez, K.N. Amato, S.M. Gaytan, J. Hernandez, D.A. Ramirez, P.W. Shindo, F. Medina, R.B. Wicker, Fabrication of metal and alloy components by additive manufacturing: examples of 3D materials science, *J. Mater. Res. Technol.* 1 (2012) 42–54, [https://doi.org/10.1016/S2238-7854\(12\)70009-1](https://doi.org/10.1016/S2238-7854(12)70009-1).
- [8] P.A. Kobryn, S.L. Semiatin, Mechanical properties of laser-deposited Ti-6Al-4V, *Solid Free. Fabr. Proc.* Austin 2001, pp. 6–8.
- [9] A. Yadollahi, N. Shamsaei, S.M. Thompson, A. Elwany, L. Bian, Mechanical and microstructural properties of selective laser melted 17-4 PH stainless steel, *ASME 2015 Int. Mech. Eng. Congr. Expo*, American Society of Mechanical Engineers, 2015 (p. V02AT02A014-V02AT02A014).
- [10] N. Shamsaei, A. Yadollahi, L. Bian, S.M. Thompson, An overview of direct laser deposition for additive manufacturing; part II: mechanical behavior, process parameter optimization and control, *Addit. Manuf.* 8 (2015) 12–35, <https://doi.org/10.1016/j.addma.2015.07.002>.
- [11] V. Bhavar, P. Kattire, V. Patil, S. Khot, K. Gujar, R. Singh, A review on powder bed fusion technology of metal additive manufacturing, *4th Int. Conf. Exhib. Addit. Manuf. Technol Sept.*, 2014, pp. 1–2.
- [12] S.K. Tiwari, S. Pandey, S. Agrawal, S.M. Bobade, Selection of selective laser sintering materials for different applications, *Rapid Prototyp. J.* 21 (2015) 630–648, <https://doi.org/10.1108/rpj-03-2013-0027>.
- [13] H. Krauss, T. Zeugner, M.F. Zah, Layerwise monitoring of the selective laser melting process by thermography, *8th Int. Conf. Laser Assist. Net Shape Eng. LANE* 2014, 56, 2014, pp. 64–71, <https://doi.org/10.1016/j.phpro.2014.08.097>.
- [14] M. Alimardani, E. Toyserkani, J.P. Huissoon, C.P. Paul, On the delamination and crack formation in a thin wall fabricated using laser solid freeform fabrication process: an experimental-numerical investigation, *Opt. Lasers Eng.* 47 (2009) 1160–1168, <https://doi.org/10.1016/j.optlaseng.2009.06.010>.
- [15] C. Selcuk, Laser metal deposition for powder metallurgy parts, *Powder Metall.* 54 (2011) 94–99.
- [16] Y. Bai, G. Wagner, C.B. Williams, Effect of bimodal powder mixture on powder packing density and sintered density in binder jetting of metals, *2015 Annu. Int. Solid Free. Fabr. Symp.* 2015, p. 62.
- [17] K. Inaekyan, V. Paserin, I. Bailon-Poujol, V. Brailovski, V.P. Karine Inaekyan IanBailon-Poujol, Vladimir Brailovski, Binder-jetting additive manufacturing with water atomized iron powders, *AMP2016 Conf. Addit. Manuf.*, Boston, USA, 2016.
- [18] A. Bailey, A. Merriman, A. Elliott, M. Basti, Preliminary testing of nanoparticle effectiveness in binder jetting applications, *27th Annu. Int. Solid Free. Fabr. Symp.* 2016, pp. 1069–1077.
- [19] S.M. Allen, E.M. Sachs, Three-dimensional printing of metal parts for tooling and other applications, *Met. Mater.* 6 (2000) 589–594.
- [20] A. Basalah, Y. Shanjani, S. Esmaeli, E. Toyserkani, Characterizations of additive manufactured porous titanium implants, *J Biomed Mater Res B Appl Biomater* 100 (2012) 1970–1979.
- [21] Y. Tang, Y. Zhou, T. Hoff, M. Garon, Y.F. Zhao, Elastic modulus of 316 stainless steel lattice structure fabricated via binder jetting process, *Mater. Sci. Technol.* 32 (2016) 648–656.
- [22] Y. Zhou, Y. Tang, T. Hoff, M. Garon, F.Y. Zhao, The verification of the mechanical properties of binder jetting manufactured parts by instrumented indentation testing, *Procedia Manuf.* 1 (2015) 327–342, <https://doi.org/10.1016/j.promfg.2015.09.038>.
- [23] E.A. Rojas-Nastrucci, J. Nussbaum, T.M. Weller, N.B. Crane, Meshed rectangular waveguide for high power, low loss and reduced weight applications, *Microw. Symp. (IMS)*, 2016 IEEE MTT-S Int., IEEE 2016, pp. 1–4.
- [24] H. Chen, H. Chen, Y.F. Zhao, Process parameters optimization for improving surface quality and manufacturing accuracy of binder jetting additive manufacturing process, *Rapid Prototyp. J.* 22 (2016) 527–538.
- [25] W. Sames, *Additive Manufacturing of Inconel 718 Using Electron Beam Melting: Processing, Post-processing, & Mechanical Properties*, Texas A&M University, 2015.
- [26] L.E. Murr, S.M. Gaytan, A. Ceylan, E. Martinez, J.L. Martinez, D.H. Hernandez, B.I. Machado, D.A. Ramirez, F. Medina, S. Collins, R.B. Wicker, Characterization of titanium aluminide alloy components fabricated by additive manufacturing using electron beam melting, *Acta Mater.* 58 (2010) 1887–1894, <https://doi.org/10.1016/j.actamat.2009.11.032>.
- [27] H. Gong, K. Rafi, H. Gu, T. Starr, B. Stucker, Analysis of defect generation in Ti-6Al-4V parts made using powder bed fusion additive manufacturing processes, *Addit. Manuf.* 1 (2014) 87–98, <https://doi.org/10.1016/j.addma.2014.08.002>.
- [28] D. Cormier, O. Harrysson, H. West, Characterization of H13 steel produced via electron beam melting, *Rapid Prototyp. J.* 10 (2004) 35–41, <https://doi.org/10.1108/13552540410512516>.
- [29] R.R. Dehoff, M.M. Kirka, W.J. Sames, H. Bilheux, A.S. Tremsin, L.E. Lowe, S.S. Babu, Site specific control of crystallographic grain orientation through electron beam additive manufacturing, *Mater. Sci. Technol.* 31 (2015) 931–938, <https://doi.org/10.1179/1743284714Y.000000734>.
- [30] S.L. Sing, J. An, W.Y. Yeong, F.E. Wiria, Laser and electron-beam powder-bed additive manufacturing of metallic implants: a review on processes, materials and designs, *J. Orthop. Res.* 34 (2016) 369–385, <https://doi.org/10.1002/jor.23075>.
- [31] E.B.M. Arcam, Welcome to Manufaturing unbound, *Education* 40150 (2017) <https://doi.org/10.1080/03632415.2015.1027159>.
- [32] E. Toyserkani, A. Khajepour, S.F. Corbin, *Laser Cladding*, CRC Press, 2004.
- [33] P. Laakso, T. Riipinen, A. Laukkonen, T. Andersson, A. Jokinen, A. Revuelta, K. Ruusuvuori, Optimization and simulation of SLM process for high density H13 tool steel parts, *9th Int. Conf. Photonic Technol. LANE* 2016, 83, 2016, pp. 26–35, <https://doi.org/10.1016/j.phpro.2016.08.004>.
- [34] T. Nakamoto, N. Shirakawa, Y. Miyata, H. Inui, Selective laser sintering of high carbon steel powders studied as a function of carbon content, *J. Mater. Process. Technol.* 209 (2009) 5653–5660, <https://doi.org/10.1016/j.jmatprotex.2009.05.022>.
- [35] R. Mertens, B. Vrancken, N. Holmstock, Y. Kinds, J.-P. Kruth, J. Van Humbeeck, Influence of powder bed preheating on microstructure and mechanical properties of H13 tool steel SLM parts, *Phys. Procedia* 83 (2016) 882–890.
- [36] K. Kempen, B. Vrancken, S. Buls, L. Thijss, J. Van Humbeeck, J.-P. Kruth, Selective laser melting of crack-free high density M2 high speed steel parts by baseplate preheating, *J. Manuf. Sci. Eng.* 136 (2014), 61026, <https://doi.org/10.1115/1.4028513>.
- [37] B. Song, S. Dong, S. Deng, H. Liao, C. Coddet, Microstructure and tensile properties of iron parts fabricated by selective laser melting, *Opt. Laser Technol.* 56 (2014) 451–460, <https://doi.org/10.1016/j.optlastec.2013.09.017>.

- [38] M. Rombouts, J.P. Kruth, L. Froyen, P. Merce, Fundamentals of selective laser melting of alloyed steel powders fundamentals of selective laser melting of alloyed steel powders, *CIRP Ann. Manuf. Technol.* 55 (2006) 187–192, [https://doi.org/10.1016/S0007-8506\(07\)60395-3](https://doi.org/10.1016/S0007-8506(07)60395-3).
- [39] J.J.S. Dilip, G.D.J. Ram, T.L. Stair, B. Stucker, Selective laser melting of HY100 steel: process parameters, microstructure and mechanical properties, *Addit. Manuf.* 13 (2017) 49–60.
- [40] A. Simchi, Direct laser sintering of metal powders: mechanism, kinetics and microstructural features, *Mater. Sci. Eng. A* 428 (2006) 148–158, <https://doi.org/10.1016/j.msea.2006.04.117>.
- [41] A. Simchi, H. Pohl, Effects of laser sintering processing parameters on the microstructure and densification of iron powder, *Mater. Sci. Eng. A* 359 (2003) 119–128.
- [42] M. Mazur, M. Leary, M. McMillan, J. Elambasseril, M. Brandt, SLM additive manufacture of H13 tool steel with conformal cooling and structural lattices, *Rapid Prototyp. J.* 22 (2016) 504–518, <https://doi.org/10.1108/RPJ-06-2014-0075>.
- [43] L.N. Carter, X. Wang, N. Read, R. Khan, M. Aristizabal, K. Essa, M.M. Attallah, Process optimisation of selective laser melting using energy density model for nickel based superalloys, *Mater. Sci. Technol.* 32 (2016) 657–661.
- [44] I. Yadroitsev, M. Pavlov, P. Bertrand, I. Smurov, Mechanical Properties of Samples Fabricated by Selective Laser Melting, 14èmes Assises Eur. Du Prototypages Fabr. Rapide, Paris, 2009 24–25.
- [45] M. Garibaldi, I. Ashcroft, M. Simonelli, R. Hague, Metallurgy of high-silicon steel parts produced using selective laser melting, *Acta Mater.* 110 (2016) 207–216, <https://doi.org/10.1016/j.actamat.2016.03.037>.
- [46] Y.-A. Song, W. Koenig, Experimental study of the basic process mechanism for direct selective laser sintering of low-melting metallic powder, *CIRP Ann. Manuf. Technol.* 46 (1997) 127–130, [https://doi.org/10.1016/S0007-8506\(07\)60790-2](https://doi.org/10.1016/S0007-8506(07)60790-2).
- [47] H.J. Niu, I.T.H. Chang, Selective laser sintering of gas atomized M2 high speed steel powder, *J. Mater. Sci.* 35 (2000) 31–38.
- [48] M.M.A. Dewidar, Direct and Indirect Laser Sintering of Metals(PhD Thesis) <http://etheses.whiterose.ac.uk/id/eprint/3973> 2002.
- [49] R.B. Eane, *Metal Powder Effects on Selective Laser Sintering*, 2002.
- [50] D.E. Cooper, The High Deposition Rate Additive Manufacture of Nickel Superalloys and Metal Matrix Composites by, University of Warwick, 2016<http://webcat.warwick.ac.uk/record=b2876003-S1>.
- [51] A. Simchi, H. Asgharzadeh, Densification and microstructural evaluation during laser sintering of M2 high speed steel powder, *Mater. Sci. Technol.* 20 (2004) 1462–1468, <https://doi.org/10.1179/026708304X3944>.
- [52] A.B. Spierings, G. Levy, Comparison of density of stainless steel 316 L parts produced with selective laser melting using different powder grades, *Proc. Annu. Int. Solid Free. Fabr. Symp.*, Austin, TX 2009, pp. 342–353.
- [53] E. Jelis, M. Clemente, S. Kerwien, N.M. Ravindra, M.R. Hespas, Metallurgical and mechanical evaluation of 4340 steel produced by direct metal laser sintering, *JOM* 67 (2015) 582–589.
- [54] H. Irrinki, Mechanical Properties and Microstructure Evolution of 17-4 PH Stainless Steel Processed by Laser-Powered Bed Fusion, 2016.
- [55] P.A. Lykov, E.V. Safonov, A.M. Akhmedianov, Selective laser melting of copper, *Mater. Sci. Forum, Trans Tech Publ* 2016, pp. 284–288.
- [56] R. Mahshid, H.N. Hansen, K.L. Hojbjørre, Strength analysis and modeling of cellular lattice structures manufactured using selective laser melting for tooling applications, *Mater. Des.* 104 (2016) 276–283, <https://doi.org/10.1016/j.matdes.2016.05.020>.
- [57] H. Chen, D. Gu, D. Dai, C. Ma, M. Xia, Microstructure and composition homogeneity, tensile property, and underlying thermal physical mechanism of selective laser melting tool steel parts, *Mater. Sci. Eng. A* 682 (2017) 279–289, <https://doi.org/10.1016/j.msea.2016.11.047>.
- [58] I. Yadroitsev, P. Krakhmalev, I. Yadroitseva, Hierarchical design principles of selective laser melting for high quality metallic objects, *Addit. Manuf.* 7 (2015) 45–56, <https://doi.org/10.1016/j.addma.2014.12.007>.
- [59] X. Zhao, B. Song, Y. Zhang, X. Zhu, Q. Wei, Y. Shi, Decarburization of stainless steel during selective laser melting and its influence on Young's modulus, hardness and tensile strength, *Mater. Sci. Eng. A* 647 (2015) 58–61.
- [60] C.D. Boley, S.C. Mitchell, A.M. Rubenchik, S.S.Q. Wu, Metal powder absorptivity: modeling and experiment, *Appl. Opt.* 55 (2016) 6496–6500, <https://doi.org/10.1364/AO.55.006496>.
- [61] M. Van Elsen, F. Al-Bender, J.-P. Kruth, Application of dimensional analysis to selective laser melting, *Rapid Prototyp. J.* 14 (2008) 15–22, <https://doi.org/10.1016/13552540810841526>.
- [62] L. Battizzati, A.L. Greer, The viscosity of liquid metals and alloys, *Acta Metall.* 37 (1989) 1791–1802, [https://doi.org/10.1016/0001-6160\(89\)90064-3](https://doi.org/10.1016/0001-6160(89)90064-3).
- [63] I. Egry, G. Lohöfer, S. Sauerland, Surface tension and viscosity of liquid metals, *J. Non-Cryst. Solids* 156 (1993) 830–832, [https://doi.org/10.1016/0022-3093\(93\)90079-D](https://doi.org/10.1016/0022-3093(93)90079-D).
- [64] R.N. Singh, F. Sommer, Viscosity of liquid alloys: generalization of Andrade's equation, *Monatsh. Chem. Chem. Mon.* 143 (2012) 1235–1242, <https://doi.org/10.1007/s00706-012-0728-2>.
- [65] I. Egry, E. Ricci, R. Novakovic, S. Ozawa, Surface tension of liquid metals and alloys – recent developments, *Adv. Colloid Interf. Sci.* 159 (2010) 198–212, <https://doi.org/10.1016/j.cis.2010.06.009>.
- [66] F.A. Halden, W.D. Kingery, Surface tension at elevated temperatures. II. Effect of C, N, O and S on liquid iron surface tension and interfacial energy with Al₂O₃, *J. Phys. Chem.* 59 (1955) 557–559, <https://doi.org/10.1021/j150528a018>.
- [67] W.M. Steen, J. Mazumder, Theory, mathematical modelling and simulation, *Laser Mater. Process.*, Springer London, London 2010, pp. 251–294 (doi:10.1007/978-1-84996-062-5_6" data-bbox="74 885 493 918">10.1007/978-1-84996-062-5_6").
- [68] F. Incropera, D. DeWitt, *Fundamentals of Heat and Mass Transfer*, 5th Edition Wiley, 2001 (doi:citeulike-article-id:7020383).
- [69] M. Dourandish, D. Godlinski, A. Simchi, 3D printing of biocompatible PM-materials, *Mater. Sci. Forum, Trans Tech Publ* 2007, pp. 453–456.
- [70] P. Nandwana, A.M. Elliott, D. Siddel, A. Merriman, W.H. Peter, S.S. Babu, Powder bed binder jet 3D printing of Inconel 718: densification, microstructural evolution and challenges☆, *Curr. Opin. Solid State Mater. Sci.* 21 (2017) 207–218.
- [71] M. Ziaeef, E.M. Tridas, N.B. Crane, E.M.T. Mohsen Ziaeef, Nathan B. Crane, Binder-jet printing of fine stainless steel powder with varied final density, *JOM* 69 (2017) 592–596.
- [72] Y. Bai, C.B. Williams, An exploration of binder jetting of copper, *Rapid Prototyp. J.* 21 (2015) 177–185.
- [73] M. Letenneur, V. Brailovski, A. Kreitberg, V. Paserin, I. Bailon-Poujol, Laser powder bed fusion of water-atomized iron-based powders: process optimization, *J. Manuf. Mater. Process.* 1 (2017) 23, <https://doi.org/10.3390/jmmp1020023>.
- [74] B. Al-Mangour, Powder metallurgy of stainless steel: state-of-the art, challenges, and development, *Stainl. Steel* (2015) 37–80.
- [75] S. Hoeges, C.T. Schade, R. Causton, Development of a maraging steel powder for additive manufacturing, *MPIF World Congr. Powder Metall. Part. Mater.*, 2015.
- [76] Y. Sun, R.J. Hebert, M. Aindow, Non-metallic inclusions in 17-4PH stainless steel parts produced by selective laser melting, *Mater. Des.* 140 (2018) 153–162, <https://doi.org/10.1016/j.matdes.2017.11.063>.
- [77] K. Kempen, E. Yasa, L. Thijss, J.-P. Kruth, J. Van Humbeeck, Microstructure and mechanical properties of selective laser melted 18Ni-300 steel, *Phys. Procedia* 12 (2011) 255–263, <https://doi.org/10.1016/j.phpro.2011.03.033>.
- [78] R. Frykholm, Y. Takeda, B.-G. Andersson, R. Carlstrom, Solid state sintered 3-D printing component by using inkjet (binder) method, *J. Jpn. Soc. Powder Powder Metall.* 63 (2016) 421–426, <https://doi.org/10.2497/jjspm.63.421>.
- [79] E. Yasa, K. Kempen, J.-P. Kruth, L. Thijss, J. Van Humbeeck, Microstructure and mechanical properties of maraging steel 300 after selective laser melting, *Solid Free. Fabr. Symp. Proc.* 2010, pp. 383–396.
- [80] K. Kempen, Expanding the Materials Palette for Selective Laser Melting of Metals, 2015.
- [81] E. Yasa, J. Deckers, J.-P. Kruth, M. Rombouts, J. Luyten, Charpy impact testing of metallic selective laser melting parts, *Virtual Phys. Prototyp.* 5 (2010) 89–98.
- [82] E. Yasa, J. Deckers, J.-P. Kruth, M. Rombouts, J. Luyten, Experimental investigation of Charpy impact tests on metallic SLM parts, *Innov. Dev. Des. Manuf. Adv. Res. Virtual Rapid Prototyp* 2009, pp. 207–214.
- [83] C. Tan, K. Zhou, X. Tong, Y. Huang, J. Li, W. Ma, F. Li, T. Kuang, Microstructure and Mechanical Properties of 18Ni-300 Maraging Steel Fabricated by Selective Laser Melting, *Proc. 2016 6th Int. Conf. Adv. Des. Manuf. Eng. (ICADME 2016)*, 2016.
- [84] D. Koutny, L. Pantalejev, J. Tomes, D. Palousek, Comparison of selective laser melting of 18Ni maraging steel by Px1 and M2 cusing, *MM Sci. J.* 2016 (2016) 1590–1596, https://doi.org/10.17973/MMSJ.2016.12_2016191.
- [85] T. Hermann Becker, T. Hermann Becker, D. Dimitrov, D. Dimitrov, The achievable mechanical properties of SLM produced maraging steel 300 components, *Rapid Prototyp. J.* 22 (2016) 487–494.
- [86] W. Du, Q. Bai, B. Zhang, A novel method for additive/subtractive hybrid manufacturing of metallic parts, *Procedia Manuf.* 5 (2016) 1018–1030.
- [87] C. Casavola, S.L. Campanelli, C. Pappalettere, Experimental analysis of residual stresses in the selective laser melting process, *Proceedings Xlth Int. Congr. Expo.* Orlando, Florida, USA, 2008.
- [88] G. Casalino, S.L. Campanelli, N. Contuzzi, A.D. Ludovico, Experimental investigation and statistical optimisation of the selective laser melting process of a maraging steel, *Opt. Laser Technol.* 65 (2015) 151–158, <https://doi.org/10.1016/j.optlastec.2014.07.021>.
- [89] G. Bi, A. Gasser, K. Wissenbach, A. Drenker, R. Poprawe, Characterization of the process control for the direct laser metallic powder deposition, *Surf. Coat. Technol.* 201 (2006) 2676–2683.
- [90] J. Choi, Y. Chang, Characteristics of laser aided direct metal/material deposition process for tool steel, *Int. J. Mach. Tools Manuf.* 45 (2005) 597–607.
- [91] J. Mazumder, A. Schifferer, J. Choi, Direct materials deposition: designed macro and microstructure, *Mater. Res. Innov.* 3 (1999) 118–131.
- [92] J. Zhao, W. Cao, C. Ge, Y. Tan, Y. Zhang, Q. Fei, Research on laser engineered net shaping of thick-wall nickel-based alloy parts, *Rapid Prototyp. J.* 15 (2009) 24–28.
- [93] Y. Yang, J.Y.H. Fuh, H.T. Loh, Y.S. Wong, A volumetric difference-based adaptive slicing and deposition method for layered manufacturing, *Trans. Soc. Mech. Eng. J. Manuf. Sci. Eng.* 125 (2003) 586–594.
- [94] A. Dolenc, I. Mäkelä, Slicing procedures for layered manufacturing techniques, *Comput. Des.* 26 (1994) 119–126.
- [95] P. Singh, D. Dutta, Multi-direction slicing for layered manufacturing, *J. Comput. Inf. Sci. Eng.* 1 (2001) 129–142.
- [96] Y. Yang, J.Y.H. Fuh, H.T. Loh, Y. San Wong, Minimizing staircase errors in the orthogonal layered manufacturing system, *IEEE Trans. Autom. Sci. Eng.* 2 (2005) 276–284.
- [97] T. Do, C.S. Shin, D. Stetsko, G. VanConant, A. Vartanian, S. Pei, P. Kwon, Improving structural integrity with boron-based additives for 3D printed 420 stainless steel, *Procedia Manuf.* 1 (2015) 263–272.
- [98] T. Do, P. Kwon, C.S. Shin, Process development toward full-density stainless steel parts with binder jetting printing, *Int. J. Mach. Tools Manuf.* 121 (2017) 50–60, <https://doi.org/10.1016/j.ijmachtools.2017.04.006>.
- [99] L. Sun, Y.-H. Kim, P. Kwon, Densification and properties of 420 stainless steel produced by three-dimensional printing with addition of Si₃N₄ powder, *J. Manuf. Sci. Eng.* 131 (2009), 61001.
- [100] William F. Gale, Terry C. Totemeier, Smithells Metals Reference Book, Eighth, Elsevier Science, Burlington, 2003<https://www.elsevier.com/books/smithells-metals-reference-book/gale/978-0-7506-7509-3>.

- [101] A. Elliott, S. AlSalhi, A.L. Merriman, M.M. Basti, Infiltration of nanoparticles into porous binder jet printed parts, *Am. J. Eng. Appl. Sci.* 9 (2016).
- [102] N.B. Crane, J. Wilkes, E. Sachs, S.M. Allen, Improving accuracy of powder-based SFF processes by metal deposition from a nanoparticle dispersion, *Rapid Prototyp. J.* 12 (2006) 266–274.
- [103] E. Sachs, E. Wylonis, S. Allen, M. Cima, H. Guo, Production of injection molding tooling with conformal cooling channels using the three dimensional printing process, *Polym. Eng. Sci.* 40 (2000) 1232–1247, <https://doi.org/10.1002/pen.11251>.
- [104] Z.C. Cordero, D.H. Siddle, W.H. Peter, A.M. Elliott, Strengthening of ferrous binder jet 3D printed components through bronze infiltration, *Addit. Manuf.* 15 (2017) 87–92, <https://doi.org/10.1016/j.addma.2017.03.011>.
- [105] T. Kasuya, N. Yuriko, Carbon equivalent and multiplying factor for hardenability of steel, *Weld. Res. Suppl.*, Detroit Mich. 1993 (p. 263–s–268–s) http://files.aws.org/wj/supplement/WJ_1993_06_s263.pdf.
- [106] S. Cheruvathur, E.A. Lass, C.E. Campbell, Additive manufacturing of 17-4 PH stainless steel: post-processing heat treatment to achieve uniform reproducible microstructure, *JOM* 68 (2016) 930–942, <https://doi.org/10.1007/s11837-015-1754-4>.
- [107] E. Liverani, S. Toschi, L. Ceschin, A. Fortunato, Effect of selective laser melting (SLM) process parameters on microstructure and mechanical properties of 316 L austenitic stainless steel, *J. Mater. Process. Technol.* 249 (2017) 255–263, <https://doi.org/10.1016/j.jmatprote.2017.05.042>.
- [108] J. Yu, M. Rombouts, G. Maes, Cracking behavior and mechanical properties of austenitic stainless steel parts produced by laser metal deposition, *Mater. Des.* 45 (2013) 228–235.
- [109] L. Wang, S. Felicelli, Process modeling in laser deposition of multilayer SS410 steel, *J. Manuf. Sci. Eng.* 129 (2007) 1028–1034.
- [110] P.A. Kobryn, E.H. Moore, S.L. Semiatin, Effect of laser power and traverse speed on microstructure, porosity, and build height in laser-deposited Ti-6Al-4V, *Scr. Mater.* 43 (2000) 299–305, [https://doi.org/10.1016/S1359-6462\(00\)00408-5](https://doi.org/10.1016/S1359-6462(00)00408-5).
- [111] J.K. Wessel, *The Handbook of Advanced Materials: Enabling New Designs, Functionally Graded Materials*, John Wiley & Sons, 2004.
- [112] J.E. Smugeresky, D.D. Gill, C.J. Atwood, New Low Cost Material Development Technique for Advancing Rapid Prototyping Manufacturing Technology, 2007 1–39 <http://www.osti.gov/servlets/purl/926378-Q96D62/>.
- [113] J.-P.P. Kruth, L. Froyen, J. Van Vaerenbergh, P. Mercelis, M. Rombouts, B. Lauwers, Selective laser melting of iron-based powder, 14th International Symp. Electromachining (ISEM XIV), 149, 2004, pp. 616–622, <https://doi.org/10.1016/j.jmatprotec.2003.11.051>.
- [114] L. Wang, P. Pratt, S.D. Felicelli, H. El Kadiri, J.T. Berry, P.T. Wang, M.F. Horstemeyer, Experimental analysis of porosity formation in laser-assisted powder deposition process, 2009 TMS Annu. Meet. Exhib., 2009.
- [115] J.B. Ferguson, B.F. Schultz, A.D. Moghadam, P.K. Rohatgi, Semi-empirical model of deposit size and porosity in 420 stainless steel and 4140 steel using laser engineered net shaping, *J. Manuf. Process.* 19 (2015) 163–170.
- [116] H.A. Hamza, C. Smith, L. Hao, Effect of build orientation on the surface quality, microstructure and mechanical properties of selective laser melting 316 L stainless steel, *Rapid Prototyp. J.* (0) (2017) <https://doi.org/10.1108/RPJ-04-2016-0068>.
- [117] J. Choi, Y. Hua, Dimensional and material characteristics of direct deposited H13 tool steel by CO₂ laser, *J. Laser Appl.* 16 (2004) 245–251.
- [118] B. Zheng, Y. Zhou, J.E. Smugeresky, J.M. Schoenung, E.J. Lavernia, Thermal behavior and microstructure evolution during laser deposition with laser-engineered net shaping: part II. Experimental investigation and discussion, *Metall. Mater. Trans. A* 39 (2008) 2237–2245.
- [119] J.D. Majumdar, A. Pinkerton, Z. Liu, I. Manna, L. Li, Microstructure characterisation and process optimization of laser assisted rapid fabrication of 316 L stainless steel, *Appl. Surf. Sci.* 247 (2005) 320–327.
- [120] L. Thijss, F. Verhaeghe, T. Craeghs, J. Van Humbeeck, J.-P. Kruth, J. Van Humbeeck, J.-P. Kruth, A study of the microstructural evolution during selective laser melting of Ti-6Al-4V, *Acta Mater.* 58 (2010) 3303–3312, <https://doi.org/10.1016/j.actamat.2010.02.004>.
- [121] X. Tan, Y. Kok, Y.J. Tan, M. Descouins, D. Mangelinck, S.B. Tor, K.F. Leong, C.K. Chua, Graded microstructure and mechanical properties of additive manufactured Ti-6Al-4V via electron beam melting, *Acta Mater.* 97 (2015) 1–16, <https://doi.org/10.1016/j.actamat.2015.06.036>.
- [122] J.D. Hunt, Steady state columnar and equiaxed growth of dendrites and eutectic, *Mater. Sci. Eng.* 65 (1984) 75–83.
- [123] D. Wang, C. Song, Y. Yang, Y. Bai, Investigation of crystal growth mechanism during selective laser melting and mechanical property characterization of 316 L stainless steel parts, *Mater. Des.* 100 (2016) 291–299, <https://doi.org/10.1016/j.matdes.2016.03.111>.
- [124] L. Thijss, K. Kempen, J.-P. Kruth, J. Van Humbeeck, Fine-structured aluminium products with controllable texture by selective laser melting of pre-alloyed AlSi10Mg powder, *Acta Mater.* 61 (2013) 1809–1819, <https://doi.org/10.1016/j.actamat.2012.11.052>.
- [125] D. Herzog, V. Seyda, E. Wycisk, C. Emmelmann, Additive manufacturing of metals, *Acta Mater.* 117 (2016) 371–392, <https://doi.org/10.1016/j.actamat.2016.07.019>.
- [126] K. Zhang, S. Wang, W. Liu, X. Shang, Characterization of stainless steel parts by laser metal deposition shaping, *Mater. Des.* 55 (2014) 104–119.
- [127] I. Yadroitsev, I. Yadroitseva, I. Smurov, Strategy of fabrication of complex shape parts based on the stability of single laser melted track, SPIE-The Int. Soc. Opt. Eng., San Francisco, California, United States, 2011 <https://doi.org/10.1117/12.875402> (p. 79210C-79210C-13).
- [128] Z. Sun, X. Tan, S.B. Tor, W.Y. Yeong, Selective laser melting of stainless steel 316 L with low porosity and high build rates, *Mater. Des.* 104 (2016) 197–204, <https://doi.org/10.1016/j.matdes.2016.05.035>.
- [129] W.M. Tucho, V.H. Lysne, H. Austbø, A. Sjolyst-Kverneland, V. Hansen, Investigation of effects of process parameters on microstructure and hardness of SLM manufactured SS316 L, *J. Alloys Compd.* 740 (2018) 910–925, <https://doi.org/10.1016/j.jallcom.2018.01.098>.
- [130] A. Yadollahi, N. Shamsaei, S.M. Thompson, D.W. Seely, Effects of process time interval and heat treatment on the mechanical and microstructural properties of direct laser deposited 316 L stainless steel, *Mater. Sci. Eng. A* 644 (2015) 171–183.
- [131] K. Abd-Elghany, D.L. Bourell, Property evaluation of 304 L stainless steel fabricated by selective laser melting, *Rapid Prototyp. J.* 18 (2012) 420–428.
- [132] H. Yu, J. Yang, J. Yin, Z. Wang, X. Zeng, Comparison on mechanical anisotropies of selective laser melted Ti-6Al-4V alloy and 304 stainless steel, *Mater. Sci. Eng. A* 695 (2017) 92–100, <https://doi.org/10.1016/j.msea.2017.04.031>.
- [133] S.M.A., J.W. Elmer, T.W. Eagar, Microstructural development during solidification of stainless steel alloys, *Metall. Trans. A* 20 (1989) 2117–2131.
- [134] L. Facchini, N. Vicente, I. Lonardelli, E. Magalini, P. Robotti, A. Molinari, Metastable austenite in 17–4 precipitation-hardening stainless steel produced by selective laser melting, *Adv. Eng. Mater.* 12 (2010) 184–188.
- [135] A. Kudzal, B. McWilliams, C. Hofmeister, F. Kellogg, J. Yu, J. Taggart-Scarff, J. Liang, Effect of scan pattern on the microstructure and mechanical properties of powder bed fusion additive manufactured 17-4 stainless steel, *Mater. Des.* 133 (2017) 205–215, <https://doi.org/10.1016/j.matdes.2017.07.047>.
- [136] T. LeBrun, T. Nakamoto, K. Horikawa, H. Kobayashi, Effect of retained austenite on subsequent thermal processing and resultant mechanical properties of selective laser melted 17-4 PH stainless steel, *Mater. Des.* 81 (2015) 44–53.
- [137] A. Yadollahi, N. Shamsaei, S.M. Thompson, A. Elwany, L. Bian, Effects of building orientation and heat treatment on fatigue behavior of selective laser melted 17-4 PH stainless steel, *Fatigue Fract. Behav. Addit. Manuf. Parts.* 94 (2017) 218–235, <https://doi.org/10.1016/j.jifatigue.2016.03.014>.
- [138] B. AlMangour, J.M. Yang, Understanding the deformation behavior of 17-4 precipitate hardenable stainless steel produced by direct metal laser sintering using micropillar compression and TEM, *Int. J. Adv. Manuf. Technol.* 90 (2017) 119–126, <https://doi.org/10.1007/s00170-016-9367-9>.
- [139] B. AlMangour, J.-M. Yang, Improving the surface quality and mechanical properties by shot-peening of 17-4 stainless steel fabricated by additive manufacturing, *Mater. Des.* 110 (2016) 914–924, <https://doi.org/10.1016/j.matdes.2016.08.037>.
- [140] B. AlMangour, J.M. Yang, Integration of heat treatment with shot peening of 17-4 stainless steel fabricated by direct metal laser sintering, *JOM* 69 (2017) 2309–2313, <https://doi.org/10.1007/s11837-017-2538-9>.
- [141] E.A. Jägle, Z. Sheng, P. Kürnsteiner, S. Ocylok, A. Weisheit, D. Raabe, Comparison of maraging steel micro- and nanostructure produced conventionally and by laser additive manufacturing, *Materials (Basel)* 10 (2017) 8, <https://doi.org/10.3390/ma10010008>.
- [142] C. Tan, K. Zhou, W. Ma, P. Zhang, M. Liu, T. Kuang, Microstructural evolution, nanoprecipitation behavior and mechanical properties of selective laser melted high-performance grade 300 maraging steel, *Mater. Des.* 134 (2017) 23–34, <https://doi.org/10.1016/j.matdes.2017.08.026>.
- [143] J.M. Pardal, S.S.M. Tavares, V.F. Terra, M.R. Da Silva, D.R. Dos Santos, Modeling of precipitation hardening during the aging and overaging of 18Ni-Co-Mo-Ti maraging 300 steel, *J. Alloys Compd.* 393 (2005) 109–113, <https://doi.org/10.1016/j.jallcom.2004.09.049>.
- [144] S.L. Campanelli, A. Angelastro, C.G. Signorile, G. Casalino, Investigation on direct laser powder deposition of 18 Ni (300) marage steel using mathematical model and experimental characterisation, *Int. J. Adv. Manuf. Technol.* (2016) 1–11.
- [145] P. Krakhmalev, I. Yadroitseva, G. Fredriksson, I. Yadroitsev, In situ heat treatment in selective laser melted martensitic AISI 420 stainless steels, *Mater. Des.* 87 (2015) 380–385, <https://doi.org/10.1016/j.matdes.2015.08.045>.
- [146] G.A. Ravi, X. Hao, N. Wain, X. Wu, M.M. Attallah, Direct laser fabrication of three dimensional components using SC420 stainless steel, *Mater. Des.* 47 (2013) 731–736.
- [147] X. Yue, J.C. Lippold, B.T. Alexandrov, S.S. Babu, continuous cooling transformation behavior in the CGHAZ of naval steels, *Weld. J.* 91 (2012) (67s–75s).
- [148] X. Yue, J.C. Lippold, Evaluation of heat-affected zone hydrogen-induced cracking in navy steels, *Weld. J.* 92 (2013) 20S–28S.
- [149] W. Wang, S. Kelly, A metallurgical evaluation of the powder-bed laser additive manufactured 4140 steel material, *JOM* 68 (2016) 869–875, <https://doi.org/10.1007/s11837-015-1804-y>.
- [150] Y. Lee, M. Nordin, S. Babu, D. Farson, Influence of fluid convection on weld pool formation in laser cladding, *Weld. J.* 93 (2014) (29S–300S).
- [151] S.Y. Wen, Y.C. Shin, J.Y. Murthy, P.E. Sojka, Modeling of coaxial powder flow for the laser direct deposition process, *Int. J. Heat Mass Transf.* 52 (2009) 5867–5877, <https://doi.org/10.1016/j.ijheatmasstransfer.2009.07.018>.
- [152] X. He, J. Mazumder, Transport phenomena during direct metal deposition advertisement, *J. Appl. Phys.* 53113 (2007) 53113, <https://doi.org/10.1063/1.2710780>.
- [153] M. Alimardani, E. Toyserkani, J.P. Huissoon, A 3D dynamic numerical approach for temperature and thermal stress distributions in multilayer laser solid freeform fabrication process, *Opt. Lasers Eng.* 45 (2007) 1115–1130, <https://doi.org/10.1016/j.optlastec.2007.06.010>.
- [154] Y. Liu, J. Zhang, Z. Pang, Numerical and experimental investigation into the subsequent thermal cycling during selective laser melting of multi-layer 316 L stainless steel, *Opt. Laser Technol.* 98 (2018) 23–32, <https://doi.org/10.1016/j.optlastec.2017.07.034>.
- [155] E.T.A. Fathi, A. Khajepour, M. Durali, Prediction of melt pool depth and dilution in laser powder deposition, *J. Phys. D. Appl. Phys.* 39 (2006) 2613–2623.
- [156] H. Tan, J. Chen, F. Zhang, X. Lin, W. Huang, Estimation of laser solid forming process based on temperature measurement, *Opt. Laser Technol.* 42 (2010) 47–54, <https://doi.org/10.1016/j.optlastec.2009.04.016>.

- [157] Y. Huang, M.B. Khamesee, E. Toyserkani, A comprehensive analytical model for laser powder-fed additive manufacturing, *Addit. Manuf.* 12 (2016) 90–99, <https://doi.org/10.1016/j.addma.2016.07.001>.
- [158] A.B.C. Körner, E. Attar, Fundamental consolidation mechanisms during selective beam melting of powders, *Model. Simul. Mater. Sci. Eng.* 21 (2013), 85011.
- [159] S.A. Khairallah, A. Anderson, Mesoscopic simulation model of selective laser melting of stainless steel powder, *J. Mater. Process. Technol.* 214 (2014) 2627–2636, <https://doi.org/10.1016/j.jmatprotec.2014.06.001>.
- [160] K.T.A. Garg, M.M. Savalani, State-of-the-art in empirical modelling of rapid prototyping processes, *Rapid Prototyp. J.* 20 (2014) 164–178, <https://doi.org/10.1108/RPJ-08-2012-0072>.
- [161] C. Panisawas, C. Qiu, M.J. Anderson, Y. Sovani, R.P. Turner, M.M. Attallah, J.W. Brooks, H.C. Basoalto, Mesoscale modelling of selective laser melting: thermal fluid dynamics and microstructural evolution, *Comput. Mater. Sci.* 126 (2017) 479–490, <https://doi.org/10.1016/j.commatsci.2016.10.011>.
- [162] J.P.K.P. Mercelis, Residual stresses in selective laser sintering and selective laser melting, *Rapid Prototyp. J.* 12 (2006) 254–265, <https://doi.org/10.1108/13552540610707013>.
- [163] M. Shiomi, K. Osakada, K. Nakamura, T. Yamashita, F. Abe, Residual stress within metallic model made by selective laser melting process, *CIRP Ann.* 53 (2004) 195–198, [https://doi.org/10.1016/S0007-8506\(07\)60067-5](https://doi.org/10.1016/S0007-8506(07)60067-5).
- [164] M.F. Knol, Thermal Modelling of Selective Laser Melting: A Semi-analytical Approach, Delft University of Technology, 2016 <https://repository.tudelft.nl/islandora/object/uuid%3Ae6b406fe-0b13-4fc-8e13-da961b3f3718>.
- [165] M. Alimardani, E. Toyserkani, J.P. Huissoon, Three-dimensional numerical approach for geometrical prediction of multilayer laser solid freeform fabrication process, *J. Laser Appl.* 19 (2007) 14–25, <https://doi.org/10.2351/1.2402518>.
- [166] I. Tabernero, A. Lamikiz, E. Ukar, L.N.L. de Lacalle, C. Angulo, G. Urbikain, L.N. López de Lacalle, C. Angulo, G. Urbikain, Numerical simulation and experimental validation of powder flux distribution in coaxial laser cladding, *J. Mater. Process. Technol.* 210 (2010) 2125–2134, <https://doi.org/10.1016/j.jmatprotec.2010.07.036>.
- [167] D.A. de Moraes, A. Czekanski, Thermal modeling of 304 L stainless steel for selective laser melting: laser power input evaluation, *Adv. Manuf.*, ASME, Vol. 2, , 2017 <https://doi.org/10.1115/IMECE2017-7224> (p. V002T02A033).
- [168] A.V. Gusarov, I. Yadroitsev, P. Bertrand, I. Smurov, Heat transfer modelling and stability analysis of selective laser melting, *Laser Synth. Process. Adv. Mater.* 254 (2007) 975–979, <https://doi.org/10.1016/j.japsusc.2007.08.074>.
- [169] I.Y.A.V. Gusarov Ph, I. Smurov Bertrand, Model of radiation and heat transfer in laser-powder interaction zone at selective laser melting, *J. Heat Transf.* 131 (2009), 72101.
- [170] J.Y. Chen, Xue, Microstructural characteristics of laser-clad AISI P20 tool steel, *Proc. 1st Int. Surf. Eng. Congr. 13th IFHTSE Congr. Mater. Park ASM Int* 2002, p. 198.
- [171] G. Link, Layered Manufacturing of Laser-Deposited Carbon Steels, 2000.
- [172] M. Griffith, M. Schlienger, L. Harwell, Thermal Behavior in the LENS Process, Solid Free. Fabr. Symp. Proceedings, Austin, TX, 1998.
- [173] G. Ramdeen Link, Layered Manufacturing of Laser-deposited Carbon Steels, Stanford University, 2000 (ocw.stanford.edu/304643712?accountid=14906).
- [174] H. El Kadiri, L. Wang, M.F. Horstemeyer, R.S. Yassar, J.T. Berry, S. Felicelli, P.T. Wang, Phase transformations in low-alloy steel laser deposits, *Mater. Sci. Eng. A* 494 (2008) 10–20.
- [175] L. Costa, R. Vilar, T. Reti, A.M. Deus, Rapid tooling by laser powder deposition: process simulation using finite element analysis, *Acta Mater.* 53 (2005) 3987–3999.
- [176] S.R. Lewis, R. Lewis, D.J. Fletcher, Assessment of laser cladding as an option for repair of rails, *Int. Conf. Contact Mech. Wear Rail/Wheel Syst.*, 330, 2012, pp. 380–385.
- [177] Z. Bergant, J. Grum, Heat treatment effects of laser cladded 12 Ni Maraging tool steel with Ni-co-Mo alloys, *HTM J. Heat Treat. Mater.* 69 (2014) 114–123.
- [178] Z. Bergant, J. Grum, Influence of laser deposition technique on surface integrity of 12 Ni maraging tool steel, *Int. J. Microstruct. Mater. Prop.* 8 (2013) 17–26.
- [179] B. Zoran, S.J. Marko, O.J. Luis, G. Janez, Laser cladding and heat treatment of Ni-Co-Mo maraging steel, *J. ASTM Int.* 8 (2011) 1–12.
- [180] J.J. Hammell, M.A. Langerman, N.P. Saunders, Radiometri and metallurgical analysis of zone formation in elementary laser deposited thin-wall structures, *ASME 2013 Int. Mech. Eng. Congr. Expo.*, American Society of Mechanical Engineers, 2013 (p. V02AT02A001-V02AT02A001).
- [181] R.S. Amano, S. Marek, B.F. Schultz, P.K. Rohatgi, Laser engineered net shaping process for 316/15% nickel coated titanium carbide metal matrix composite, *J. Manuf. Sci. Eng.* 136 (2014), 51007.
- [182] C.H. Gür, B.O. Tuncer, Investigating the microstructure-ultrasonic property relationships in steels, 16th WCNDT-World Conf. NDT, 2004.
- [183] A.S.M.I.H. Committee, *ASM Handbook-Volume 1: Properties and Selection: Irons, Steels, and High Performance Alloys*, ASM Int., 1990 950–980.
- [184] J. Li, D. Deng, X. Hou, X. Wang, G. Ma, D. Wu, G. Zhang, Microstructure and performance optimisation of stainless steel formed by laser additive manufacturing, *Mater. Sci. Technol.* 32 (2016) 1223–1230.
- [185] K. Saiedi, L. Kvetková, F. Lofaj, Z. Shen, Austenitic stainless steel strengthened by the in situ formation of oxide nanoinclusions, *RSC Adv.* 5 (2015) 20747–20750, <https://doi.org/10.1039/C4RA16721J>.
- [186] D. Wang, D. Wang, Y. Liu, Y. Liu, Y. Yang, Y. Yang, D. Xiao, D. Xiao, Theoretical and experimental study on surface roughness of 316 L stainless steel metal parts obtained through selective laser melting, *Rapid Prototyp. J.* 22 (2016) 706–716.
- [187] P. Krakhmalev, I. Yadroitseva, G. Fredriksson, I. Yadroitsev, Microstructural and thermal stability of selective laser melted 316 L stainless steel single tracks, *south African, J. Ind. Eng.* 28 (2017) 12–19, <https://doi.org/10.17166/28-1-1466>.
- [188] R. Rashid, S.H. Masood, D. Ruan, S. Palanisamy, R.A. Rahman Rashid, M. Brandt, Effect of scan strategy on density and metallurgical properties of 17-4PH parts printed by selective laser melting (SLM), *J. Mater. Process. Technol.* 249 (2017) 502–511, <https://doi.org/10.1016/j.jmatprotec.2017.06.023>.
- [189] C. Sanz, V. Navas Garcia, O. Gonzalo, G. Vansteenkiste, V. García Navas, Structural integrity of direct metal laser sintered parts subjected to thermal and finishing treatments, *J. Mater. Process. Technol.* 213 (2011) 2126–2136, <https://doi.org/10.1016/j.jmatprotec.2013.06.013>.
- [190] L. Costa, R. Vilar, Laser powder deposition, *Rapid Prototyp. J.* 15 (2009) 264–279.
- [191] A.S.M. Handbook, Vol. 3: Alloy Phase Diagrams, 9, , ASM Int., 1992 2.
- [192] W. Hofmeister, M. Wert, J. Smugeresky, J.A. Phillip, M. Griffith, M. Ensz, Investigating solidification with the laser-engineered net shaping (LENSTM) process, *JOM* 51 (1999) 1–6.
- [193] M. Hedges, Rapid Prototyping: Laser Engineered Net Shaping (TM)-Technology, Applications and Opportunities, *Eur. Congr. Exhib. Powder Metall. Eur. PM Conf. Proc.*, the European Powder Metallurgy Association 2003, p. 1.
- [194] G.K. Lewis, E. Schlienger, Practical considerations and capabilities for laser assisted direct metal deposition, *Mater. Des.* 21 (2000) 417–423, [https://doi.org/10.1016/S0261-3069\(99\)00078-3](https://doi.org/10.1016/S0261-3069(99)00078-3).
- [195] J. Smugeresky, D. Keicher, J. Romero, M. Griffith, L. Harwell, Laser engineered net shaping (LENSTM) process: optimization of surface finish and microstructural properties, *Proc. of the World Congress on Powder Metallurgy and Particulate Materials*, Princeton, NJ, 1997.
- [196] H. El Cheikh, B. Courant, S. Branchu, X. Huang, J.-Y. Hascoët, R. Guillén, Direct laser fabrication process with coaxial powder projection of 316 L steel. Geometrical characteristics and microstructure characterization of wall structures, *Opt. Lasers Eng.* 50 (2012) 1779–1784.
- [197] J.O. Milewski, G.K. Lewis, D.J. Thoma, G.I. Keel, R.B. Nemec, R.A. Reinert, Directed light fabrication of a solid metal hemisphere using 5-axis powder deposition, *J. Mater. Process. Technol.* 75 (1998) 165–172.
- [198] M. Ma, Z. Wang, D. Wang, X. Zeng, Control of shape and performance for direct laser fabrication of precision large-scale metal parts with 316 L stainless steel, *Opt. Laser Technol.* 45 (2013) 209–216.
- [199] P.L. Blackwell, The mechanical and microstructural characteristics of laser-deposited IN718, *J. Mater. Process. Technol.* 170 (2005) 240–246.
- [200] A. Ahmadi, R. Mirzaei, N.S. Moghaddam, A.S. Turabi, H.E. Karaca, M. Elahinia, Effect of manufacturing parameters on mechanical properties of 316 L stainless steel parts fabricated by selective laser melting: a computational framework, *Mater. Des.* 112 (2016) 328–338, <https://doi.org/10.1016/j.matdes.2016.09.043>.
- [201] W.F. Smith, *Structure and Properties of Engineering Alloys*, McGraw-Hill, 1993 (doi:6.0-6).
- [202] B. Zhang, C. Coddet, Selective laser melting of iron powder: observation of melting mechanism and densification behavior via point-track-surface-part research, *J. Manuf. Sci. Eng.* 138 (2016) 51001.
- [203] K. Abdelghany, Evaluating the properties of products fabricated from commercial steel powders using the selective laser micro-welding rapid manufacturing technique, *J. New Gener. Sci.* 8 (2010) 1–10.
- [204] K. Guan, Z. Wang, M. Gao, X. Li, X. Zeng, Effects of processing parameters on tensile properties of selective laser melted 304 stainless steel, *Mater. Des.* 50 (2013) 581–586, <https://doi.org/10.1016/j.matdes.2013.03.056>.
- [205] M.T.E.M.L. Griffith, J.D. Puskar, C.V. Robino, J.A. Brooks, J.A. Phillip, E. Smugeresky, W.H. Hofmeister, M.T.E.M.L. Griffith, J.D. Puskar, C.V. Robino, J.A. Brooks, J.A. Phillip, Understanding the microstructure and properties of components fabricated by laser engineered net shaping (lens), *Mater. Res. Soc.* 625 (2000).
- [206] J. Safka, M. Ackermann, L. Volesky, Structural properties of H13 tool steel parts produced with use of selective laser melting technology, *J. Phys. Conf. Ser.*, IOP Publishing 2016, p. 12004, <https://doi.org/10.1088/1742-6596/709/1/012004>.
- [207] P.B.M. Mazur, M. Leary, M. Brandt, Numerical and experimental evaluation of a conformally cooled H13 steel injection mould manufactured with selective laser melting, *Int. J. Adv. Manuf. Technol.* 93 (2017) 881–900, <https://doi.org/10.1007/s00170-017-0426-7>.
- [208] S.K. Shah, F. Czerwinski, W. Kasprzak, J. Friedman, D.L. Chen, Effect of transition metals on energy absorption during strain-controlled fatigue of an aluminum alloy, *Int. J. Fatigue* 87 (2016) 456–470, <https://doi.org/10.1016/j.ijfatigue.2016.02.008>.
- [209] M. Zhang, C.-N. Sun, X. Zhang, P.C. Goh, J. Wei, D. Hardacre, H. Li, Fatigue and fracture behaviour of laser powder bed fusion stainless steel 316 L: influence of processing parameters, *Mater. Sci. Eng. A* 703 (2017) 251–261, <https://doi.org/10.1016/j.msea.2017.07.071>.
- [210] L.M.S. Santos, J.A.M. Ferreira, J.S. Jesus, J.M. Costa, C. Capela, Fatigue behaviour of selective laser melting steel components, *Theor. Appl. Fract. Mech.* 85 (2016) 9–15.
- [211] F. Liu, X. Lin, H. Yang, X. Wen, Q. Li, F. Liu, W. Huang, Effect of microstructure on the fatigue crack growth behavior of laser solid formed 300 M steel, *Mater. Sci. Eng. A* 695 (2017) 258–264, <https://doi.org/10.1016/j.msea.2017.04.001>.
- [212] Y. Chew, J.H.L. Pang, G. Bi, B. Song, Effects of laser cladding on fatigue performance of AISI 4340 steel in the as-clad and machine treated conditions, *J. Mater. Process. Technol.* 243 (2016) 246–257, <https://doi.org/10.1016/j.jmatprotec.2016.12.020>.
- [213] S. Da Sun, Q. Liu, M. Brandt, V. Luzin, R. Cottam, M. Janardhana, G. Clark, Effect of laser clad repair on the fatigue behaviour of ultra-high strength AISI 4340 steel, *Mater. Sci. Eng. A* 606 (2014) 46–57, <https://doi.org/10.1016/j.msea.2014.03.077>.
- [214] J.M. Lourenço, S. Da Sun, K. Sharp, V. Luzin, A.N. Klein, C.H. Wang, M. Brandt, Fatigue and fracture behavior of laser clad repair of AerMet® 100 ultra-high strength steel, *Int. J. Fatigue* 85 (2016) 18–30, <https://doi.org/10.1016/j.ijfatigue.2015.11.021>.
- [215] S. Bhattacharya, G.P. Dinda, A.K. Dasgupta, H. Natu, B. Dutta, J. Mazumder, Microstructural evolution and mechanical, and corrosion property evaluation of Cu-30Ni alloy formed by direct metal deposition process, *J. Alloys Compd.* 509 (2011) 6364–6373.

- [216] B. AlMangour, D. Grzesiak, Jenn-Ming Yang, Selective laser melting of TiC reinforced 316 L stainless steel matrix nanocomposites: influence of starting TiC particle size and volume content, *Mater. Des.* 104 (2016) 141–151, <https://doi.org/10.1016/j.matdes.2016.05.018>.
- [217] B. AlMangour, D. Grzesiak, J.-M. Yang, Nanocrystalline TiC-reinforced H13 steel matrix nanocomposites fabricated by selective laser melting, *Mater. Des.* 96 (2016) 150–161, <https://doi.org/10.1016/j.matdes.2016.02.022>.
- [218] B. AlMangour, D. Grzesiak, J.-M. Yang, In situ formation of TiC-particle-reinforced stainless steel matrix nanocomposites during ball milling: feedstock powder preparation for selective laser melting at various energy densities, *Powder Technol.* 326 (2018) 467–478, <https://doi.org/10.1016/j.powtec.2017.11.064>.
- [219] S. Wang, S. Zhang, C.H. Zhang, C.L. Wu, J. Chen, M.B. Shahzad, Effect of Cr3C2content on 316 L stainless steel fabricated by laser melting deposition, *Vacuum* 147 (2018) 92–98, <https://doi.org/10.1016/j.vacuum.2017.10.027>.
- [220] J. Hashim, L. Looney, M.S.J. Hashmi, Particle distribution in cast metal matrix composites—part I, *J. Mater. Process. Technol.* 123 (2002) 251–257, [https://doi.org/10.1016/S0924-0136\(02\)00098-5](https://doi.org/10.1016/S0924-0136(02)00098-5).
- [221] B. AlMangour, M.-S. Baek, D. Grzesiak, K.-A. Lee, Strengthening of stainless steel by titanium carbide addition and grain refinement during selective laser melting, *Mater. Sci. Eng. A* 712 (2018) 812–818, <https://doi.org/10.1016/j.msea.2017.11.126>.
- [222] B. AlMangour, D. Grzesiak, T. Borkar, J.-M. Yang, Densification behavior, microstructural evolution, and mechanical properties of TiC/316 L stainless steel nanocomposites fabricated by selective laser melting, *Mater. Des.* 138 (2018) 119–128, <https://doi.org/10.1016/j.matdes.2017.10.039>.
- [223] B. AlMangour, D. Grzesiak, J.-M. Yang, Selective laser melting of TiB2/H13 steel nanocomposites: influence of hot isostatic pressing post-treatment, *J. Mater. Process. Technol.* 244 (2017) 344–353, <https://doi.org/10.1016/j.jmatprotc.2017.01.019>.
- [224] B. Almangour, D. Grzesiak, J.M. Yang, Rapid fabrication of bulk-form TiB2/316L stainless steel nanocomposites with novel reinforcement architecture and improved performance by selective laser melting, *J. Alloys Compd.* 680 (2016) 480–493, <https://doi.org/10.1016/j.jallcom.2016.04.156>.
- [225] B. AlMangour, F. Yu, J.-M. Yang, D. Grzesiak, Selective laser melting of TiC/H13 steel bulk-form nanocomposites with variations in processing parameters, *MRS Commun.* 7 (2017) 84–89, <https://doi.org/10.1557/mrc.2017.9>.
- [226] B. AlMangour, D. Grzesiak, J.-M. Yang, Selective laser melting of TiB2/316 L stainless steel composites: the roles of powder preparation and hot isostatic pressing post-treatment, *Powder Technol.* 309 (2017) 37–48, <https://doi.org/10.1016/j.powtec.2016.12.073>.
- [227] B. AlMangour, D. Grzesiak, J.-M. Yang, Scanning strategies for texture and anisotropy tailoring during selective laser melting of TiC/316 L stainless steel nanocomposites, *J. Alloys Compd.* 728 (2017) 424–435, <https://doi.org/10.1016/j.jallcom.2017.08.022>.
- [228] B. AlMangour, D. Grzesiak, J.M. Yang, In-situ tic particle reinforced 316 L stainless steel matrix nano composites: powder preparation by mechanical alloying and selective laser melting behaviour, *Solid Free. Fabr.* 2016 Proc. 27th Annu. Int. solid free. Fabr. Symp., Austin, Texas 2016, pp. 584–591<https://sffsymposium.engr.utexas.edu/sites/default/files/2016/044-AlMangour.pdf>.
- [229] Q. Wei, S. Li, C. Han, W. Li, L. Cheng, L. Hao, Y. Shi, Selective laser melting of stainless-steel/nano-hydroxyapatite composites for medical applications: microstructure, element distribution, crack and mechanical properties, *J. Mater. Process. Technol.* 222 (2015) 444–453.
- [230] L. Hao, S. Dadbakhsh, O. Seaman, M. Felstead, Selective laser melting of a stainless steel and hydroxyapatite composite for load-bearing implant development, *J. Mater. Process. Technol.* 209 (2009) 5793–5801.
- [231] W.H. Jiang, R. Kovacevic, Laser deposited TiC/H13 tool steel composite coatings and their erosion resistance, *J. Mater. Process. Technol.* 186 (2007) 331–338.
- [232] N. Axén, K.-H. Zum Gahr, Abrasive wear of TiC-steel composite clad layers on tool steel, *Wear* 157 (1992) 189–201, [https://doi.org/10.1016/0043-1648\(92\)90197-G](https://doi.org/10.1016/0043-1648(92)90197-G).
- [233] S. Gu, G. Chai, H. Wu, Y. Bao, Characterization of local mechanical properties of laser-cladding H13-TiC composite coatings using nanoindentation and finite element analysis, *Mater. Des.* 39 (2012) 72–80.
- [234] D. Novichenko, L. Thivillon, P. Bertrand, I. Smurov, Carbide-reinforced metal matrix composite by direct metal deposition, *Phys. Procedia* 5 (2010) 369–377, <https://doi.org/10.1016/j.phpro.2010.08.158>.
- [235] X. Wang, M. Zhang, S. Qu, Development and characterization of (Ti, Mo) C carbides reinforced Fe-based surface composite coating produced by laser cladding, *Opt. Lasers Eng.* 48 (2010) 893–898.
- [236] S. Qu, X. Wang, M. Zhang, Z. Zou, Microstructure and wear properties of Fe–TiC surface composite coating by laser cladding, *J. Mater. Sci.* 43 (2008) 1546–1551.
- [237] X.H. Wang, M. Zhang, L. Cheng, S.Y. Qu, B.S. Du, Microstructure and wear properties of in situ synthesized VC carbide reinforced Fe-based surface composite coating produced by laser cladding, *Tribol. Lett.* 34 (2009) 177–183.
- [238] Q. Zhang, J. He, W. Liu, M. Zhong, Microstructure characteristics of ZrC-reinforced composite coating produced by laser cladding, *Surf. Coat. Technol.* 162 (2003) 140–146, [https://doi.org/10.1016/S0257-8972\(02\)00697-7](https://doi.org/10.1016/S0257-8972(02)00697-7).
- [239] J. Dutta Majumdar, A. Kumar, L. Li, Direct laser cladding of SiC dispersed AISI 316 L stainless steel, *Tribol. Int.* 42 (2009) 750–753, <https://doi.org/10.1016/j.triboint.2008.10.016>.
- [240] B. Du, Z. Zou, X. Wang, S. Qu, In situ synthesis of TiB2/Fe composite coating by laser cladding, *Mater. Lett.* 62 (2008) 689–691, <https://doi.org/10.1016/j.matlet.2007.06.036>.
- [241] D. Novichenko, A. Marants, L. Thivillon, P.H.P.H. Bertrand, I. Smurov, Metal matrix composite material by direct metal deposition, *Phys. Procedia* 12 (2011) 296–302, <https://doi.org/10.1016/j.phpro.2011.03.038>.
- [242] M. Doubenskaia, I. Smurov, S. Grigoriev, M. Pavlov, Complex analysis of elaboration of steel–TiC composites by direct metal deposition, *J. Laser Appl.* 25 (2013), 42009.
- [243] A. Emanian, S.F. Corbin, A. Khajepour, Effect of laser cladding process parameters on clad quality and in-situ formed microstructure of Fe–TiC composite coatings, *Surf. Coat. Technol.* 205 (2010) 2007–2015, <https://doi.org/10.1016/j.surfcoat.2010.08.087>.
- [244] A. Emanian, M. Alimardani, A. Khajepour, Correlation between temperature distribution and in situ formed microstructure of Fe–TiC deposited on carbon steel using laser cladding, *Appl. Surf. Sci.* 258 (2012) 9025–9031, <https://doi.org/10.1016/j.apsusc.2012.05.143>.
- [245] A.P.I. Popoola, B.A. Obadele, O.M. Popoola, Effects of tic-particulate distribution in aisi 304l stainless steel matrix, *Dig. J. Nanomat. Biostruct.* 7 (2012) 1245–1252.
- [246] B. Du, Z. Zou, X. Wang, S. Qu, Laser cladding of in situ TiB2/Fe composite coating on steel, *Appl. Surf. Sci.* 254 (2008) 6489–6494, <https://doi.org/10.1016/j.apsusc.2008.04.051>.
- [247] J.D. Majumdar, L. Li, Studies on direct laser cladding of SiC dispersed AISI 316 L stainless steel, *Metall. Mater. Trans. A* 40 (2009) 3001.
- [248] K. Zhang, W. Liu, X. Shang, Research on the processing experiments of laser metal deposition shaping, *Opt. Laser Technol.* 39 (2007) 549–557.
- [249] J.C. Betts, The direct laser deposition of AISI316 stainless steel and Cr3C2 powder, *J. Mater. Process. Technol.* 209 (2009) 5229–5238, <https://doi.org/10.1016/j.jmatprotc.2009.03.010>.
- [250] B. Han, M. Li, Y. Wang, Microstructure and wear resistance of laser clad Fe–Cr3C2 composite coating on 35CrMo steel, *J. Mater. Eng. Perform.* 22 (2013) 3749–3754.
- [251] P. Xu, C. Lin, C. Zhou, X. Yi, Wear and corrosion resistance of laser cladding AISI 304 stainless steel/Al2O3 composite coatings, *Surf. Coat. Technol.* 238 (2014) 9–14, <https://doi.org/10.1016/j.surfcoat.2013.10.028>.
- [252] U. Scheithauer, A. Bergner, E. Schwarzer, H.-J. Richter, T. Moritz, Studies on thermoplastic 3D printing of steel–zirconia composites, *J. Mater. Res.* 29 (2014) 1931–1940.
- [253] U. Scheithauer, T. Slawik, E. Schwarzer, H.J. Richter, T. Moritz, A. Michaelis, Additive manufacturing of metal-ceramic-composites by thermoplastic 3D-printing (3DTP), *J. Ceram. Sci. Technol.* 6 (2015) 125–132, <https://doi.org/10.4416/JCST2014-00045>.
- [254] K. Agarwal, S. Vangapally, A. Sheldon, Binder Jet Additive Manufacturing of Stainless Steel–Tricalcium Phosphate Biocomposite for Bone Scaffold and Implant Applications, *Solid Free. Fabr.* 2017 Proc. 28th Annu. Int. Solid Free. Fabr. Symp. – An Addit. Manuf. Conf. 2017 2376–2388<https://sffsymposium.engr.utexas.edu/TOC2017>.
- [255] D.S.D. Uduwage, Binder Jet Additive Manufacturing of Stainless Steel–hydroxyapatite Bio-composite, Minnesota State University–Mankato, 2015<https://cornerstone.lib.mnsu.edu/etds/432>.



Full Length Article

Mechanical properties of additive manufactured nickel alloy 625

Harvey Hack^{a,*}, Richard Link^b, Erik Knudsen^c, Brad Baker^b, Scott Olig^d^a Northrop Grumman Corporation, Undersea Systems, P. O. Box 1488, MS 9105, Annapolis, MD 21409, United States^b United States Naval Academy, United States^c Vision Point Systems, Fairfax VA 22030, United States^d Naval Research Laboratory, Washington, D.C. 20375, United States

ARTICLE INFO

Article history:

Received 23 September 2016

Received in revised form

21 December 2016

Accepted 8 February 2017

Available online 13 February 2017

Keywords:

Additive manufacturing

Alloy 625

Laser powder bed fusion

Mechanical properties

Fracture toughness

ABSTRACT

The mechanical, metallurgical and corrosion properties of Alloy 625 produced using the laser powder bed fusion (L-PBF) manufacturing process were investigated and compared with typical performance of the alloy produced using conventional forging processes. Test specimens were produced near net shape along with several demonstration pieces that were produced to examine the geometric complexity that could be achieved with the process. The additively manufactured specimens exhibited strength, fracture toughness and impact toughness that was equal to or better than properties typically achieved for wrought product. There was no evidence of stress corrosion cracking susceptibility in 3.5% NaCl solution at stress intensities up to 70 ksi-in^{1/2} after 700 h exposure. The microstructure was equiaxed in the plane of the powder bed build platform (X-Y) and exhibited a columnar shape in the Z direction although there was not any significant evidence of anisotropy in the mechanical properties.

© 2017 Elsevier B.V. All rights reserved.

1. Introduction

The project aims to develop information that can be used to reliably define the part geometry and production method (including drawing notes, raw materials and process specifications), perform quality assurance (including geometrical and internal inspections), verify the properties of the materials produced (including microstructure, strength, toughness, fracture toughness, susceptibility to stress corrosion, fatigue and corrosion fatigue, and salt water corrosion performance), and determine the limitations on the geometries that can be produced (both size and configuration). This project is a joint effort between NGUS, the United States Naval Academy, and the Naval Research Laboratory.

This paper summarizes the following portions of this project: microstructural analysis, mechanical testing, and environmental cracking testing conducted to date on Alloy 625, UNS N06625 (also known as Inconel 625 and, in this case, as IncodALLOY 625) produced by AM using the laser powder-bed process.

2. Experimental approach

A survey of the various methods of producing AM metal parts was conducted and Direct Metal Laser Sintering (DMLS), a laser powder-bed process, was chosen since it provides the best surface finishes and tolerances of the various techniques available. The vendor chosen to build the test specimens was Incodema3D in Ithaca New York. The virgin powder feedstock was EOS IncodALLOY 625. The specimens were built on an EOS 270 machine using the EOS default build parameters: "IN625_Performance_101" and were post-build heat treated in accordance with ASTM F3056 Class A [1] for stress relief per AMS 2774 [2] at 1900° F (1038 °C), held long enough to stabilize at temperature and then air cooled. The manufacturer's recommendation for post build heat treatment states that an anneal should be conducted in accordance with AMS 2774, in which an anneal at 1900° F (1038 °C) may be used as a stress relief treatment. Specification F3056 is consistent with AMS 2774. No hot isostatic pressing was performed on these specimens. The specimen types and demonstration pieces are listed in Table 1, along with the information expected to be gained from testing each specimen or from building each demonstration piece. Test sample final machining and testing was performed by the United States Naval Academy (USNA) and by the United States Naval Research Laboratory (NRL). The as-delivered specimens built by Incodema3D are shown in Fig. 1.

* Corresponding Author.

E-mail address: harvey.hack@ngc.com (H. Hack).

Table 1
Test and Demonstration Specimens.

TYPE	ORIENTATION ^a	NO.	INFORMATION SOUGHT
Large compact tension 399_CT_3W	Parallel (Y-X)	3	Crack propagation and hydrogen embrittlement
Large compact tension 399_CT_3W	Perpendicular (X-Z)	3	Crack propagation and hydrogen embrittlement
Small compact tension 1T (CT)	Parallel (Y-X)	3	Fracture toughness
Small compact tension 1T (CT)	Perpendicular (X-Z)	3	Fracture toughness
Rotating bending fatigue	Parallel (X)	12	Air and seawater fatigue
Rotating bending fatigue	Perpendicular (Z)	12	Air and seawater fatigue
Charpy V Notch	Parallel (X-Y)	3	Impact toughness
Charpy V Notch	Perpendicular (Z-X)	3	Impact toughness
Subsize tensile	Parallel (X)	3	Microstructure and mechanical properties
Subsize tensile	Perpendicular (Z)	3	Microstructure and mechanical properties
Stepped flat plate	Parallel (X-Y)	1	Warping
Stepped flat plate	Perpendicular (X-Z)	1	Warping
Threaded test block with deliberate internal defects	Threaded holes Parallel (X) and perpendicular (Z)	1	As-built and tapped threads, internal defect detectability
Valve internal part 8900074-202		1	Large demonstration part with high complexity
Lower hinge part 9002661		1	Large demonstration part with medium complexity
Upper hinge part 9002627		1	Demonstration part with simple geometry

^a Orientation in accordance with ISO/ASTM 52921 [3].



Fig. 1. Post Heat-Treated AM Alloy 625 Specimens.

All rectangular specimens were built at a seven degree angle to the edge of the build plate to prevent the recoater blade that spreads the powder on each layer from catching on an edge that is parallel to the wiper. This seven degree angle can be seen in Figs. 2–7. It took five builds to manufacture all of these parts for the test program, with each build using virgin powder. The layouts of these builds are shown in Figs. 3–7. Duplicated parts in the figures were the result of that part in the earlier build being unusable and scrapped. A small portion of one rejected subsize tensile specimen was removed for study of a heat treatment scale (black in color) that had formed due to leakage of oxygen into the furnace during the post-build stress

relief heat treatment. This scale was found to be chromium oxide, and was machined off of any test surface that was deemed to be critical to the test results such as the gage length of tensile and fatigue specimens and surfaces of fracture specimens.

3. Results and discussion

3.1. Microstructural analysis

Sections of the subsize tensile specimens Perpendicular 1 and S1 were used for microstructural analysis using a Scanning Elec-

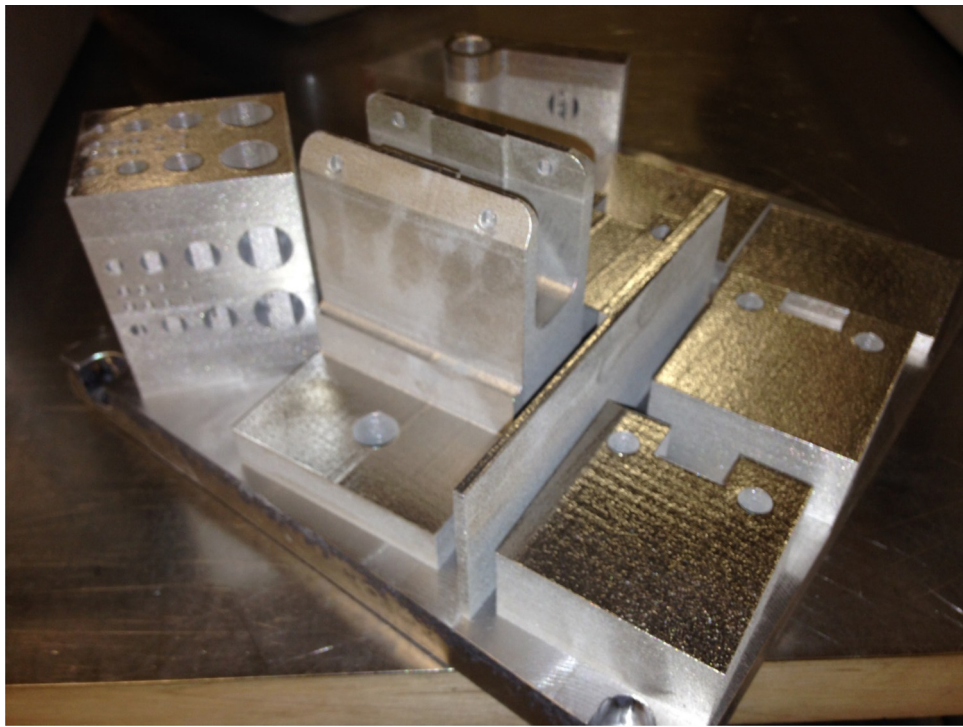


Fig. 2. AM Alloy 625 Specimens on Build Plate 1 before Stress Relief Heat Treatment.

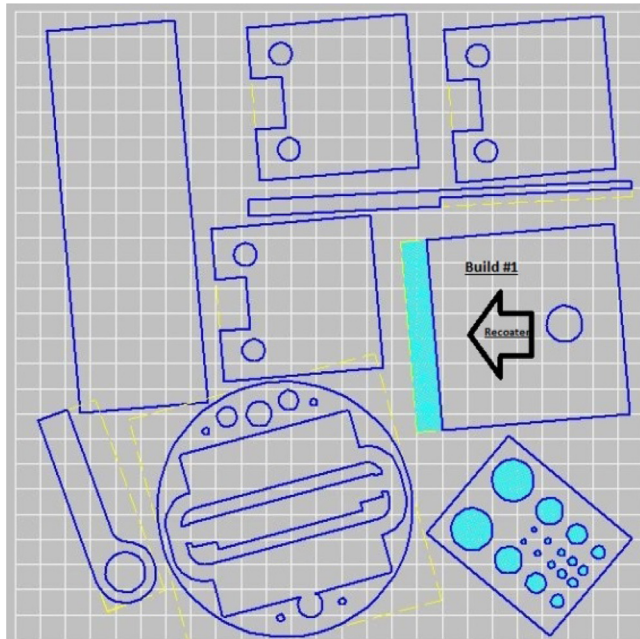


Fig. 3. Alloy 625 Build Plate 1.

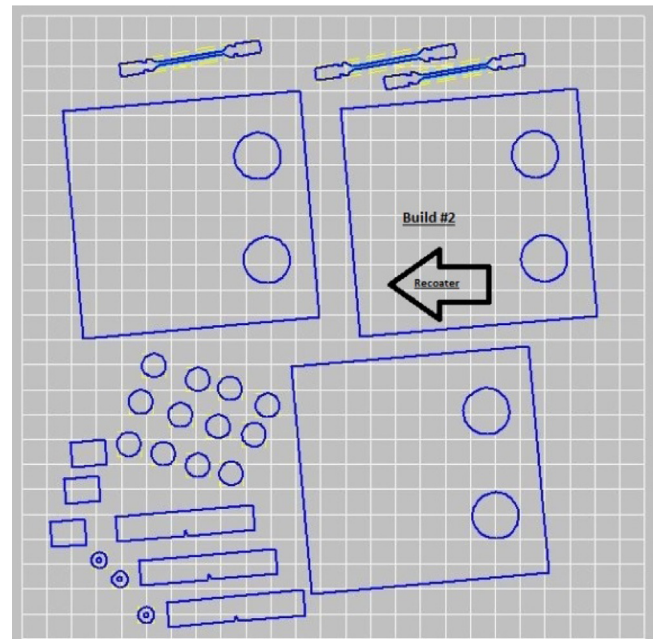


Fig. 4. Alloy 625 Build Plate 2 .

tron Microscope (SEM) with Energy Dispersive Spectroscopy (EDS) and Electron Backscatter Diffraction (EBSD). Material was taken from the grip sections of tensile samples which were not subject to elongation during tensile testing. The specimens were metallographically prepared using silicon carbide (SiC) paper and diamond polishing solutions with a final preparation polish using $0.05\text{ }\mu\text{m}$ colloidal silica on a vibratory polisher. They were not etched since grain boundary resolution was to be accomplished with EBSD. The specimens were not subjected to any additional heat treatment or stress during sample preparation.

3.1.1. Composition

The elemental composition results obtained by EDS are shown in Table 2 with ASTM F3056 required chemical composition shown for comparison. Results for carbon were not included due to inaccuracies associated with the low energy x-ray values associated with carbon. Results for phosphorous and sulfur were not included due to their limited amounts as impurities ($<0.1\text{ wt\%}$). Results for cobalt were not included because of the energy overlap between x-rays from cobalt and nickel causing high inaccuracies in cobalt measurement. Representative compositional results from six specimens analyzed are presented in Table 2 and indicate that the

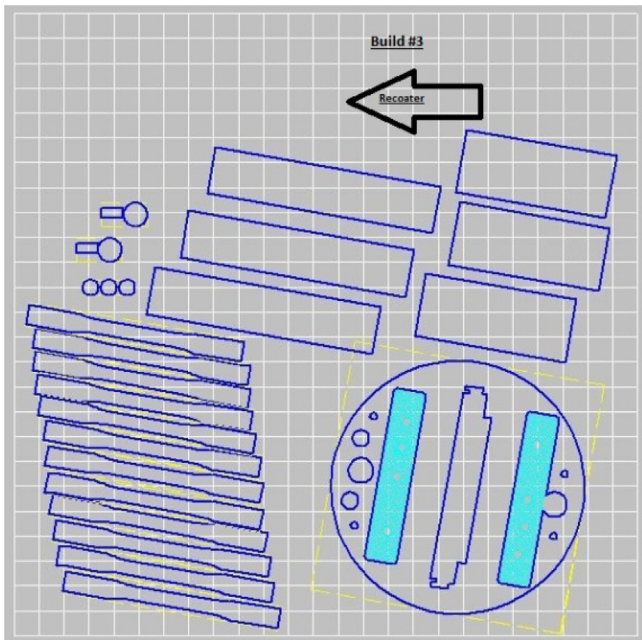


Fig. 5. Alloy 625 Build Plate 3.

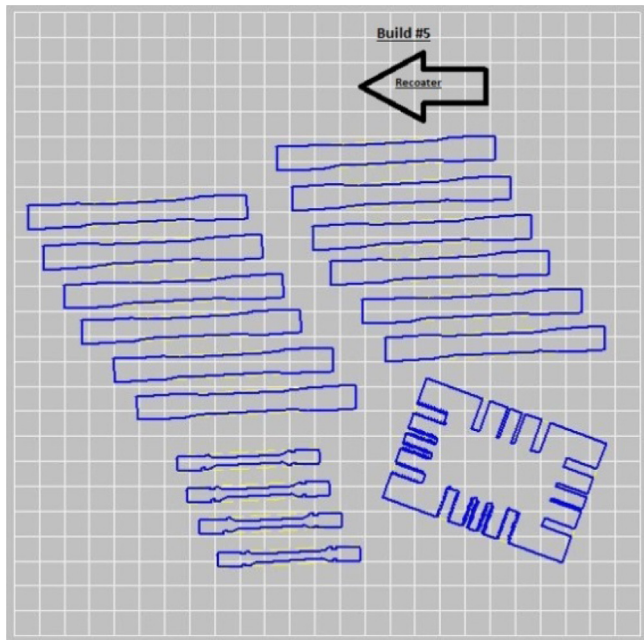


Fig. 7. Alloy 625 Build Plate 5.

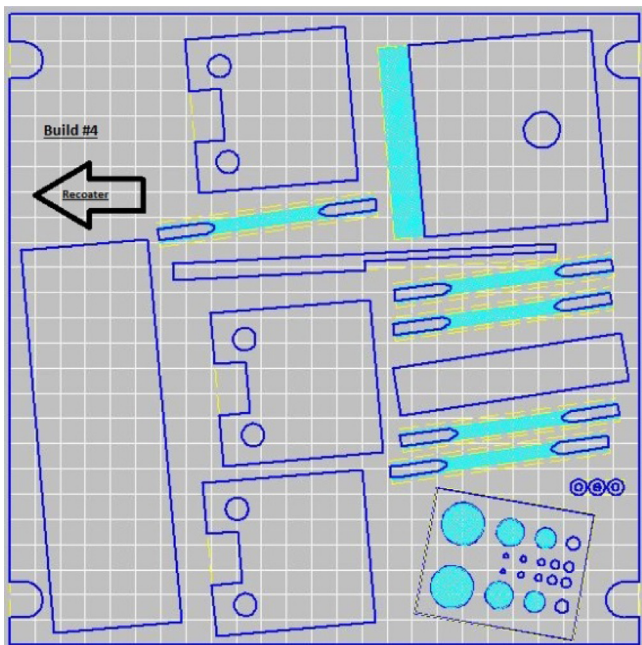


Fig. 6. Alloy 625 Build Plate 4.

Table 2

Elemental Composition of IncodALLOY 625, wt% (average of six samples).

Element	EDS results of AM Samples	ASTM F3056 [1]
Manganese	0.4	0.50 max
Silicon	1.03	0.50 max
Chromium	22.18	20.00–23.00
Molybdenum	8.79	8.00–10.00
Niobium	3.27	3.15–4.15
Titanium	1.83	0.40 max
Aluminum	2.16	0.40 max
Iron	6.6	5.00 max
Nickel	53.72	(balance)

produced material failed to meet ASTM specifications for silicon, titanium, aluminum and iron. All of these elements exceeded the maximum allowable limits as shown in Table 2.

In addition to the compositional values shown in Table 2, EDS showed a homogenous distribution of elements within specimens at the same length scale used for grain size mapping. Fig. 8 shows the elemental distribution of titanium, aluminum, iron, and nickel within a typical specimen. Of all of the elements in IncodALLOY 625 only titanium and aluminum were ever found to be consolidated into larger particles and even then only into particles on the order of up to tens of microns in size. For consistency with grain analysis, no attempts were made to analyze elemental distribution below the length scale used for grain mapping. Chromium which is present in the second largest amount in the specimens (approximately 22 wt%) was uniformly distributed in every sample tested. Iron, the fourth most prevalent element was nearly uniformly distributed without ever forming distinct iron particles. The predominant alloy, nickel, was uniformly distributed everywhere forming the base metal matrix.

3.1.2. Grain structure

In order to analyze grain structure of the additively manufactured IncodALLOY 625 specimens were analyzed using EBSD using a field emission gun SEM at 20 keV and nominal working distance of 20 mm. The face centered cubic structure of nickel in the base alloy produced excellent diffraction patterns and provides accurate orientation imaging data that was used to create inverse pole figure (IPF) maps which show grain size and shape. Exact orientation direction of IPF maps is not included since the only desirable result was grain boundaries within specimens. Additional data of texture and mis-orientation angles as well as other diffraction pattern based information can be extracted from this data but is not included for brevity. Samples of each specimen were prepared to view three orthogonal planes, parallel and perpendicular to the build direction (Z-axis). Results using EBSD are shown in Fig. 9.

The inverse pole figure maps in Fig. 9 show a highly random and unorganized grain structure, in particular in the x and y planes which are orthogonal to the build direction. In contrast, the grain structure in the z-plane is more regular, with elongation in the z-direction corresponding to grains being formed in a

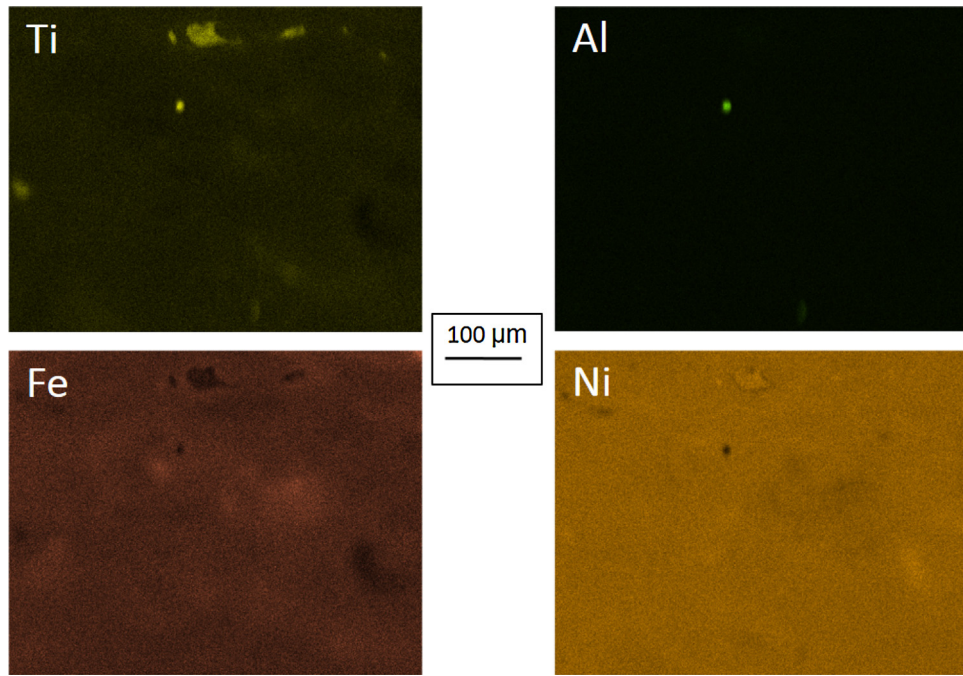


Fig. 8. Elemental distribution of major constituents in Incodalloy 625 specimens as determined by EDS. Of all elements present, only titanium and aluminum were ever found to be present in distinct particles at the same length scale used for grain mapping.

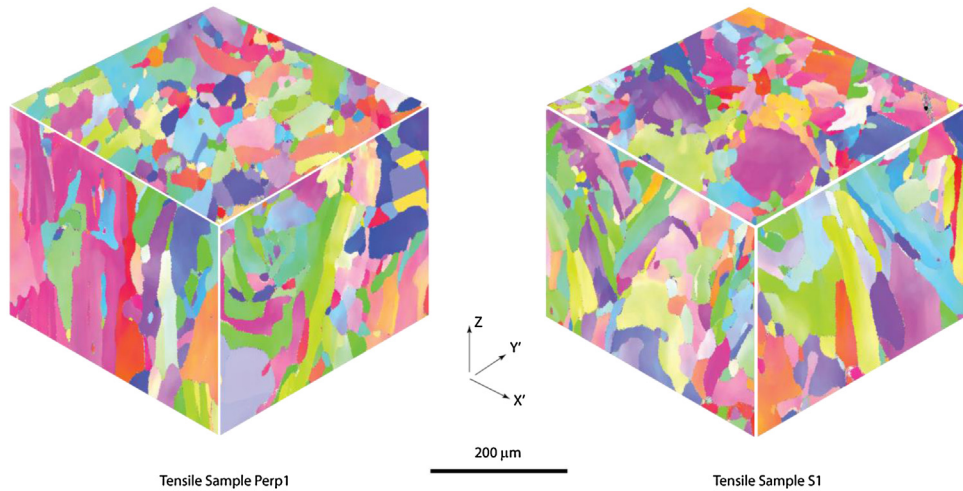


Fig. 9. Comparison of Inverse Pole Figure Maps Showing Grain Microstructure on Three Orthogonal Planes for Samples Removed from the Unstrained Ends of Tensile Specimens.

roughly columnar structure as the component is built in layers. This microstructural evolution matches what would be expected from the build process. There were not enough fields imaged to perform meaningful grain size calculations but the overall grain size and morphology between the two samples appeared very similar and does not present an obvious reason for any differences in material performance. The build direction anisotropy shown here is similar to the anisotropy seen by other authors in both nickel based superalloys and steels [4–6].

For comparison, an example inverse pole figure map taken from an as-manufactured extruded rod made from Inconel 625 by Special Metals is shown in Fig. 10. As manufactured samples shown in Fig. 10 were prepared by identical processes as AM samples shown in Fig. 9 and were made during the same nominal time frame. The grain structure of the as-manufactured Inconel 625 extruded rod shows a more organized, equiaxed, and heav-

ily twinned microstructure due to the extrusion process. Although there were no notable differences in material performance between the AM and the extruded material that appear to be directly relatable to grain structure in this study, the stark differences between the grain structure of the AM sample (Fig. 9) and the as-manufactured equivalent sample (Fig. 10) are of concern. The irregular grain structure in planes orthogonal to the build direction might produce anisotropic material performance and may have to be considered in engineering applications. Additionally, conditions which are sensitive to grain boundary morphology, such as corrosion, might change significantly between AM components and as-manufactured components. An additional option may be to anneal specimens beyond stress relief in attempts to recrystallize or further change the grain structure.

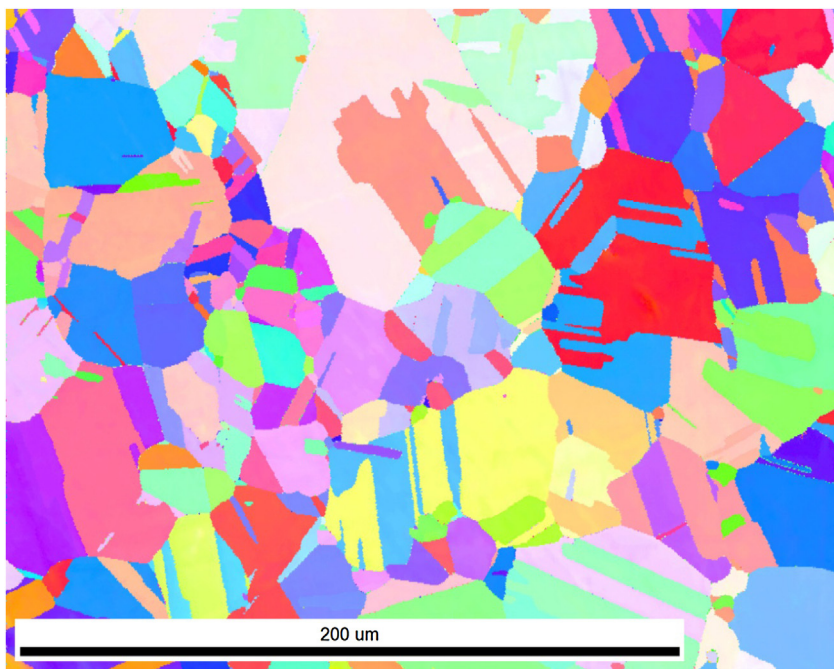


Fig. 10. Single Plane Inverse Pole Figure Maps from an Inconel 625 Extruded Rod Showing Relatively Equiaxed and Heavily Twinned Grain Structure in contrast to Fig. 9. Additional planes were analyzed and showed a similar structure.

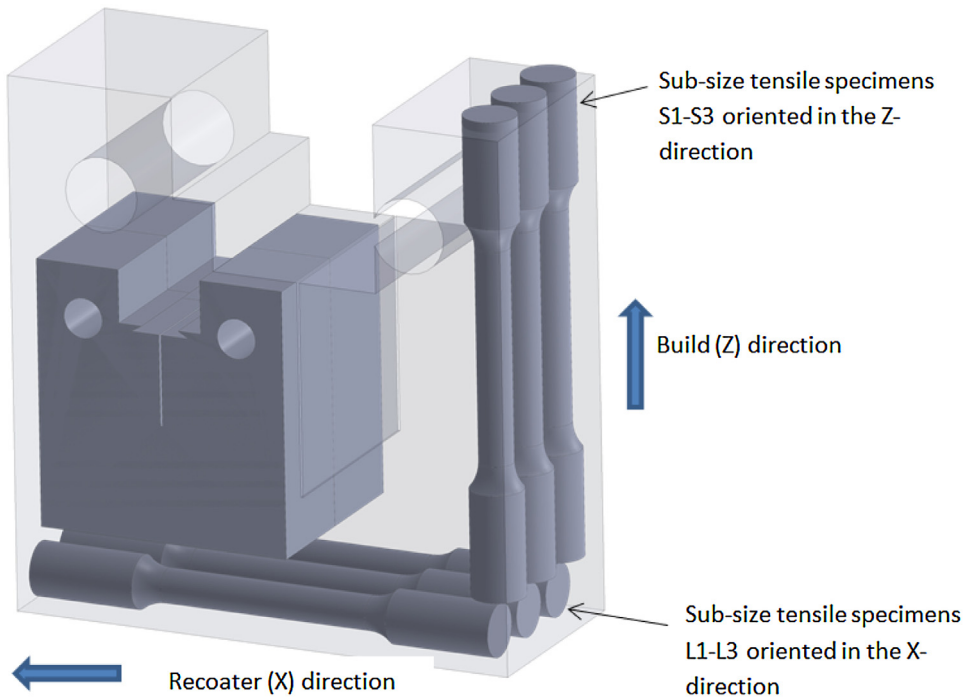


Fig. 11. Layout of Specimens Taken From Improperly Machined Compact Tension Specimen.

3.2. Mechanical testing

Mechanical testing was performed on this material in order to fully characterize its properties. This included sub-size tensile tests, Charpy impact tests, fracture toughness tests, and seawater environmental cracking tests.

3.2.1. Tensile testing

Tensile tests were conducted in accordance with ASTM Standard E08 and the data from these specimens is shown in Table 3

along with the advertised properties for IncodALLOY 625 from a data sheet and the properties for wrought material from ASTM Standards B443, B444, B446, and F3056. Highlighted test values are below specification minimums for wrought annealed or solution annealed plate. All test data for all specimens exceeded the values for wrought annealed or solution annealed plate except for elongation for two of the specimens that were oriented perpendicular to the build plate. For one of these specimens the lower limit of the elongation was estimated; the actual value could well have exceeded the value for wrought material. For the other specimen,

Table 3

Tensile Test Results for Laser Powder-Bed Stress Relieved Alloy 625 (shaded values indicate results that are below specification minimums, each row is for an individual specimen).

ID and Orientation	YS, ksi (MPa)	UTS, ksi (MPa)	ELONG, %	COMMENTS	Source
Specifications and Data Sheets					
ASTM B443, B444, B446, SAE AMS 5666: annealed	60 (414) min	120 (827) min	30 min	Wrought	[7–10]
ASTM B443, B444, B446 solution anneal	40 (276) min	100 (689) min	30 min	Wrought	[7–10]
ASTM F3056	40 (276) min	70 (483) min	30 min	Wrought	[11]
L-PBF Inco [®] ALLOY 625	40 (276) min	70 (483) min	30	annealed + HIP	[12]
L-PBF (Z)	104 (720)	151 (1040)	35	Stress relieved	[13]
L-PBF (Z)	94 (650)	135 (930)	44	Stress relieved	[13]
L-Direct Energy Deposition (X-Y)	101 (694)	153 (1052)	33	As fabricated	[14]
L-Direct Energy Deposition (Z)	71 (490)	120 (829)	43	As fabricated	[14]
L-Direct Energy Deposition	84.7 (584)	136.0 (938)	38		[15]
This Study (individual specimens)					
Parallel 1 (X)	63.8 (440)	135.9 (937)	50.3	Est. elongation from stroke	USNA
Parallel 2 (X)	60.9 (420)	130.9 (903)	50.9		USNA
Parallel 3 (X)	63.7 (439)	132.3 (912)	41	Est. elongation. Failed outside gage	USNA
L1 (X)	80.9 (558)	139.7 (963)	>45	Failed outside gage section	USNA
L2 (X)	78.1 (538)	138.9 (958)	>47	Failed at knife edge	USNA
L3 (X)	80.2 (553)	138.3 (954)	>38	Failed at knife edge	USNA
Perpendicular 1 (Z)	99.8 (688)	146.3 (1009)	>28	Est. elongation. Failed outside gage	USNA
Perpendicular 2 (Z)	96.8 (667)	140.2 (967)	29.4		USNA
Perpendicular 3 (Z)	99.6 (687)	142.5 (983)	32.8		USNA
S1 (Z)	74.5 (514)	131.1 (904)	58		USNA
S2 (Z)	74.1 (511)	128.2 (884)	51		USNA
S3 (Z)	76.0 (524)	129.4 (892)	>54	Failed at knife edge	USNA
Other Investigators					
L-PBF (X-Y)	79.6–84.6 (548.8–583.3)	139.5–143.2 (961.8–987.3)	29–33	Stress relieved and HIP	[16]
L-PBF (Z)	75.6–79.6 (521.2–548.8)	127.8–129.4 (881.1–892.2)	37–46	Stress relieved and HIP	[16]
L-PBF (X-Y)	55.7 (384)	130.2 (898)	60	As fabricated	[17]
L-PBF (Z-45)	54.5 (376)	128.1 (883)	57	As fabricated	[17]
L-PBF (X-Y)	104.4 (720)	155.2 (1070)	9	As fabricated	[18]
L-PBF (Z)	116.0 (800)	149.4 (1030)	9	As fabricated	[18]
L-PBF (X-Y)	52.2 (360)	127.6 (880)	58	Solution annealed + HIP	[19]
L-PBF (X-Y)	55.1 (380)	130.5 (900)	58	Solution annealed + HIP	[19]
EB-PBF (Z)	59.5 (410)	108.8 (750)	44	As fabricated	[19–207]
EB-PBF (Z)	47.9 (330)	111.7 (770)	69	Solution annealed + HIP	[19,20]
L-DED (X-Y)	69.2 (477)	107.9 (744)	48	As fabricated	[21]
L-DED (Z)	75.1 (518)	115.6 (797)	31	As fabricated	[21]
L-DED (X-Y)	69.6 (480)	127.9 (882)	36	As fabricated	[22,23]
L-DED (Z)	95.1 (656)	145.0 (1000)	24	As fabricated	[22,23]
L-DED (Z)	86.7 (598)	115.3 (795)	14	Unknown	[24]

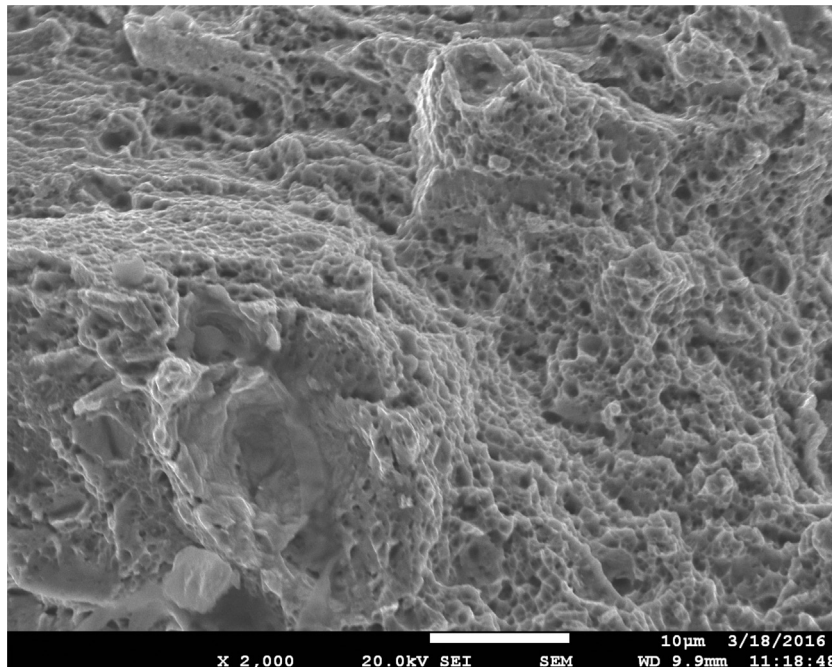
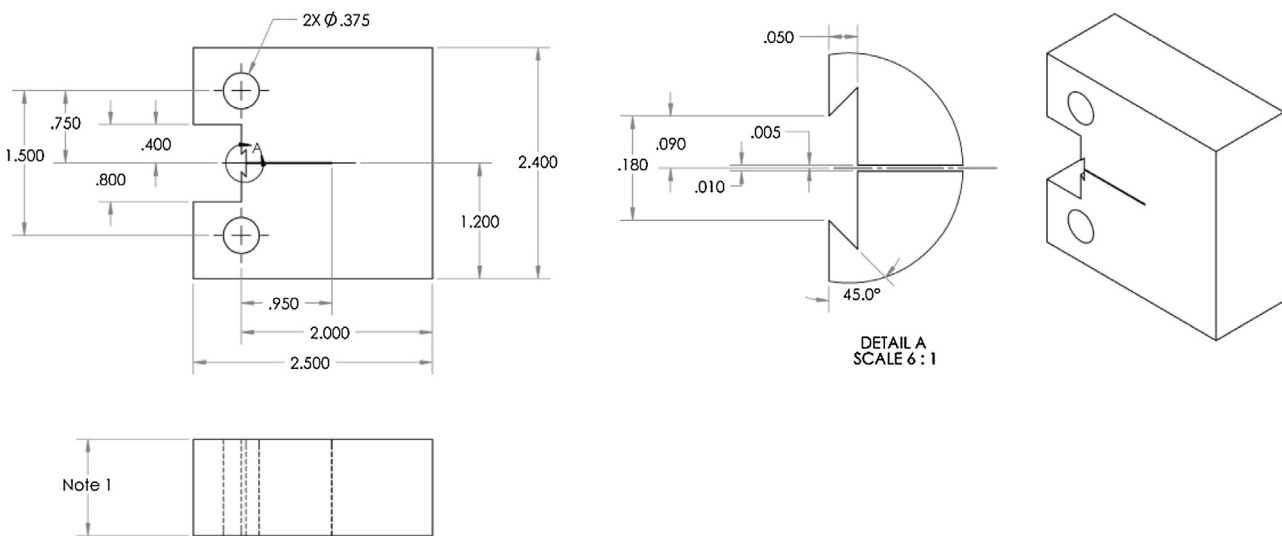


Fig. 12. Dimpled Rupture on Fracture Surface Parallel to the Build Plate.



Notes:
1. Nominal dimension is 1.000 less amount required for surface clean-up.

Fig. 13. 1T C(T) Specimens Used for Fracture Toughness Tests (all dimensions are in inches).

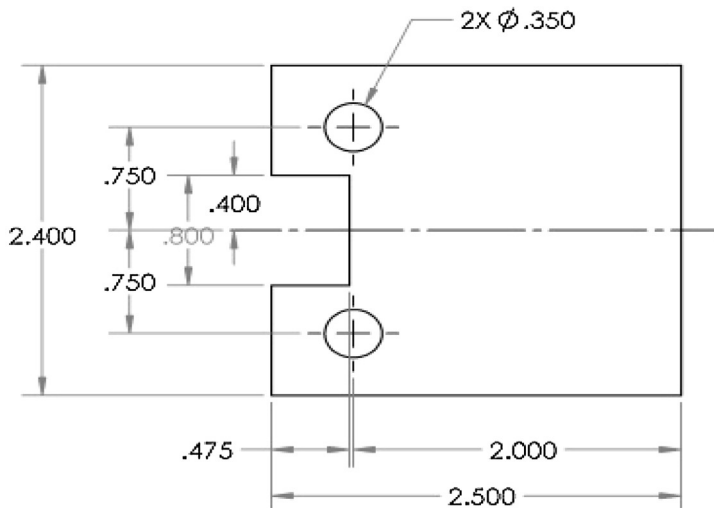


Fig. 14. Schematic Drawing of Specimen Blank Produced Using DMLS (all dimensions are in inches).

the value was within 0.6% of the wrought specification minimum. This indicates that the DMLS material had properties which were equal to, or exceeded, wrought specification minimums. One of the 0.75-in. (19-mm) thick compact tension specimens was improperly final-machined. A smaller compact tension specimen and some additional subsize tensile specimens were then taken from this improperly machined specimen as shown in Fig. 11.

There was considerable difference in the yield strength values measured for the specimens that were fabricated in the tensile specimen geometry and those that were removed from the compact specimen blank. For the specimens oriented in the X-direction (tensile axis parallel to the recoater direction), the as-fabricated specimens had a yield strength 17% less than the specimens removed from the C(T) blank. In the case of the specimens oriented in the Z-direction (tensile axis normal to the build plate), the as-fabricated specimens exhibited a yield strength about 30%

higher than specimens removed from the compact specimen blank. These differences in performance between specimens produced from near-net-shape blanks and those produced from the C(T) blank were similar in both orientations but to a much lesser degree (on the order of 5% difference). These results were unexpected since the build parameters for all of the builds were reported by Incodema3D to be identical. Even though the strength was well in excess of the specification minimums, such large variability in properties from presumably identical process parameters makes optimizing designs based on strength challenging. Higher strengths in the Z direction are likely due to the laser melting through several layers during each pass, resulting in complete fusion, whereas the rastering pattern in the X and Y directions results in partial overlap of melt pools which may not be complete, leading to gaps between raster lines that weaken the material in those directions. Some variability between properties of specimens from near-net-shape

Table 4

Charpy Impact Energy for Laser Powder-Bed Alloy 625 Stress Relieved.

ID AND ORIENTATION	Energy, ft-lb (J)
Special Metals Data Sheet	46–51.5 (62–69.8)
Parallel to build plate (X-Y)	>69 ^a , 85, 110 (>94 ^a , 115, 149)
Perpendicular to build plate (Z-X)	97, 106, 111 (131, 144, 150)

^a Energy indicator disturbed before reading actual value which was higher.

blanks and those from C(T) specimens may be due to the difference in thermal history of a large block as compared to that of a smaller specimen blank due to the different proximity of surfaces and mass where heat can be rejected. Rastering speed changes at the surfaces where the laser beam direction reverses direction may also lead to a different thermal history at surfaces from that in the bulk, leading to surface properties which are different from bulk properties. These differences can average out to result in different presented test properties. It has also been anecdotally stated that sequential builds on the same machine using identical sets of build parameters and identical feedstock may still result in some variability of properties, the reason for this being unknown at present.

Data from other investigators is quite varied and so it is difficult to compare with this study. The most thorough study on using the laser powder bed fusion (L-PBF) process was that done by EWI [16], which agreed well with this study. Strengths for L-PBF investigators other than EWI and Yadroitsev [18] tended to be lower than was found in this study, and frequently were less than the specification minimums for wrought material. In almost all cases, elongation was at least as good as wrought material however. The electron beam powder bed process (EB-PBF) performed by Murr and Amato [19] and [20] generally gave lower strengths and higher toughness than obtained in this study using L-PBF. The variability in their results makes comparisons to the EB-PBF data in this study too difficult.

3.2.2. Charpy impact testing

Room temperature Charpy impact tests were also conducted at the USNA. The Charpy energy data from these specimens is presented in Table 4, along with typical impact properties as listed in the manufacturer's data sheet for the wrought alloy. All Charpy energies for the AM material were well in excess of the typical values for wrought plate. The scatter was high enough that there was no effect of build direction that could be ascertained from the data. Charpy impact energies from this study were better than those produced by Ganesh [23], who found impact energies for as-produced material of 35–37 ft-lb (48–50J) and for stress relieved material of 37–40 ft-lb (50–54J).

The fracture surface of one of the Charpy specimens where fracture was parallel to the build plate was examined under a scanning electron microscope. Dimpled rupture was observed, as expected from the high values of fracture energy. This is shown in Fig. 12.

3.2.3. Fracture toughness testing

Fracture toughness was determined in accordance with ASTM E1820-13 [27], Standard Test Method for Measurement of Fracture Toughness using one-inch (25-mm) thick compact specimens, 1T C(T), shown in Fig. 13. The specimen blanks were fabricated to near final dimensions with the notch detail omitted and the pin holes slightly under-sized to permit finish machining to the final dimensions as shown in Fig. 14. The specimens were oriented with respect to the build platform as shown in Fig. 14. The crack planes were oriented in the X-Z and Y-X directions, following the convention for designating the crack orientation of ASTM E1823 [28]. In this nomenclature, the first letter designates the normal to the crack plane and the second letter designates the direction of crack propagation. The X and Y directions are in the plane of the build platform with the powder recoater traversing in the X-direction.

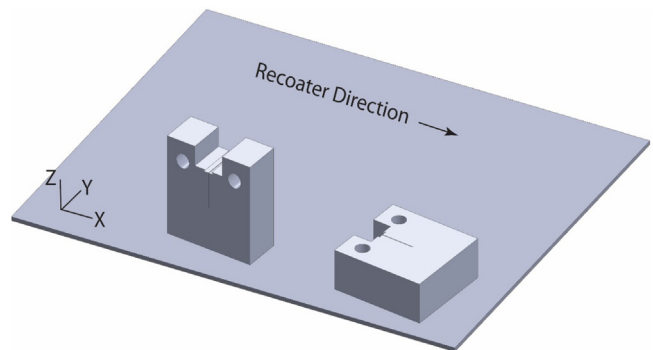


Fig. 15. Schematic Drawing of Specimen Orientation on the Build Platform (specimen sides are rotated 7° from the X-axis).

Table 5

Fracture Toughness Test Results for Laser Powder-Bed Alloy 625 Stress Relieved.

Specimen ID	Orientation	J_Q , in-lb/in ² (kJ/m ²)	Valid J_{IC}
T1	Perpendicular (X-Z)	2488 (435.7)	No
T2	Perpendicular (X-Z)	2196 (384.6)	No
Average	Perpendicular (X-Z)	2333 (408.6)	
L4	Parallel (Y-X)	2172 (380.4)	Yes
L5	Parallel (Y-X)	2611 (457.3)	Yes
L6	Parallel (Y-X)	2216 (388.1)	Yes
Average	Parallel (Y-X)	2342 (410.1)	

The specimen blanks were not oriented exactly parallel to the X and Y axes but rotated seven degrees about the Z axis as discussed previously and as shown in Fig. 15. Upon receipt of the fabricated specimens, the pin holes and notch details were finish machined using a wire electric-discharge machining process (EDM). After fatigue pre-cracking, 10% side-grooves were machined along the crack plane.

All of the specimens exhibited stable ductile tearing with no indications of crack instability. The results are summarized in Table 5 and the J-R curves are plotted in Fig. 16. All of the specimens in the X-Y orientation yielded fully qualified J_{IC} fracture toughness values. The results for the specimens in the X-Z orientation are reported as J_Q since the predicted crack extension accuracy during the test did not meet the requirements of E1820. Nevertheless, the fracture toughness values reported are representative of the material. The average fracture toughness in the two orientations was nearly identical at 2333 in-lb/in² (408.6 kJ/m²) in the Y-X orientation and 2342 in-lb/in² (410.1 kJ/m²) in the X-Z orientation. These values represent excellent fracture toughness for this alloy. The resistance curves for all of the specimens show good tearing resistance and all of the curves are very consistent.

There is not much data on the fracture toughness of wrought or cast UNS N06625 alloy available in the literature. Fracture toughness tests on centrifugally-cast Alloy 625 and rolled plate were performed by the Naval Surface Warfare Center, Carderock Division in the early 2000's.¹ This data was never published in the open literature but is useful for comparison. The rolled plate had a yield strength of 81 ksi (558 MPa) and an average fracture toughness of 963 in-lb/in² (168 kJ/m²) in the T-L orientation and 1412 in-lb/in² (247.3 kJ/m²) in the L-T orientation. The centrifugally cast specimens had much higher toughness than the plate but the yield strength of the centrifugally cast product was in the 40–50 ksi (276–345 MPa) range so it was not possible to measure a valid fracture toughness using the 1-in (25-mm) thick specimens. The toughness of the centrifugally cast material was in excess of 2100

¹ Private communication, C. Roe, Naval Surface Warfare Center, Carderock Division, 2015.

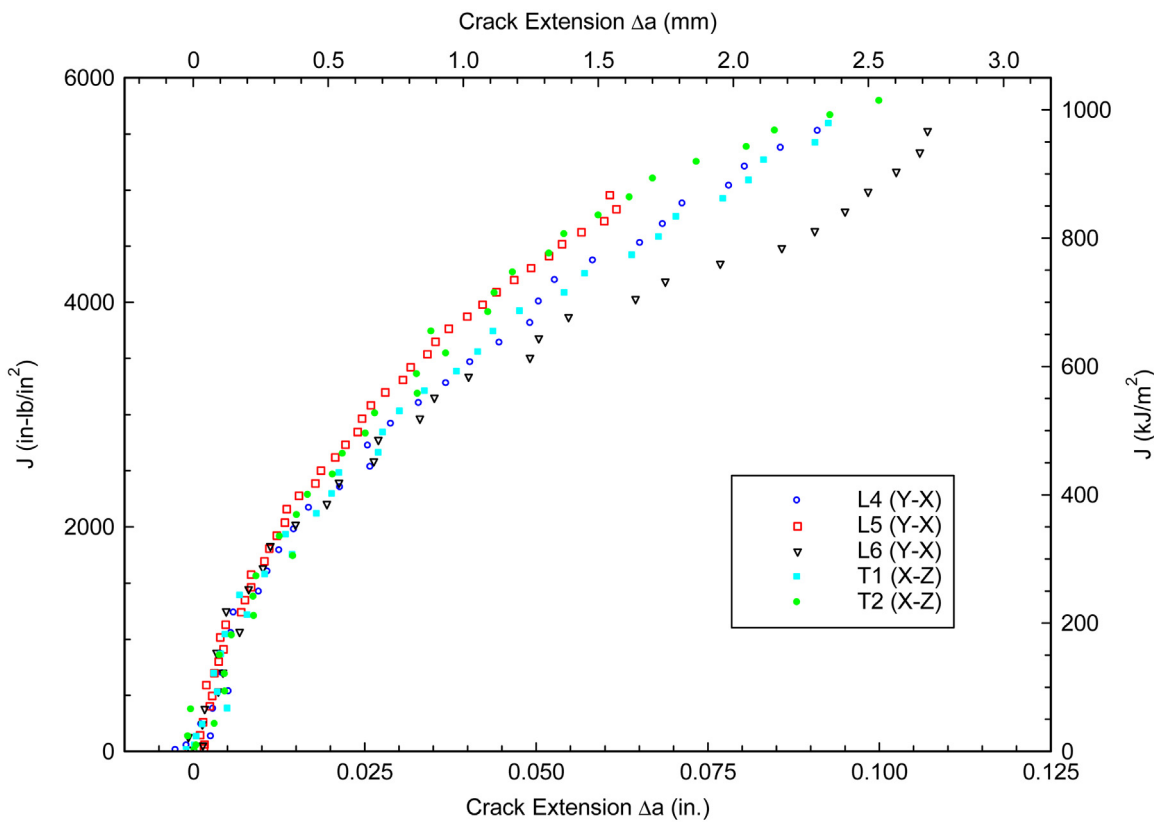


Fig. 16. J-R curves for the direct laser sintered UNS N066250 alloy.

in-lb/in² (367.8 kJ/m²); however, given the very low yield strength of the cast product, it is not a good material for comparison with the direct laser sintered material in this study.

Ganesh et al. [26] performed fracture toughness tests on laser rapid manufactured Alloy 625 material and reported J-integral fracture toughness in the range of 1140–1450 in-lb/in² (200–254 kJ/m²) for material with a yield strength of 78 ksi (538 MPa) and a tensile strength of 100 ksi (689 MPa).

In summary, the UNS N06625 material evaluated in the present study exhibited excellent fracture toughness of 2333–2342 in-lb/in² (408.6–410.1 kJ/m²) that was superior to values reported for rolled plate and other laser rapid manufactured product with similar tensile properties. There was no observed effect of specimen orientation on the fracture toughness.

3.3. Environmental cracking testing

Six compact tension fracture samples were built to be tested in 3.5% (0.6 M) NaCl under quiescent conditions. The electrolyte was circulated via an aquarium pump and was changed every 1–2 weeks. The samples were fatigue pre-cracked at the USNA and tested at the Naval Research Laboratory. The tests were run under constant displacement conditions and the applied load was recorded during the test. A marked decrease in load is indicative of a growing crack. The step loading testing protocol used on parallel specimens 1 and 3 and on perpendicular specimen 1 is described in Table 6, however parallel specimen 5 was directly loaded to 70 ksi-in^{1/2} (77 MPa-m^{1/2}) and held for 700 h.

No load drop was seen at K levels of 70 ksi-in^{1/2} (77 MPa-m^{1/2}) for any specimen for 600–700 h. The AM material therefore shows promise for this modest hold time to have toughness greater than or equal to that which would be expected from typical wrought plate.

Table 6
Step Loading Protocol for First Two Specimens.

K, ksi-in ^{1/2} (MPa-m ^{1/2})	Time, hours
40 (44)	100
50 (55)	100
60 (66)	100
70 (77)	600

3.4 Threaded test block

4. Conclusions

All testing to date indicates that Alloy 625 produced by additive manufacturing using the laser powder-bed process with a post-build stress-relief heat treatment but without HIP demonstrates properties similar to, or better than wrought material. The AM process produced a nearly homogenous distribution of elements which closely matched ASTM requirements. The evolved grain structure appears to be columnar in nature with respect to the build direction and random in planes orthogonal to the build direction that are hypothesized to lead to anisotropic material performance; however, there were no direct material property consequences that were relatable to this irregular grain structure. The tensile properties, particularly the yield strength, showed up to 30% variability between builds but exceeded specification minimums for wrought material in all cases. Possible reasons for the differences are presented. It is likely that good performance of this alloy when produced by AM is relatively insensitive to the build parameters, since this alloy gets its strength from solid solution strengthening and not from precipitation hardening.

For this material, although female threads can be directly built of almost any size and require minimal clean-up to function, the threads so produced have a rough surface which is not suitable

for use in aerospace applications where a defined torque-tension relationship is needed for proper screw pre-load.

Future work

Attempts to further change the grain structure of AM alloys by post manufacturing heat treatments are planned in order to see if the grain structure can be made to more closely resemble a traditionally manufactured grain structure. Both fatigue and environmental fatigue testing in seawater is planned to be conducted on the alloy 625 specimens already built, both parallel and perpendicular to the build (Z) axis, using an R.R. Moore-type rotating cantilever fatigue machine at the Naval Research Laboratory. Additional environmental toughness tests on this material will be done on the remaining alloy 625 specimens with cathodic protection applied up to 70 ksi-in^{1/2}. It is planned to repeat this entire testing protocol for titanium-6Al-4V ELI (grade 23) built by the laser powder-bed process.

Acknowledgements

This work was supported by the Engineering Special Projects program at Northrop Grumman Corporation, Undersea Systems, administered by Jeff Luente. The support and encouragement of Mr. Alan Jennings is gratefully acknowledged. Portions of this work were supported by the Project Support Branch of the United States Naval Academy, and by the Naval Research Laboratory, administered by Dr. Paul Natishan.

References

- [1] Standard Specification for Additive Manufacturing nickel Alloy (UNS N06625) with Powder Bed Fusion, Standard F3056 ASTM International, West Conshohocken, PA, 2015.
- [2] Heat Treatment, Wrought Nickel Alloy and Cobalt Alloy Parts, AMS 2774, SAE International, Warrendale, PA.
- [3] ISO/ASTM52921-13: Standard Terminology for Additive Manufacturing—Coordinate Systems and Test Methodologies, ISO/ASTM 52921, ASTM International, West Conshohocken, PA, 2015.
- [4] M. Cloots, P.J. Uggowitzer, K. Wegener, Investigations on the microstructure and crack formation of IN738LC samples processed by selective laser melting using Gaussian and doughnut profiles, *Mater. Des.* 89 (2016) 770–784, 1/5.
- [5] L.N. Carter, C. Martin, P.J. Withers, M.M. Attallah, The influence of the laser scan strategy on grain structure and cracking behaviour in SLM powder-bed fabricated nickel superalloy, *J. Alloys Compound* 615 (2014) 338–347, 12/5.
- [6] T. Niendorf, S. Leuders, A. Riemer, H.A. Richard, T. Tröster, D. Schwarze, Highly anisotropic steel processed by selective laser melting, *Metall. Mater. Trans. B* 44 (2013) 794–796.
- [7] Standard Specification for Nickel-Chromium-Molybdenum-Columbium Alloy (UNS N06625) Plate, Sheet, and Strip, Standard B443, ASTM International, West Conshohocken, PA.
- [8] Standard Specification for Nickel-Chromium-Molybdenum-Columbium Alloys (UNS N06625) Pipe and Tube, Standard B444, ASTM International, West Conshohocken, PA.
- [9] Standard Specification for Nickel-Chromium-Molybdenum-Columbium Alloy (UNS N06625) and Nickel-Chromium-Molybdenum-Silicon Alloy (UNS N06219) Rod and Bar, Standard B446, ASTM International, West Conshohocken, PA.
- [10] Nickel Alloy, Corrosion and Heat Resistant, Bars, forgings, Extrusions, and Rings, 62Ni –21.5 Cr –9.0Mo –3.65 (Cb + Ta), Annealed, AMS 5666, SAE International, Warrendale, PA.
- [11] Standard Specification for Additive Manufacturing Nickel Alloy (UNS N06625) with Powder Bed Fusion, Standard F3056, ASTM International, West Conshohocken, PA.
- [12] Inodalloy Materials Chart, Document I3D8.1r2, Inodalloy3D, Ithaca, NY.
- [13] Data sheet EOS NickelAlloy IN625 TMS, Weil/10.2011.
- [14] Data Sheet, LENS Superalloys, Optomec, Inc., Albuquerque, NM, January 2015.
- [15] Metal 3d Printing Materials, <http://www.optomec.com/3d-printed-metals/lens-materials/>, Optomec Additive Manufacturing, 8/6/2015.
- [16] Volume 1: Development and Measurement Analysis of Design Data for Laser Powder Bed Fusion Additive Manufacturing of Nickel Alloy 625 – Final Technical Report, Cooperative Agreement No. 70NANB12H264 delivered to NIST, Project No. 53776GTH, EWI, August 28, 2014.
- [17] E.M. Betts, Using innovative technologies for manufacturing rocket engine hardware, in: JANNAF 6th Liquid Propulsion Subcommittee Meeting, 5–9 Dec. 2011; Huntsville, AL, 2011.
- [18] I. Yadroitsev, et al., Mechanical properties of samples fabricated by selective laser melting, in: 14èmes Assises Européennes Du Prototypage & Fabrication Rapide, 24–25 Juin 2009, Paris, 2009.
- [19] K.N. Amato, J. Hernandez, L.E. Murr, E. Martinez, S.M. Gaytan, P.W. Shindo, Comparison of microstructures and properties for a Ni-Base superalloy (Alloy 625) fabricated by electron and laser beam melting, *J. Mater. Sci. Res. Can. Center Sci. Educ.* 1 (2) (2012).
- [20] L.E. Murr, E. Martinez, S.M. Gaytan, D.A. Ramirez, B.I. Machado, P.W. Shindo, J.L. Martinez, F. Medina, J. Wooten, D. Cisca, U. Ackelid, R.B. Wicker, Microstructural architecture, microstructures, and mechanical properties for a nickel-base superalloy fabricated by electron beam melting, *Metall. Mater. Trans. A: Phys. Metall. Mater. Sci.* 42 (June (11)) (2011) 3491–3508.
- [21] L. Xue, et al. Investigation of laser consolidation for manufacturing functional net-shape components for potential rocket engine applications ICALO, 2007, Paper 402 p. 161–169, 2007.
- [22] M. Rombouts, et al. Material study of laser cladded Inconel 625. Innovative Developments in Virtual and Physical Prototyping, eds. Bartolo et al., p. 333–337, 2011.
- [23] M. Rombouts, Laser metal deposition of Inconel 625: microstructure and mechanical properties, *J. Laser Appl.* 24 (2012) 052007.
- [24] B. Dutta, et al., Rapid manufacturing and remanufacturing of DoD components using direct metal deposition, *AMMTIAC Q.* 6 (2) (2011) 5–9.
- [25] G.P. Dinda, A.K. Dasgupta, J. Mazumder, Laser aided direct metal deposition of Inconel 625 superalloy: microstructural evolution and thermal stability, *Mater. Sci. Eng. A* 509 (2009) 98–104.
- [26] Ganesh Puppala, Aniruddha Moitra, S. Sathyaranayanan, Rakesh Kaul, G. Sasikala, Ram Chandra Prasad, Lalit M. Kukreja, Evaluation of fracture toughness and impact toughness of laser rapid manufactured inconel-625 structures and their co-relation, *Mater. Des.* 59 (2014) 509–515.
- [27] ASTM E 1820-13 Standard Test Method for Measurement of Fracture Toughness, ASTM Annual Book of Standards, Vol. 03.01 ASTM International, West Conshohocken, PA, 2013.
- [28] ASTM E 1823-12 Standard Terminology Relating to Fatigue and Fracture Testing, ASTM Annual Book of Standards, Vol. 03.01 ASTM International, West Conshohocken, PA, 2012.
- [29] P. Ganesh, R. Kaul, C.P. Paul, Pragya Tiwari, S.K. Rai, R.C. Prasad, L.M. Kukreja, Fatigue and fracture toughness characteristics of laser rapid manufactured inconel 625 structures, *Mater. Sci. Eng. A* 527 (2010) 7490–7497.



LiM 2011

Process and Mechanical Properties: Applicability of a Scandium modified Al-alloy for Laser Additive Manufacturing

K. Schmidtke^{a,c,*}, F. Palm^a, A. Hawkins^b, C. Emmelmann^c

^aEADS Innovation Works, Munich 81663, Germany

^bEADS Innovation Works, Bristol BS99 7AR, England

^cHamburg University of Technology, Hamburg 21073, Germany

Abstract

The applicability of an aluminium alloy containing scandium for laser additive manufacturing (LAM) is considered. Modified aluminium alloys with a scandium content beyond the eutectic point offer great potential to become a high prioritized aerospace material. Depending on other alloying elements like magnesium or zirconium, strongly required weight reduction, corrosion resistance and improved strength properties of metallic light weight alloys can be achieved. The development, production and testing of parts built up by a laser powder bed process will be presented with regard to the qualification of the new material concept “ScalmalloyRP®” for laser additive manufacturing.

Keywords: Laser Additive Manufacturing (LAM); scandium; Al alloy; ScalmalloyRP; mechanical properties; microstructure

1. Introduction

Although high performance materials like carbon fibre reinforced plastics gain more and more importance, aluminium alloys will furthermore play an important role in aircraft industry in the future. Existing Al-alloys were improved within the last few decades and static strength properties have reached a level over 600MPa (e.g. 7xxx or 2xxx Al-alloys). But not only improved strength properties are required for structural efficiency of high performance aerospace applications, high plasticity as well as good corrosion and fatigue resistance has to be guaranteed. Over the last years scandium and zirconium as alloying elements have become a major interest for researchers all over the world [1-9]. The improvements of properties that can be achieved by adding these elements to an Al-alloy are remarkable. Depending on the composition a significant increase of strength behaviour by precipitation hardening after annealing as well as grain refinement can be achieved [2,7]. Higher strengths (e.g. at 7xxx Al-alloys) are normally associated with an increase of corrosion susceptibility and decrease of ductility. Scandium is the key element of alloy investigations at EADS Innovation Works since 2002 regarding the combination of high strength properties with a reduction of density.

* Corresponding author. Tel.: +49-(0)89-607-20836; Fax: +49-(0)89-607-25408.
E-mail address: katja.schmidtke@eads.net

These alloy investigations were based on 5xxx AlMg-alloys, which offer high solid solution hardening addition as well as an improved corrosion resistance. The main idea of the material concept Scalmalloy® is now to combine these positive effects to get an optimized all-in-one high strength Al-alloy. Literature has shown that high cooling rates are necessary to freeze a hypereutectic Al-Scandium composition in solid solution [1-2].

Increasing requests of new metallic material concepts are closely connected with the application of new and improved manufacturing methods. Rapid manufacturing techniques became great attention in the aerospace community because they enable a rapid development of complex and topology optimized parts with few process steps. Lightweight structures can be manufactured with a high degree of geometric freedom and almost without manufacturing limits. New design possibilities like thin walled structures or complex lattice interior structures can be considered by the application of additive manufacturing concepts of metal parts. A virtual model is sliced into several layers which are built up successively. Meanwhile there are several of additive techniques available. The laser based powder bed technique, used for the following investigation, offers powder layers of a certain thickness in which the target geometry is melted by a laser. The central question then becomes: Does the laser melting process offer rapid solidification with cooling rates that are sufficient to keep all alloyed scandium in a hyper eutectic Al-scandium composition? In this case, how might the use of LAM affect the properties of ScalmalloyRP material?

2. Experimental procedures

There are variants of suitable alloy systems depending on the percentage of scandium and magnesium applicable at the moment. ScalmalloyRP0,66-4,5 with a moderate scandium content of 0,66wt.% and a relative high content of 4,5wt.% magnesium was chosen for the first series of tests. Fabrication of the metal powder was done by gas atomization. Aluminium scandium master alloy (2 wt % Sc) was molten and magnesium, manganese, and zirconium were added. The composition of the alloy was determined chemically and is given in Table 1.

This ScalmalloyRP powder variant was combined with a laser based additive manufacturing process that realizes a layer wise fabrication of a 3D structure from CAD-data. That is done by melting or welding lattice structures directly in the metal powder layer of a predefined thickness. For the following investigation, the EOS M 270 machine was used. Influencing process parameters are 1st laser related (laser power, spot size etc), 2nd powder related (particle shape, size, distribution, layer thickness etc.) and 3rd scan related (scan speed, scan strategy, scan spacing) [10]. Scanning was divided in two different modes. The contour mode was used for the outline of the cross section, and the fill mode was used for the rest of the cross section. This was done because of accuracy and surface finishing reasons [10]. The Laser power of the EOS machine is limited to 200W, therefore it was set to 195W and a layer thickness of 20µm was chosen. To determine scan related, applicable parameters for an equally and non-porous consolidation of the welding paths, 20 test cubes were manufactured within one build sequence by variation of hatch distance and scan speed. The microstructure of each cube was evaluated by means of optical microscopy at various magnifications. After this initial study tensile test specimen were built up in three different orientations (different angles of 0°; 45°; 90°) and afterwards mechanically milled in accordance to DIN 50125.

The most suitable ageing response was expected at 325° for 4 hours [3, 8-9]. To assess if the desired hardening effect of Al3Sc precipitates occurs, Vickers hardness tests were done on one test cube in “as built up” condition and in “after artificial ageing” condition. Afterwards all tensile test specimens were aged at 325°C for 4 hours.

After testing the tensile test specimen in accordance to DIN EN ISO 6892 the fracture appearance was characterized macroscopically and also microscopically with a scanning electron microscope.

Table 1 chemical composition of ScalmalloyRP0,66-4,5 (wt.%)

Alloy	Sc	Mg	Zr	Si	Fe	Cu	Mn	Cr	Zn	Ti	Ni	Pb	Sn
ScalmalloyRP0,66-4,5	0,66	4,5	0,37	0,17	0,068	<0,001	0,51	0,002	0,036	0,006	<0,001	<0,001	0,009

3. Results

3.1. Ageing response

Vickers micro hardness tests were performed to determine whether artificial ageing of the LAM ScalmalloyRP0,66-4,5 material at 325°C for 4 hours showed the desired effect. In Figure 1 two hardness curves (for “as built up”- and “after artificial ageing” condition) are shown. The average hardness (HV0,3) of the “as built up” cube is approximately 105. For the “after artificially ageing” cube, a value of 177 was achieved. The significant increase in hardness indicates a distinct hardening effect.

3.2. Microstructure

The results of the parameter study regarding density are shown in Figure 2. This matrix consists of micro sections of the test cubes for different scan speeds and hatch distances. A broadened hatch distance (in direction of arrow) leads to a noticeable loss of density as well as an increasing scan speed (in direction of arrow). For several process parameters micro pores occur in an acceptable range for the investigated application. The used combination (encircled in Figure 2) was chosen for the final build up of tensile test specimen time due to time restraints and an acceptable density value.

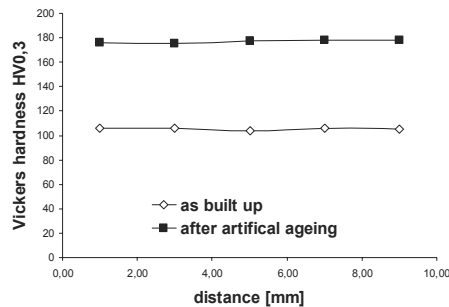


Figure 1. Vickers hardness curves of test cubes in “built up” and “after artificial” ageing condition [325°C/ 4h]

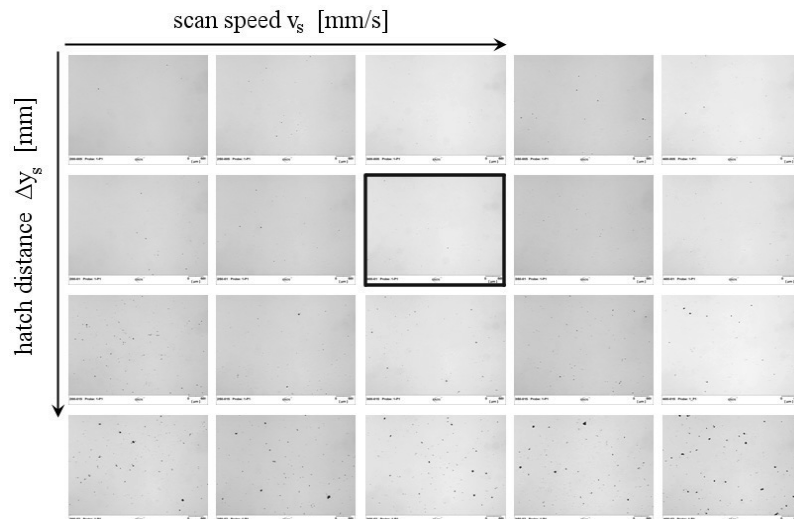


Figure 2. Matrix of parameter study with increasing hatch distance and scan speed; chosen parameter is encircled

3.2.1. Static mechanical properties

The average results of each orientation are shown in Figure 3(a). Each build-up orientation (0° ; 45° , 90°) obtained yield strengths over 500MPa and tensile strengths over 520MPa. A correlation of the strengths with the build-up orientation was observed, although the variation of the strength behaviour was less than 5%. The test specimens tested parallel to the layer build up orientation, have the highest tensile strength with over 530MPa. In addition to the high strength properties, the ductility of the additive manufactured ScalmalloyRP material was remarkable. The mean elongation was 14% and the reduction of area was 20%.

3.2.2. Fractography

A precise fractography study of the fracture surface was performed after testing the additive manufactured and aged specimen. The fracture appearance can be seen in Figure 3(b) - Figure 4(a),(b). It shows fast fracture at 45° , a visible reduction of area, and the existence of micro pores. The reduction of area is one characteristic that indicates ductility. Furthermore, the fine dimple structures shown in Figure 4 (a) proves the occurrence of ductile fracture. In addition to ductility features, several types of inclusions are observed at the base of a few grains. Some fractographs also show small areas without full coalescence (Figure 4 (b)).

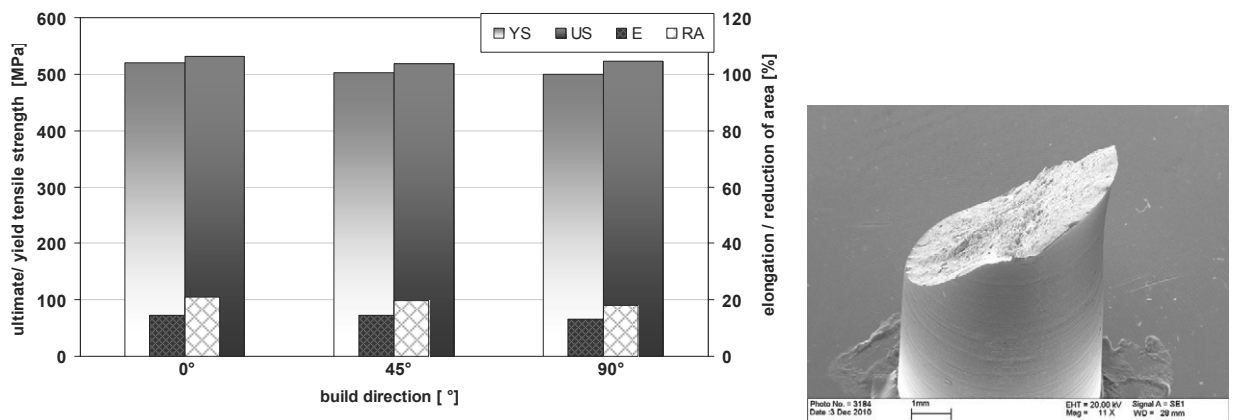


Figure 3. (a) Mechanical properties: ultimate strength, yield strength, reduction of are, elongation; (b) appearance of fracture: reduction of area

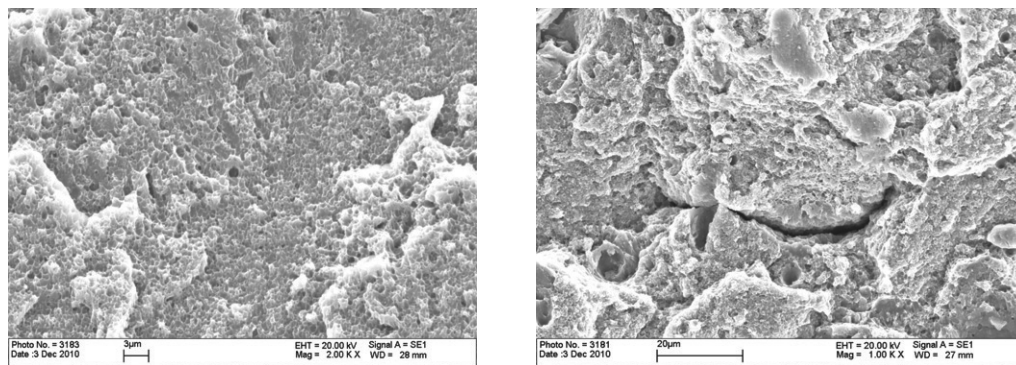


Figure 4. (a) appearance of fracture: dimple structure; (b) feature in microstructure without full coalescence

4. Discussion

The primary goal of ScalmalloyRP material for the use of additive manufacturing is to obtain a microstructure with maximum density while simultaneously forming a supersaturated solid solution. As described in literature [1-2], high cooling rates are required to constrain a supersaturated solid solution and to get high precipitation hardening effects after ageing. The addition of Scandium has enhanced the strength properties by forming a considerable amount of Al₃Sc after ageing at 325°C over 4 hours. A detailed investigation of the exact amount of Al₃Sc and/or Al(Zr_xSc_y) precipitates will be done in further research. The precipitation hardening effect was most likely increased by the addition of Zirconium which precipitates on the Sc rich core, forming a shell. Magnesium is another element which contributed to the high strength results by solid solution hardening. It is established that Scandium leads to grain refinement in Al-Mg alloys and this has a major effect on the ductility. High elongation and reduction of area values for an Al-alloy are without doubt a proof of plasticity. The grain refinement was observed on several fractographs which showed areas of very fine grains of 1 µm. The existence of micro voids and process pores did not influence the static mechanical properties. Small micro cracks and areas without full coalescence arose during the laser melting process. Poorly bonded powder grains, layer or inclusions at the base of grains arise for example due to powder contamination or because of less convenient process parameter. Another test series will be done to identify next to the grain size, the grain distribution of the powder regarding density and inclusions in grains.

The high strength properties indicate that sufficiently high cooling rates occurred during the laser additive manufacturing and that a supersaturated solid solution was realised. An unexpected high process stability level was achieved with a scatter of results less than 1% for each build-up orientation. The stress-strain-curves of the specimens were nearly identical for each orientation. The mean measured tensile strength of horizontally (0°) built up test specimens exceeded the measurement of vertical and 45° build ups by only 1,5% and 3% respectively. Nearly the same applies to the yield strength. The variation in each orientation in elongation and reduction of area was insignificant.

The suitability of the ScalmalloyRP for aerospace applications in combination with laser additive manufacturing is proofed. In Table 2 a comparison of alternatives to ScalmalloyRP and laser additive manufacturing is given. Another variant to produce complex high strength parts for aerospace application is, for example, milling of a 7050 plate. The ultimate and yield strength are equivalent to ScalmalloyRP material but only on the expense of ductility. On the other hand casting of AC42200 can provide higher ductility but it can not assure high strength mechanical values. Manufacturing restrictions regarding geometric freedom in contrast to laser additive manufacturing are for both, milling and casting, limited. One alternative, in combination with LAM, could be AlSi10Mg. The achievable strength properties are comparable to AlSi10Mg cast material but still circa 180 MPa lower than ScalmalloyRP strength values. The advantages of the combination of LAM and ScalmalloyRP are numerous and will be investigated in more detail in further research.

Table 2 Comparison of alternatives to ScalmalloyRP0,66-4,5 combined with LAM (mean values)

alloy [temper] + process	ultimate strength [MPa]	yield strength [MPa]	elongation [%]	geometric freedom [low - moderate - high]
7050 [T7651] + milling [L]	524	455	7	moderate
AC42200 [T6] + casting	320	240	6	moderate
AlSi10Mg + LAM	340	275	8	high
Scalmalloy RP0,66-4,5[325°C/4h] + LAM	530	520	14	high

5. Conclusion

- The applicability of a laser additive manufacturing process with ScalmalloyRP0,66-4,5 powder is proofed. A hyper eutectic Al-Scandium composition was achieved.
- The increase of hardness between non aged and aged test specimen is due to Al₃Sc precipitates.
- Static mechanical properties exceeded the expected level. The addition of scandium led to high strength but ductile behavior. A grain refinement was achieved that caused high plasticity compared to other high strength Al-alloys (e.g. 7050)
- At this stage, there is no comparable alternative Al-alloy, regarding static mechanical properties, and manufacturing process, regarding geometric freedom.

Acknowledgements

The research leading to these results has received funding from the [European Community's] [European Atomic Energy Community's] Seventh Framework Programme ([FP7/2007-2013] [FP7/2007-2011]) under grant agreement n° 233766.

References

- [1] Røyset, J.; Ryum, N.: Scandium in Aluminium alloys. In: International Mater. Rev 50 (2005), 19-44
- [2] Røyset, J.: Scandium in Aluminium alloys overview: physical metallurgy, properties and applications. In: Metallurgical Science and Technoloy, Vol. 25(2) (2007), 11-21
- [3] Jia, Z.; Fobord, B.; Røyset, J.; Solberg, J.K.: Effect of Heat Treatments on Hardening of Al-Zr-Sc-Alloys. In: Aluminium Alloys, 141-146
- [4] Toropova, L.S.; Eskin, D.G.; Kharakterova, M.L.; Dobatkina, T.V.: Advanced Aluminum Alloys Containing Scandium: Structure and Properties. Gordon and Breach Science Publishers, The Netherlands, 1998.
- [5] Berezina, A.L.; Monastyrskaya, T.O.; Molebny, O.A.; Kotko, A.V.: Phase Transformation: Al₃Sc/Al₃Zr Composite Particles Formation in Deformed Al-Mg Alloys. In: Aluminium Alloys Vol.1 (2008), 1034-1039
- [6] Emadi, D.; Prasada Rao, A.K.; Mahfoud, M.: Influence of scandium on the microstruktur and mechanical properties of A319 alloy. In: Materials Science and Engineering A 527 (2010), 6123-6132
- [7] Zakharov, V.V.: Effect of scandium on the structure and properties of aluminium alloys. In: Metal Science and Heat Treatment Vol.45 (2003), 246-253
- [8] Kaiser, M.S.; Datta, S.; Roychowdhury, A.; Banerjee, M.K.: Effect of Scandium Additions on the Tensile Properties of Cast Al-6Mg alloys. In: Journal of Materials Engineering and Performance Vol. 17(6) (2008), 902-907
- [9] Kaiser, M.S.; Banerjee, M.K.: Effect of Ternary Scandium and Quaternary Zirconium and Titanium Additions on the Tensile and Precipitation Properties of Binary Cast Al-6Mg Alloy. In: Jordan Journal of Mechanical and Industrial Engineering Vol.2 (2008), 93-99
- [10] Gibson, I.; Rosen, D. W.; Stucker, B.: Additive Manufacturing Technologies. Springer, New York, 2010



GE Additive



316L

Stainless steel 316L can be used for the production of acid and corrosion resistant parts in the following fields: plant engineering, automotive industry, medical technology, jewelry and components for molds.

Data in this document represents material built with 50 µm layer thickness and in an Nitrogen atmosphere on an M2 / M2 Multilaser machine. Values listed are typical.

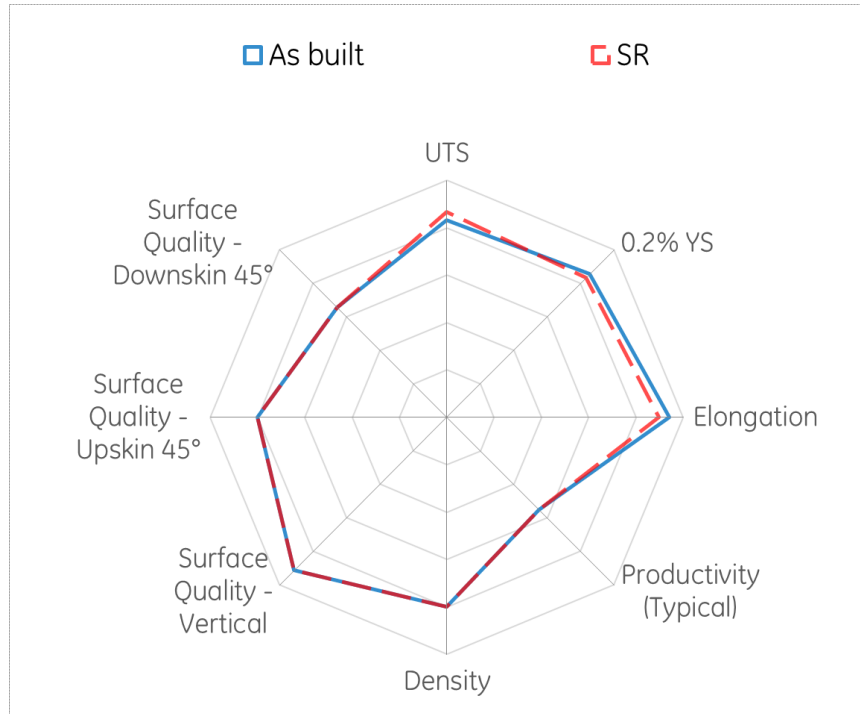
26
Fe

POWDER CHEMISTRY

Element	Indicative value (wt%)
Cr	16.5-18.0
Ni	10.0-13.0
Mo	2.0-2.5
Mn	0-2.0
Si	0-1.0
P	0-0.045
C	0-0.030
S	0-0.030
Fe	Balance

316L (powder) chemical composition et al. according to DIN EN 10088-3

SPIDER PLOT



MACHINE CONFIGURATION

- M2 / M2 Multilaser
- Nitrogen Gas
- Rubber blade
- Layer thickness 50µm

- Build rate dual laser w/ coating *[cm³/h] : 16.5
- Max. Build rate per Laser** [cm³/h]: 21.9

*Measured by using Factory Acceptance Test layout

**Calculated (layer thickness x scan velocity x hatch distance)

THERMAL STATES

1. AS BUILT
2. STRESS RELIEF (SR): 3h to 550°C, hold 6h hour at 550°C

PHYSICAL DATA AT ROOM TEMPERATURE

Thermal State	Surface Roughness - Overhang (μm)						Surface Roughness (μm)	
	45°			60°			75°	
	H	V	H	V	H	V	H	V
As-Built	12	9	8				H	12
VSR	17	12	10				V	8

Thermal State	Porosity (% Density)			Hardness (HV10)		Poisson's Ratio		
	H		V	H	V	H	V	
	As-Built	99.8	99.8	222	--	--	--	--
VSR		99.8	99.8	223	--	--	--	--

Thermal State	Thermal Conductivity (W/m·K)	Coeff. Of Thermal Expansion (mm/mm/K)	Thermal Diffusivity (m ² /s)	Specific Heat (J/K·kg)	
	H	V	H	V	
	As-Built	12.6	15.6 x 10 ⁻⁶	3.4 x 10 ⁻⁶	476
VSR	--	--	--	--	--

Thermal State	Thermal Conductivity (W/m·K)	Coeff. Of Thermal Expansion (mm/mm/K)	Thermal Diffusivity (m ² /s)	Specific Heat (J/K·kg)	
	H	V	H	V	
	As-Built	12.3	15.6 x 10 ⁻⁶	3.4 x 10 ⁻⁶	460
VSR	--	--	--	--	--

TENSILE DATA

Tensile testing done in accordance with ASTM E8 and ASTM E21

Temperature: RT

Thermal State	Modulus of Elasticity (GPa)		0.2% YS (MPa)		UTS (MPa)		Elongation (%)		Reduction of Area (%)		
	H	V	H	V	H	V	H	V	H	V	
	As-Built	182	150	545	480	655	595	44	50	-	-
VSR		198	178	535	465	680	620	40	39	-	-

H: HORIZONTAL (XY) orientation
V: VERTICAL (Z) orientation

* All of the figures contained herein are approximate only. The figures provided are dependent on a number of factors, including but not limited to, process and machine parameters, and the approval is brand specific and/or application specific. The information provided on this material data sheet is illustrative only and cannot be relied on as binding.

316 L

SPECIFICATIONS

EU X2CrNiMo17-12-2

WN 1.4404

USA S31603

MATERIAL DESCRIPTION

- Austenitic stainless steel with high ductility, often used for its good resistance to corrosion.

COMPOSITION

weight %

Fe	—	Balance
Cr	—	17
Ni	—	12
Mo	—	2
Mn	—	1,5
C	—	0,03

APPLICATIONS



MATERIAL SHEET

Typical mechanical properties

The data provided in this document represent typical but not guaranteed values.

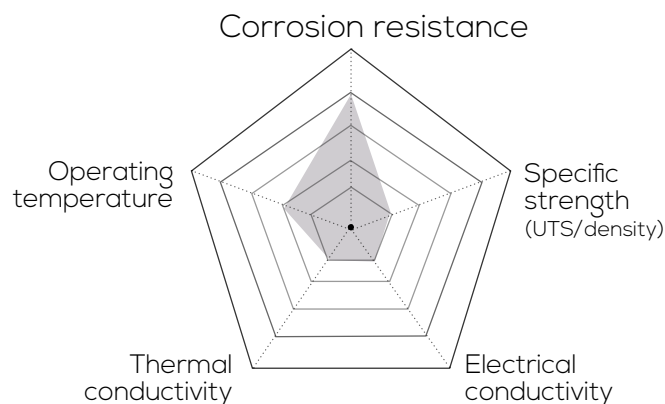
	Stress-relieved	Heat treated*
Ultimate Tensile Strength UTS, MPa	770	600
Yield Strength YS, MPa	640	400
Elongation at break E 5D, %	30	40

* Heat treatment: 1050°C/1h.

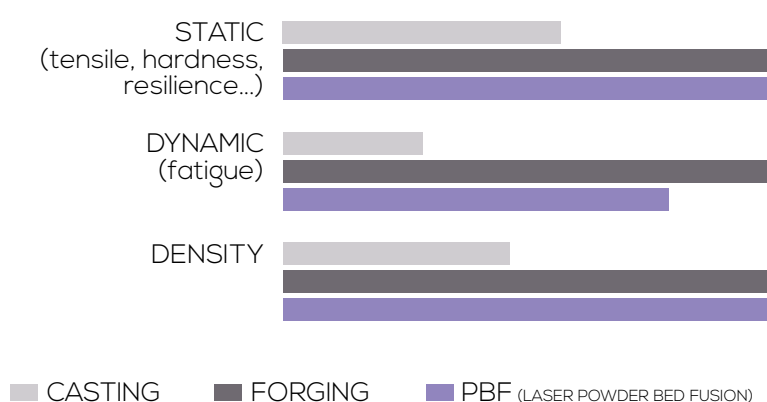
The mechanical characteristics along the Z axis are lowered by about 100 MPa after manufacturing.

The anisotropy is significantly reduced, if not eliminated, after heat treatment.

Physical properties



Qualitative comparison according to processes



Technical data

PARTICLES SIZE :

Available in different granulometries.

SUPPLIERS :

AddUp will provide support with your choice of powder supplier.

Applications, in detail



AUTOMOTIVE

Heat exchanger

316L is well-suited for fluid transfer applications. Its good corrosion resistance allows for long service life.

Metal additive manufacturing allows for the opportunity to develop new designs that incorporate complex, cooling channels. It is also an excellent method to optimize and increase the efficiency of heat transfer.



LUXURY

Watch strap

316L has other advantages including the ability to obtain an improved surface finish. In addition, it also exhibits hypoallergenic properties as it does not cause skin irritations.

Metal additive manufacturing has the ability to produce parts with complex and unique geometries, often reducing the amount of processing steps. It is possible to incorporate various features and mechanisms without subsequent assembly operation.



POWER GENERATION

Mixing blade

316L is used for ductility and corrosion resistance. Generally, mixing blades undergo regular shocks in a corrosive environment. Therefore, these blades need to have high resistance to impacts making 316L suitable for this application.

In addition, metal additive manufacturing allows for the opportunity to utilize topology optimization in the geometric design of this blade.



INDUSTRY

Tapfaucet

When a designer works on a new faucet, he/she may conceptualize new designs including very complex fluid exchanges in order to hide the water flow within the structure of the tap.

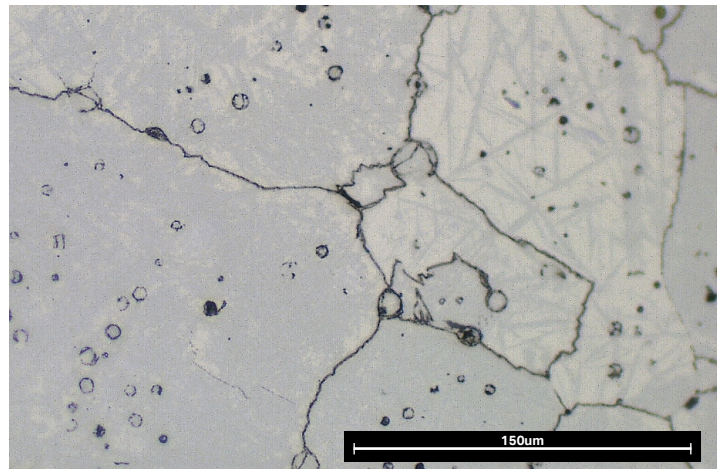
Through conventional manufacturing techniques, it would be extremely difficult, if not impossible, to fabricate parts with these complex shapes and geometries.

A2 Tool Steel

Other Designations: UNS T30102, DIN 1.2363 , X100CrMoV5, SKD12, BA2

A2 Tool Steel is a highly versatile air-hardening tool steel often regarded as a "universal" cold work steel. It offers a combination of good wear resistance (between O1 and D2) and toughness. Considered relatively easy to machine in the annealed condition, it has a high compression strength and good dimensional stability during hardening and tempering. It's used for a wide variety of cold-work tools, from forming and cutting equipment to high wear parts.

Composition	Amount
Chromium	4.75-5.5%
Molybdenum	0.9-1.4%
Carbon	0.95-1.05%
Manganese	0.4-1%
Phosphorus	0.3% max
Vanadium	0.15-0.5%
Silicon	0.1-0.5%
Iron	bal



Typical Mechanical Properties	Standard	Markforged Heat-Treated ¹	Wrought Heat Treated
0.2% Compressive Yield Strength	ASTM E9	1170 MPa	—
Elastic Modulus	ASTM E9	160 GPa	190 GPa
Hardness ³	ASTM E18	50 HRC	63 HRC
Relative Density ⁴	ASTM B923	94.5%	100%

Heat Treatment

A2 Tool Steel can be heat-treated to increase hardness and durability. Markforged recommends heat-treating A2 Tool Steel to optimize material properties for target applications.

1. Heat A2 Tool Steel part in a standard (non vacuum) furnace to 970°C (1780°F) . Hold part at temperature for 30-45 minutes.
2. Air quench part to below 65°C (150 °F).
3. Double temper A2 Tool Steel part in a standard furnace. For each temper, heat part to 150-550°C² (302-1022°F) and temper for 2 hours, or 1 hour per inch of thickness. If double tempering, let part cool to room temperature between temps.

1. Markforged heat-treated A2 Tool Steel was heated to 970°C (1780°F) and single tempered at 200°C (392°F) for 30 minutes.

2. Tempering temperature has a significant effect on final material properties. For higher hardness, temper at low temperatures. For higher toughness, temper at higher temperatures.

3. As-sintered hardness can vary significantly based on furnace loading and ambient environment. Markforged recommends post-sinter heat treatment for maximum hardness and compression strength.

4. Relative density for A2 assumes a density of 7.86 g/cm3.

These data represent typical values for Markforged A2 Tool Steel. Markforged samples were printed with solid fill. Relative density was tested in house. All other data were tested and confirmed by outside sources. These representative data were tested, measured, or calculated using standard methods and are subject to change without notice. Markforged makes no warranties of any kind, express or implied.

AlSi7Mg0.6

DÉNOMINATIONS

- EU** EN AC-42 200
- FR** AS7G06
- USA** UNS357.0

MATERIAL DESCRIPTION

- Aluminium alloy with low density and good corrosion resistance, combined with good mechanical, thermal, and electrical properties.

COMPOSITION

weight %

Al	—	Balance
Si	—	7
Mg	—	0,6

APPLICATIONS



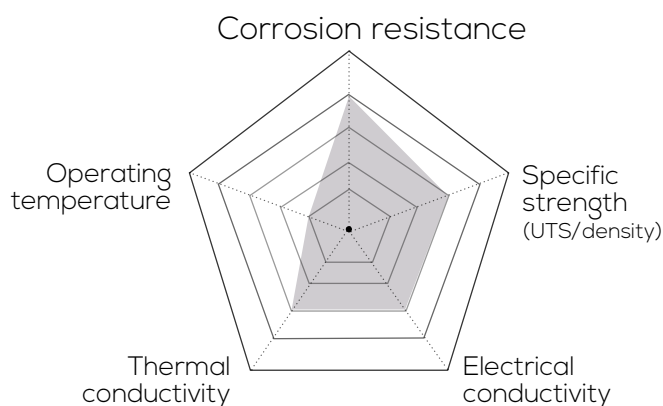
MATERIAL SHEET

Typical mechanical properties

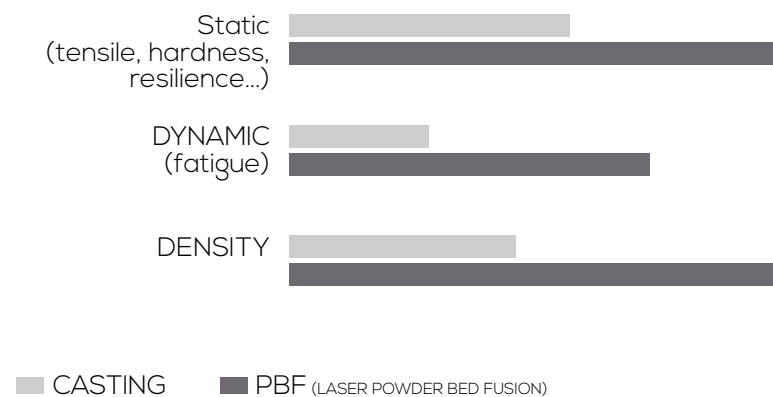
The data provided in this document represent typical but not guaranteed values.

On the FormUp®	
Ultimate Tensile Strength UTS, MPa	425
Yield Strength YS, MPa	250
Elongation at break E 5D, %	14

Physical properties:



Qualitative comparison according to processes



Technical data

PARTICLES SIZE :
Available in different granulometries.

SUPPLIERS :
AddUp will provide support with your choice of powder supplier.

Applications, in detail



AUTOMOTIVE

Engine part

A classical use of aluminium alloys are in car engine parts.

The low weight of AISi7Mg0.6 coupled with additive manufacturing process possibilities allow for complex parts like cylinder heads to be built.



AERONAUTIC

Sub-assembly

AISi7Mg0.6 is a light-weight commonly used in aeronautics applications.

Its low weight combined with design benefits of using additive manufacturing (i.e. increased geometric complexities and topology optimization) can greatly increase the range of use applications.



POWER GENERATION

Heat Exchanger

AISi7Mg0.6 can be used to build heat exchangers because of its excellent thermal conductivity and ability to be easily printed. This increases the geometric complexities as well as surface area, which results in an overall decrease of subsequent parts assembly.

Aluminum F357

Material & Process Capability

Aluminum F357 is an Al-Si-Mg alloy originally developed for castings. It is a lightweight, corrosion resistant alloy with high strength and toughness and excellent thermal conductivity. It is typically used for heat transfer and structural applications in the defense and automotive industries. F357 is easily weldable and machinable and is heat treatable to T6.

The Velo^{3D} intelligent additive printing solution uniquely enables companies to build the parts they need without compromising design or quality—resulting in complex parts higher in performance than traditional casting techniques or other additive methods.



General Process

This data sheet specifies the expected mechanical properties and characteristics of this alloy when manufactured on a Velo^{3D} Sapphire® System. Parts built from Aluminum F357 on a Sapphire® System can be heat treated using processes similar to those used on parts manufactured by other methods. All data is based on parts built with Velo^{3D} standard 50 µm layer thickness parameters. Velo^{3D} uses Tekna Aluminium F357.

Accuracy, Small Parts	±0.050 (±0.002)	(in)
Accuracy, Large Parts	±0.2	percent
Minimum Wall Thickness; up to 500:1 aspect ratio	0.200 (0.008)	(in)
Typical Volume Rate ¹	80	cc per hr
Density	2.67 (0.097)	g/cc (lbs/in ³)
Relative Density	99.9+	percent
Surface Finish, Sa ²	6 (240)	µm (µin)

Mechanical Properties at Room Temperature

Property ³	As Printed		After Heat Treatment ⁵		After Hot Isostatic Pressing ⁶		GPa
	Mean -3σ/ Min	Average	Mean -3σ/ Min	Average	Mean -3σ/ Min	Average	
Modulus of Elasticity ⁴	53.4	73.0	48.2	71.8	49.2	75.8	
Ultimate Tensile Strength	332 (48.1)	350 (50.7)	279 (40.5)	307 (44.5)	302 (43.8)	329 (47.7)	MPa (KSI)
Yield (0.2% Offset)	230 (33.4)	238 (34.5)	225 (32.6)	252 (36.6)	226 (32.8)	262 (37.9)	MPa (KSI)
Elongation At Break	2.61	7.09	5.45	10	9.12	12.76	percent

1. Geometry-dependent. 2. Depends on orientation and process selected. 3. Mechanical & test samples printed in vertical orientation. 4. For reference; estimated from ASTM E8 tensile testing. 5. Heat treatment solution at 540°C for 30 minutes, water quench and age at 160°C for 6 hours. 6. HIP at 510°C at 15 KSI for 4 hours, rapid cool, solution at 540°C for 30 minutes, water quench and age at 160°C for 6 hours.

Headquarters:

511 Division Street
Campbell CA 95008

To learn more visit:

www.velo3d.com
info@velo3d.com

Arcam A2

Setting the standard for
Additive Manufacturing



Additive Manufacturing Realized

The Arcam A2 is the ultimate solution for Additive Manufacturing in the digital age. It is developed for cost-effective production of demanding applications such as structural Aerospace components meeting the highest material standards.

Features include:

- Large build volume for manufacturing of large components.
- Two interchangeable build tanks delivered with each machine. Choose between wide and tall depending on the build at hand.
- MultiBeam™ technology, for high productivity and surface quality.
- Easy to use operator interface.
- LogStudio™, a tool for process validation and quality control.



Race car gearbox casing manufactured with Arcam EBM in Ti6Al4V



The EBM technology

The Arcam A2 is designed for production of any functional part within Aerospace and General Industry. The parts are built up layer-by-layer of metal powder melted by a powerful electron beam. Each layer is melted to the exact geometry dictated by the 3D CAD model. The Electron Beam Melting technology allows for high energy to be used providing high melting capacity and productivity. Parts are built in vacuum at elevated temperatures resulting in stress relieved parts with material properties better than cast and comparable to wrought material.

The Arcam A2 is capable of delivering a beam power of up to 3500 W while maintaining a scan speed that allows melting at multiple points simultaneously. The vacuum system is designed to maintain a vacuum level of 1×10^{-4} mBar or better throughout the entire build cycle.

Powder Recovery System

The Arcam A2 is delivered with a Powder Recovery System enabling 95% recovery of unmelted powder in a build. The Powder Recovery System runs with minimal dust generation for safe operation, closed-loop material recovery and elimination of magnetic materials and fine particles.



The Arcam Powder Recovery System in action.

After the recovery process the recycled powder is ready for re-use in the EBM process.

Materials

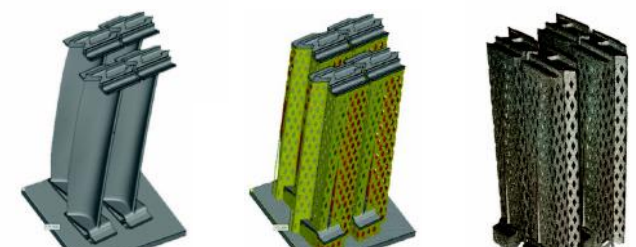
The materials supplied by Arcam are extensively tested before release to customers and the configuration of the powder is optimised for safe and reliable operation of the EBM process.

Support, Maintenance and Training

Arcam offers support and maintenance to ensure highest possible performance of the Arcam A2 throughout its lifetime. This is offered on different levels and includes on-line and application support, preventative maintenance, emergency visits, spare parts and software updates. Training packages are available to ensure a smooth and efficient start-up of the Arcam A2 as well as more in-depth training for continuous improvements.



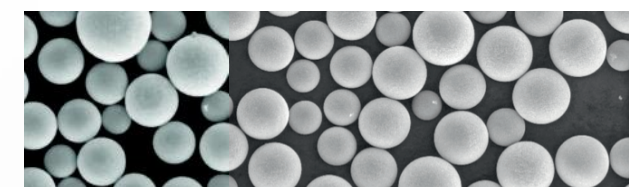
Full size y-TiAl low pressure turbine blades manufactured with EBM.



3D CAD-model.

3D CAD-model with support structure.

As-built blades still with support structure.



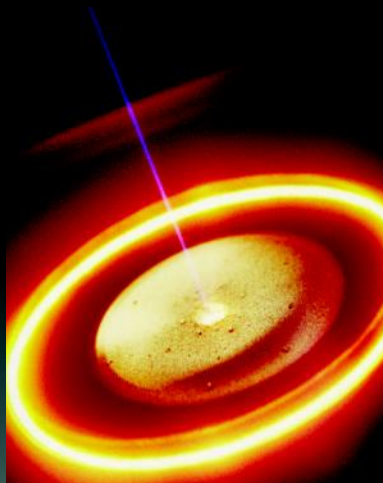
Spherical metal powders supplied by Arcam are optimized for reliable and safe operation.

ARCAM A2 TECHNICAL DATA

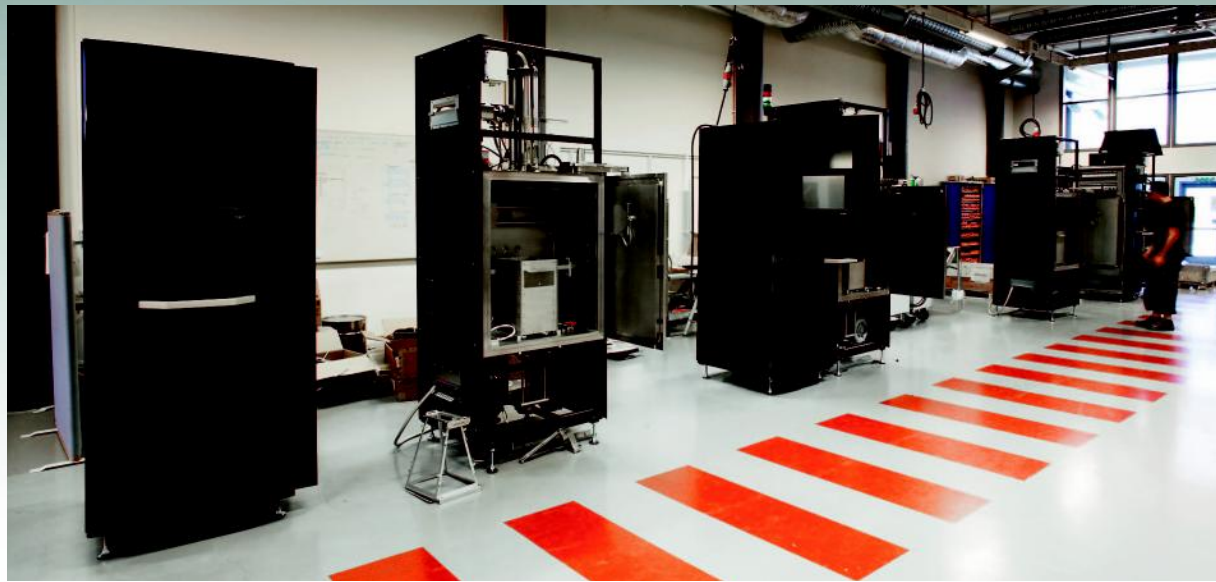
Build tank volume	250x250x400 mm and 350x350x250 mm (W x D x H)
Maximum build size	200x200x350 mm and Ø 300x200 mm (W x D x H)
Model-to-Part accuracy, long range ¹	+/- 0.20 mm (3σ)
Model-to-Part accuracy, short range ¹	+/- 0.13 mm (3σ)
Surface finish (vertical & horizontal) ²	Ra25/Ra35
Beam power	50–3500 W (continuously variable)
Beam spot size (FWHM)	0.2 mm–1.0 mm (continuously variable)
EB scan speed	up to 8000 m/s
Build rate ²	55/80 cm ³ /h (Ti6Al4V)
No. of Beam spots	1–100
Vacuum base pressure	<1x10 ⁻⁴ mBar
Power supply	3x 400 V, 32 A, 7 kW
Size and weight	1850 x 900 x 2200 mm (W x D x H), 1420 kg
Process computer CAD interface	PC
CAD interface	Standard: STL
Network	Ethernet 10/100/1000
Certification	CE

¹ Long range: 100 mm, Short range: 10 mm, measured on Arcam Standard Test Part (ASTP).

² Measured on Arcam Standard Test Part (ASTP).
Settings optimized for fine surface quality/Settings optimized for high build speed.



Inside the Arcam EBM process – a melt pool in the Ti6Al4V powder bed is created by the powerful electron beam.



Arcam A2 assembly line.



Arcam **EBM** system

ASTM F75 CoCr Alloy



www.arcam.com

ASTM F75 CoCr Alloy

General characteristics

Cobalt-based alloys have been used in demanding applications for as long as investment casting has been available as an industrial process. Arcam's Electron Beam Melting technology competes directly with investment casting and is a viable choice for manufacturing complex parts in cobalt-based alloys.

The majority of investment castings made from the cobalt super alloys are cast in an open atmosphere. With Arcam's Electron Beam Melting process the vacuum atmosphere provides a controlled environment and enables superior material properties in the manufactured parts.

CoCrMo alloys are widely used for medical prosthetic implant devices. The alloys are especially used where high stiffness or a highly polished and extremely wear-resistant material is required. CoCrMo alloys are the materials of choice for applications such as knee implants, metal-to-metal hip joints and dental prosthetics.

Cobalt alloys also play an important role in the performance of aero- and land-based gas turbines. While vacuum cast nickel alloys predominate in the hot sections of modern aero turbine engines, cobalt alloys are routinely specified for particularly demanding applications such as fuel nozzles and vanes for industrial gas turbines.

Arcam ASTM F75 is a non-magnetic CoCrMo alloy exhibiting high strength, corrosion resistance, and excellent wear resistance. It is widely used for orthopaedic and dental implants. Highly polished components include femoral stems for replacement hips and knee condyles.

Other cobalt medical implants include acetabular cups and tibial trays. In all cases, but especially in hip components, material quality is imperative as parts are heavily loaded and subject to fatigue.



Hip stem implant.

Special characteristics

The Arcam ASTM F75 CoCr alloy is also suitable for Rapid Manufacturing of production tools for injection moulding of plastic parts. The high hardness of the material and the excellent material qualities allow polishing components to optical or mirror-like finishes, and ensures long tool life.

Tools can be built with complex geometries, and the conformal cooling channels further enhance the tool's life and increase productivity, part and surface quality.

Applications

CoCr is typically used for:

- Gas turbines
- Orthopaedic implants
- Dental implants

Powder specification

The Arcam ASTM F75 CoCr alloy powder for EBM is produced by gas atomization and the chemical composition complies with the ASTM F75 standard's specification. The particle size is 45–100 microns. This limitation of the minimum particle size ensures safe handling of the powder.

Please refer to the Arcam MSDS (Material Safety Data Sheet) for more information about the handling and safety of the Arcam ASTM F75 CoCr alloy.

CHEMICAL COMPOSITION

	Arcam ASTM F75*	ASTM F75 Required
Chromium, Cr	28,5%	27–30%
Molybdenum, Mo	6%	5–7%
Nickel, Ni	0,25%	<0,5%
Iron, Fe	0,2%	<0,75%
Carbon, C	0,22%	<0,35%
Silicone, Si	0,7%	<1%
Manganese, Mn	0,5%	<1%
Tungsten, W	0,01%	<0,2%
Phosphorus, P	0,01%	<0,02%
Sulphur, S	0,005%	<0,01%
Nitrogen, N	0,15%	<0,25%
Aluminium, Al	0,05%	<0,1%
Titanium, Ti	0,01%	<0,1%
Bor, B	0,006%	<0,01%
Cobalt, Co	Balance	Balance

* Typical

MECHANICAL PROPERTIES

	Arcam, as-built*	Arcam, after heat treatment*	ASTM F75-07, required
Rockwell Hardness	47 HRC	34 HRC	25–35 HRC
Tensile Strength, Ultimate		960 MPa 140,000 psi	655 MPa 95,000 psi
Tensile Strength, Yield		560 MPa 80,000 psi	450 MPa 65,000 psi
Elongation at Break	Not applicable	20%	>8%
Reduction of Area	Not applicable	20%	>8%
Fatigue limit, Rotating Beam Fatigue		>10 million cycles at 610 MPa (90 ksi)	

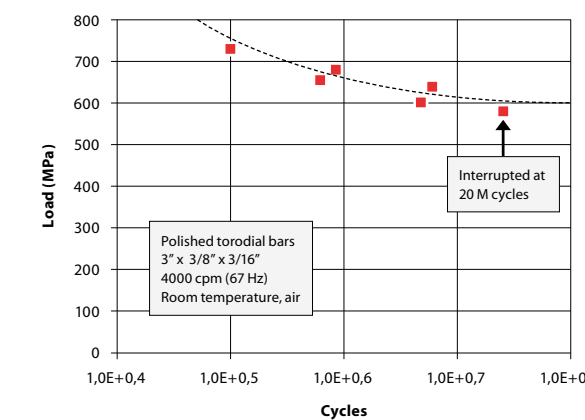
* Typical

Knee implant.

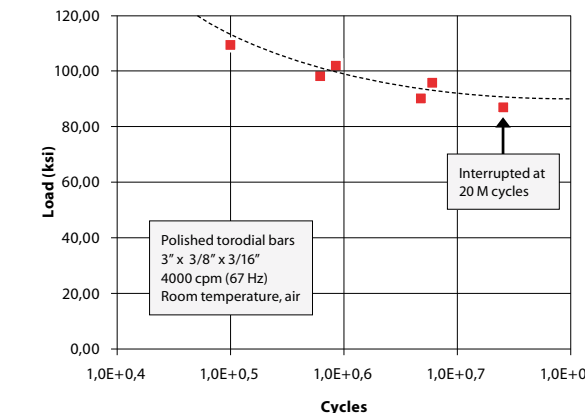


Arcam ASTM CoCr F75 Rotating Beam Fatigue Test

RBF S/N diagram in MPa units



RBF S/N diagram in ksi units



POST PROCESSING

Heat treatment

The following heat treatment program is recommended.

1. Hot isostatic pressing (HIP) in a shared cycle, with the following parameters:

- 1200 °C
- 1000 bar argon
- 240 minutes.
- 2. Homogenisation (HOM) heat treatment, with the following parameters:

- 1220 °C
- 0,7–0,9 mbar argon
- 240 minutes.

As rapid quench rate as possible, from 1220°C to 760°C in 8 minutes maximum. The purpose is to dissolve carbides and improve the isotropy of the microstructure, reducing the brittleness of the as-built EBM material.

Machining

Parts manufactured in the EBM process feature good machinability. Parts produced using the Arcam EBM process demonstrate excellent results when using any conventional machining process.

The excellent properties displayed by the parts manufactured with EBM allow polishing of the parts to a mirror or optical finish for use in dies and other applications requiring a superior surface finish.

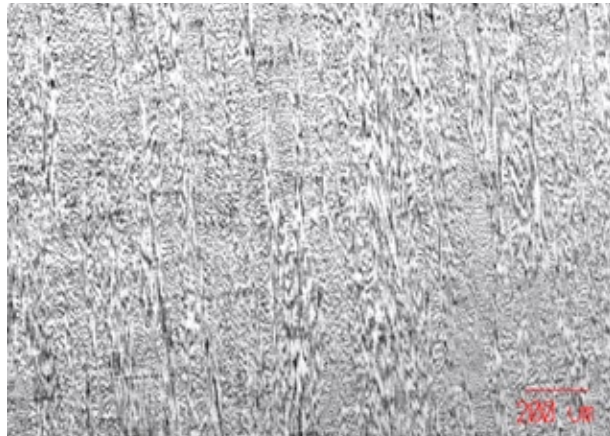
Microstructure

Manufacturing CoCr parts with EBM results in fully dense parts without weld lines in the material before or after heat treatment (HIP+HOM).

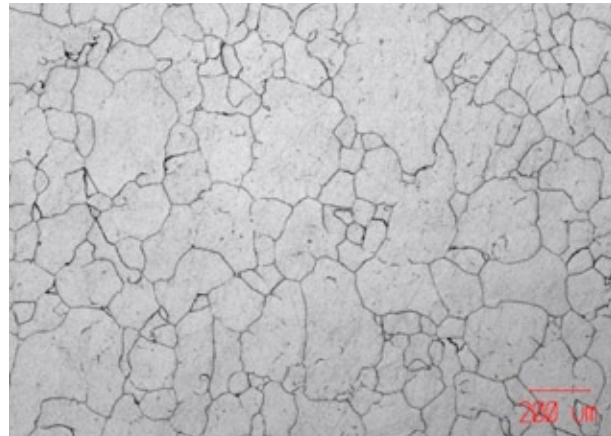
The as-built material consists of elongated grains containing carbide precipitation. Heat treatment transforms the microstructure into an isotropic structure with a substantial reduction of visible carbides.

The images below show the typical microstructure before and after heat treatment (HIP+HOM). The as-built material has elongated grains in the build direction (Z). It contains a high density of carbides that result in the high hardness of the as-built material.

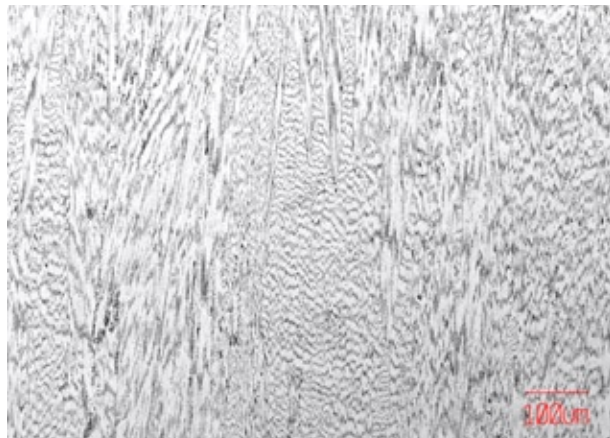
HIP+HOM completely transforms the microstructure into an isotropic state. The carbides are dissolved, leading to the increased ductility and reduced hardness demonstrated in the after the heat treatment specifications. There is no porosity in the as built or in the HIP+HOM material.



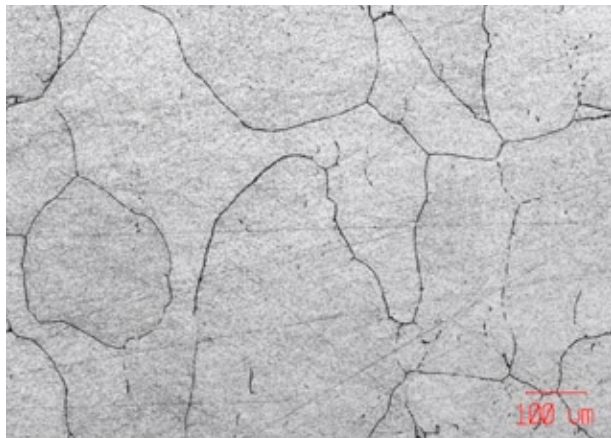
As-built microstructure, etched cross-section along the Z-direction, 50x



Microstructure after HIP+HOM, etched cross-section along the Z-direction, 50x



As-built microstructure, etched cross-section along the Z-direction, 100x



Microstructure after HIP+HOM, etched cross-section along the Z-direction, 100x



Arcam **EBM** system

Ti6Al4V ELI Titanium Alloy



CAD TO METAL
arcam
Arcam AB®

www.arcam.com

Ti6Al4V ELI Titanium Alloy

General characteristics

The high strength, low weight ratio and outstanding corrosion resistance inherent to titanium and its alloys has led to a wide and diversified range of successful applications which demand high levels of reliable performance in surgery and medicine as well as in aerospace, automotive, chemical plant, power generation, oil and gas extraction, sports, and other major industries.

In the majority of these and other engineering applications, titanium replaces heavier, less serviceable or less cost-effective materials. Designs made using the properties provided by titanium often result in reliable, economic and more durable systems and components. These titanium components often substantially exceed performance and service life expectations at a lower overall cost.

Titanium is available in several different grades. Pure titanium is not as strong as the different titanium alloys are. Ti6Al4V is the most widely used titanium alloy. It features good machinability and excellent mechanical properties. The alloy offers the best all-round performance for a variety of weight reduction applications in aerospace, automotive and marine equipment.

Ti6Al4V also has numerous applications in the medical industry. The biocompatibility of Ti6Al4V is excellent, especially when direct contact with tissue or bone is required.

Special characteristics

Ti6Al4V ELI (Grade 23) is very similar to Ti6Al4V (Grade 5), except that Ti6Al4V ELI contains reduced levels of oxygen, nitrogen, carbon and iron. ELI is short for "Extra Low Interstitials", and these lower interstitials provide improved ductility and better fracture toughness for the Ti6Al4V ELI material.

Applications

Ti6Al4V ELI is typically used for:

- Biomedical implants
- Aerospace components
- Cryogenic applications
- Offshore equipment



Scull with lattice custom implant.

The alloy's high resistance to stress corrosion cracking (SCC) in sea water makes Ti6Al4V ELI an obvious choice in applications that require both high strength and corrosion resistance.

Powder specification

The Arcam Titanium Ti6Al4V ELI (Grade 23) is a gas-atomized powder with a particle size between 45 and 100 microns. This limit on the minimum particle size ensures safe handling of the powder.

Please refer to the Arcam MSDS (Material Safety Data Sheet) for more information about the handling and safety of the Arcam Ti6Al4V ELI alloy.

CHEMICAL SPECIFICATION

	Arcam Ti6Al4V ELI*	Ti6Al4V ELI Required**
Aluminium, Al	6,0%	5,5–6,5%
Vanadium, V	4,0%	3,5–4,5%
Carbon, C	0,03%	< 0,08%
Iron, Fe	0,1%	< 0,25%
Oxygen, O	0,10%	< 0,13%
Nitrogen, N	0,01%	< 0,05%
Hydrogen, H	< 0,003%	< 0,012%
Titanium, Ti	Balance	Balance

* Typical ** ASTM F136

MECHANICAL PROPERTIES

	Arcam Ti6Al4V ELI*	Ti6Al4V ELI Required**
Yield Strength (Rp 0,2)	930 MPa	795 MPa
Ultimate Tensile Strength (Rm)	970 MPa	860 MPa
Rockwell Hardness	32 HRC	30–35 HRC
Elongation	16%	>10%
Reduction of Area	50%	>25%
Fatigue strength @ 600 MPa	>10,000,000 cycles	>1,000,000 cycles
Modulus of Elasticity	120 GPa	114 GPa

* Typical ** ASTM F136

The mechanical properties of materials produced in the EBM process are comparable to wrought annealed materials and are better than cast materials.

POST PROCESSING

Heat treatment

Hot Isostatic Pressing (HIP) is recommended for fatigue-loaded components. The following HIP parameters are recommended:

- 920°C
- 1000 bar
- 120 minutes

Machining

Ti6Al4V ELI parts manufactured in the EBM process feature good machinability and can be machined without additional operations.

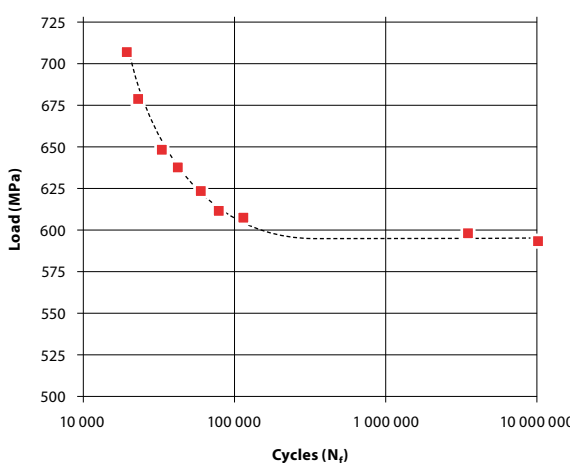
The following factors contribute to efficient machining of Ti6Al4V ELI parts:

- Low cutting speeds
- High feed rate
- Generous quantities of cutting fluid
- Sharp tools
- Rigid setup

Welding

Ti6Al4V ELI may be welded by a wide variety of conventional fusion and solid-state processes, although its chemical reactivity typically requires special measures and procedures.

Arcam Ti6Al4V ELI Rotating Beam Fatigue Test



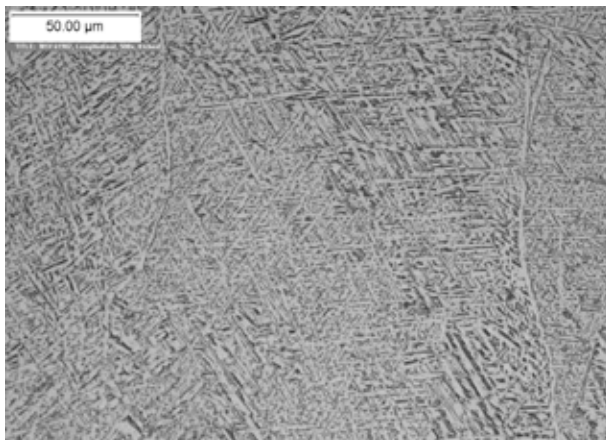
Titanium powder.



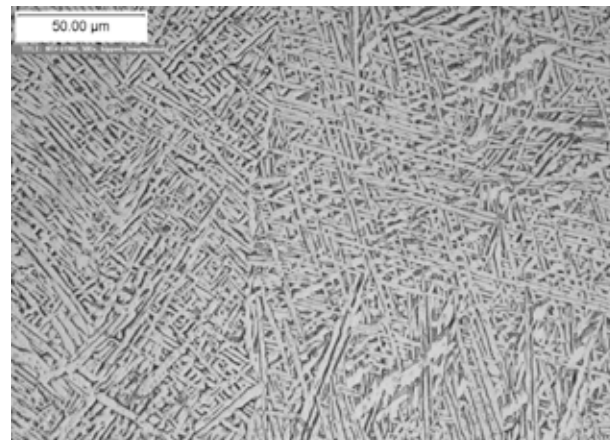
Microstructure

Ti6Al4V ELI parts manufactured in the EBM process have a microstructure better than cast Ti6Al4V ELI containing a lamellar α -phase with larger β -grains, and with a higher density and significantly finer grain, thanks to the rapid cooling of the melt pool.

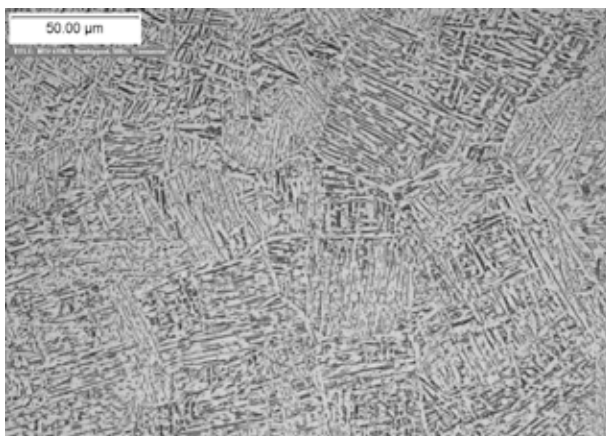
The build chamber is kept at an elevated temperature throughout the entire build process, and the material therefore comes out of the EBM process in a naturally aged condition.



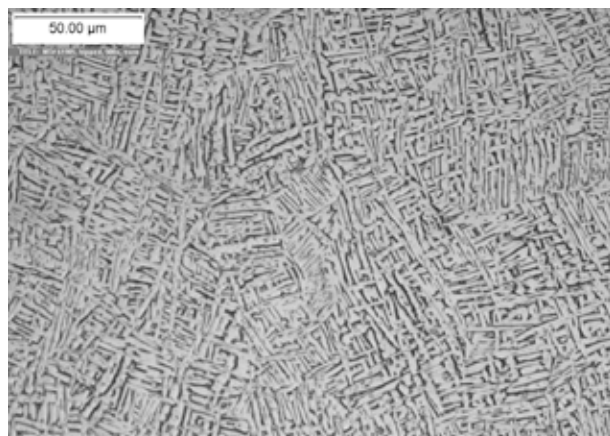
Micrograph of Arcam Ti6Al4V ELI material, 500x.
Longitudinal



Micrograph of Arcam Ti6Al4V ELI material, 500x.
Hipped, longitudinal



Micrograph of Arcam Ti6Al4V ELI material, 500x.
Transverse



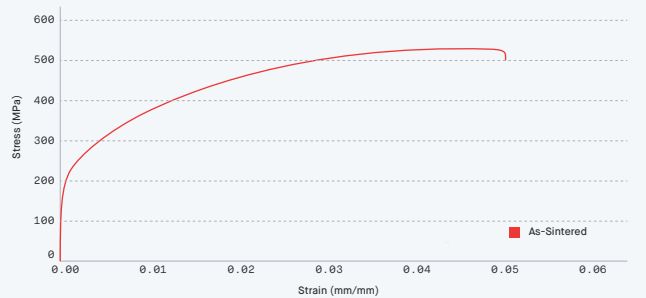
Micrograph of Arcam Ti6Al4V ELI material, 500x.
Hipped, transverse



[Material Data Sheet]

316L v.2

Stainless Steel

**COMPOSITION %**

Fe	bal
Ni	10 - 14
Cr	16 - 18
Mo	2 - 3
Mn	2.0 (max)
Si	1.0 (max)
C	0.03 (max)

**MECHANICAL PROPERTIES**

	Standard	Studio System™ 2 As-Sintered	MIM - MPIF 35 Min As-Sintered	Wrought For reference
Ultimate tensile strength (MPa)	ASTM E8M	533	450	425
Yield strength (MPa)	ASTM E8M	169	140	170
Elongation (%)	ASTM E8M	66	40	40
Hardness (HRB)	ASTM E18	66	67 (typ)	95 (max)
Density (relative)	ASTM B311	97%	95%	100%

PERFORMANCE

	Standard	Studio System™ 2 As-Sintered
Boil test (corrosion)	ASTM F1089	Pass
Copper sulfate test (corrosion)	ASTM F1089	Pass

OTHER STANDARD DESIGNATIONS

UNS S31603

EN 1.4404

- Per MPIF Standard 35, Materials Standards for Metal Injection Molded Parts (MPIF 35-MIM, 2018).
- Wrought values based on ASTM A240 standards.
- Prior to corrosion resistance testing, all test samples were machined and passivated in accordance with ASTM F1089.
- Listed designations are for reference purposes only. Composition and mechanical properties may vary.

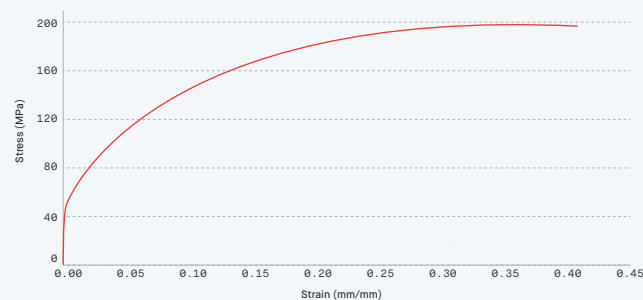
End-use material performance is impacted (+/-) by certain factors including but not limited to part geometry and design, application and evaluation conditions, etc.

Tensile properties and density data reported are mean values minus 1 sigma.

Due to the material's high elongation, strain values were obtained from crosshead displacement. In conformance with ASTM E8M, total elongation was obtained from scribed marks on the gage length and yield strength was calculated from extensometer measurements.

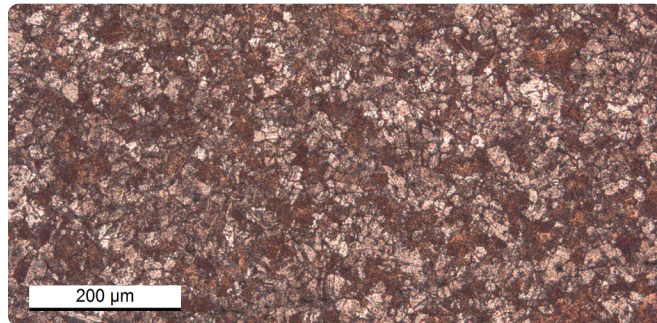
[Material Data Sheet]

Copper



COMPOSITION %

Cu	99.9
O	0.01
Other	Balance



PERFORMANCE

	Standard	Studio System™ As-Sintered	MIM - MPIF 35 typ ¹ As-Sintered
Electrical conductivity	ASTM E1004	85.2 %IACS	n/a
Coefficient of thermal expansion (CTE)	ASTM E228 20 - 38 °C	17.01 *10⁻⁶ /°C	15.7 *10 ⁻⁶ /°C
	ASTM E228 20 - 66 °C	17.15 *10⁻⁶ /°C	16 *10 ⁻⁶ /°C
	ASTM E228 20 - 93 °C	17.22 *10⁻⁶ /°C	16.4 *10 ⁻⁶ /°C
	ASTM E228 20 - 121 °C	17.33 *10⁻⁶ /°C	16.7 *10 ⁻⁶ /°C
	ASTM E228 20 - 149 °C	17.43 *10⁻⁶ /°C	16.9 *10 ⁻⁶ /°C

MECHANICAL PROPERTIES

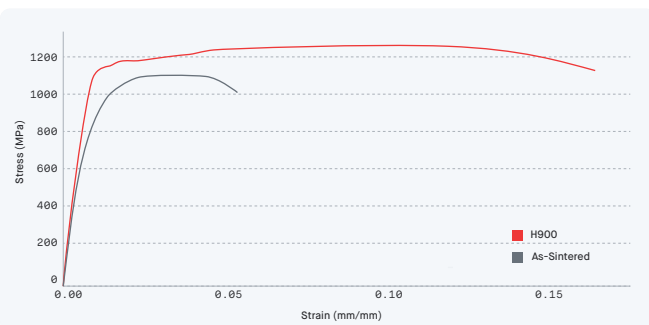
	Standard	Studio System™ As-Sintered	MIM - MPIF 35 typ ¹ As-Sintered
Ultimate tensile strength (MPa)	ASTM E8M	195	207
Yield strength (MPa)	ASTM E8M	45	69
Elongation (%)	ASTM E8M	37	30
Density (g/cc)	ASTM B311	8.75	8.5 (min)

1. Per MPIF Standard 35, Materials Standards for Metal Injection Molded Parts (MPIF 35-MIM, 2018). End-use material performance is impacted (+/-) by certain factors including but not limited to part geometry and design, application and evaluation conditions, etc.

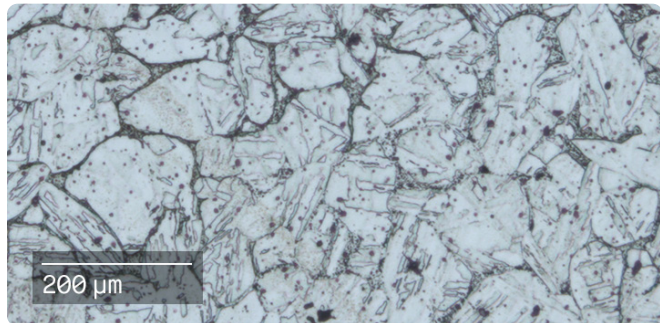
End-use material performance is impacted (+/-) by certain factors including but not limited to part geometry and design, application and evaluation conditions, etc.
Tensile properties, density, and electrical conductivity data reported are mean values minus 1 sigma.

[Material Data Sheet]

17-4 PH Stainless Steel

**COMPOSITION %**

C	0.07 (max)
Cr	15.5-17.5
Ni	3-5
Cu	3-5
Mn	1.0 (max)
Nb+Ta	0.15-0.45
Fe	bal

**MECHANICAL PROPERTIES**

	Standard	Studio System™ + As-Sintered	MIM - MPIF 35 min ² As-Sintered	Studio System™ + H900 Heat Treat	MIM - MPIF 35 min ² H900 Heat Treat
Yield strength (MPa)	ASTM E8M	616	650	1020	970
Ultimate tensile strength (MPa)	ASTM E8M	1092	790	1253	1070
Elongation at break (%)	ASTM E8M	6.3	4	16.4	4
Hardness (HRC)	ASTM E18	30	27 (typ)	42	33 (typ)
Density (g/cc)	ASTM B311	7.6	7.5	7.6	7.5

OTHER STANDARD DESIGNATIONS ¹

UNS S17400

EN 1.4542

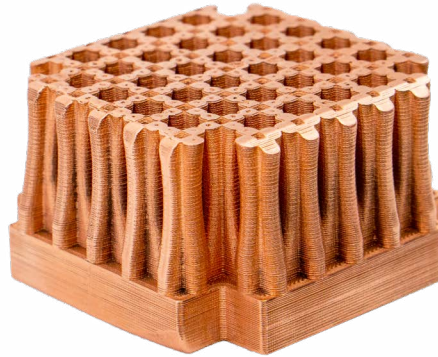
ISO 4542-174-00-I

- Listed designations are for reference purposes only. Composition and mechanical properties may vary.
 - Per MPIF Standard 35, Materials Standards for Metal Injection Molded Parts (MPIF 35-MIM, 2018). End-use material performance is impacted (+/-) by certain factors including but not limited to part geometry and design, application and evaluation conditions, etc.
- Tensile properties, hardness, and density data reported are mean values minus 1 sigma.

Copper

Copper is a soft, ductile metal used primarily for its electrical and thermal conductivity. Copper's high conductivity makes it an ideal material for many heat sinks and heat exchangers, power distribution components such as bus bars, manufacturing equipment including spot welding shanks, antennae for RF communications, and more. The ability to print pure copper using Metal X enables geometrically optimized parts that were previously expensive, time consuming, or impossible to make.

Composition	Amount
Copper	99.8% min
Oxygen	0.05% max
Iron	0.05% max
Other	bal



Typical Mechanical Properties	Standard	Temp	Markforged As-Sintered	MIM Standard
Ultimate Tensile Strength	ASTM E8	Room Temp	193 MPa ¹	207 MPa
0.2% Tensile Yield Strength	ASTM E8	Room Temp	26 MPa ¹	69 MPa
Elongation at Break	ASTM E8	Room Temp	45% ¹	30%
Relative Density	ASTM B923	Room Temp	98% ²	98%
Electrical Conductivity	ASTM E1004	Room Temp	84% IACS ³	—
Thermal Conductivity	ASTM E1461	Room Temp	350 W/mK ⁴	328 W/mK
Coefficient of Thermal Expansion	ASTM E831-19 ⁵	68-100°F	9.6 x 10 ⁻⁶ /°F	8.7 x 10 ⁻⁶ /°F
	ASTM E228	68-150°F	9.7 x 10 ⁻⁶ /°F	8.9 x 10 ⁻⁶ /°F
		68-200°F	9.8 x 10 ⁻⁶ /°F	9.1 x 10 ⁻⁶ /°F
		68-250°F	9.9 x 10 ⁻⁶ /°F	9.3 x 10 ⁻⁶ /°F
		68-300°F	10.0 x 10 ⁻⁶ /°F	9.4 x 10 ⁻⁶ /°F
		68-500°F	10.1 x 10 ⁻⁶ /°F	—
		68-750°F	10.5 x 10 ⁻⁶ /°F	—

1. Tensile bars are sub-sized and are sliced with default copper settings except raft is turned off. Copper defaults to solid parts.

2. Density is based on a theoretical value of 8.96g/cc.

3. Electrical conductivity, when evaluated with eddy current instruments, is usually expressed as a percentage of the conductivity of the International Annealed Copper Standard (% IACS). The conductivity of the Annealed Copper Standard is defined to be 0.58×108 S/m (100 % IACS) at 20°C.

4. Thermal diffusivity measured per ASTM E1461. Diffusivity was converted to Conductivity using, Thermal Conductivity = Thermal Diffusivity * Density * Specific Heat. Assuming specific heat of Copper = 0.385 J/g-K per "Handbook of Chemistry and Physics 72nd Edition."

5. Markforged as-sintered Coefficient of Thermal Expansion (CTE) was measured by a 3rd party lab using Thermal Mechanical Analysis (ASTM E831). The MIM handbook reference used a Push Rod Dilatometer (ASTM E228)

These data represent typical values for Markforged Copper as-sintered. Markforged samples were printed with Solid Infill setting. All values based on 3rd party testing except for relative density which was tested by Markforged. These representative data were tested, measured, and calculated using standard methods and are subject to change without notice. Markforged makes no warranties of any kind, express or implied.